



LABORATORI NAZIONALI DI FRASCATI
SIS – Pubblicazioni

LNF-05/26 (P)
20 Dicembre 2005

Papers presented at PAC 2005

Accelerator Division

Presented at the
2005 Particle Accelerator Conference (PAC 2005)
Knoxville, Tennessee, USA - May 16-20, 2005

CONTENTS

Invited Oral

Frontiers of RF Photoinjectors

M. Ferrario 7

Progress and Plans for R&D and the Conceptual Design of the ILC Injector Systems

S. Guiducci 12

DAΦNE Operation and Plans for DAΦNE2

M. Zobov, D. Alesini, G. Benedetti, M.E. Biagini, C. Biscari, R. Boni, M. Boscolo, A. Clozza, G. Delle Monache, G. Di Pirro, A. Drago, A. Gallo, A. Ghigo, S. Guiducci, M. Incurvati, C. Ligi, F. Marcellini, G. Mazzitelli, C. Milardi, L. Pellegrino, M. A. Preger, P. Raimondi, R. Ricci, C. Sanelli, M. Serio, F. Sgamma, B. Spataro, A. Stecchi, A. Stella, C. Vaccarezza, M. Vescovi, LNF-INFN; E. Levichev, P. Piminov, D. Shatilov, BINP; J. Fox, D. Teytelman, SLAC..... 17

Contributed Oral

Temporal E-Beam Shaping in an S-Band Accelerator

H. Loos, D. Dowell, S. Gilevich, C. Limborg-Deprey, SLAC; Y. Shen, J. Murphy, B. Sheehy, T. Tsang, X. Wang, Z. Wu, BNL; L. Serafini, INFN-Milano, M. Boscolo, M. Ferrario, M. Petrarca, C. Vicario, INFN-LNF 22

Proposal of an Experiment on Bunch Length Modulation in DAΦNE

C. Biscari, D. Alesini, G. Benedetti, M.E. Biagini, R. Boni, M. Boscolo, A. Clozza, G. Delle Monache, G. Di Pirro, A. Drago, A. Gallo, A. Ghigo, S. Guiducci, M. Incurvati, C. Ligi, F. Marcellini, G. Mazzitelli, C. Milardi, L. Pellegrino, M.A. Preger, P. Raimondi, R. Ricci, C. Sanelli, M. Serio, F. Sgamma, B. Spataro, A. Stecchi, A. Stella, C. Vaccarezza, M. Vescovi, M. Zobov, LNF-INFN; C. Pagani, INFN-Milano LASA; E. Levichev, P. Piminov, D. Shatilov, BINP; J. Byrd, F. Sannibale, LBL; J. Fox, D. Teytelman, SLAC 25

Contributed Posters

Recent Observations on a Horizontal Instability in the DAΦNE Positron Ring

A. Drago, M. Zobov, INFN-LNF; Dmitry Teytelman, SLAC 28

The Project PLASMONX for Plasma Acceleration Experiments and a Thomson X-Ray Source at SPARC

D. Alesini, M. Bellaveglia, S. Bertolucci, M.E. Biagini, R. Boni, M. Boscolo, M. Castellano, A. Clozza, G. Di Pirro, A. Drago, A. Esposito, M. Ferrario, L. Ficcadenti, D. Filippetto, V. Fusco, A. Gallo, G. Gatti, A. Ghigo, S. Guiducci, M. Incurvati, C. Ligi, F. Marcellini, M. Migliorati, A. Mostacci, L. Palumbo, L. Pellegrino, M. Preger, R. Ricci, C. Sanelli, M. Serio, F. Sgamma, B. Spataro, A. Stecchi, A. Stella, F. Tazzioli, C. Vaccarezza, M. Vescovi, C. Vicario, INFN-LNF; F. Alessandria, A. Bacci, R. Bonifacio, I. Boscolo, F. Broggi, S. Cialdi, C. DeMartinis, D. Giove, C. Maroli, M. Mauri, V. Petrillo, N. Piovella, R. Pozzoli, M. Romè, L. Serafini, INFN-MI and Univ. of Milano; M. Mattioli, P. Musumeci, M. Petrarca, INFN-Roma1; U. Bottigli, B. Golosio, P. Oliva, A. Poggiu, S. Stumbo, INFN/Cagliari and Univ. of Sassari; A. Barbini, W. Baldeschi, C.A. Cecchetti, M. Galimberti, A. Giulietti, D. Giulietti, L.A. Gizzi, P. Koester, L. Labate, S. Laville, A. Rossi, P. Tomassini, CNR-IPCF/Pisa and Univ. of Pisa..... 31

RF and Magnetic Measurements on the SPARC Photoinjector and Solenoid at UCLA J.B. Rosenzweig, A.M. Cook, M.P. Dunning, P. Frigola, G. Travish, UCLA; C. Sanelli, F. Tazzioli, INFN-LNF; D.T. Palmer, SLAC	34
A Preliminary Interaction Region Design for a Super B-Factory M. Sullivan, M. Donald, S. Ecklund, A. Novokhatski, J. Seeman, U. Wienands, SLAC; M. Biagini, INFN-LNF	37
Parameters of a Super-B-Factory Design Seeman, Y. Cai, S. Ecklund, J. Fox, S. Heifets, N. Li, P. McIntosh, A. Novokhatski, M. Sullivan, D. Teytelman, U. Wienands, SLAC; M. Biagini, INFN-LNF	40
Performance of the PEP-II B-Factory Collider at SLAC J. Seeman, M. Browne, Y. Cai, W. Colocho, F.-J. Decker, M. Donald, S. Ecklund, R. Erickson, A. Fisher, J. Fox, S. Heifets, R. Iverson, A. Kulikov, N. Li, A. Novokhatski, M. Ross, P. Schuh, T. Smith, K. Sonnad, M. Stanek, M. Sullivan, P. Tenenbaum, D. Teytelman, J. Turner, M. Weaver, D. Van Winkle, U. Wienands, M. Woodley, Y. Yan, G. Yocky, SLAC; W. Kozanecki, CEA/Saclay; G. Wormser, Orsay; M. Biagini, INFN-LNF; C. Steier, A. Wolski, LBNL	43
X-Band Dipole Mode Deflecting Cavity for the UCLA Neptune Beamline R. J. England, B. O'Shea, J. B. Rosenzweig, G. Travish, UCLA D. Alesini, INFN/LNF	46
Design of a Multi-Cell, Hom Damped Superconducting Cavity for the Strong RF Focusing Experiment at DAΦNE D. Alesini, C. Biscari, R. Boni, A. Gallo, F. Marcellini, M. Zobov, INFN-LNF; Carlo Pagani, INFN-LASA and DESY	49
Optimization of RF Compressor in the SPARX Injector M. Boscolo, M. Ferrario, B. Spataro, INFN-LNF; C. Ronsivalle, ENEA-Frascati; L. Serafini, INFN-MI	52
SPARC Working Point Optimization for a Bunch with Gaussian Temporal Profile M. Boscolo, M. Ferrario, V. Fusco, M. Migliorati, INFN-LNF; C. Ronsivalle, ENEA-CR; S. Reiche, UCLA	55
Preliminary Results on Beam Dynamics of Laser Pulse Shaping Effects in SPARC M. Boscolo, M. Ferrario, M. Migliorati, INFN-LNF; F. Castelli, S. Cialdi, A. Flacco, INFN-MI	58
Magnesium Film Photocathodes for High Brilliance Electron Injectors G. Gatti, F. Tazzioli, C. Vicario, INFN-LNF; I. Boscolo, S. Cialdi, Milan University and INFN-MI; L. Cultrera, A. Perrone, Lecce University. and INFN-Lecce; M. Rossi, Rome University La Sapienza; S. Orlanducci, M.L. Terranova, Rome University Tor Vergata and INFN-RM2	61
The SPARC RF Synchronization System Alessandro Gallo, David Alesini, Marco Bellaveglia, Roberto Boni, Giampiero Di Pirro, Franco Tazzioli INFN-LNF	64
Klystron Linearizer for Use with 1.2 MW 476 MHz Klystrons in PEP-II RF Systems J. Fox, T. Mastorides, D. Teytelman, D. Van Winkle, Y. Zhou, SLAC; A. Gallo, INFN-LNF	67

Phase-Space Dynamic Tracking by a two Pickups Data Acquisition System	
A. Drago, M.E. Biagini, S. Guiducci, C. Milardi, M. Preger, C. Vaccarezza, M. Zobov, INFN- LNF	70
The Care Accelerator R&D Programme in Europe	
O. Napoly, R. Aleksan, A. Devred, CEA/DSM/DAPNIA; R. Garoby, R. Losito, L. Rinolfi, F. Ruggiero, W. Scandale, D. Schulte, M. Vretenar, CERN; H. Mais, D. Proch, DESY; A. Ghigo, INFN-LNF; V. Palladino, INFN-NA; T. Garvey, F. Richard, LAL, Orsay; E. Gschwendtner, University of Geneva; A. Den Ouden, Twente University, Enschede	73
Commissioning and first Measurements on the CTF3 Chicane	
A. Ghigo, D. Alesini, G. Benedetti, C. Biscari, M. Castellano, A. Drago, D. Filippetto, F. Marcellini, C. Milardi, B. Preger, M. Serio, F. Sgamma, A. Stella, M. Zobov INFN-LNF; R. Corsini, T. Lefevre, F. Tecker, CERN	76
Status of the SPARC Project	
D. Alesini, S. Bertolucci, M. Bellaveglia, M.E. Biagini, R. Boni, M. Boscolo, M. Castellano, A. Clozza, G.Di Pirro, A. Drago, A. Esposito, M. Ferrario, L. Ficcadenti, D. Filippetto, V. Fusco, A. Gallo, G. Gatti, A. Ghigo, S. Guiducci, M. Incurvati, C. Ligi, F. Marcellini, M. Migliorati, A. Mostacci, L.Palumbo, L. Pellegrino, M. Preger, R. Ricci, C. Sanelli, M. Serio, F. Sgamma, B. Spataro, A. Stecchi, A. Stella, F. Tazzioli, C. Vaccarezza, M. Vescovi, C. Vicario, INFN-LNF; F. Alessandria, A. Bacci, I. Boscolo, F. Broggi, S. Cialdi, C. De Martinis, D. Giove, C. Maroli, M. Mauri, V. Petrillo, M. Romè, L. Serafini, INFN-MI and Univ. of Milano; D. Levi, M. Mattioli, G. Medici, P. Musumeci, D. Pelliccia, M. Petrarca, INFN-Roma1; A. Cianchi, L. Catani, E. Chiadroni, E. Gabrielli, S. Tazzari, INFN-Roma2; F. Ciocci, G. Dattoli, A. Dipace, A. Doria, F. Flora, G.P. Gallerano, L. Giannessi, E. Giovenale, G. Messina, P.L. Ottaviani, S. Pagnutti, G. Parisi, L. Picardi, M. Quattromini, A. Renieri, G. Ronci, C. Ronsivalle, M. Rosetti, E. Sabia, M. Sassi, A. Torre, A.Zucchini, ENEA-Frascati; S. De Silvestri, M. Nisoli, S. Stagira, Politecnico Milano; J.B. Rosenzweig, UCLA; D.H. Dowell, P. Emma, C. Limborg, D. Palmer, SLAC	79
Design and Measurements of an X-Band Accelerating Cavity for SPARC	
D. Alesini, M. Ferrario, B. Spataro, INFN-LNF; A. Bacci, INFN-LASA; A. Falone, M. Migliorati, A. Mostacci, F. Palpini, L. Palumbo, Rome Univ. "La Sapienza"	82
Start to end Simulation for the SPARX Project	
Boni, M. Boscolo, M. Ferrario, V. Fusco, M. Migliorati, L. Palumbo, B. Spataro, C. Vaccarezza, M. Vescovi, INFN-LNF; L. Giannessi, M. Quattromini, C. Ronsivalle, ENEA Frascati; L. Serafini, INFN-MI	85
Recent Results from and Future Plans for the VISA II SASE FEL	
G. Andonian, R. Agustsson, P. Frigola, A. Murokh, C. Pellegrini, S.Reiche, J. Rosenzweig, G. Travish, UCLA; M. Babzien, I. Ben-Zvi, V. Litvinenko, V. Yakimenko, BNL; I. Boscolo, S. Cialdi, A. Flacco, INFN-Milano; M. Ferrario, L. Palumbo, C. Vicario, INFN/LNF; J. Huang, PAL, Pohang, S. Korea	88
Electron Cloud Build-up Study for DAΦNE	
R. Cimino, A. Drago, C. Vaccarezza, M. Zobov, INFN-LNF; G. Bellodi, CCLRC/RAL/ASTeC, Didcot; D. Schulte, F. Zimmermann, CERN; G. Rumolo, GSI; K. Ohmi, KEK; M. Pivi, SLAC	91
Experimental Determination of E-Cloud Simulation Input Parameters for DAΦNE	
N. Mahne, TASC-INFM Trieste; A. Giglia, S. Nannarone, TASC-INFM Trieste and Univ. Modena e RE Modena; R. Cimino, C. Vaccarezza, LNF-INFN	94

FRONTIERS OF RF PHOTOINJECTORS

Massimo Ferrario, INFN-LNF Frascati (Rome), Italy

Abstract

New ideas have been recently proposed to achieve ultra-high brightness electron beams, as particularly needed in SASE-FEL experiments, and to produce flat beams, as required in linear colliders. By proper radial shaping of the photoemission laser pulses, a pancake bunch can be created that will evolve automatically into a uniformly filled 3D ellipsoid, i.e. into the ideal bunch. Low emittance schemes already foreseen for split normal conducting photoinjectors have been applied to the superconducting case in order to produce high peak and high average beam brightness. RF compressor techniques have been partially confirmed by experimental results. Research and experiments in the flat beam production from a photoinjector as a possible alternative to damping rings are in progress. An overview of recent advancements and future perspectives in photoinjector beam physics is reported in this paper.

INTRODUCTION

The research and development of high brightness (high current, low emittance) beam production by photoinjectors has been driven in the last decade mainly by self amplified, spontaneous emission, free-electron laser (SASE FEL) applications. Beams with normalized emittances lower than $1 \mu\text{m}$, with peak current of some kA, are required for example for the new x-ray SASE FEL projects [1,2]. Usually, to enhance brightness one has to expose emitting cathode to a very high electric field, and also to introduce magnetic solenoid fields within the photoinjector gun region. These focusing fields allow control and mitigation of space-charge effects, a process termed emittance compensation [3]. In the following sections we describe how a beam can be manipulated in straightforward ways to obtain high peak and average brightness in FELs, and the possibility of high luminosity in linear colliders.

In the FEL context a beam dynamics regime of RF photoinjectors, dealing with a violent bunch elongation under the action of longitudinal space charge forces, the Blow-Out regime, has been recently re-considered as a possible alternative to laser pulse shaping techniques [4,5,6]. A revival of longitudinal focusing techniques with a deeper understanding of emittance compensation theory [7] has opened up a new possibility of compressing the beam inside an RF structure or in a downstream drift, with a proper beam control employed through solenoid focusing to avoid the emittance degradation [8]. This option may avoid the serious phase space degradations observed in magnetic chicanes caused by coherent synchrotron radiation (CSR) emitted in the bends [9]. Kilo-ampere beams with low emittance have been predicted by simulations for the so-called velocity bunching configuration [8]. At DUVFEL (BNL) [10],

Tokyo University (UTNL) [11], and PLEIADS (LLNL) [12] preliminary experimental results (in non-optimized beam lines) have verified the usefulness of this idea for strongly compressing photoinjector-derived beams, despite the space charge induced emittance degradation observed.

With the advent of proposed superconducting energy recovery linacs (ERL) dedicated to production of radiation [13] that operate at high average current (high duty factor), the demand for high peak and high average brightness, pushes the injector community to consider also the possibility of using a superconducting RF photoinjector.

In a different context, a new technique has been proposed [14] and recently tested [15] at FNAL, the so-called flat beam production, which is an important goal for linear colliders. It consists in a simple transformation of a magnetized round beam, with equal emittances in both transverse planes, produced by a photo-cathode embedded in a solenoid field, which is then followed by a skew quadrupoles triplet. With proper matching, a flat beam with high transverse emittance ratio (300) as required by linear colliders, may in principle be obtained. Experimental results have achieved so far an emittance ratio of 100.

HIGH BRIGHTNESS BEAM PRODUCTION

A uniformly filled 3D ellipsoid, the so called “waterbag”, is the ideal bunch [16]. The waterbag is characterized by perfectly linear behavior: it is the only charged particle distribution whose internal space charge force field is a linear function of position. The generation of such a bunch configuration directly from the cathode has been recently investigated and its excellent features in terms of negligible emittance growth has been verified by numerical simulations in a realistic photoinjector beam line [17]. Unfortunately the generation of a 3D ellipsoid with uniform charge distribution directly from the cathode is not an easy task and demands challenging solution of the laser pulse shaping system. The techniques proposed in [17] foresee the stacking of a number of Gaussian pulses of different radii or a spectral control of UV beam using four-gratings with masking array in dispersive environment. The demonstration of feasibility of such a laser system is the main challenge for this scheme.

Another way to produce waterbag like bunches has been also recently re-considered [5]. The use of femtosecond photoemission laser pulses in high-gradient RF photoinjectors enables the production of electron bunches whose rest-frame bunch length is much smaller than the bunch radius, the so-called ‘pancake’ bunch. By proper radial shaping of the photoemission laser pulses a pancake bunch can be created that will evolve

automatically into a uniformly filled 3D ellipsoid, the so called “blow-out” regime [4]. The clear advantage of this scheme is that longitudinal laser pulse shaping is not anymore an issue, in addition once the beam has reached its final waterbag configuration at the exit of the gun the invariant envelope [7] matching conditions with the booster still hold and the emittance compensation process can be accomplished, as reported in [6]. On the other hand high charge operation (\sim nC) becomes difficult, because image charge on the cathode may drive incorrect final state. The simulation result [5] shown in Fig 1 is the projection in the x - z plane at the exit of the gun. The cathode was illuminated with a 100 fs long pulse with 1 mm spot size and the extracted charge was 100 pC. The current profile is close to the parabolic shape expected for a uniform ellipsoidal distribution, Fig 2a, and the distribution in the longitudinal phase space is characterized by perfectly linear behavior, Fig 2b.

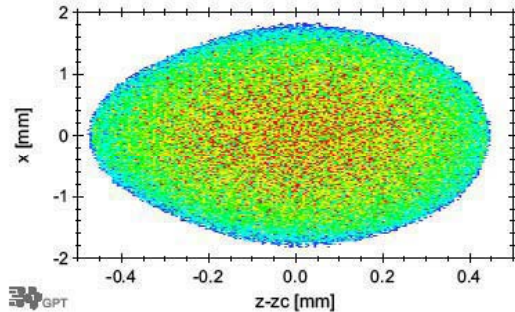


Fig. 1: Projection in the $x - z$ plane of the electron bunch at the exit of the gun.

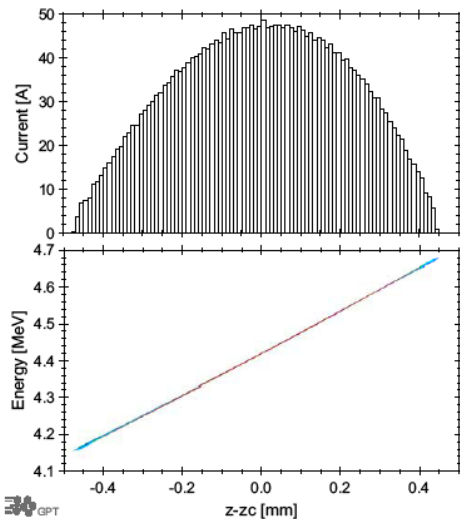


Fig. 2: a) upper plot: current profile b) lower plot: longitudinal phase space distribution of the bunch.

Very interesting progress have been reported concerning the generation of a “beer can” bunch with uniform charge distribution. The laser system equipped with a Dazzler

crystal described in [18] will soon allow the generation of a flat top laser pulse with sub ps rise time. An important prerequisite for the optimal operation of the photoinjector working point described in [19], adopted by many photoinjector projects like LCLS, TESLA X-FEL, SPARC [20]. A preliminary confirmation of the usefulness of such a working point has been demonstrated at the Tesla Test Facility, where a 1 nC beam with longitudinal Gaussian profile has been transported up to the exit of the first cryomodule at 100 MeV, i. e. above the space charge dominated beam threshold, with a measured normalized emittance of $2 \mu\text{m}$ in very good agreement with the simulations predictions [21]. A very remarkable results considering that a flat top pulse, when available, should reduce the emittance by a factor 2, meeting the requirements for the X FEL injector. In the next fall a dedicated experiment will be performed at the SPARC photoinjector to investigate in more details the emittance compensation process by means of a movable emittance meter device [22], in order to fully characterise the 6D phase space of this working point.

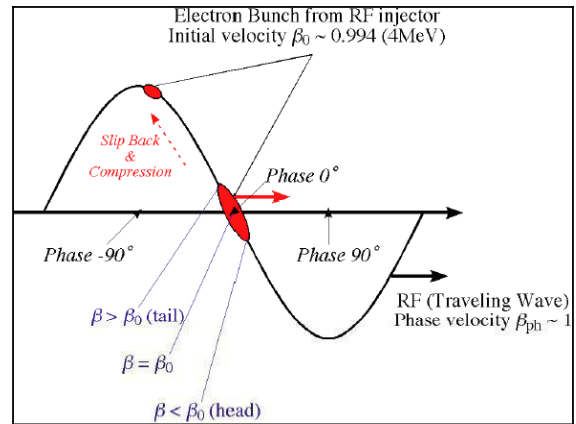


Fig. 3: Scheme of the velocity bunching mechanism.

Since the impact of magnetic compressors on the beam quality is a relevant and compelling topic, with the tendency to have serious emittance growth due to coherent synchrotron radiation effects in bends, a new method able to compress the bunch at moderate energies (tens of MeV), using rectilinear trajectories, and integrated in the emittance compensation process, has been proposed [8]. This scheme, see Fig. 3, named *velocity bunching*, has the following characteristics: although the phase space rotation in this process is still based on a correlated velocity chirp in the electron bunch, in such a way that electrons on the tail of the bunch are faster (more energetic) than electrons in the bunch head, this rotation does not happen in free space but inside the longitudinal potential of a traveling RF wave which accelerates the beam inside a long multi-cell traveling wave (TW) RF structure, applying at the same time an off crest energy chirp to the injected beam. This is possible if the injected beam is slightly slower than the phase velocity of the RF wave so that, when injected at the

crossing field phase (no field applied), it will slip back to phases where the field is accelerating, but at the same time it will be chirped and compressed. The key point is that compression and acceleration take place at the same time within the same linac section, actually the first section following the gun, that typically accelerates the beam, under these conditions, from a few MeV (> 4) up to 25-35 MeV.

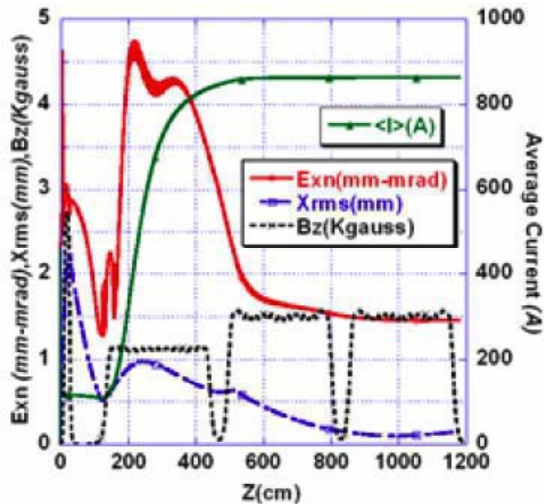


Fig. 4: Average current, transverse emittance and envelope, axial magnetic field vs z for a 860 A compressed beam.

A careful optimization of a high brightness photoinjector, with integrated velocity bunching as required for the SPARX project has been reported in [23]. The plots in Fig. 4, of the peak current and the transverse normalized rms emittance (a thermal emittance of 0.3 mm is included) as a function of the distance from the cathode computed by PARMELA for 100 K particles, show that a peak current of 860 A can be reached with a transverse rms normalized emittance of 1.5 μm . The final beam energy is only 150 MeV, so additional care must still be taken after this point in order to properly damp residual emittance oscillation driven by space charge correlations. The integration of a velocity bunching in a long linac (1 GeV) with additional magnetic compression has been also investigated [24] showing the excellent performance of such an hybrid scheme. The experimental results achieved so far are compared in Tab 1. It is important to note that none of the velocity bunching experiment has been performed on a machine specifically designed for this kind of process: the DUV-Fel experiment was performed in a sufficiently high energy linac but without solenoid around the accelerating structures so that emittance control during bunching was impossible. In the Tokyo University experiment the accelerating structure was equipped with the solenoid but the final energy was too low for such an high charge density bunch, nevertheless they have demonstrated the compression for a high charge

beam and pointed out the sensitivity to phase jitters. Only the LLNL layout was close to the optimized case and in fact they succeed to demonstrate the possibility to compensate emittance while bunching, down to the level of the non-compressed beam. Anyway the final results in terms of emittance (10 μm) is not yet satisfactory. A fully optimized dedicated photo-injector for application of the velocity bunching technique still does not exist: one of the missions of the SPARC project is indeed to design and commission such a system

Table 1: Velocity bunching experiments

	BNL	UCLA	DUV-FEL	UTNL	LLNL
Charge [nC]	0.04	0.2	0.2	1	0.2
Length [ps]	0.37	0.39	0.5	0.5	< 0.3
C.R.	6	15	> 3	> 13	10
Reference	[25]	[12]	[10]	[11]	[12]

SUPERCONDUCTING RF GUN

In the past, for an implementation of SRF guns it was always assumed that one needs strong focusing inside the gun, near the photocathode. This assumption has been partially driven by relatively low achievable gradient in SRF guns. An interesting solution which avoids use of solenoid fields in transverse beam control near the cathode, so-called “rf focusing”, has been proposed in [26]. Unfortunately this method requires a deformation of the cathode plane, causing nonlinear field perturbations that may cause significant emittance growth in the injector. The improvement in superconducting cavity fabrication allows today accelerating gradient higher than 30 MV/m, corresponding to peak field of 60 MV/m [27]. An alternative scheme in which rf focusing is not required can today be considered.

A very attractive approach has been proposed at BNL [28]. The basic idea is to illuminate with UV laser the back wall of the superconducting Nb cavity accelerating in this way photo-emitted electrons. An optimized configuration has been proposed in [29], in which the working point described in [19] has been scaled also to an L-band SC gun design.

This configuration shown in Fig. 5 has a focusing solenoid geometry that keeps most of the magnetic field outside the cavity. In fact in the superconducting case the magnetic field must not penetrate the super-conducting cavity, to avoid thermal breaks down when the critical field of 200 mT is exceeded. The residual fringing field at the level of few Gauss is tolerable in that the focusing is applied only after cool down and the small field is excluded from the superconducting cavity through the Meissner effect, thus avoiding any residual flux trapping that may cause cavity Q0 degradation. In such a design one can obtained the same performance of a normal

conducting gun with the additional option to work in CW operation, and hence to obtain high average current.

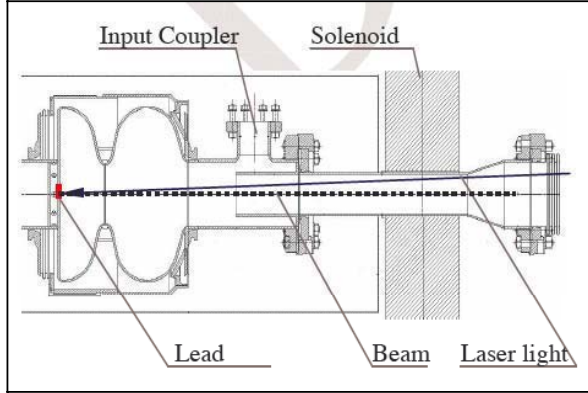


Fig. 5: SC RF gun with Lead cathode.

Another proposed scheme is to excite a TE magnetic mode inside the cavity that focuses the electron beam and prevents the increase of the transverse emittance [30]. Operation with high average beam current requires photocathodes having enhanced quantum efficiency (η). When superconductor is used as a photoemitter, high η minimizes the thermal load on the superconducting surface. More generally, high η implies that one may keep the size and cost of the high duty cycle laser system used to illuminate the photocathode within reasonable limits. It has been recently proposed to use lead as a photocathode deposited on the back wall of the gun cavity. Preliminary measurement [32] show a $\eta = 1.7 \cdot 10^{-3}$ for a lead cathode illuminated by a 213 nm laser. With such a good η a 3 W laser could generate 1 nC beam at 1 MHz.

The extreme case of ampere class superconducting guns is discussed in [31]. These devices require careful control of the higher order mode trapping and are specifically designed with wide beam tubes so to facilitate damping of unwanted trapped HOM.

FLAT BEAM PRODUCTION

In the context of electron-positron linear collider (LC) projects, the goals of electron sources are even more challenging. Linear colliders in fact require high charge, polarized electron beams with extremely low normalized emittances, with geometric average $\sqrt{\epsilon_{nx} \cdot \epsilon_{ny}} \approx 10^{-1} \mu\text{m}$. The recent analytical and numerical efforts in understanding beam dynamics in RF photo-injectors have again raised the question whether the performance of an RF electron gun based injector could be competitive with respect to a damping ring. An injector for a linear collider must provide a flat beam in order to reduce beamstrahlung effects at the interaction point, thus implying $\epsilon_{n,y} \ll \epsilon_{n,x}$. But a production of a flat beam directly from the cathode surface would increase the difficulties for emittance compensation, easily achieved by means of a symmetric solenoid. A flat beam is

typically delivered by a damping ring. Nevertheless a transformation of a round beam derived from a photoinjector into a flat beam has been recently proposed [33] by means of simple linear beam optics adapter at the exit of an injector.

This transformation is possible with a magnetized beam, as produced by an rf gun with a cathode embedded in a solenoid field [14]. At the exit of the gun/solenoid system the beam has an angular momentum given by

$p_\theta = \frac{I}{2} e B_{z,c} R_c^2$ where $B_{z,c}$ is the on cathode magnetic field, and R_c the laser spot radius. Both transverse planes are thus coupled by the beam rotation. Such rotation can be arrested by a suitable choice of a skew quadrupole triplet that, in addition, changes the emittance ratio according to the relation,

$$\frac{\epsilon_x}{\epsilon_y} = 1 + \frac{2\sigma_r^2}{\beta^2 \sigma_r'^2}$$

for a beam with rms size σ_r and rms angular spread σ_r' . The final emittance ratio is thus simply variable by adjusting the free parameter $\beta = 2p_\theta / e B_{z,c}$, via the magnetic field on the cathode. A first successful demonstration of this method was recently achieved at the A0 experiment at FNAL [15].

In Fig. 6 the beam images at different positions along the beam line of the FNAL experiment are shown. It has been verified that the beam remains flat as it drifts farther downstream, an important experimental achievement that demonstrate the effectiveness of the linear beam optics adapter in the context of RF photoinjector. The measured ratio of emittances is about 100, with $\epsilon_{nx} = 41 \mu\text{m}$ and $\epsilon_{ny} = 0.41 \mu\text{m}$ for a 0.5 nC beam, which yields a geometric mean emittance that is still rather high at $4 \mu\text{m}$. Additional experiments are foreseen in the near future to optimize the emittance compensation process.

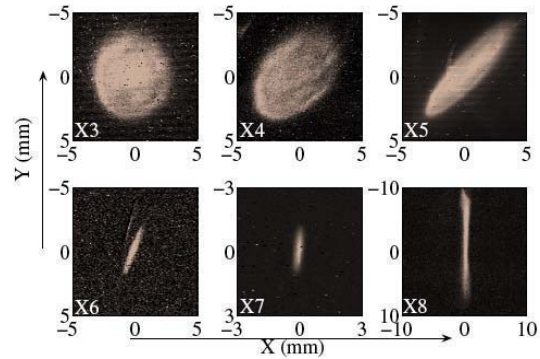


Fig. 6: Measured beam transverse density evolution in the flat beam transformer section.

ACKNOWLEDGEMENT

This work has been partially supported by the EU Commission in the sixth framework programme, contract no. 011935 EUROFEL

REFERENCES

- [1] Linac Coherent Light Source (LCLS) Conceptual Design Report, SLAC-R-593 (2002).
- [2] TESLA XFEL, Technical Design Report (Supplement), DESY 2002-167, TESLA-FEL 2002-09, (2002).
- [3] B. E. Carlsten, Nucl. Instrum. Methods A **285**, 313 (1989).
- [4] L. Serafini, AIP Conf. Proc. **413**, 321 (1997)
- [5] O. J. Leuten et al., Phys. Rev. Lett, **93**, (1997), n. 9
- [6] J. B. Rosenzweig et al., "Emittance compensation with dynamically optimized photoelectron beam profiles", Proc. of ERL05, to be published on N.I.M.
- [7] L. Serafini, J. B. Rosenzweig, Phys. Rev. E **55** (1997) 7565.
- [8] L. Serafini, M. Ferrario, "Velocity Bunching in PhotoInjectors", AIP CP 581, 2001, pag.87.
- [9] P. Emma, "Accelerator physics challenges of X-rays FEL SASE sources", Proc. of EPAC-02, Paris 2002.
- [10] P. Piot, et al., "Subpicosecond compression by velocity bunching in a photoinjector", Phys. Rev. ST-AB, **6**, 033503 (2003).
- [11] H. Iijima et al., "Experimental Verification of Velocity Bunching via Shot-by-Shot Measurement at S-Band Photoinjector and Linac, submitted to Japanese Journal of Applied Physics
- [12] S. G. Anderson et al., "Velocity bunching of high-brightness electron beams", Phys. Rev. ST-AB, **8**, 014401 (2005).
- [13] L. Merminga, "Technical approaches for high-average-power free-electron lasers", Rev. Modern Phys., **74**, (2002)
- [14] R. Brinkmann, Y. Derbenev, and K. Flöttmann "A low emittance, flat-beam electron source for linear colliders", Phys. Rev. ST Accel. Beams **4**, 053501 (2001)
- [15] Y. E. Sun et al., "Generation of angular-momentum-dominated electron beams from a photoinjector", Phys. Rev. ST-AB, **7**, 123501 (2004).
- [16] M. Reiser, "Theory and Design of Charged Particle Beams", J. Wiley & Sons, (1994).
- [17] C. Limborg, Proc. of ERL05, to be published on N.I.M.
- [18] H. Loos et al., "Temporal e-beam shaping in an S-Band accelerator", this conference.
- [19] M. Ferrario et al., "HOMDYN Study For The LCLS RF Photo-Injector" Proc. of the 2nd ICFA Adv. Acc. Workshop on "The Physics of High Brightness Beams", UCLA, Nov., 1999, see also SLAC-PUB-8400
- [20] L. Serafini et al., "Status of the SPARC Project", this conference.
- [21] Y. Kim, "Emittance Damping in TTF2 Booster Linac with Gaussian Longitudinal Laser Beam Profile", this conference.
- [22] L. Catani et al., "Design Study of a Movable Emittance Meter Device for the SPARC Photoinjector", Proc. of EPAC 2004
- [23] C. Ronsivalle et al., "Optimization of RF compressor in the SPARX injector", this conference.
- [24] C. Vaccarezza et al., "Start to end simulation for the SPARX project", this conference.
- [25] X.J. Wang et al, Phys. Rev. E **54**, R3121 (1996).
- [26] D. Janssen, V. Volkov, Nucl. Instr. and Meth. A **452** (2000), 34.
- [27] L. Lilje, "Achievement of 35 MV/m in the TESLA Superconducting Cavities Using Electropolishing as a Surface Treatment", Proc. of EPAC 2004.
- [28] T. Srinivasan-Rao et al., "Design, Construction and Status of All Niobium Superconducting Photoinjector at BNL", PAC03, Portland 2003, USA
- [29] J. Sekutowicz et al., "Proposed Continuous Wave Energy Recovery Operation of an XFEL", Phys. Rev. ST-AB, **8**, 010701 (2005).
- [30] K. Floettman et al., "Emittance compensation in a superconducting rf gun with a magnetic mode", Phys. Rev. ST-AB, **7**, 090702 (2004).
- [31] I. Ben-Zvi et al., "Ampere Average Current Photoinjector and Energy Recovery Linac", Proc of FEL 2004.
- [32] J. Smedley, "Progress on Lead Photocathodes for Superconducting Injectors", this conference.
- [33] Ya Derbenev, Adapting Optics for High Energy Electron Collider, UM-HE-98-04, Univ. Of Michigan, 1998.

PROGRESS AND PLANS FOR R&D AND THE CONCEPTUAL DESIGN OF THE ILC INJECTOR SYSTEMS

S. Guiducci, INFN-LNF, Frascati, Italy

Abstract

The International Linear Collider (ILC) Injector is a complex of different subsystems that are strictly correlated: positron source, polarized electron source, damping rings and bunch compressor. The choice of parameters of each subsystem has a strong influence on the others. A description of the critical items requiring further R&D in order to finalize the choice of the parameters needed for the Conceptual Design is given. The status and plans of R&D in progress on these items at a global level are reported.

INTRODUCTION

After the choice of the Super Conducting RF “cold” technology by the International Recommendation Panel in August 2004, the 1st International Linear Collider Workshop [1] was held at KEK to start the collaboration toward an international design between Asia, Europe and US. Workshops and meetings are used to provide communication between different groups working on the injector subsystems.

A 2nd Workshop will be held at Snowmass in August to start the definition of the baseline ILC configuration for the Conceptual Design Report.

The injection system is one of the crucial issues of this decision process. The success of ILC will depend also on the capability of the injector to produce high intensity, low emittance beams with good efficiency and low losses.

The ILC Injector Systems

The ILC Injector is a complex of strictly correlated subsystems, which must provide electrons and positrons

inject them into Damping Rings (DR) to reduce the transverse emittances, and transfer them into the Main Linacs travelling through bunch length compressors. Polarization of both beams is highly desirable for the experiments. For polarized beams a spin rotator system is needed before transfer to the Main Linacs.

The choice of the parameters of each Injector Subsystem has an influence on the others and the quality and stability of the extracted beam has an impact on the luminosity. The optimization of the IS parameters is therefore a crucial task.

A schematic design of the ILC showing the injector subsystems is presented in Fig.1. The nominal design parameters for the ILC injector system [2] are given in Table I.

Table I: ILC main parameters

Rep. rate (Hz)	5	Particles/bunch	$2 \cdot 10^{10}$
Train length (ms)	~ 1	Norm.horizontal emit. $\gamma\epsilon_x$ (m)	$8 \cdot 10^{-6}$
N. bunches/train	2820	Norm.vertical emit. $\gamma\epsilon_y$ (m)	$2 \cdot 10^{-8}$
Bunch dist. (ns)	337	Bunch length (μm)	300
Luminosity @500 GeV c.m. ($\text{cm}^{-2} \text{s}^{-1}$)		$2.0 \cdot 10^{34}$	

POLARIZED ELECTRON SOURCE

The design of an electron source for ILC will be based on well tested systems; only the polarized source poses new R&D challenges. A polarized electron source successfully operated already at the SLC [3]: 80% polarization was achieved with a strained lattice GaAs cathode with a quantum efficiency of 0.1%.

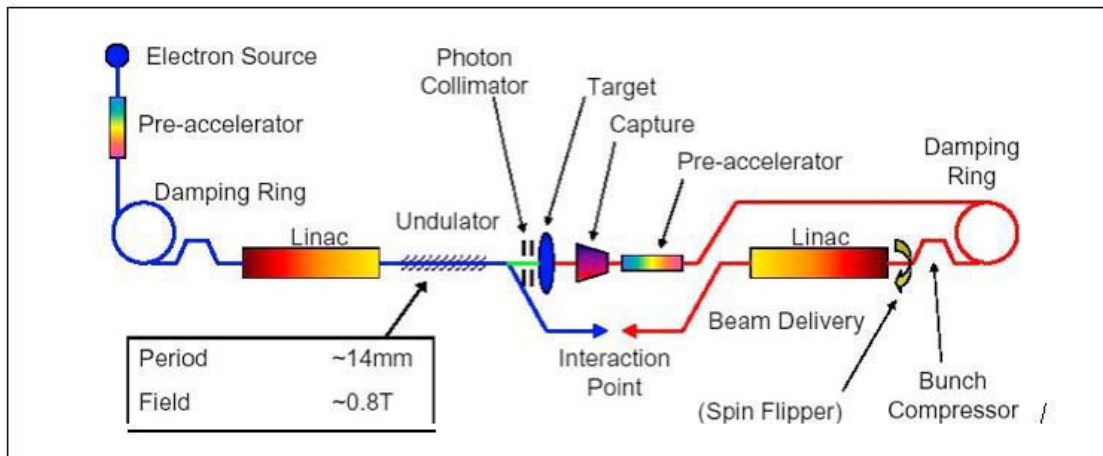


Figure 1: Schematic layout of ILC

* Work supported in part by the Commission of the European Communities under the 6th Framework Programme “Structuring the European Research Area”, contract number RIDS-011899.

A design capable of delivering a much higher charge per bunch was made for NLC [4]. The characteristics of a source for a SC linac, similar to that required for ILC, are also described in the TESLA TDR [5]: the charge per bunch needed is nearly the same as for NLC but the different time structure of the bunches poses more demanding requirements on the laser system.

The present status of R&D on polarized e- injector for ILC is very briefly summarized below [6].

Polarization larger than 85% is assured using well-tested GaAs/GaAsP strained lattice photocathodes, with R&D continuing towards 100% polarization. Photoemission study for the long ILC linac pulse (~1 ms) is needed. The large charge required for ILC can be produced using SLC type systems; many good technologies have been developed to design a state of the art gun. ILC laser needs substantial R&D.

POSITRON SOURCE

The positron charge needed for ILC is a factor 10^3 larger than that achieved at SLC and therefore this is one of the most demanding items of the injection system. For a “conventional” source like the SLC one it is very challenging to achieve such a large number of positrons, and therefore an “undulator based” novel scheme has been proposed [2]; more recently alternative schemes based on Compton scattering have been also put forward [7]. A conventional source uses electrons hitting on a target, while the other two schemes use photons and therefore, by means of polarized photons, can also produce polarized positrons.

Undulator based source

The high energy, low emittance electron beam passing through a long undulator produces a high flux of photons (10-40 MeV). The electrons are deviated by a small angle bend and sent to the Interaction Point, the photons are collimated and sent on a thin (0.4 radiation length X_0) Ti Alloy target to produce positrons. The capture system after the target is similar for all the schemes: an adiabatic matching device (high field pulsed focusing lens) and a high gradient RF capture section surrounded by a focusing solenoid. Positrons need then to be transported back to the beginning of the linac (see Fig. 1).

The main advantages of this source with respect to a conventional one are the lower neutron production rate and lower energy deposition in the target, which reduce the problems of heat removal, radiation damage and shielding in the target area and in the capture system.

Another advantage is the smaller transverse emittance of the positrons which, probably, can be matched to the DR acceptance without the need of a large acceptance pre-Damping Ring.

With this scheme polarization of the positron beam can be achieved by using a helical undulator, which produces circularly polarized photons, instead of a flat one. However, the design of the flat undulator is straightforward while for the helical one R&D is needed. There

are proposals for permanent magnet and SC prototypes [8].

The disadvantages of the undulator scheme are due to the use of high energy colliding electrons to produce positrons. This increases the complexity of the system and has a negative impact on commissioning and availability.

‘Conventional’ source

The conventional source consists of a 6 GeV electron beam [9] hitting a thick target (4.5 X_0) made of a WRe alloy. The target is a wheel rotating at 360 m/s and is cooled with water in flow channels. The capture system is similar to that of the undulator source but is more demanding due to the larger energy deposition and the larger emittance of the positrons. Due to the large positron emittance, the increase of the DR acceptance with a pre-DR could be needed to increase the positron yield. The region of the source is a high radiation environment: radiation hard components and remote handling for maintenance and repair are necessary.

All the problems related to power removal, heat damage, radiation damage and radiation shielding are more challenging with respect to the undulator source. On the other hand a conventional source allows separation of positron production from colliding electrons, which improves commissioning and availability and allows more operational flexibility.

Compton source

There is a proposal of producing polarized positrons using circularly polarized photons obtained by Compton backscattering of laser light by an electron beam. Production of polarized positrons with this method has been demonstrated at ATF [7,10]. The photon flux obtained in the laser-electron beam collision is much lower than that required for the ILC positron source: different schemes have been proposed to multiply the number of collision points. These schemes are at an early design stage but could be a promising alternative in the future.

DAMPING RING

DR are used to reduce the large normalized emittance of the source in order to get the very small beam sizes at the IP needed for the design luminosity. DR requirements are: low emittance, short damping time and high current. In the following the main DR issues are summarized.

For positrons, nearly 7 damping times are needed to reach an extracted emittance very close to the equilibrium one; this condition determines the required betatron damping time: $\tau_{x,y} < 28\text{ms}$ at 5 Hz repetition rate.

In order to compress the long linac pulse train (~300 Km) down to the DR length the rise and fall time of injection/extraction kickers must be shorter than the DR bunch distance. The 17 Km long DR of the TESLA design [2] is based on a 20 ns bunch distance. Shortening the linac pulse affects directly the luminosity, therefore it is clear that the feasibility of ultra fast kickers is the key issue for the DR design.

Large DR acceptance is needed to get high positron injection efficiency; this in turn asks for large magnetic apertures, i.e. high costs, strong kickers and a large Dynamic Aperture (DA). A long wiggler section is also necessary to get a short damping time but nonlinearities in the wiggler field could reduce the DA. A dedicated study of this issue is in progress. The high current and short bunch distance can cause instabilities and collective effects, which limit the maximum current and deteriorate the emittance. Fast ion instability in the e^- ring and e-cloud effect in the e^+ one are a concern. Studies to estimate and mitigate these effects are in progress [11]. Space charge incoherent tune shift becomes important due to the long circumference and small emittance.

As an example typical DR parameters are compared with those of some operating machines in Table II.

The characteristics of the B and Φ -Factories [12] are: large number of particles per bunch, short bunch distance, short bunch length, the same as for the DR, but their emittances are much larger. The powerful longitudinal and transverse feedback systems used in the Factories to damp instabilities can be implemented in the DR as well. However it should be understood if it is possible to use feedbacks without causing emittance growth. In any case the DR will have lower current and faster radiation damping, which should mitigate instabilities.

The Accelerator Test Facility (ATF) DR at KEK has been designed as a test machine to produce a low vertical emittance beam and to test the advanced diagnostics (laser wire beam profile monitor, high resolution BPMs, etc.) required to measure it.

A 4 pm vertical emittance, the smallest emittance ever achieved, has been measured at low current [13]. Due to the low energy, a beam size growth due to Intra Beam Scattering is observed at higher current. At 1×10^{10} part/bunch there is an increase by a factor 1.5; however the normalized emittance is still smaller than that required for the DR.

ATF is a very short ring with redundant diagnostics (96 BPMs in each plane), and redundant orbit and coupling correction systems (97 orbit correctors, 68 skewers). It is important to understand how its achievements can be scaled to a 17 Km DR.

The feasibility of 2 pm vertical emittance has to be demonstrated. It depends on the capability of achieving ultra low values of closed orbit, coupling and vertical dispersion and requires efficient correction algorithms.

DR Layouts

For the DR there are still critical items which require a decision before finalizing the baseline design for the CDR. First of all the layout: there are proposals for 17, 6 and 3 Km long DRs. For TESLA (17 Km) a dogbone design with two long straight sections in the linac tunnel, connected by relatively short arcs (total arc length ~ 2 Km) has been proposed. This solution allows to save on tunnel length but has a negative impact on commissioning and availability and could affect the low emittance due to the stray fields in the linac tunnel. On the other hand, a short ring would be accommodated in a dedicated tunnel with evident advantages in terms of availability.

Many different DR lattices and layouts have been proposed, and a list of their parameters is reported in Table III. The lattices are based on different arc cells (FODO, TME, π) and have different lengths. All the lattices show an horizontal emittance smaller than the nominal one, demonstrating that there is a reasonable safety margin on this parameter.

The radiated energy per turn, needed to achieve the nominal damping time, is proportional to the ring length. Therefore long lattices require a long wiggler section and a large RF voltage. For short lattices it is easier to achieve the nominal damping time or even shorter.

A comparative study of the lattices performances, by applying the same tools and assumptions to all them, will produce the necessary input to the CDR baseline configuration.

The final choice will be based on many issues; in particular the following items certainly need more studies and experimental tests:

- Minimum achievable emittance
- e-cloud and fast ion instability
- Incoherent space charge tune shift
- Other collective effects
- Wiggler optimization and dynamic aperture

Table II: Comparison of DR parameters with operating storage rings

	DAFNE	KEK-B LER/HER	PEP-II LER/HER	ATF	DR
E (GeV)	0.5	3.5/8	3.1/8.99	1.28	5
C (m)	98	3016	2199	138	17000/3000
N (10^{10})	2.0	7.7/5.9	9.3/5.	0 - 1.0	2.0
Bunch distance (ns)	2.7	7.8	6.3	2.8	20./3.
$\gamma\epsilon_x$ ($\mu\text{m-rad}$)	400	120/380	200/860	3/5	8
$\gamma\epsilon_y$ ($\mu\text{m-rad}$)	1.0	5.6/11	12/44	0.01/0.015	0.02
ϵ_x (m-rad)	4.1×10^{-7}	$(1.8 - 2.4) \times 10^{-8}$	$(3.3 - 4.9) \times 10^{-8}$	$(1.2 - 2.0) \times 10^{-9}$	8.2×10^{-10}
ϵ_y (m-rad)	1.0×10^{-9}	$(8.2 - 7.1) \times 10^{-10}$	$(2.0 - 2.5) \times 10^{-9}$	$(4 - 6) \times 10^{-12}$	$2. \times 10^{-12}$
σ_z (mm)	19	8.0/6.0	12	5/9	6.0
τ_x (ms)	36	43/46	62/37	18	<28
I average (A)	1.0	1.6/1.2	2.1/1.1	0.07	0.16/0.9

Table III - Parameter list for different DRs

Lattice	PPA	OTW	OCS	BRU	MCH	DAS	TESLA
E [GeV]	5	5	5.066	3.74	5	5	5
Circum [m]	2824	3223	6114	6333	15935	17023	17000
Arc Cell	FODO	TME	TME	FODO	FODO	π	TME
ξ (x,y)	-63, -61	-88, -75	-66, -56	-61, -69	-69, -75	-105, -107	-125, -68
ac [e-4]	2.83	3.62	1.59	11.9	4.09	1.14	1.2
tx [ms]	20	12.1	27.6	25.5	26.9	27	28
U0 [MeV]	4.7	8.9	7.5	6.2	19.8	21	21
$\gamma\epsilon_x$ [μm]	4.24	3.80	6.67	2.76	6.60	6.10	8.00
V_{RF} [MV]	18	22	23	54	48	50	50
f_{RF} [MHz]	500	714	500	650	650	500	500
σ_I [mm]	6	6	6	9	9	6	6
Nb [e10]	2	2	2	2	2	2	2
Nbunches	2820	2820	2820	2820	2820	2820	2820
Dt_{bunch} [ns]	3.35	3.82	7.25	7.51	18.90	20.19	20.16
IAv [mA]	955	837	441	426	169	159	159

Dynamic aperture

A large DA is necessary to assure large acceptance and to reduce injection losses. DA calculations have been performed for some of the lattices. The feasibility of a large DA depends on the details of the lattice and the sextupole configuration rather than on the layout. As it is shown in ref.[14] achieving a large DA is more difficult for a dogbone layout, since sextupoles in the arcs must correct the arc and long straight sections chromaticity. However, for example, a 16 Km FODO lattice (MCH) [15] designed as a dogbone showed a large dynamic aperture ($> 10 \sigma_{x,y}$ for $\gamma\epsilon_{x,y} = 0.01$ m) see Fig. 2. Tracking of a realistic positron distribution, produced by a simulation of an undulator positron source, has been done for lattices (MCH, OCS) [15,16]. The injection losses were of the order of 1% for both lattices.

The wigglers used to achieve short damping times can be harmful to the DA. Studies on the effect of wigglers on the damping ring DA have been presented at the “WIGGLE 05” Workshop in Frascati [17]. Different models have been proposed to reproduce measured field distributions and tracking with different wigglers has been performed. A suitable wiggler design can be found to minimize the field nonlinearity and avoid significant DA reduction. This item will require more R&D in the next future.

Kickers

Kickers are definitely the DR system that requires more R&D. Their challenging requirements are listed below:

- Linac pulse frequency 5 Hz,
- Bunch frequency (for 1 ms) 3 MHz
- Deflection angle 0.5 mrad,
- Rise and fall time 20 nsec - 3ns
- Pulse to pulse reproducibility at extraction $\geq \pm 0.07\%$.

If the positrons will be produced by an undulator source, extraction of damped bunches is performed at the same time of injection of new bunches. In this case a large kicker deflection angle is needed for both injection and extraction. By adopting a conventional e^+ source or a pre-DR, this can be avoided and the extraction deflection angle, which has a tight stability constraint, can be much smaller (0.03 mrad).

Kickers R&D is in progress in many laboratories [18]: Strip line kicker and pulser (KEK, SLAC, DESY, LBNL, LLNL, Cornell), Fourier series kicker (FNAL, UIUC), CTF3-like RF deflectors (LNF), crab cavity deflector scheme (Cornell). A short pulse stripline kicker powered by a pulser based on Fast Ionization Dynistor (FID) technology has been tested at ATF using turn by turn BPMs [19]. The characteristics are: length 0.33 m, voltage ± 5 KV, kick angle 60 μrad .

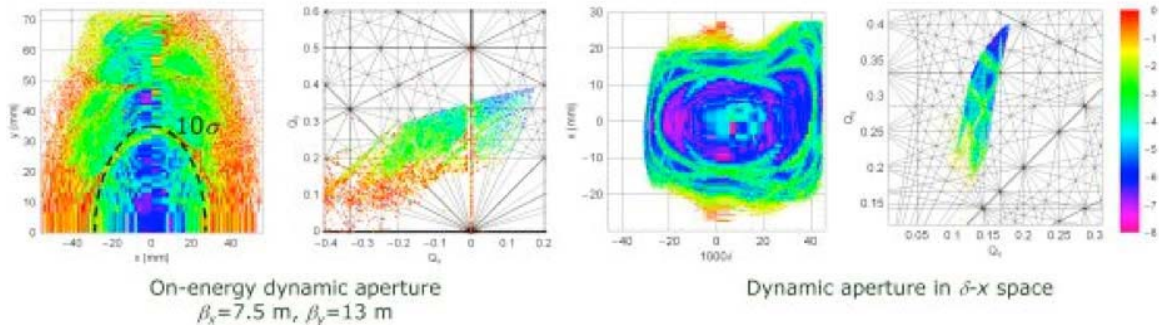


Figure 2: Dynamic aperture of 16 Km dogbone FODO lattice (MCH)

A short pulse stripline kicker powered by a pulser based on Fast Ionization Dynistor (FID) technology has been tested at ATF using turn by turn BPMs [18]. The characteristics are: length 0.33 m, voltage ± 5 KV, kick angle $60 \mu\text{rad}$. The kicker pulse envelope was measured by scanning the pulse timing. A preliminary result is shown in Fig. 3 where a 2.2 ns rise/fall time has been achieved.

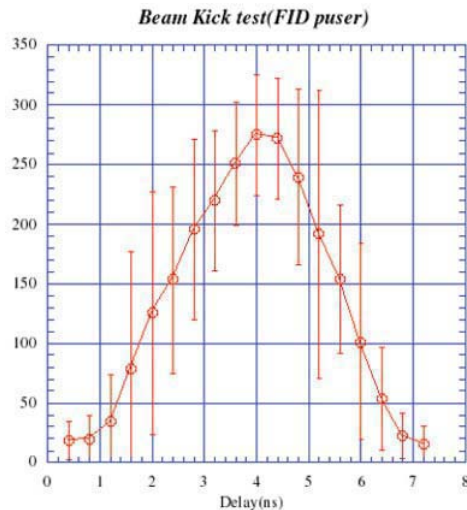


Figure 3: Amplitude of the betatron oscillation as a function of the kicker timing.

BUNCH COMPRESSOR

The job of matching the MDR bunch length requirements to the IP bunch length requirements is performed by a specialized beam line, a "bunch compressor", which reduces the rms bunch length while increasing the rms energy spread. A single stage bunch compressor scheme with a compression factor of 20, from 6 mm to $300 \mu\text{m}$ has been proposed for the TESLA TDR. To keep the maximum rms energy spread small, a two or three stages compressor has been also proposed [20]. It can compress the bunch length down to $150 \mu\text{m}$ allowing for more flexibility in the choice of the collision parameters.

CONCLUSIONS

For the injector system some decisions have still to be taken: the major issues are the positron source, which can be 'conventional' or undulator based, and the DR layout. The tasks needed for injector configuration selection have been identified and assigned in an international collaboration. The intent is to provide the documentation to start the decision process at the 2nd ILC Workshop at Snowmass.

The ILC Baseline Configuration Document should be ready by the end of 2005 and the Complete CDR, including cost and schedule plans should be completed by the end of 2006.

ACKNOWLEDGEMENTS

This paper is based on the work done worldwide by a large number of people. In particular the contributions of G. Dugan, M. Kuriki, A. Wolski, J. Sheppard, J. Clark, T. Maruyama, P. Tenenbaum must be mentioned.

REFERENCES

- [1] [1] 1st ILC Workshop, Nov. 04, KEK (JP) WG3 Injector <http://lcdev.kek.jp/ILCWS/WG3.php>
- [2] T. Raubenheimer, "Suggested ILC Beam Parameter Range", (2005) <http://www-project.slac.stanford.edu/ilc/acceldev/beamparameters.html>
- [3] R. Alley et al., "The Stanford Linear Accelerator Polarised Electron Source", Nucl.Inst. & Meth. A365, (1995).
- [4] The NLC Design Group., "Zeroth Order Design Report for the NLC", SLAC Report 474, pp28-34 (1996).
- [5] "TESLA TDR", DESY 2001-011.
- [6] T. Maruyama, "Polarised Electron Sources Overview", 1st ILC Workshop, Nov. 04, KEK (2004).
- [7] T. Omori "Compton e⁺ source" 1st ILC Workshop, Nov. 04, KEK (JP) WG3 Injector.
- [8] J. Clarke, "Undulator based e⁺ source issues", Workshop on e⁺ sources for ILC, April 05, Daresbury, UK.
- [9] J. Sheppard, "Conventional e⁺ source", Workshop on positron sources for ILC, Apr. 05, Daresbury (UK)
- [10] M. Kuriki, "Polarized e⁺ production and measurement at KEK", Workshop on e⁺ sources for ILC, Apr. 05.
- [11] F. Zimmermann, "Collective effects and instabilities" 1st ILC Workshop, Nov. 04, KEK (JP) WG3 Injector.
- [12] ICFA Lepton Colliders database, http://www.lnf.infn.it/icfa/icfa_db_v8.xls
- [13] A. Wolski et al. "Coupling Correction in the KEK ATF Using ORM Analysis", ATF Report-04-09 (2005).
- [14] Y. Cai, "Dynamic Aperture in DR with realistic Wigglers", "Wiggler Workshop", Frascati, 2005
- [15] A. Wolski, "Lattices with Large Dynamic Aperture for ILC DR", LBNL-57045 (2005).
- [16] L. Emery et al., "Studies Pertaining to a Small DR for the ILC", FERMILAB-TM-2272-AD-TD (2004).
- [17] "Wiggler Workshop", Frascati, 2005, (<http://www.lnf.infn.it/conference/wiggle2005/prog.html>)
- [18] T. Mimashi, "Kickers Overview" 1st ILC Workshop, Nov. 04, KEK (JP) WG3 Injector
- [19] M. Kuriki, "ATF Status", (2005).
- [20] "LET: Bunch Compressor Design Study", <http://www-project.slac.stanford.edu/ilc/acceldev/LET/BC/>

DAΦNE OPERATION AND PLANS FOR DAΦNE2

M. Zobov, D. Alesini, G. Benedetti, M.E. Biagini, C. Biscari, R. Boni, M. Boscolo, A. Clozza, G. Delle Monache, G. Di Pirro, A. Drago, A. Gallo, A. Ghigo, S. Guiducci, M. Incurvati, C. Ligi, F. Marcellini, G. Mazzitelli, C. Milardi, L. Pellegrino, M. A. Preger, P. Raimondi, R. Ricci, C. Sanelli, M. Serio, F. Sgamma, B. Spataro, A. Stecchi, A. Stella, C. Vaccarezza, M. Vescovi, LNF-INFN, Frascati, Italy
 E. Levichev, P. Piminov, D. Shatilov, BINP, Novosibirsk, Russia
 J. Fox, D. Teytelman, SLAC, Stanford, USA.

Abstract

The e+e- collider DAΦNE, a 1.02 GeV c.m. Φ-factory, has reached a peak luminosity of about $1.4 \times 10^{32} \text{ cm}^{-2} \text{ s}^{-1}$ and a peak integrated luminosity in one day of about 8.6 pb^{-1} . With the current rates the physics program of the three main experiments DEAR, FINUDA and KLOE will be completed by the end of 2007. In this paper we describe in detail the steps which have led to the luminosity improvement and the options for the upgrade of the collider towards higher energy and/or luminosity.

INTRODUCTION

The DAΦNE [1] complex consists of two independent rings having two common interaction regions (IR) and an injection system composed of a full energy linear accelerator, a damping/accumulator ring and the relative transfer lines. The main present DAΦNE parameters during operations are listed in Table 1.

Table 1: DAΦNE parameters

Energy [GeV]	0.51
Trajectory length [m]	97.69
RF frequency [MHz]	368.26
Harmonic number	120
Damping time, τ_E/τ_x [ms]	17.8/36.0
Bunch length at 0 current [cm]	1.0
Bunch length at full current [cm]	2.5
Beam currents e-/e+ [Amps]	1.7/1.3
Number of colliding bunches	107
Beta functions β_x/β_y [m]	1.6/0.017
Emittance, ϵ_x [mm·mrad] (KLOE)	0.34
Emittance ratio at 0 current [%]	0.25
Emittance ratio at full current [%]	0.60
e- Tunes Qx/Qy	0.091/0.1660
e+ Tunes Qx/Qy	0.1090/0.1910

Since 2000 DAΦNE has been delivering luminosity to three experiments: KLOE [2], FINUDA [3] and DEAR [4]. The KLOE detector has been permanently installed in the first interaction region (IR1), FINUDA and DEAR detectors share, one at a time, the second interaction region (IR2).

A wide spectrum of experiments is also being carried out at the DAΦNE beam test facility (BTF) [5], a dedicated beam transfer line delivering electron or

positron beams in the energy range 25-725 MeV with intensities varying from 10^{10} particle/pulse down to a single-electron. Moreover, two separate beam lines are used for synchrotron radiation (SR) studies, extracting the SR light from a wiggler and a bending magnet, respectively [6].

The luminosity performances for the 3 experiments are shown in Figure 1, while the details of 2004-5 KLOE run are shown in Figure 2.

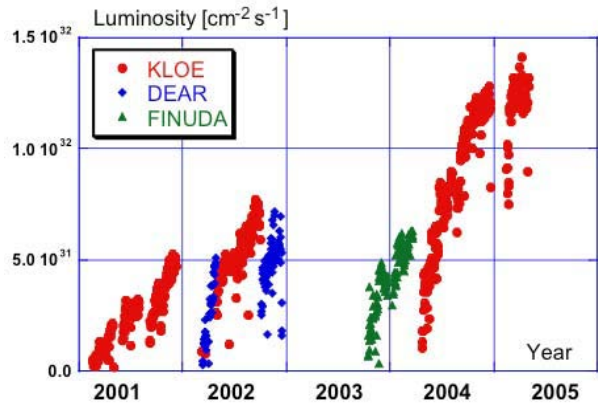


Figure 1: DAΦNE peak luminosity history. Red: Kloe runs, Blue: Dear runs, Green: FINUDA runs.

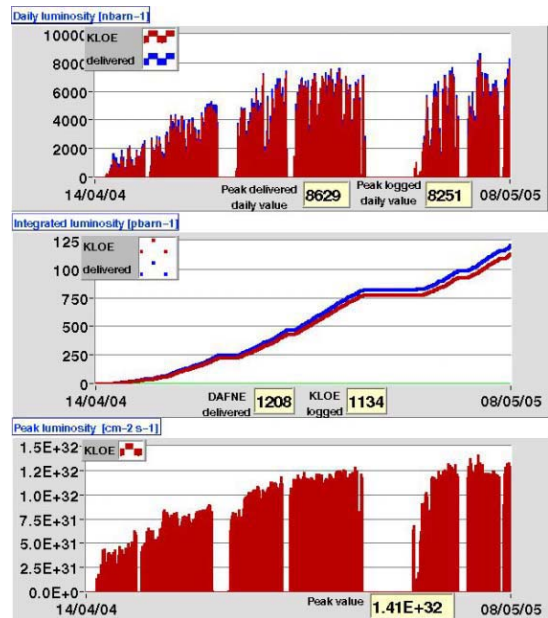


Figure 2: DAΦNE performances in the 2004-5 KLOE run.

As shown in Table 2 the high energy and nuclear physics programs on DAΦNE is scheduled to be completed by end 2007. For this reason the DAΦNE team, in collaboration with the Frascati physics community has started a study for a possible upgrade of the collider to extend its physics reach. In addition we are also studying possible machine experiments to explore novel techniques to further increase the design luminosity of a new collider.

Table 2: Schedule of physics experiments at DAΦNE

	2004	2005	2006	2007
KLOE	> 2 fb ⁻¹			
FINUDA			1	
SIDDHARTA				.5

LUMINOSITY OPTIMISATION

The steady luminosity progress shown in Fig. 1 was achieved by the optimization of the machine parameters and hardware changes implemented during a 6 months long shut down in 2003 with the goal of doubling the luminosity and beam lifetime (and also to install the FINUDA detector on IR2). The main accelerator physics issues that have been studied and optimized can be summarized as follows [7]:

- Working point choice.
- Coupling correction.
- Optimization of collision point parameters (betas, emittances, crossing angles etc.)
- Collider optics modeling.
- Nonlinear beam dynamics study.
- Single and multibunch instability cures.
- Fine tuning of all parameters in collisions during data taking.

The most relevant hardware changes made during the 2003 shut down [8] are:

- New KLOE and FINUDA Interaction Regions.
- Long straight sections modification.
- Wiggler magnets modification.
- Shorter injection kicker pulse.
- Additional feedback amplifiers.
- Maintenance of bellows and scrapers.

Continuous work on the optics with a particular care on wiggler modeling resulted in a satisfactory agreement between model predictions and measurements of beta functions, dispersion, second order dispersion, chromaticities etc. [9]. The model reliably reproduces and predicts the machine optical functions allowing us to test very quickly for a wide range of lattice configurations (e.g. lattices with a momentum compaction factor varying from +0.04 to -0.02). The linear optics model has proven to be a good base for coupling correction, dynamic aperture optimization and nonlinear dynamics studies. At present DAΦNE operates with coupling corrected down 0.2-0.3% and the dynamic aperture as large as 14-15 σ_x .

The new KLOE IR (doublet configuration) allowed a reduction of both the IP beta functions without chro-

maticity increase together with a reduction of the non-linear forces due to the parasitic beam-beam crossings. Independent rotations of all IR quadrupoles provides local coupling correction and possibility of operation with arbitrary values of the KLOE solenoid field. For the KLOE lattice configuration the values of $\beta_x=1.6$ m and $\beta_y=1.7$ cm at the IP have been reached, to be compared to 4.5 m and 4.5 cm, respectively, of the initial design values. The horizontal emittance has also been reduced by about a factor 3 with respect to the design to further reduce the effect of the parasitic collisions. As a result we now collide routinely with 108 consecutive bunches out of available 120, the short gap is still needed for ion clearing in the e- ring.

The poles of the wiggler magnets have been modified by adding longitudinally and horizontally shimmed plates [10]. Moreover, an extra sextupole component has been added on one of the terminal poles of each wiggler to ease the dynamic aperture optimization. Field measurements and beam tests showed a significant reduction of the second and fourth order terms in the fields and revealed almost a factor 2 improvement in the energy acceptance. These modifications were essential for keeping satisfactory lifetime despite the emittance reduction.

The longitudinal feedback systems were originally designed to damp only dipole multibunch oscillations excited by the beam interaction with parasitic high order modes. However, after filter modifications and overall tuning now they are capable to damp also the 0-mode and quadrupole instabilities [11]. In turn, with additional power amplifiers the transverse feedbacks can keep under control the transverse multibunch instabilities with a rise time as fast as 17 μ s [12].

Installation of three octupoles in each ring (the number is limited by allowable space) [13] helped to increase the dynamic aperture and to compensate the lattice cubic nonlinearity that is a necessary condition to obtain good luminosity performance [14]. They proved particularly useful to compensate the effect of the nonlinearities from the parasitic beam-beam crossings, increasing the lifetime by about 30% when colliding at the maximum currents.

A dedicated work on background reduction including orbits and optical functions correction, working point fine tuning, sextupole and octupole strengths and scraper position optimization have allowed to operate the collider in the “topping up” mode without switching off the KLOE drift chamber during injection. This resulted in a significant increase of the integrated luminosity .

PERFORMANCE LIMITATIONS

The major limits to a further increase of the luminosity in DAΦNE at present are:

- Positron beam instability.
- Single beam (bunch) transverse size enlargement with current.
- Lifetime due to the parasitic crossings.
- Vertical size enlargement due to the beam-beam interaction.

At present the maximum storable positron beam current is limited at 1.3 A by a very fast horizontal instability. Several indications are in favour of interpreting it as an electron cloud instability. In particular, we measure a large positive tune shift with the beam current and observe an anomalous vacuum pressure rise. Moreover, such a fast instability rise time can not be explained only by the beam interaction with parasitic HOM or resistive walls.

The instability has a beam break up nature: it is faster than the synchrotron period and depends strongly on injection conditions. We have increased substantially the maximum storable current by shortening the injection kickers pulse and optimizing the 2 kickers injection closed bump. The threshold of the instability decreased by at least a factor 2 after the 2003 shut down and it is still not clear why. The smaller emittance and/or the longer Landau damping due the reduction of the machine non linearities are possible candidates and we plan to test their influence.

Several simulations are being made with particular attention on the e-cloud creation in the wiggler sections since nonlinear field components of the wigglers were modified [15].

The transverse beam size enlargement with current, takes place even with single beams and depends on the single bunch current. Recent machine studies showed a clear correlation between the observed effect and the longitudinal microwave instability:

- the transverse beam blow up and the instability have the same single bunch current threshold;
- the threshold scales as the square root of the RF voltage;
- the threshold increases more than linearly for higher momentum compaction factors;
- the effect is more pronounced for the electron ring, which has a higher beam coupling impedance.

The mechanism of the coupling of the instability between the transverse and longitudinal axis is still to be understood.

The main lifetime limitation in collisions comes from parasitic crossings of the closely spaced bunches in DAΦNE. Some further optimization it is still possible, but we think that significant improvements now can be made only with additional hardware upgrades.

The vertical enlargement due to the beam-beam could be further reduced by a refinement of the coupling correction and by changing the machine working points, either closer to the integer (around 0.06/0.09) or to the half integer like in the B-Factories (around 0.53/0.56)

LUMINOSITY UPGRADE PLANS

A scientific program beyond the scheduled physics runs (Table 2) is a matter of discussion in the physics and accelerator communities at Frascati. There are a few options being considered as a basis for the future DAΦNE upgrade [16]. These are briefly discussed in the following.

Energy upgrade (DAΦNE2)

The first proposal of DAΦNE upgrade consists in extending the collider energy from the Φ-resonance to the threshold of n-nbar production (1.1 GeV/beam) preserving the present machine layout [17]. This essentially requires:

- new dipole magnets fitting the existing vacuum chamber and providing 2.4 T magnetic field;
- new low beta superconducting quadrupoles;
- energy upgrade of the injection system or implementation of a ramping scheme in the main rings.

All other magnets, their power supplies and existing accelerator subsystems (such as vacuum, RF, feedbacks etc.) are basically compatible with high-energy operation.

Preliminary studies have shown that the high field dipole magnets are feasible, but still more work is needed to get a reliable design that provides the required field quality [18].

Concerning injection, the upgrade of the linac to full energy (without damping ring) [19] would allow for a fast and flexible injection procedure. The main drawback is obviously the cost. This solution would also require upgrading the kickers and injection septum magnets in each ring. In turn, energy ramping is possible with existing hardware [20], but this option does not allow topping-up injection during high-energy operation.

The required luminosity at the energy of the n-nbar threshold of $10^{32} \text{ cm}^{-2} \text{ s}^{-1}$ can be obtained with 0.5 A in each beam of 30 bunches. These parameters are conservative since the lower operating current with respect to DAΦNE is largely overcome by all the advantages that come from the higher energy (increased damping, reduced beam-beam, weaker instabilities etc.). The operation at the Φ energy should still be possible since the hardware and the layout basically remain the same, although with a small increase of the damping time.

Luminosity upgrade (DAΦNE2)

The second possibility is DAΦNE2, a collider with a peak luminosity in the range $1\text{-}3 \times 10^{33} \text{ cm}^{-2} \text{ s}^{-1}$. Our studies are based on maintaining as much as possible the present layout and infrastructures. The key ingredients for the upgrade are:

- Shorter bunch and lower β_y .
- Stronger damping.
- Higher number of bunches.
- Increasing colliding currents (between 2 and 3 Amps)
- Lower tunes (closer to the integers or half-integers).

We expect to decrease the bunch length and, respectively the vertical beta at the IP, by a factor of 2-2.5. This can be done by means of a lattice with a large negative momentum compaction (see following Section) and/or reducing the beam vacuum chamber coupling impedance.

More bunches can be put in collisions by increasing the RF frequency from the present 368 MHz to 500 MHz. The IR must be redesigned in order to decrease the harmful effects of the parasitic collisions and to provide smaller beta functions at the IP. This could be done with stronger quadrupoles (permanent magnets should work, but we do not exclude a SC solution).

We also plan to reduce the damping time by a factor >2 . This can be done, first, by reducing the gap of the existing wigglers, thus increasing the gap field and at the same time improving the field quality in the beam region and by adding new wigglers in the second IR (possibly superconducting).

At present there are no severe limitations on the maximum current in the electron beam. We plan also to overcome the positron beam limit due to the e-cloud instability: one of the possible cures is Ti coating of the positron ring vacuum chamber and enlargement of the antechamber gap.

Optimisation of the dynamic aperture would give a possibility to move the working points closer to the integer (or half integer) tunes where, according to numerical simulations, another factor 1.5-2 in luminosity can be gained.

Tau-Charm Factory

There is interest in the Frascati particle physics community to build a tau-charm factory with peak luminosity of the order of $10^{34} \text{ cm}^{-2} \text{ s}^{-1}$ at the energy of 3.8 GeV (c. m.). Neither detailed nor feasibility study has started yet, but preliminary evaluations have shown that such a factory could be housed inside the existing DAΦNE building. A set of parameters providing the required luminosity is illustrated in Table 3.

Table 3: Parameters of a tau-charm factory

E, GeV	1.89	B, T	1.8
C, m	105	U_0 , keV	328
L , $\text{cm}^{-2} \text{ s}^{-1}$	1034	V_{RF} , MV	2
f_{RF} , MHz	500	$V_{3\text{RF}}$, MV	2
ϵ_x , m rad	1.5×10^{-7}	α_c	0.022
β_x, β_y , m	0.5-0.005	σ_E/E	8.7×10^{-4}
k	0.003	P_{rad} , kW	900
N_{bunch}	160	σ_z , mm	6
N_{part}	3.5×10^{10}	I_{thresh} , mA	25
ξ_x, ξ_y	0.03-0.05	I_{tot} , A	2.7

EXPERIMENTAL ACTIVITIES

It is known that there can be several advantages for collider operation with a negative momentum compaction lattice (see, for example, [21] and references therein):

- the bunches are shorter and exhibit a more regular shape;

- longitudinal beam-beam effects, such as coherent and incoherent instabilities and synchrotron resonances are less dangerous;
- since the head-tail instability with a negative α_c takes place with a positive chromaticity, requirements on sextupole strength can be relaxed.

Lattices with a negative momentum compaction factor have been tried successfully in a few storage rings. However, to our knowledge, high current multibunch operation and beam-beam collisions have never been tested with a negative α_c . This was one of the reasons why we dedicated some machine time to study DAΦNE operation with $\alpha_c < 0$. Yet another point in favour of $\alpha_c < 0$ is that, if successful, the principle can be used in all the DAΦNE upgrade options: energy or luminosity upgrade, super Φ -factory or tau-charm factory. Briefly summarising the results of these studies:

- the bunches shorten (see Fig. 3) as predicted by numerical simulations;
- the DAΦNE optical model reproduces well optical functions with $\alpha_c < 0$. This also makes us confident that the model will be reliable for a proposed experiment on Terahertz CSR requiring low momentum compaction factors [22];
- a single bunch with a current of 40 mA is stable with negative chromaticity;
- there are no problems with RF cavities and feedbacks: about 1 A of stable current has been stored in both beams;
- coupling and geometric luminosity is as in usual operating conditions (or even better for the e- ring);
- first collisions have been tested at low current (about 300mAmps) obtaining about $L \sim 2.5 \times 10^{31} \text{ cm}^{-2} \text{ s}^{-1}$.

Unfortunately above 3mAmps/bunch the electron vertical sizes grows very fast due to microwave instability threshold. The problem can be overcome either by increasing the absolute value of α_c or by decreasing the electron ring impedance (higher because the presence of the ion-clearing electrodes). Both these solutions can be implemented only with hardware changes, so have to be considered only for future upgrades.

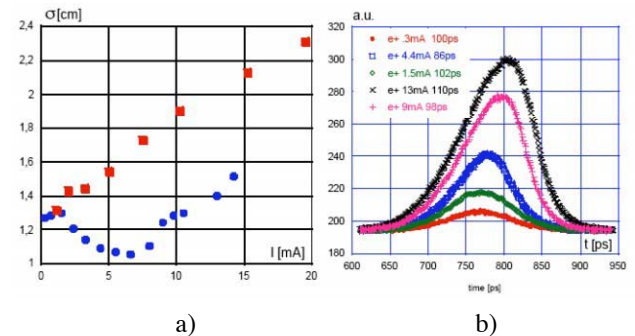


Figure 3: a) Bunch length with negative (blue) and positive (red) momentum compaction factor; b) bunch shape for different bunch currents with $\alpha_c < 0$.

The DAΦNE team is working also at the project of a super Φ-factory with a luminosity of the order of $10^{34} \text{ cm}^{-2} \text{ s}^{-1}$. A preliminary proposal has been published [23]. The ultra-high luminosity design is based on standard together with new accelerator physics concepts, the most relevant being:

- strong radiation emission to increase the radiation damping (all wiggling machine);
- lattice with a high negative momentum compaction α_c .
- strong RF focusing (longitudinal bunch length modulation) scheme to get bunch length in the mm scale at the interaction point [24,25].

Before going on with the super factory design, the new concepts should be tested experimentally. In particular, the longitudinal bunch length modulation along the ring has never been tried in any storage ring. For this reason we are considering the possibility to perform an experiment on bunch length modulation in DAΦNE [26].

Moreover, in the strong longitudinal focusing regime the beam dynamics becomes essentially three-dimensional. This means that all dynamical features, such as dynamic aperture, lifetime, high current operation, beam-beam collision etc. need to be fully investigated.

CONCLUSIONS

The Φ-factory DAΦNE has proved very successful to increase the know-how and expertise of the accelerator physics community. The particle physics programs have also been extremely important. These results have stimulated the Frascati community to push the frontier even further:

- 1) energy upgrade to reach the n-nbar threshold by building new dipoles and changing the injection procedure;
- 2) luminosity upgrade to $L > 2 \times 10^{32} \text{ cm}^{-2} \text{ s}^{-1}$ requiring major changes of the existing facilities;

- 3) a tau-charm factory inside the DAΦNE building with peak luminosity of the order of $10^{34} \text{ cm}^{-2} \text{ s}^{-1}$.

An experimental activity aimed at testing accelerators concepts that could help pushing the luminosity at the Φ resonance energy towards $10^{34} \text{ cm}^{-2} \text{ s}^{-1}$ level is well under way.

REFERENCES

- [1] G. Vignola, PAC93, p. 1993.
- [2] The KLOE Collaboration, LNF-92/019 (IR), 1992.
- [3] The FINUDA Collaboration, LNF-93/021 (IR), 1993.
- [4] The DEAR Collaboration, LNF-95/055 (IR), 1995.
- [5] A.Ghigo et al., Nucl.Instrum.Meth.A515:524-542, 2003.
- [6] see http://www.lnf.infn.it/esperimenti/sr_dafne_light/
- [7] M. Zobov, ICFA Newslett.31:14-29, 2003.
- [8] C. Milardi et al., e-print Archive :physics/0312072.
- [9] C. Milardi et al., PAC03, p. 2949.
- [10] S. Guiducci et al., EPAC2004, p. 1678.
- [11] A. Drago et al., PRSTAB 6:052801, 2003.
- [12] A. Drago, EPAC2004, p. 2613.
- [13] C. Vaccarezza et al., EPAC2002, p. 1314.
- [14] M. Zobov, e-print Archive:physics/0311129.
- [15] C. Vaccarezza et al., this proceedings.
- [16] A. Gallo et al., e-print Archive:physics/0411156.
- [17] G. Benedetti et al., PAC03, p. 2279.
- [18] C. Ligi, R. Ricci, eConf c0309101:FRWA003,2003.
- [19] R. Boni, e-print Archive:physics/0402081.
- [20] C. Milardi, e-print Archive:physics/0403044.
- [21] F. Ruggiero, M. Zobov, eConf c0309101:SAPL004.
- [22] C. Biscari et al., ICFA Newslett.35:107-117, 2004.
- [23] C. Biscari et al., EPAC2004, p. 680.
- [24] A. Gallo, P. Raimondi, M. Zobov, physics/0404020.
- [25] C. Biscari et al., LNF-05/04 (IR), 2005.
- [26] C. Biscari et al., this conference.

TEMPORAL E-BEAM SHAPING IN AN S-BAND ACCELERATOR

H. Loos*, D. Dowell, S. Gilevich, C. Limborg-Deprey, SLAC, Menlo Park, CA 94025, USA
 Y. Shen, J. Murphy, B. Sheehy, T. Tsang, X. Wang, Z. Wu, BNL, Upton, NY 11973, USA
 L. Serafini, INFN-Milano, Milan, Italy
 M. Boscolo, M. Ferrario, M. Petrarca, C. Vicario, INFN/LNF, Frascati (Rome), Italy

Abstract

New short-wavelength SASE light sources will require very bright electron beams, brighter in some cases than is now possible. One method for improving brightness involves the careful shaping of the electron bunch to control the degrading effects of its space charge forces. We study this experimentally in an S-band system, by using an acousto-optical programmable dispersive filter to shape the photocathode laser pulse that drives the RF photoinjector. We report on the efficacy of shaping from the IR through the UV, and the effects of shaping on the electron beam dynamics.

INTRODUCTION

The experiments reported here were conducted at the DUV-FEL facility at BNL/NSLS with a suitable photoinjector and drive laser in collaboration with the SPARC Project at INFN-LNF providing the acousto-optical programmable dispersive filter (AOPDF) used to temporally shape the laser pulses.

The DUV-FEL facility [1] consists of a frequency tripled Ti:Sapphire amplifier laser, a 250 MeV S-band accelerator, and the NISUS undulator for SASE and High Gain Harmonic Generation FEL experiments in the IR and deep UV [2]. The accelerator features a 6 MeV BNL/SLAC/UCLA gun, 2 SLAC-type accelerating structures providing 70 MeV followed by a 4 dipole chicane and three more accelerating structures with a final energy of up to 250 MeV after a recent energy upgrade [3]. A spectrometer dipole after the last structure enables energy spectra and time resolved measurements [4].

The first part of this paper describes the laser system and the pulse shaping method. The second part reports on the measurements of the electron beam properties using shaped drive laser pulses.

LASER SHAPING

The principle of an AOPDF [5] is to generate an acoustic wave in a birefringent crystal (tellurium oxide) which diffracts the incident light wavelength dependent. The small scaling factor $\alpha = \Delta n V/c$ (acoustic speed V and index difference Δn) of typically 10^{-7} between the acoustic and optic wave allows the diffraction of 800 nm light with a 50 MHz rf signal. In frequency domain, the diffracted light

wave is $E_{out}(\omega) = E_{in}(\omega) S(\alpha\omega)$ with an acoustic wave $S(\omega)$, thus allowing arbitrary modulations of phase and amplitude within the temporal limits given by the crystal length.

The DUV-FEL photocathode laser system is shown in Fig. 1. A 5 W green Millennia V laser pumps a 10 nJ, 100 fs Ti:Sapphire oscillator. The oscillator pulse is stretched to 200 ps and amplified in a flash-lamp YAG pumped regenerative oscillator to 2 mJ and in a 2-pass amplifier to 20 mJ. After a grating compressor 9 mJ remaining infrared are doubled and tripled in a 500 μm and a 100 μm BBO crystal giving 500 μJ of UV light. A spatial filter consisting of a pin-hole and an iris aperture reduces the UV to 50 μJ being sent to the photo-cathode.

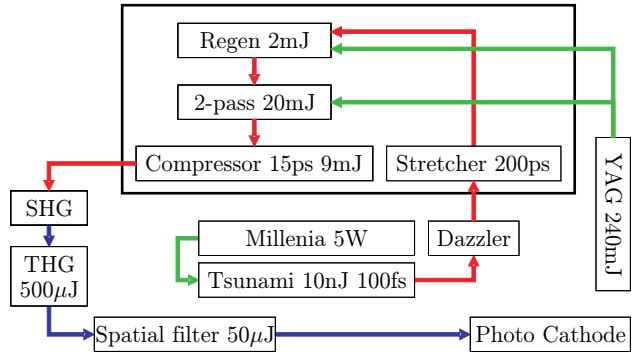


Figure 1: Layout of the DUV-FEL laser system including the DAZZLER.

The AOPDF (a DAZZLER from FASTLITE) was inserted behind the Ti:Sa oscillator considering the damage threshold of the device. At that location the pulse shape of the final UV pulse will be affected by both the amplification and the harmonic conversion process, which has to be taken into account to find the appropriate amplitude and phase filter for the AOPDF.

Laser Diagnostics

Both spectral and temporal diagnostics were used to characterize the 800, 400, and 266 nm light. Single shot and averaged spectra were obtained with a monochromator using an 1800/mm grating. The SHG and THG light spectra were taken in second and third order. Time distributions at all wavelengths were obtained with a streak camera with 2 ps resolution in synchro-scan mode and with a scanning cross-correlator for the UV light with a resolution of 200 fs.

*loos@slac.stanford.edu

Shaping Results

The goal of the study was to generate a 10 ps long τ at-top UV laser pulse with a 1 ps rise/fall time and a τ atness of 10%. These parameters were shown to be optimal in a similar experiment using an LCSLM [6]. Three different methods were pursued to obtain the proper filter for the AOPDF. The first strategy relied on the time-wavelength correlation of a chirped pulse in creating a 10th order super-gaussian spectrum which corresponds to a nearly τ at-top time distribution within the requirements. To account for the saturation effect in the amplifier, a few iterations were necessary, in which the ratio between the actual spectrum and the goal spectrum was used as a multiplicative correction to the amplitude filter of the AOPDF. The second method was the implementation of a genetic algorithm to optimize the time shape directly. Simulations showed good conversion after several hundred iterations. However, the fact that no single shot measurement with high resolution was available, made this method unfeasible. The third method was to manually tune amplitude and phase of the filter function.

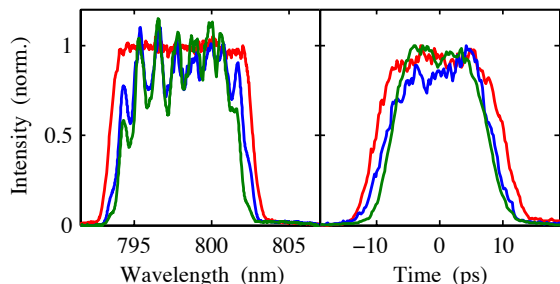


Figure 2: Spectra and streak camera time profiles of 15 ps long shaped laser pulse.

The results of the iterative spectrum optimization are shown in Figs. 2 and 3. The incident 10 nm wide Gaussian oscillator spectrum was shaped into a 9 nm wide τ at-top IR spectrum. The slight loss of bandwidth in the blue light is due to the bandwidth limitation of the 500 μm thick SHG crystal. An even larger loss in the UV bandwidth could be prevented by replacing the original 250 μm crystal with a 100 μm thick one. The time distributions from the streak camera show a corresponding shortening between the IR and the blue. The comparison of the high resolution cross-correlation and the UV spectrum exhibit a strong correlation between the spectral and the temporal modulation. The source of this modulation was found to be the stretcher and the regenerative amplifier. Further experiments confirmed that small amplitude modulations in the oscillator pulse eventually create large modulations in the UV spectrum with a gain of about 10. The mechanism is presumably a Kerr-effect in the regenerative amplifier crystal which converts amplitude into phase modulation. This phase modulation becomes apparent only in the spectra of the generated harmonics and also produces temporal modulation.

Since the spectral phase changes are not influenced by the amplification process, the Kerr-induced phase modula-

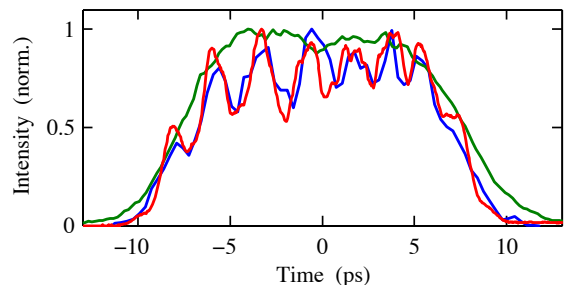


Figure 3: Time profile of 15 ps long shaped UV laser pulse. The blue line shows the cross-correlation, the green the streak camera, and the red the UV spectrum scaled to match the time distribution.

tions could in principle be corrected with a phase filter for the AOPDF. However, the modulation period of about 1 nm is too fine considering the effective resolution of the Dazzler of 1 nm. Furthermore, the modulation amplitude was fluctuating up to 50% from shot to shot due to small variations in the saturation power of the regen and thus limiting the ability to suppress the modulation.

To produce the required 10 ps UV pulse for the photoinjector, the IR pulse was shortened in the studies with the electron beam. The resulting UV pulse was 8 ps long with 1 ps long edges, but 30% variation throughout the pulse.

ELECTRON BEAM MEASUREMENTS

The electron beam was generated with the gun phase at 30° and both phases of linac 1 and 2 set to maximize the energy to 65 MeV and to minimize residual chirp. The following chicane was not powered to measure the uncompressed beam. Electron beam images were generated at various YAG screens and measured with CCD cameras. The projected transverse emittances were measured using three screens along linacs 3 and 4, which were not powered then. Time resolved measurements were taken at the screen after the spectrometer dipole with linac 3 or 4 set to zero phase to impose a known, variable chirp to the beam. The time resolved vertical slice emittance was obtained by vary-

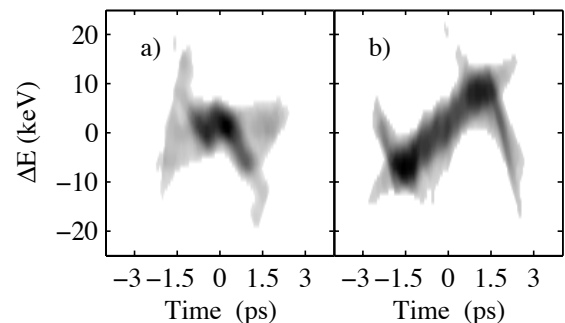


Figure 4: Longitudinal phase space reconstructions for 70 pC. Panel a) shows the Gaussian, b) the τ at-top case.

ing a quadrupole upstream of the spectrometer to generate a vertical focus and correlating the horizontal energy distribution of the beam to a time coordinate with the known chirp. The longitudinal phase space parameters were measured by varying the sign and amplitude of the chirp while recording the energy distribution. Analyzing the energy spread gives the longitudinal emittance and bunch length, whereas a tomographic reconstruction [7] using the energy profiles resolves the phase space distribution and thus the energy time correlation and the beam current distribution.

The experiments were done for bunch charges of 70 pC and 300 pC and an non-shaped Gaussian and a shaped \dagger at-top UV laser pulse. The filter for the AOPDF was manually tuned to minimize the modulation in the laser pulse by monitoring the modulation in the energy spectrum of the electron beam. The reconstructed longitudinal phase space for the low charge case is shown in Fig. 4, the corresponding slice energy deviation and the electron and laser beam time distributions are displayed in Fig. 5. The vertical slice emittance and the beam mismatch parameter $\xi = (\gamma_0\beta - 2\alpha_0\alpha + \beta_0\gamma)/2$ are shown in Fig. 6. The Twiss parameters of the central slice were used as reference for the mismatch.

Table 1: Laser and electron beam parameters

Shaped Charge		pC	No	Yes	No	Yes
Laser σ_z rms	ps	2.0	2.7	2.0	2.8	
Laser σ_z fwhm	ps	4.8	7.8	4.8	7.5	
σ_z	ps	1.15	1.43	1.7	1.9	
ΔE proj	keV	5.7	8.0	5.1	6.8	
$\epsilon_{z,n}$	μm	5.5	8.1	10	15	
ΔE ave	keV	4.3	4.0	4.3	7.0	
$\Delta E/E$ ave	10^{-5}	7	6	7	10	
$\epsilon_{y,n}$ proj	μm	1.7	1.4	2.0	1.5	
Matched Charge	pC	42	50	217	270	

The electron beam and corresponding laser parameters obtained from these measurements are listed in Table 1. The average energy spread values are taken over all slices disregarding the correlation which increases the projected values. The matched charge value is the amount of charge with a mismatch parameter of less than 1.15. The projected vertical emittance in the low charge case was calculated from the slice measurement, whereas the numbers at high charge are from the three screen measurement. In both cases, a significant reduction of vertical emittance could be observed due to the shaping of the laser, which is due to a better slice alignment.

SUMMARY

The desired pulse length and rise time of the UV laser pulse could be obtained by using an AOPDF for shaping. The lack of a fast temporal diagnostic made the optimization of the required \dagger atness unfeasible. The electron

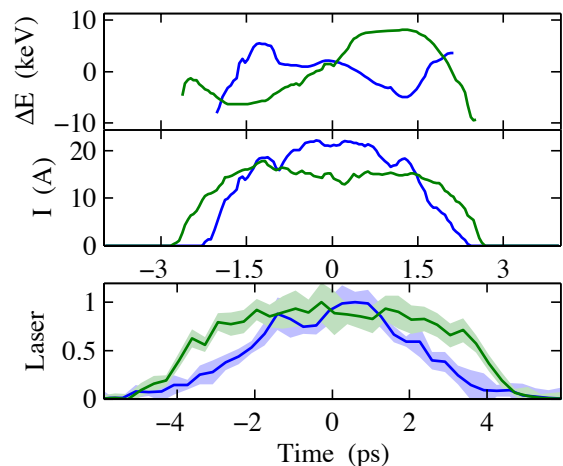


Figure 5: Time distributions from phase space reconstruction. Blue indicates the Gaussian, green the \dagger at-top case. The top panel shows the correlation between slice energy vs. time, the middle shows the current distribution, and the bottom the corresponding UV laser pulse distributions.

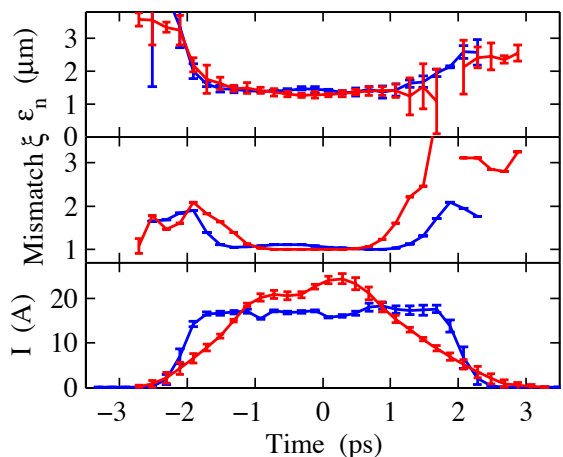


Figure 6: Vertical slice emittances for 70 pC. Red indicates the Gaussian, blue the \dagger at-top case.

beam with the shaped laser had a more uniform longitudinal phase space, a reduced projected transverse emittance, and a larger part of the pulse with matched slices.

This work was supported by DOE Contracts DE-AC03-76SF00515 and DE-AC02-98CH10886.

REFERENCES

- [1] W. S. Graves et al., PAC 2001, Chicago, June 2001, p. 2860
- [2] L.H. Yu et al., Phys. Rev. Lett. **91** (2003) 074801
- [3] X.J. Wang et al., these proceedings, TOAB003
- [4] W. S. Graves et al., PAC 2001, Chicago, June 2001, p. 2224
- [5] F. Verluise et al., Opt. Lett. **25** (2000) 575
- [6] J. Yang et al., EPAC 2002, Paris, June 2002, p. 1828
- [7] H. Loos et al., Nucl. Instrum. Meth. A 528 (2004) 189

PROPOSAL OF AN EXPERIMENT ON BUNCH LENGTH MODULATION IN DAΦNE

C. Biscari, D. Alesini, G. Benedetti, M.E. Biagini, R. Boni, M. Boscolo, A. Clozza, G. Delle Monache, G. Di Pirro, A. Drago, A. Gallo, A. Ghigo, S. Guiducci, M. Incurvati, C. Ligi, F. Marcellini, G. Mazzitelli, C. Milardi, L. Pellegrino, M.A. Preger, P. Raimondi, R. Ricci, C. Sanelli, M. Serio, F. Sgamma, B. Spataro, A. Stecchi, A. Stella, C. Vaccarezza, M. Vescovi, M. Zobov, LNF-INFN, Frascati, Italy; C. Pagani, INFN, Milano, LASA, Italy
E. Levichev, P. Piminov, D. Shatilov, BINP, Novosibirsk, Russia
J. Byrd, F. Sannibale, LBL, USA; J. Fox, D. Teytelman, SLAC, USA

Abstract

Obtaining very short bunches is an issue especially for colliders but also for CSR sources. The modulation of the bunch length in a strong rf focusing regime had been proposed, corresponding to a high value of the synchrotron tune. A ring structure where the function R56 along the ring oscillates between large positive and negative values will produce bunch length modulation. The synchrotron frequency can be tuned both by the rf power and by the integral of the function R₅₆, up to the limit of zero value corresponding to the isochronicity condition. The proposal of a bunch length modulation along the ring in DAΦNE is here described. DAΦNE lattice can be tuned to positive or negative momentum compaction values, or to structures in which the two arcs are respectively set to positive/negative integrals of the R56 function. With the installation of an extra rf system at 1.3 GHz, experiments on bunch length modulation both in the regime of high and low synchrotron tune can be realized.

INTRODUCTION

Short bunches are interesting for both e+e- circular colliders and synchrotron light source storage, the first to overcome the luminosity degradation due to the hourglass effect at very low β*, the second to produce in a controlled way Coherent Synchrotron Radiation (CSR). All factory upgrades use minimization of the bunch length by high rf voltages as an essential feature of their projects, while CSR sources base the feasibility of very short bunches on the isochronicity regime.

In the framework of superfactories studies the strong rf focusing regime (SRFF) [1] was used as one of the principles for a Φ factory design. This regime is based on a high rf voltage and a high momentum compaction (α_c) ring lattice which together produce a bunch length modulation along the ring. The microwave instability effects on the bunch lengthening in principle can be controlled by placing the high impedance objects in the ring zones corresponding to the longer bunch, with the collision point placed at the shorter bunch position.

An evolution of the SRFF principle has been recently proposed[2]: a ring structure where the dependence of the longitudinal position of a particle on its energy oscillates between large positive and negative values along the ring

can also produce a bunch length modulation. The synchrotron frequency can be controlled by means of the rf voltage and the momentum compaction. This regime overcomes one of the critical points of the SRFF principle, where due to the large synchrotron tune Q_s both the dynamic aperture and beam-beam effect depend critically on the 3D working point choice[3].

No storage ring has been so far operated in such a regime. The DAΦNE magnetic structure can be tuned both on the high and low synchrotron tune regimes, and with a new rf system at 1.3 GHz[4] the bunch length modulation can be enhanced. This paper will be focused mainly on the beam dynamics aspects of the experiment, referring the reader to [4,5] for hardware details.

PRINCIPLE FOR THE BUNCH LENGTH MODULATION

In a ring with one rf cavity placed at s_{rf} (peak voltage V, wavelength λ_{rf}), whose gradient is given by:

$$U = \frac{2\pi}{E} \frac{V}{\lambda_{rf}} \quad (1)$$

where E is the beam energy, the general expressions of the generalised longitudinal Twiss parameters are[1,2]:

$$\begin{aligned} \cos \mu &= 1 - \frac{\alpha_c L}{2} U \\ \beta_L(s) &= \frac{1}{\sin \mu} (\alpha_c L - R_1(s) R_2(s) U) \\ \gamma_L &= \frac{U}{\sin \mu} \end{aligned} \quad (2)$$

where μ is the longitudinal ring phase advance, L the closed orbit length and R_i(s) the longitudinal drift functions defined as:

$$R_1(s) = \int_s^{s_{rf}} \frac{D(s')}{\rho(s')} ds' \quad \text{and} \quad R_2(s) = \alpha_c L - R_1(s) \quad (3)$$

D is the dispersion function and ρ the dipole bending radius. Notice that R₁(L) = α_cL, and therefore the function β_L is periodic in L. The beam energy spread, proportional to γ_L, is constant along the ring:

$$\left(\frac{\sigma_E}{E} \right)^2 = \frac{\gamma_L}{2} C_L \frac{\gamma^5}{L \alpha_{\parallel}} \int \frac{\beta_L(s)}{|\rho(s)|^3} ds \quad (4)$$

with $C_L = 2.15 \cdot 10^{-19} \text{ m}^3 \text{ sec}^{-1}$, and α_{\parallel} the longitudinal damping constant. The longitudinal emittance ε_L is:

$$\varepsilon_L = \frac{1}{\gamma_L} \left(\frac{\sigma_E}{E} \right)^2 \quad (5)$$

and the bunch length is $\sigma_L(s) = \sqrt{\varepsilon_L \beta_L(s)}$. The modulation in β_L and bunch length becomes not negligible if U is high and the drift functions large. Two regimes can be used:

- the function $R_I(s)$ is *monotonic* in s , corresponding to the SRFF regime[1], with a large synchrotron tune Q_s .
- $R_I(s)$ is *non-monotonic*, and has a large derivative with opposite signs in two different zones of the ring[2]. As $R_I(L)$ tends to zero the ring becomes isochronous. Most storage rings lattices are not flexible enough to reach the necessary $R_I(L)$ variation, and/or do not have the necessary powerful and concentrated rf system.

DEDICATED DAΦNE STRUCTURE

The dispersion in DAΦNE can be tuned on a wide range thanks to the independently powered quadrupoles, while the rf system is dimensioned for the usual collider operation: the present U parameter must be increased at least one order of magnitude to reach a measurable bunch length modulation. An extra SC rf cavity at 1.3 GHz, with a maximum voltage of 10 MV[4] can be installed in either of the two Interaction Regions (IRs), serving both rings. The IRs are usually occupied by different experiments[6], and since vacuum aperture is needed to install the rf cavity, our proposed accelerator physics experiment can be scheduled between two physics runs, using a detuned optics for both IRs, without low-beta insertions.

The maximum α_c value and $R_I(s)$ variation are limited by the physical and dynamic aperture of the ring. Three different structures are considered: structure A) in *monotonic* regime, where the contributions of all dipoles to the drift function is positive, as shown with black ; in Fig. 1, which shows the $R_I(s)$ behaviour for all three cases; α_c is 0.073, about three times larger than the present one. With high values of V , Q_s approaches the half integer, as shown in Fig.2. Structure B) (violet empty dot in figures) corresponds to *non-monotonic* regime with negative dispersion in two of the short arc dipoles, and a value of α_c similar to the present one (0.02). Structure C) (blue full dot in figures) is also *non-monotonic* but with a much lower value of α_c (0.004).

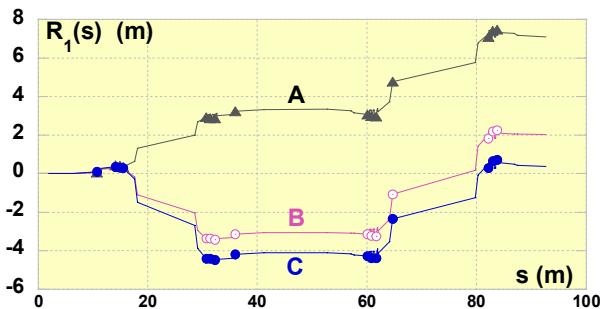
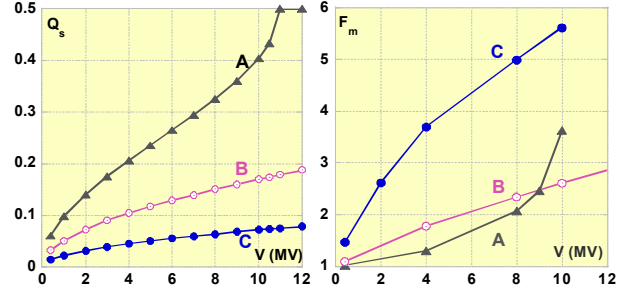


Figure 1 : Behaviour of $R_I(s)$ along the ring with $s_{rf} = 0$.

The main goal of the experiment is to measure the bunch length modulation factor, $F_m = \sigma_{Lmax}/\sigma_{Lmin}$. For structure A) F_m becomes noticeably larger than unity for high V (see fig.3), when μ approaches π . In structure B) F_m is measurable also with low rf voltage. In C) F_m is larger since it is enhanced when approaching isochronicity.



Figures 2-3 : Q_s and F_m as a function of V .

In the *monotonic* case (A) the minimum bunch length is in the IR opposite to the cavity position, since it occurs in the point where $R_I(s) = \alpha_c L/2$ [1,2], while in B) and C) it is near the rf cavity position. In the whole range the bunch length is of the order of few mm, as shown in Fig 4, which represents σ_{Lmax} and σ_{Lmin} for the three structures.

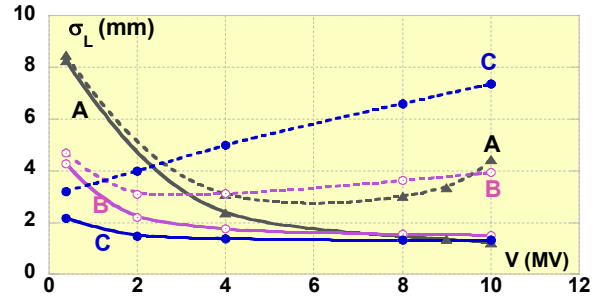


Figure 4 – σ_{Lmin} (full) and σ_{Lmax} (dashed) on V

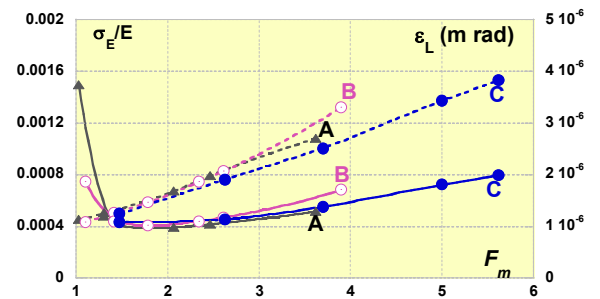


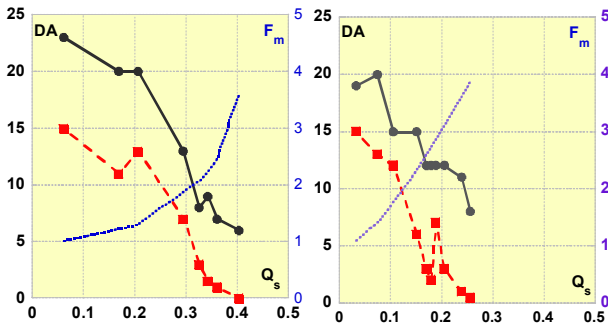
Figure 5 – σ_E/E (dashed) and ε_L (full) as functions of F_m .

The energy spread increases with F_m , as can be deduced from eq.(4). ε_L is large for low V , decreases up to a minimum, and then increases again. An interesting result is that the behaviour of σ_E/E and ε_L with F_m is very similar for all the structures (see Fig.5).

Dynamic aperture

The horizontal and longitudinal planes in the bunch length modulation regime are strongly coupled. Also on-energy particles, due to the coupling non-linear terms, oscillate with large amplitudes in the longitudinal plane.

The dynamic aperture (DA) for the *monotonic* structure A ($Q_x = 4.82$, $Q_y = 5.21$, $\varepsilon_x = 0.54$ mm mrad) and the *non-monotonic* B ($Q_x = 5.81$, $Q_y = 5.15$, $\varepsilon_x = 0.6$ mm mrad) has been computed with the MAD8 code, after a first optimisation of the sextupole configurations for chromaticity correction. Figures 6 and 7 represent the horizontal dynamic aperture in terms of σ_x on energy (black) and at $6\sigma_E/E$ (red) as functions of Q_s . Since σ_E/E increases with Q_s (see eq(4) and Fig,5), each point in the red line corresponds to a different off-energy absolute value. In the figures also F_m has been represented (right vertical scale): for the same value of F_m the *non-monotonic* regime has a wider DA.



Figures 6-7 – Horizontal DA for structures A-B on energy (black dots) and at $6\sigma_E/E$ (red squares) as Q_s functions, and corresponding F_m (blue right scale).

There are different effects affecting the aperture as Q_s changes: the stronger longitudinal kick, the corresponding increase in the value of σ_E/E , and the resonances: in the curves the effect of $Q_s = 0.166$ and 0.33 is evident. The typical island representation to which we are used in the transverse planes, appears now also in the longitudinal phase plane, as in the example of Fig.8 corresponding to Q_s near 0.33 (structure A, $V = 8$ MV).

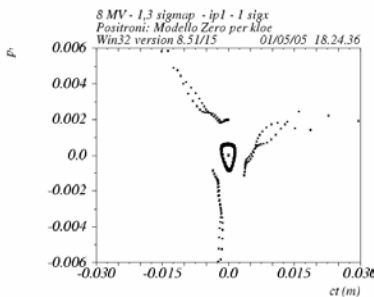


Figure 8 - Longitudinal phase plane with $Q_s = 0.33$

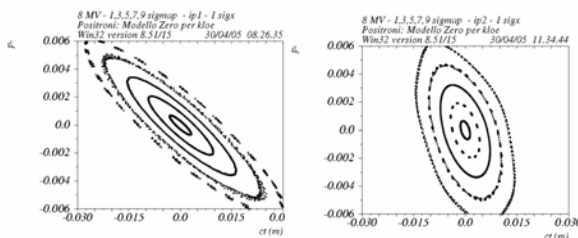


Figure 9 – Longitudinal phase plane at IP_2 and IP_1 for structure B, $V = 8$ MV.

Figure 9 represents the longitudinal phase plane at the cavity position (IP_2) and in the opposite side (IP_1) of the ring for structure B with $V = 8$ MV. The ellipse projection on the horizontal axis is proportional to the bunch length, and there is about a factor 2 between the two points. Results show that the experiment is feasible, but give a special warning on the sensitivity of the working point choice, specially for the *monotonic* case.

CONCLUSIONS

We propose an accelerator physics experiment in DAΦNE to test the bunch length modulation regime in storage rings. It is not meant for increasing the collider performances with the present design, since a luminosity increase would need a different IR, a stronger variation of the drift functions, more radiation damping and a lower impedance, specially on the e- ring [6].

The experiment offers anyway a wide range of different results. The measurement of the modulation factor is the first and essential aim of the experiment, and can be done even at very low current, single bunch operation. The high synchrotron frequency (above the MHz for case A) which can be reached with these structures asks for feedback system modification to test multibunch operation at high currents.

Other results of the experiment are:

- The measurement of the microwave instability threshold in different regimes with very short bunches. In fact the two DAΦNE rings have different impedances due to the presence in the e-ring of ion clearing electrodes. The two IRs will have also different impedance since one will house the new rf cavity, and the bunch length is minimum in IR_1 or IR_2 according to which of the two regimes are used.
- The Touschek effect observation as a function of the bunch length modulation.
- Beam dynamics and dynamic aperture with high synchrotron frequency.
- Localized production of stable CSR and comparison with the distributed production along the ring.

REFERENCES

- [1] A. Gallo, P. Raimondi, M. Zobov, e-Print Archive: physics/0404020.
- [2] C. Biscari, “Bunch length modulation in storage rings with low synchrotron tune”, to be published
- [3] C. Biscari et al., “Feasibility study for a very high luminosity Φ -Factory”, Proceedings of EPAC04, Lucerne, Suisse, July 2004
- [4] D. Alesini et al, “Design of a Multi-Cell, HOM Damped Superconducting Cavity for the SRFF Experiment at DAΦNE”, this conference
- [5] A. Gallo et al , “Proposal of a Strong RF Focusing Experiment at DAΦNE”, Proceedings of EPAC 04
- [6] M. Zobov et al, “DAΦNE Operation and plans for DAΦNE2”, this conference.

RECENT OBSERVATIONS ON A HORIZONTAL INSTABILITY IN THE DAFNE POSITRON RING

Alessandro Drago, Mikhail Zobov (INFN / LNF, Frascati, Italy), Dmitry Teytelman (SLAC, Menlo Park, California, USA)

Abstract

A strong horizontal instability limits the maximum positron current storable in the DAFNE Phi-Factory. A powerful feedback system makes it possible to store and put in collision more than 1300 mA of positron current in 105-109 bunches. Nevertheless, a much higher current ($>2.4A$) has been successfully stored in the twin electron ring. Measurements have been carried out to understand the positron current limit and to characterize the behavior of the horizontal instability at high current with different bunch patterns. Grow/damp turn-by-turn data obtained by turning off the horizontal feedback have been acquired and analyzed. Spectral analysis and growth rates of the instability are shown. In particular, the -1 mode has strong evidence and fast growth rate. Its growth rate behavior is analyzed at different beam currents and bunch patterns.

109 bunches. The ring has been filled almost completely (the harmonic number is 120) with contiguous bunches spaced by 2.7 nsec.

Nevertheless, a much higher current ($> 2.4A$) has been successfully stored in the twin electron ring.

Measurements have been carried out to understand the positron current limit and to characterize the behavior of the horizontal instability at high current with different bunch spacings and patterns.

INTRODUCTION

In DAFNE [1], after the 2003 shutdown, a very fast horizontal instability limits the maximum positron current storable in the DAFNE Phi-Factory at $\sim 0.5A$. A powerful feedback system makes it possible to store and put in collision more than 1300 mA of positron current in 105-

SYSTEMS AND TOOLS DESCRIPTION

To study the strong horizontal multibunch instability, the authors have recorded and analyzed the transverse displacements for each bunch on a turn-by-turn basis.

The data acquisition system and preliminary measurements have been presented in a previous paper[2]. The apparatus is able to switch off one or both the transverse feedbacks for short time periods and to put the recorded data in ASCII formatted files. A LABVIEW recording program generates automatically a time stamp directory tree database with the data files [3]. Other LAVIEW analysis tools allow evaluating the stored data.

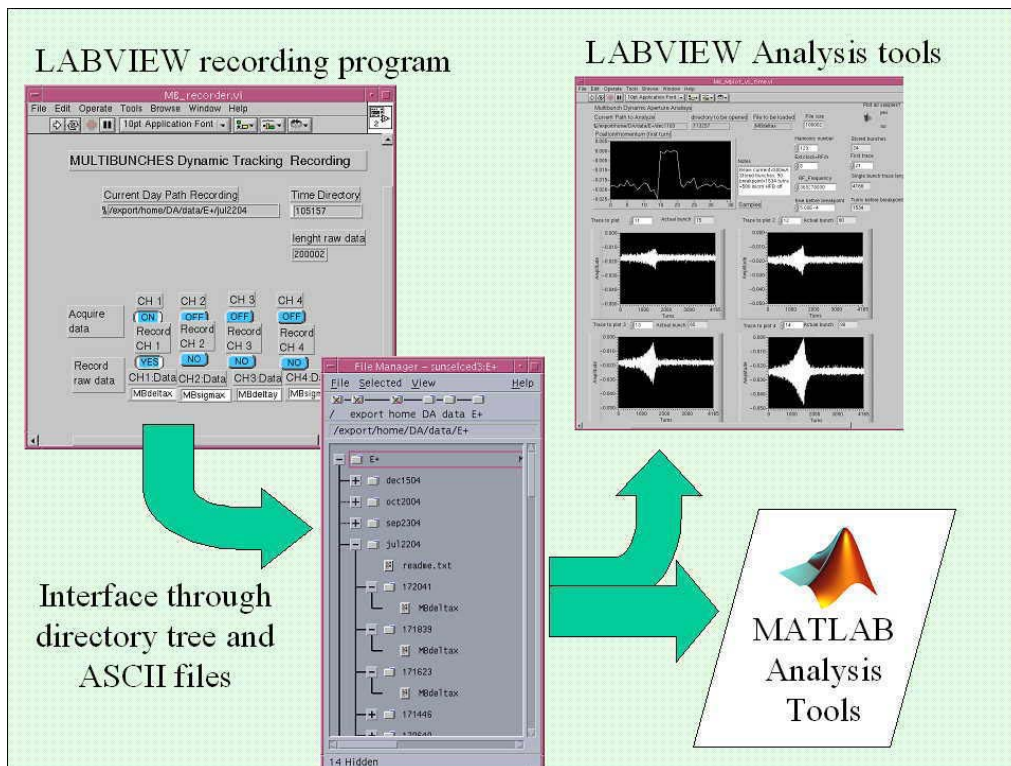


Figure 1: Scheme of the software tools used to record the transients and to analyze the data.

Using this system, it has been possible to estimate the instability growth rates for each bunch at different beam currents and to evaluate the tune shift along the bunch train. In particular, a strong dependence of oscillation amplitudes on the bunch position along the train has been observed.

The database files can be converted offline to standard format to be analyzed by the MATLAB analysis tools developed by the SLAC feedback team [4], [5].

Fig.1 shows a scheme of the software tools used to record the transients and to analyze the data.

The transverse feedbacks utilize, as input to the low power electronics, the same type of pickups and hybrid junctions used by the data acquisition system. The feedback system front-end is composed by a baseband amplification stage, a high pass filter to cut the 50Hz noise and a low pass filter to avoid the aliasing in the following section. The low pass filter is a commercial device with flat group delay for low pulse distortion.

The feedback system generates the correction signal by a partially digital approach [6]. An 8-bits analog to digital converter samples the oscillation signal for each bunch. Simple operations, like bunch-by-bunch timed multiplication for 1, -1 or zero, are implemented to manage the input data flow at 368 MHz. The signal sampling is useful also to stretch the output signal to a bucket period and to make less critical the feedback timing.

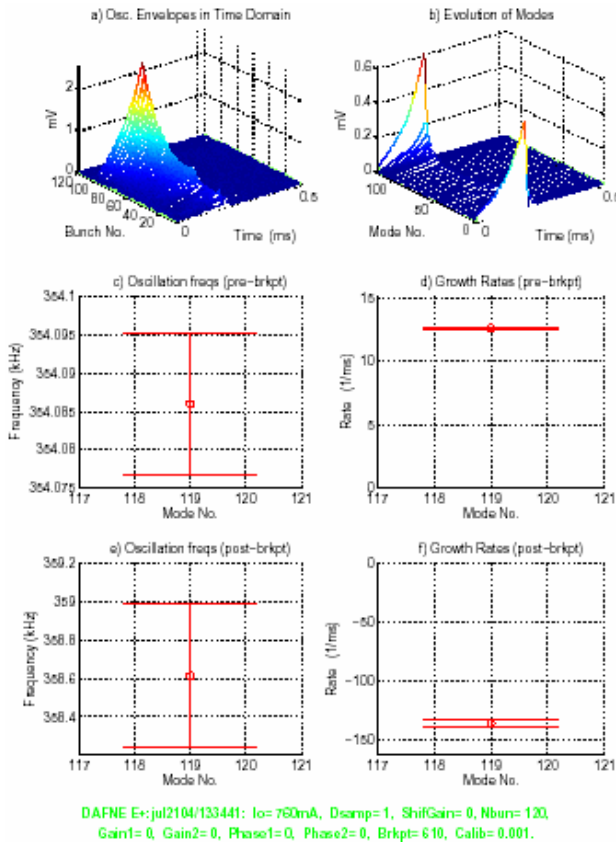


Figure 2: Horizontal grow-damp in the e^+ main ring.

In real time every 2.7 nsec, through a digital to analog converter, a bunch-by-bunch correction signal is sent to the power section and to the kickers. The feedback system can manage for each bunch oscillation frequencies up to the Nyquist limit (revolution frequency divided by two). Each feedback makes use of two 250W power amplifiers.

OBSERVATIONS ON THE INSTABILITY

Grow/damp measurements have been done with the setup plotted in Fig.1. A typical grow/damp shows very fast damping with a high transverse feedback gain. We consistently see only one eigenmode in all horizontal grow/damps: -1. Fig.2 shows results from a horizontal grow-damp in the e^+ main ring. There is some tune shift between open and closed loop. The eigenvalue shift is $148 * 10^3 \text{ s}^{-1} + 28 * 10^3 \text{ rad/s}$.

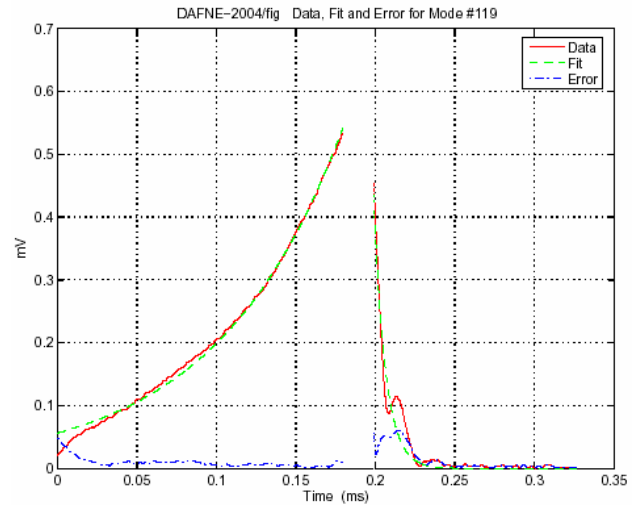


Figure 3: Data fit and error for mode #119.

It is remarkable to note from the figure that the horizontal feedback damping time is $\sim 7 \mu\text{sec}$.

Fig. 3 shows a complex exponential that fits to growth and damping transients.

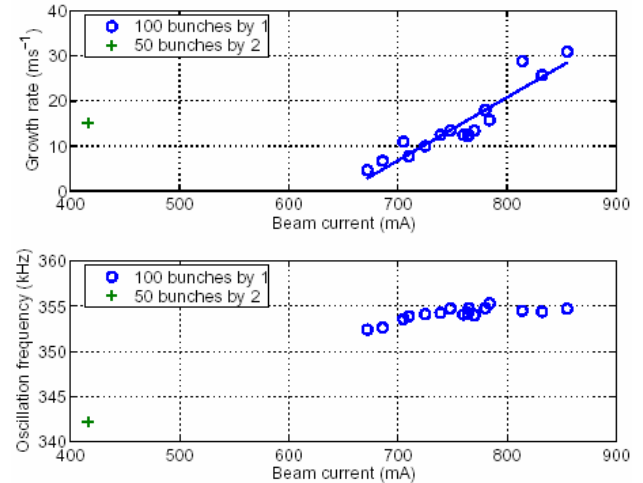


Figure 4: Horizontal growth rate and tune shift recorded on July 21, 2004.

Excellent open-loop fit indicates that growth rate and oscillation frequency have weak dependence on oscillation amplitude.

The growth rates of mode -1 versus beam current and fill pattern are plotted in Fig. 4: these data have been recorded on July 21.

The growth rate shows a roughly linear behavior versus current, as it is plotted in the figure. However changing bunch spacing from one to two RF buckets scales the growth rate by a factor 2. Growth rates induced by constant impedance should scale with total current. The instability behavior could be compatible with the presence of an electron cloud [7].

To understand better the problem, other data have been recorded the day after changing the bunch spacing. The results are plotted in Fig. 5.

The growth rate increases with beam current spacing the bunches by one or two or three. Instead, it decreases with bunch spacing by four or more.

This behaviour could be compatible with an electron cloud decay time of ~ 9 nsec.

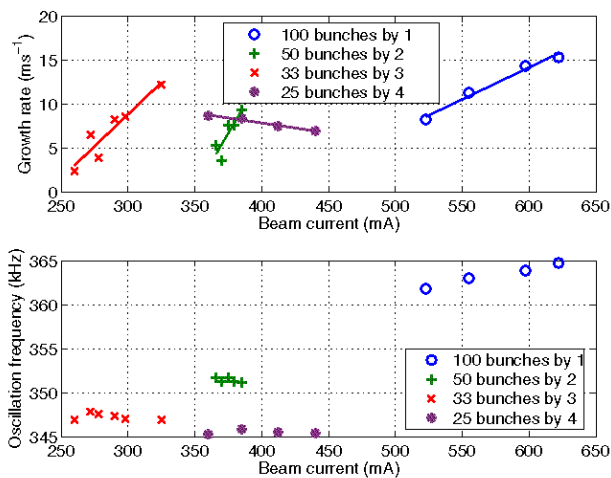


Figure 5: Horizontal growth rate and tune shift recorded on July 22, 2004.

DISCUSSION

Grow/damp turn-by-turn data obtained by turning off the horizontal feedback have been acquired and analyzed. Spectral analysis and growth rates of the instability have been shown. In particular, the -1 mode has strong evidence and fast growth time ($\sim 10\mu\text{s}$).

The instability is very fast.

A so fast instability growth rate cannot be explained only by the beam interaction with HOMs or resistive walls. Growth rates as a function of fill pattern show that this motion is not due to fixed impedance (resistive wall). Its growth rate behavior is analyzed at different beam currents and bunch patterns. The growth rate increases with beam current spacing the bunches by one or two or

three. Differently, it decreases with bunch spacing at least four.

Besides, the rise time scales almost linearly with bunch current (at least, for bunch patterns with spacing 1, 2, 3), while a conventional multibunch instability due to HOMs should scale with the total beam current.

When the bunch spacing becomes larger (4 or more), the rise time decreases. This is compatible with the presence of an electron cloud with ~ 9 nsec decay time. These measurements, together with observations of anomalous vacuum pressure rise and with numerical simulations reported in [7], are in favor of interpreting the instability as an electron cloud one.

CONCLUSIONS

A very fast ($10 \mu\text{sec}$) horizontal instability limits the utmost beam current storable in the DAΦNE positron ring. A strong feedback system helps to increase the current limit from 0.5A to >1.3 A. In the twin ring, the electron beam current is not limited by a similar instability. Transverse grow-damp measurements give results that are compatible with electron cloud instability with a decay time of ~ 9 nsec.

REFERENCES

- [1] M.Zobov et al., "DAΦNE Operation and Plans for DAFNE2", ROAA001, this conference.
- [2] Alessandro Drago, "Horizontal Instability and Feedback Performance in DAFNE e+ Ring", Proceedings of EPAC2004, July 5-7, 2004, Lucerne, Switzerland; LNF-04/18(P), 30/07/04.
- [3] A.Drago, A.Stella, "The Dynamic Tracking Acquisition System for DAΦNE e+/e- Collider", DIPAC2001 Proceedings, 5th European Workshop on Diagnostics and Beam Instrumentation, may 13-15, 2001, Grenoble, France.
- [4] S.Prabhakar, "New diagnostic and Cure for Coupled Bunch Instabilities", PHD Thesis, Stanford Un., SLAC-Report-554, February 2000.
- [5] J.D. Fox et al., "Programmable DSP Based Multibunch Feedback: Operational Experience from Six Installations". BIW 2000, Cambridge, Mass., May 2000. SLAC-PUB-8410.
- [6] A.Drago et al., "Fast Electronics for the DAΦNE Transverse Feedback Systems", ICALEPCS-2001-WEAP048, Nov 2001. 3pp. Contributed to 8th International Conference on Accelerator and Large Experimental Physics Control Systems (ICALEPCS 2001), San Jose, California, 27-30 Nov 2001. Published in eConf C011127: WEAP048, 2001. e-Print Archive: physics/0111209.
- [7] C.Vaccarezza et al., "Electron Cloud Build-Up Study for DAΦNE", FPAP001, this conference.

THE PROJECT PLASMONX FOR PLASMA ACCELERATION EXPERIMENTS AND A THOMSON X-RAY SOURCE AT SPARC

D. Alesini, M. Bellaveglia, S. Bertolucci, M.E. Biagini, R. Boni, M. Boscolo, M. Castellano, A. Clozza, G. Di Pirro, A. Drago, A. Esposito, M. Ferrario, L. Ficcadenti, D. Filippetto, V. Fusco, A. Gallo, G. Gatti, A. Ghigo, S. Guiducci, M. Incurvati, C. Ligi, F. Marcellini, M. Migliorati, A. Mostacci, L. Palumbo, L. Pellegrino, M. Preger, R. Ricci, C. Sanelli, M. Serio, F. Sgamma, B. Spataro, A. Stecchi, A. Stella, F. Tazzioli, C. Vaccarezza, M. Vescovi, C. Vicario,
INFN-LNF, Frascati, Italy

F. Alessandria, A. Bacci, R. Bonifacio, I. Boscolo, F. Broggi, S. Cialdi, C. DeMartinis, D. Giove, C. Maroli, M. Mauri, V. Petrillo, N. Piovella, R. Pozzoli, M. Romè, L. Serafini*,
INFN-MI and Univ. of Milano, Milano, Italy

M. Mattioli, P. Musumeci, M. Petrarca, *INFN-Roma1, Rome, Italy*

U. Bottigli, B. Golosio, P. Oliva, A. Poggio, S. Stumbo, *INFN/Cagliari and Univ. of Sassari, Italy*

A. Barbini, W. Baldeschi, C.A. Cecchetti, M. Galimberti, A. Giulietti, D. Giulietti, L.A. Gizzi, P. Koester, L. Labate, S. Laville, A. Rossi, P. Tomassini, *CNR-IPCF/Pisa and Univ. of Pisa, Italy.*

Abstract

We present the status of the project PLASMONX, recently approved by INFN. This project, based on a collaboration between INFN and CNR-IPCF, aims at a long term upgrade of the SPARC system with the goal to develop at LNF an integrated facility for advanced beam-laser-plasma research in the field of advanced acceleration techniques and ultra-bright X-ray radiation sources and related applications. The project, in its first phase, foresees the development at LNF of a High Intensity Laser Laboratory (HILL) whose main component is a 100 TW-class Ti:Sa laser system synchronized to the SPARC photo-injector. Experiments of self-injection and acceleration of electrons into laser driven plasma waves will be conducted at HILL-LNF, early in this first project phase. Eventually an additional beam line will be built in the SPARC bunker in order to transport the SPARC electron beam at an interaction point, where a final focus system will allow to conduct experiments either of laser-beam co-propagation in plasma waves for high gradient acceleration, or experiments of laser-beam head-on collisions to develop a Thomson source of bright ultra-short X-ray radiation pulses, with X-ray energies tunable in the range 20 to 1000 keV and pulse duration from 30 fs to 20 ps. Preliminary simulations of plasma acceleration with self-injection are illustrated, as well as external injection of the SPARC electron beam.

DEVELOPMENT OF A 100 TW-CLASS LASER SYSTEM AT LNF

While the SPARC Project is in progress at LNF aiming at the construction by the year 2006 of an advanced photoinjector driving a FEL[1], its long term upgrade, based on the project PLASMONX, has just been launched

after approval by INFN, with a first phase aimed at building at LNF a 100 TW-class laser system as the core system of a High Intensity Laser Laboratory (HILL), and a final goal of constituting a national facility merging advanced technologies and expertises in high brightness electron beams and high intensity laser beams, as well as plasma wave formation, control and diagnostics. Under this respect, the collaboration between INFN and CNR-IPCF is considered to be strategic to the realization of the final phase of the facility, where synchronized electron and photon beams of ultra-high performances, in terms of brightness, intensity and brevity will be driven to interact in several fashions, in order to allow investigations of high gradient acceleration techniques and/or X-ray production via Thomson back-scattering in the spontaneous incoherent mode or, eventually, in the coherent collective mode. The proposed time schedule for this initiative is tightly correlated with the progress of the SPARC project: according to this schedule, final completion of the SPARC&PLASMONX facility is foreseen by the year 2009.

The proposed laser system[2] must have unique performances in terms of power, pulse duration, flexibility and reliability: it will be installed inside the dedicated HILL building at LNF, presently under design, located just on top of the SPARC bunker. The laser system, based upon the C.P.A. technique, will deliver < 50 fs, 800 nm, >100 TW, laser pulses at 10 Hz rep. rate. The 5 J laser pulses will be transported uncompressed from the HILL laboratory down into the SPARC bunker. The proposed system combines the reliability of established Ti:Sa technology with novel additional devices aimed at overcoming known issues typical of large Ti:Sa systems.*

* Luca.Serafini@mi.infn.it

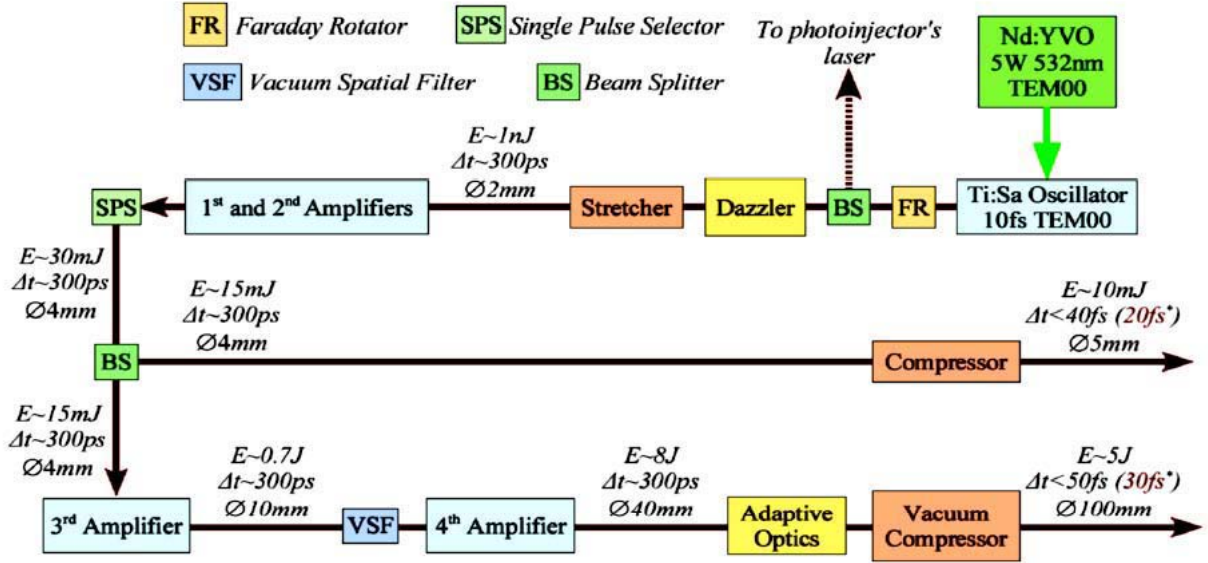


Figure 1: Block diagram of the PLASMON-X laser system showing the main functional components needed for the amplification of the stretched oscillator pulse, its compression and control of spectral and spatial features of the pulse.

One of these issues concerns the power contrast ratio, namely the ratio between the main CPA pulse and the so-called “pedestal”, a spurious precursor radiation arising from amplified spontaneous emission (ASE) by amplifiers. The block diagram of Figure 1 shows the main components of the system, including the devices necessary for ensuring the high quality of the final output.

The oscillator produces a 10 fs pulse that is stretched and pre-amplified by a two stage amplifier up to the 30 mJ level per pulse. Approximately half of this energy is extracted and compressed to provide a low energy beam for probing/diagnostic purposes. The remaining part of the pulse is further amplified to the 8 J level and finally compressed under vacuum. Besides the standard vacuum spatial filter necessary for beam cleaning, we plan to insert an adaptive optics before the vacuum compressor. This device will enable us to remove aberrations on the beam which may result in a poor performance of the compressor as well as poor quality of the focal spot after focusing. Concerning the control of the pulse duration, the system includes a Dazzler device which will enable correction of the spectral features of the pulse prior to stretching. These corrections are necessary in order to keep the final pulse-length well below the 100 fs level. In fact, we aim at reaching the < 50 fs pulse-length which is now regarded as the minimum pulse duration achievable in a multi-joule Ti:Sa laser system. The main beam characteristics after the vacuum compressor are foreseen to be: pulse energy 5 J, peak power > 100 TW, contrast ratio < 10^{-5} .

We plan to conduct R&D on the OPCPA technique (Optical Parametric Chirped Pulse Amplification), that exploits the non-linear properties of some crystals for the amplification of optical pulses: we aim at an inherently low ASE system in which the ASE level is drastically

reduced in the initial amplifier stages. In fact, it is estimated that with an OPCPA system in place, the final pulse length could be as short as 30 fs, thus leading to a peak power as high as 170 TW on target and a contrast ratio smaller than 10^{-8} .

Most of the proposed programme relies on the synchronisation of the laser system with the SPARC Linac and, in particular, with the photoinjector laser system. This can be done either using an electro-optics based approach or optically. In the first way the laser oscillator is synchronized with an external rf signal, by changing dynamically the oscillator cavity length: a jitter between the rf and the laser pulse of less than 1ps is typically achieved. The fully optical approach consists in synchronising the two laser systems. This can be done either by using the same oscillator for both lasers or by measuring the change in delay between the two laser pulses (*i.e.* using a single shot second order cross correlator) with a precision of tens of femtoseconds, and then adjust dynamically a delay line in one of the two laser system.

PLASMA ACCELERATION EXPERIMENTS

Here we describe two possible plasma acceleration experiments that can be performed at HILL (first phase) and inside the SPARC bunker (final phase, external injection).

Self-injection

Following a scheme proposed by Bulanov et al.[3], we studied by simulations the self-injection of electrons trapped by a plasma wave driven across a density transition, as depicted in Fig.2. A 17 fs (FWHM) laser pulse of intensity $I=2.5 \cdot 10^{18}$ W/cm² is focused to a 20 μ m

waist into the plasma: a bunch of 10^8 electrons with energy $E \approx 10$ MeV is generated, with small energy spread $\Delta T/T \approx 5\%$, very short bunch length, $\sigma_z \approx 5 \mu\text{m}$, and quite low transverse emittance, 0.1 mm mrad.

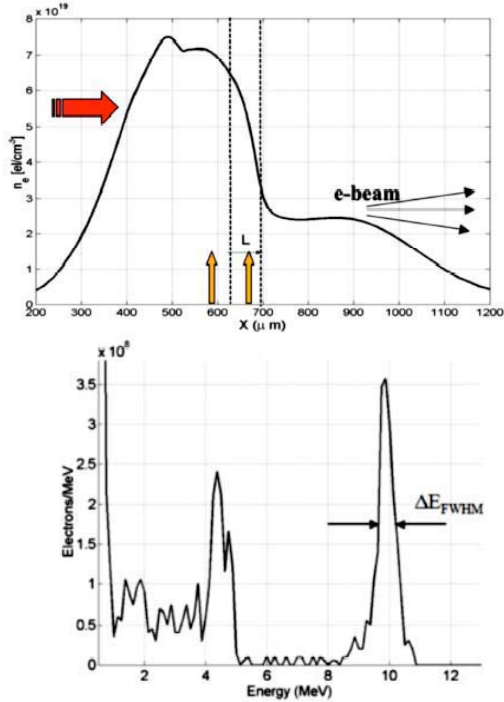


Figure 2 – (lower diagram) Energy spectrum of the accelerated electrons in a plasma with sharp density depletion (upper diagram), generated by 2-d hydrodynamic simulations of an exploding two-foil target (marked by yellow arrows). Red arrow shows the laser pulse propagation.

External Injection

A numerical experiment of injecting an electron bunch produced by the SPARC Linac into a plasma is based on a simulation technique using a test-particle code that assumes a quasi-static field approximation. Transverse fields are at least two orders of magnitude less than the longitudinal ones and are safely neglected, while non-linear effects are treated in a 2-d representation. The injected electron bunch has a charge of 21 pC at an energy of 130 MeV, with $8 \mu\text{m}$ (rms) transverse size and rms length of $\sigma_z = 12 \mu\text{m}$. The energy spread is about 0.1%. The electron bunch has been obtained by a start-to-end simulation of the beam dynamics in the SPARC photo-injector, and transported through the PLASMONX beam-line to the interaction point[4]. The simulation uses a 4J laser pulse with 50 fs pulse length at 800 nm wavelength, focused in a $50 \mu\text{m}$ spot into a preformed plasma of density of $5 \times 10^{16} \text{ cm}^{-3}$. The bunch has a longitudinal extent which is small but not negligible compared to the wavelength of the plasma wave. The energy distribution of the electrons at the exit of the plasma is shown in Figure 3 for two different plasma

acceleration lengths of 20 mm and 100 mm (this implies guiding the laser pulse into a plasma channel [2] or a capillary discharge).

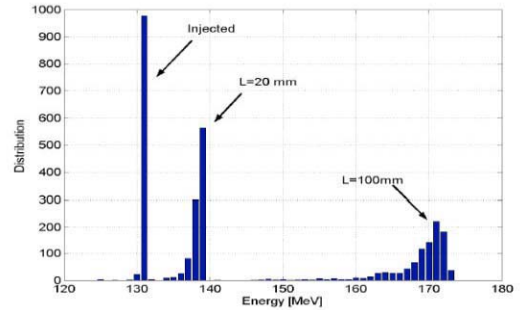


Figure 3 - Electron energy distribution at the exit of a plasma of $5 \times 10^{16} \text{ cm}^{-3}$ for an acceleration length of 20 mm, corresponding to twice the Rayleigh length Z_R of the focusing optics. Also shown in the plot is the result of an accelerator length of 100 mm, assuming a laser pulse guiding over $5 Z_R$. The energy spread of the output electrons is 3% (rms).

X-RAY THOMSON SOURCE

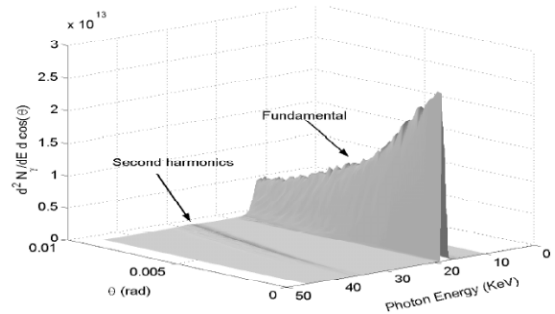


Figure 4 – Angular and spectral distribution of the Thomson source radiation: unguided 3 ps laser pulse focused to $12.5 \mu\text{m}$ beam waist size

By colliding in vacuum the SPARC electron beam[4] and the HILL laser pulse (3 ps, 4 J) we evaluated[5] a yield of $9.3 \cdot 10^8$ photons/s at a tunable energy in the 20-1000 keV range, with angular and spectral distribution as shown in Fig.4. By guiding the laser pulse one can upgrade the photon yield per pulse up to $1.6 \cdot 10^9$.

REFERENCES

- [1] D. Alesini et al., *NIM A* **528** (2004) 586
D. Alesini et al., *Status of the SPARC Project*, these proceedings
- [2] D. Giulietti et al., *PLASMONX: Conceptual Design Report on PLASMA acceleration and MONO-chromatic X-ray production*, unpublished
- [3] S.V. Bulanov et al., *Phys. Rev. E* **58** (5) R5257
- [4] D. Alesini et al., *Design Study for Advanced Acceleration Experiments and Monochromatic X-ray Production @ SPARC*, Proc. EPAC-2004, pag. 695, ISBN: 92-9083-231-2A
- [5] P. Tomassini et al, *Appl. Phys. B* **89** 419-436 (2005)

RF AND MAGNETIC MEASUREMENTS ON THE SPARC PHOTOINJECTOR AND SOLENOID AT UCLA

J.B. Rosenzweig, A.M. Cook, M.P. Dunning, P. Frigola, G. Travish, UCLA Dept. of Physics and Astronomy, Los Angeles, CA 90095, C. Sanelli, F. Tazzioli, INFN-LNF, Frascati (RM) 00044, Italy, and D.T. Palmer, SLAC, Menlo Park, CA 90120

Abstract

The rf photocathode gun and the solenoid for the SPARC project at INFN-LNF (Frascati) have been fabricated and undergone initial testing at UCLA. The advanced aspects of the design of these devices are detailed. Final diagnosis of the tuning of the RF gun performance, including operating mode frequency and field balance, is described. The emittance compensating solenoid magnet, which is designed to be tuned in longitudinal position by differential excitation of the coils, has been measured using Hall probe scans for field profiling, and pulsed wire methods to determine the field center. Comparisons between measurements and the predictions of design codes are made.

DESIGN OVERVIEW

The SPARC project [1], which is an INFN-ENEA-university collaboration centered at the INFN-LNF (Frascati) lab, is designed to demonstrate a state-of-the-art, high brightness electron source, and utilize this source for experiments. These experiments demand the highest beam performance levels, and include radiation production (e.g. FEL [2] and inverse Compton scattering) and advanced acceleration schemes (e.g. laser-plasma and inverse FEL) [3].

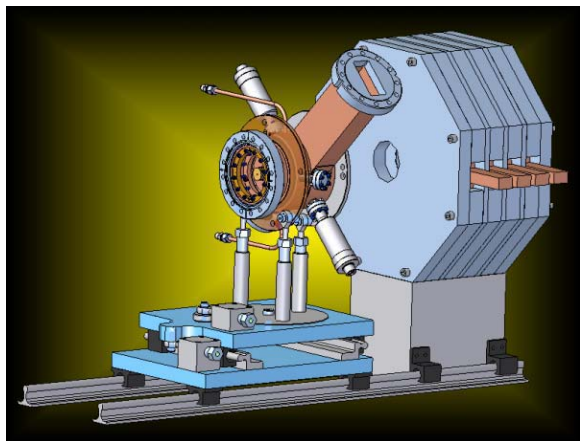


Figure 1. Schematic of SPARC photoinjector RF gun and emittance compensation solenoid. Supports not as built, cathode flange removed.

The electron source for SPARC, shown schematically in Fig. 1, is very close in design to the photoinjector sources designed for the LCLS X-ray SASE FEL [4], and deployed recently at the NLCTA-ORION. The source is based on the 1.6 cell 2856 MHz BNL/SLAC/UCLA RF

photoinjector gun, run at high gradient (120-140 MV/m on-axis field), which demands 11-15 MW of RF power. It is fitted with Cu or higher-quantum efficiency Mg photocathodes. The cathode is illuminated with a 266 nm pulse of frequency-tripled laser light which is spatially and temporally shaped into a flat-top, uniform intensity profile [2].

The gun is followed by an emittance compensation solenoid approximately 20 cm in length, and a drift to a linac section (entrance 150 cm from the cathode). This linac section has an additional solenoid focusing applied around it, to aid in the emittance compensation process, as called for in the so-called Ferrario working point [4] that forms the basis of many high brightness designs at present.

Both the gun and emittance compensation solenoid were redesigned through collaborative work at UCLA and INFN, with fabrication and initial testing occurring at UCLA. The 1.6 cell gun is close in design to the ORION model [5], which was also created by UCLA in collaboration with SLAC. Recent lessons learned from the ORION gun include, most importantly, the need to remove the insertable (at the outer wall) tuners from the full cell. This avoids breakdown at modest levels of RF power in the gun that afflicts nearly all known version of this gun. The ORION gun [5], with its tuners essentially out of the circuit, has been conditioned to over 15 MW with little arcing; similar experience is reported at the BNL ATF [6].

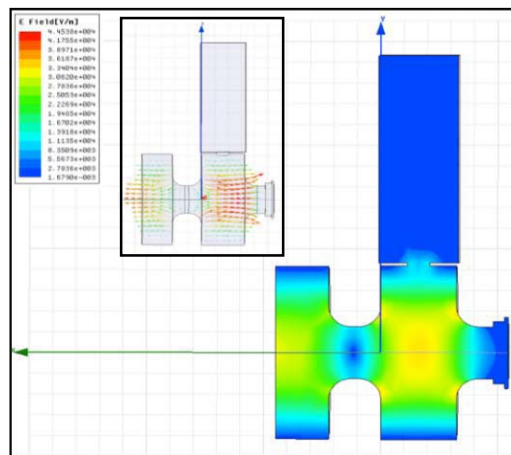


Figure 2. Output of HFSS, showing coupling to waveguide, and field balance in gun.

Thus a major goal of the SPARC gun construction is to remove the reliance on full cell tuners, which also serves to remove much of the quadrupole field component of the

RF profile. It will be seen that removal of the tuners yields gun improvement in the general RF behavior.

In the course of the design process, the gun was simulated using 2- and 3-D codes. In order to model the coupling of the gun to the wave-guide, as well as to accurately predict power dissipation at this relatively high average power (10 Hz, 3 μ sec RF fill) HFSS 3D calculations were performed, as illustrated in Fig. 2.

The SPARC solenoid was designed to be similar to, but more flexible than, the standard BNL/LCLS type of device. Like previous versions, it employs field stiffening iron between coil sections, but in our case there are only four sections (see Fig. 1). Further, these coils are independently powered, in order to tailor the field profile. By asymmetrically exciting the coils (Fig. 3), this centroid of the field can be made with variable center in z , thus allowing choice of distance from the cathode to the effective solenoid lens center. The effect of this variation on the emittance compensation process is shown in Fig. 4. This “knob” will be used in the first phase of the project (no linac post-acceleration) to experimentally identify the optimum conditions for emittance compensation.

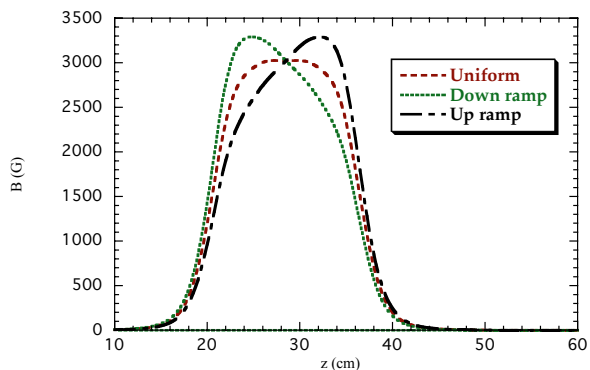


Figure 3. Field profiles in flat, ramp-up and ramp-down excitations of the SPARC solenoid, 60% variation of current between end coils.

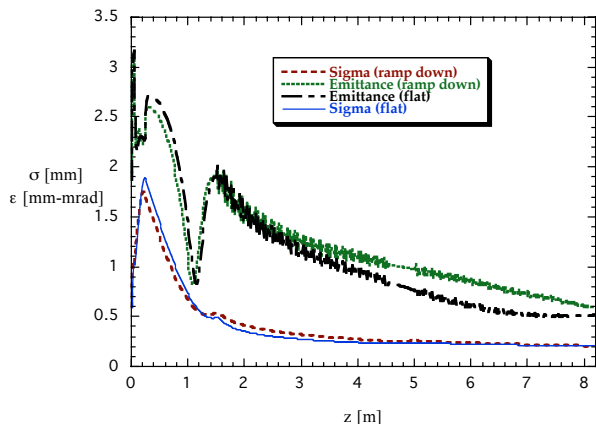


Figure 4. Rms beam size and emittance evolution in the SPARC injector, comparison between flat and ramp-down solenoid settings.

The solenoid was simulated using both POISSON (2D approx.) and Radia (3D). It was constructed with an octagonal outer yoke shape, and utilized coils that have large reservoir cooling, instead of center-core cooling. This allowed a current of 300 A (total current per coil section of 21,600 A-turns).

RF GUN PERFORMANCE

After fabrication and tuning at UCLA and SLAC, the gun underwent final testing at UCLA, and was shipped to Frascati in Jan. 2005. The testing involved: the identification of 0 and π -mode frequencies and their separation; the π -mode field balance, quality factor Q ; external coupling β ; and full cell coupling loop calibration. The results of these measurements are summarized in Table 1.

All measurements require that the gun field be balanced to yield correct running conditions. This balancing is accomplished by deforming the cathode shape using a tuning nut on the exterior center of the cathode. The (excellent) results of this optimization are shown in Figure 5.

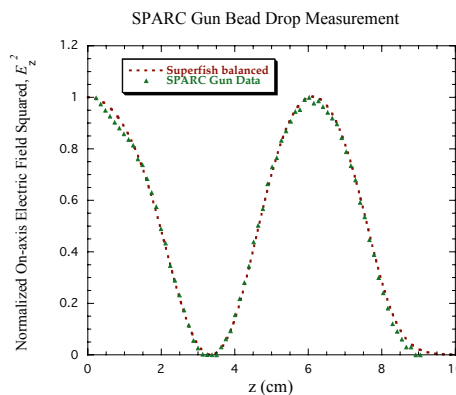


Figure 5. Bead drop data analyzed to show E_z^2 , along with SUPERFISH prediction. Deviations near $z=0$ are caused by image charge effects.

Table 1. SPARC gun measurement summary.

Mode separation (0- π)	3.06 MHz
Coupling β (also VSWR)	1.22
Q_0	12,500
Reflected power	1 %
Running temperature	42° C
Full cell coupling calib.	-65.4 dB

Despite the use of a standard power slot, the external coupling was found to be somewhat higher than in the past ($\beta=1.22$), or 1% reflected power. This small reflection has no significance for operations, but does indicate an interesting difference from past devices — the

cavity Q_0 was found to be 12,500, which is roughly 8% higher than in past guns, and (now) in agreement with simulations. This implies that significant power loss was occurring in the tuner joints.

The full-cell power monitor coupling loop was calibrated, but it was noted that this measurement was quite sensitive to temperature, as the differential expansion of steel (the coupler tube) and copper changes the position of the loop in the evanescent field region. Final calibration must be performed at the operating temperature.

SOLENOID PERFORMANCE

The solenoid B_z profile was scanned using Hall probes, for two different scenarios: 150 A in all for coils, and 150 A in only two downstream coils. The results are compared to the predictions of Radia (Fig. 6) 3D and Poisson (Fig. 7) 2D simulations. The overall profile is accurate in both cases, but the 2D model overestimates the field amplitude by ~4%. This discrepancy is in part due to the yoke geometry being octagonal, not cylindrical, as assumed in the 2D model.

The case of Fig. 6 corresponds to the setting required for running the gun at 132 MV/m. As the coils can be run at nearly twice this current, a considerable overhead is available in B_z . This overhead will allow maximum flexibility in the differential excitation in the four coils.

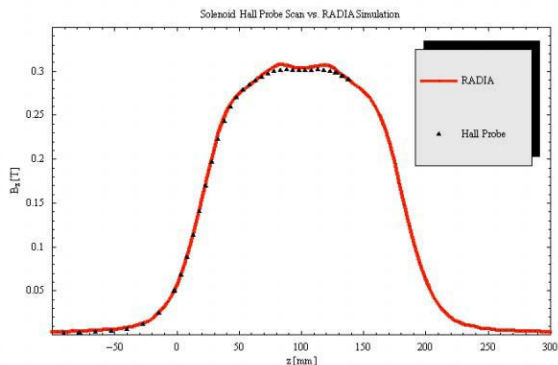


Figure 6. SPARC solenoid Hall probe scan (150 A on all coils); predictions of Radia 3D model.

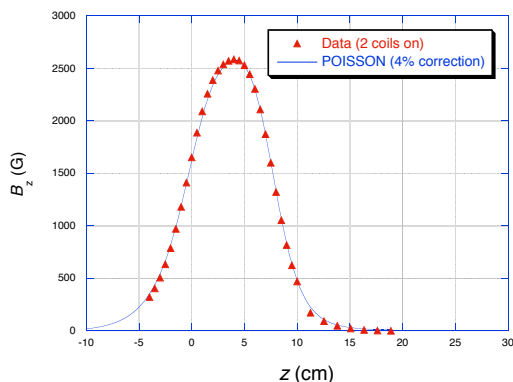


Figure 7. SPARC solenoid Hall probe scan with only two downstream coils excited at 150 A; predictions of POISSON model (4% correction).

Perhaps the most important measurement to check in the scan of Fig. 6, however, is the residual field at the cathode position. For the measured conditions, this residual field is 7 G. This corresponds, for a 1 mm radius (design) beam spot, to a contribution of 0.03 mm-mrad to the normalized emittance, an ignorable value.

The magnetic center of the solenoid was determined using a pulsed-wire apparatus. It was observed that the magnetic center was aligned to the mechanical center of the solenoid, to better than two wire widths (100 microns), when the adjustment screws were positioned all the way out (coils resting directly in the yoke support).

OUTLOOK

The SPARC photoinjector gun is due to be installed and aligned at the SPARC facility the LNF in June of 2005, with first high power RF conditioning in October 2005. At that point, dedicated measurements of the RF and magnetic performance of the system will begin, commencing with the measurement of emittance evolution at low energy (5.5 MeV) as a function of laser, RF gun, and magnet parameters. The emittance will be characterized also as a function of distance from the gun. During this phase of experiments, it is also expected that different cathodes may be studied.

After this initial period of testing, the full acceleration system will be installed. This will allow the beam energy to be increased to above 150 MeV, and allow the full range of beam dynamics experiments (e.g. velocity bunching, RF deflector-based diagnostics), and FEL studies to begin.

REFERENCES

- [1] D. Alesini *et al.*, *NIM A* **528** (2004) 586.
M. Ferrario *et al.*, Proc. EPAC-2004, pag. 399, ISBN: 92-9083-231-2A
Renieri *et al.*, *Status report on the SPARC Project*, Proc. of FEL-2004.
- [2] *Technical Design Report for the SPARC Advanced Photoinjector*, Eds. L. Palumbo and J. Rosenzweig, www.lnf.infn.it .
- [3] D. Alesini *et al.*, *The Project PLASMONX for Plasma Acceleration Experiments and a Thomson X-ray Source at SPARC*, these proceedings.
- [3] M. Ferrario *et al.*, *Homodyn Studies for the LCLS RF Photoinjector*, in *The Physics of High Brightness Beams*, J.Rosenzweig and L.Serafini ed., World Sci. ISBN 981-02-4422-3, June 2000
- [5] D.T. Palmer, *et al.*, *The ORION Photo-injector*, these proceedings.
- [6] V. Yakimenko, private communication.

A PRELIMINARY INTERACTION REGION DESIGN FOR A SUPER B-FACTORY*

M. Sullivan[†], M. Donald, S. Ecklund, A. Novokhatski, J. Seeman, U. Wienands
(SLAC, Menlo Park, California)

M. Biagini (INFN/LNF, Frascati (Roma))

Abstract

The success of the two B-Factories (PEP-II and KEKB) has encouraged us to look at design parameters for a B-Factory with a 30-50 times increase in the luminosity of the present machines to a luminosity of $L \sim 1 \times 10^{36} \text{ cm}^{-2} \text{ sec}^{-1}$. We present an initial design of an interaction region for a “SuperB” accelerator with a crossing angle of ± 14 mrad and include a discussion of the constraints, requirements and concerns that go into designing an interaction region for these very high luminosity e^+e^- machines.

INTRODUCTION

The PEP-II B-Factory has achieved a luminosity of $9 \times 10^{33} \text{ cm}^{-2} \text{ sec}^{-1}$ and KEKB the B-Factory at KEK has reached a luminosity of $1.5 \times 10^{34} \text{ cm}^{-2} \text{ sec}^{-1}$. Both B-Factories are performing well over design specifications in both peak and in integrated luminosity. This has sparked an interest into looking at a design for a higher luminosity machine of the order 1×10^{36} . In order to achieve this high luminosity in a PEP-II design, the β_y^* values are reduced from 11 mm to 1.5 mm, the number of bunches is increased from 1725 to 6900 and the bunch currents are increased. Total beam currents are 10 A for the high-energy beam (HEB) and 23 A for the low-energy beam (LEB). Table 1 summarizes the machine parameters for the present PEP-II and for a SuperB PEP-II [1,2].

Table 1. The present PEP-II and a SuperB PEP-II .

Parameter	PEP-II	SuperB
e^+ energy (GeV)	3.1	8
e^- energy (GeV)	9	3.5
β_x^* (e^+/e^-) (cm)	50/28	15/15
β_y^* (e^+/e^-) (mm)	11/11	1.5/1.5
ϵ_x (e^+/e^-) (nm-rad)	30/50	40/40
ϵ_y (e^+/e^-) (nm-rad)	1.25/2.10	0.43/0.43
Bunch length (mm)	11	1.7
Crossing angle (mrad)	0	± 14
Number of bunches	1588	6900
Beam current (e^+/e^-) A	2.45/1.55	10.1/23.0
Particles/bunch ($\times 10^{10}$)	7.1/4.5	6.7/15.3
Bunch current (e^+/e^-)(mA)	1.54/0.98	1.46/3.33
Lum. ($\times 10^{34} \text{ cm}^{-2} \text{ sec}^{-1}$)	0.92	100

*Work supported by the Department of Energy under contract number DE-AC03-76SF00515.

[†]sullivan@slac.Stanford.edu

INTERACTION REGION DESIGN

The PEP-II SuperB interaction region design has a ± 14 mrad horizontal crossing angle. The crossing angle collision separates the beams enough of 0.155 m, the 1st parasitic crossing for 6900 bunches, to keep the beam-beam effects minimized at this first near miss location. The first magnet from the IP is a shared vertically focusing quadrupole (QD1) located at 0.35 m – 0.85 m from the IP. This horizontally defocusing magnet further separates the two beams horizontally and allows for the placement of the first septum magnet (QF2) to be located at 2.5 m from the IP. The fact that the QD1 magnets are shared and that the two beams have different trajectories through these magnets means that the beams will be bent in these magnets and the bending will generate synchrotron radiation power. At the high beam currents of 10 A and 23 A any amount of bending can generate significant levels of SR power. Bending the beams before the collision can generate backgrounds by sweeping off-energy particles onto the detector beam pipe and bending in the beams after the collision can generate backgrounds proportional to the luminosity by sweeping the off-energy beam particles from radiative bhabhas onto the nearby beam pipe.

In order to try to strike a balance between backgrounds from beam gas events and backgrounds from luminosity terms, the locations of the QD1 magnetic axes with respect to the two beam orbits are considered free parameters. The present design has the QD1 axis for the incoming LEB very nearly centered on the beam orbit while the QD1 on the incoming HEB side is shifted toward the outgoing LEB orbit. This shift decreases the amount of bending the outgoing LEB experiences thereby decreasing the luminosity background term for the LEB at the expense for generating a little more SR power from the HEB by bending the upstream HEB a small amount. For the incoming LEB, shifting the QD1 axis toward the outgoing HEB generates a SR fan that either strikes or comes too close to a detector beam pipe. Figure 1 shows a layout of this initial interaction region design. The QF2 magnets complete the final focusing of the LEB and the two sets of magnets QD4 and QF5 are the primary magnets for the final focusing of the HEB. The axes of these magnets were located on the beam trajectories in this initial design. At this stage, bending radiation from magnets further outboard of the IP is ignored. We believe that soft bends can be placed before any outboard bending magnets so as to minimize the incoming SR.

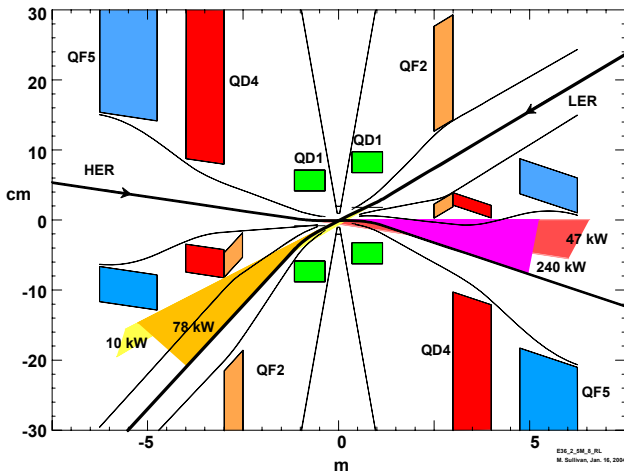


Figure 1. Plan view of the initial Super B-factory IR design. Note the exaggerated vertical scale. The collision angle is ± 14 mrad. Some additional bending is introduced into the upstream HEB in order to minimize the total beam bending of both beams. The two small horizontal lines inside the QD1 magnets indicate the centerline of each magnet. The detector acceptance of ± 300 mrad is shown in the middle of the picture.

SYNCHROTRON RADIATION

The next step in checking the feasibility of the design is to look at synchrotron radiation from the local final focusing quads. In this case, we have QD1 and QF2 for the LEB and QD1, QD4 and QF5 for the HEB. An initial design for the detector beam pipe is a round pipe with a 25 mm inside radius that is ± 15 cm long and with masking located at ± 15 cm from the IP. The masks are disks that have a smaller radius than the detector beam pipe radius. The assembly is oriented along the HEB collision axis.

The first look at the SR background indicated that there are too many photons directly striking the detector beam pipe from both incoming beams. The physics window of the beam pipe is considered to be ± 10 cm from the IP. Closer inspection reveals that the source of the photons striking the beam pipe is from the focusing in the x plane near the outboard end of QF2 for the LEB and focusing in the x plane near the inboard end of QF5 for the HEB. The beam particles that produce the background are between 7 and 10 beam sigmas in x. Table 2 is a summary of the SR backgrounds for various cases and it includes a comparison with the design values for the PEP-II B-factory. The estimated integrated radiation dose from SR for a silicon detector in the PEP-II design was 11 krad/yr. If we scale this dose rate up to the values of the initial baseline for the SuperB we get a dose rate of 650 Mrad/yr from the HEB alone.

In order to ameliorate the SR backgrounds from the HEB, we offset the QD4 magnet from the incoming beam axis by 10 mm. The induced bend in the beam orbit redirects the radiation from 7-10 σ particles in the upstream QF5 magnet away from the detector beam pipe. In a similar manner, the QF2 magnetic axis is offset from

the LEB orbit by 12 mm and the resulting bend in the beam again redirects the SR from the 7-10 σ particles in the outboard part of QF2 away from the detector beam pipe. The background results are shown in table 2.

Table 2. Summary of SR background numbers for various improvements to the initial baseline design. The photon counts are photons that are greater than 4 keV.

Cases	$\gamma/xing$	γ/sec
PEP-II design values	10	2.4×10^9
Baseline HER	46500	4.4×10^{13}
Baseline LER	57100	5.4×10^{13}
Offset QD4 10 mm HER	141	1.3×10^{11}
Offset QF2 12 mm LER	244	2.3×10^{11}
Cut at 8σ instead of 10σ HER	140	1.3×10^{11}
Beam tail dist. #1 HER	5.8	5.5×10^9
Beam tail dist. #1 LER	9.6	9×10^9
Beam tail dist. #2 HER	0.10	9.4×10^7
Beam tail dist. #2 LER	0.15	1.4×10^8
No beam tail dist. HER	7×10^{-14}	6.5×10^{-5}
No beam tail dist. LER	1×10^{-11}	0.012

Figure 2 shows a plan view of the present SuperB IR design with the offset QD4 and QF2 magnets. The picture also shows the initial beam pipe design. The offset upstream magnets, while generating more total synchrotron radiation, greatly reduce the detector backgrounds from SR. The background values achieved by this method are probably acceptable; they are only about 10-20 times higher than the PEP-II design value. A test was made to verify that the background is dominated by the 7-10s particle distribution by cutting the particle density scan at 8σ instead of 10σ . The result is shown in Table 2 where the backgrounds from the HEB drop to the level of the offset QD4 case. Table 3 summarizes the SR power for the interaction region magnets.

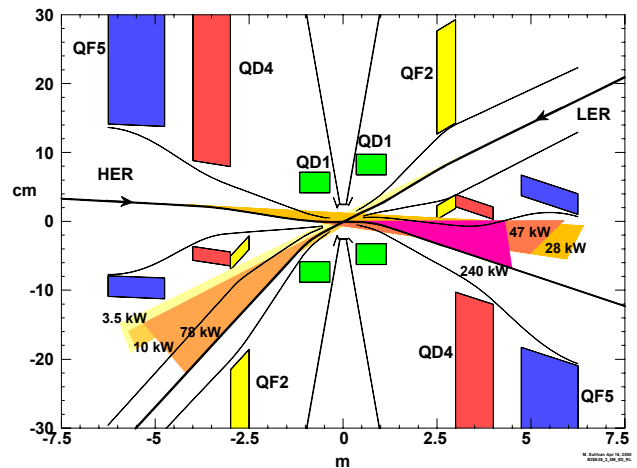


Figure 2. Plan view of the present IR design for a SuperB factory. Note the two extra SR fans generated by the offset QD4 and offset QF2 magnets. The beam pipe design shows a mask present on the incoming HEB side and little or no mask on the incoming LEB side.

Table 3. A summary of the synchrotron radiation power produced from the interaction region magnets. The first column is from the on-axis baseline design and the second column is for the present design with the offset QF2 and QD4 on the incoming beam orbits.

Magnet	Baseline (kW)	Present (kW)
Upstream LER QF2	0.24	3.48
Upstream LER QD1	10.21	10.21
Downstream LER QD1	78	78
Downstream LER QF2	0.24	0.24
Upstream HER QF5	1.67	1.67
Upstream HER QD4	1.00	27.75
Upstream HER QD1	47.42	47.42
Downstream HER QD1	240	240
Downstream HER QD4	1.00	1.00
Downstream HER QF5	1.67	1.67
Totals	381	411

BEAM TAILS

The head-on collision of the PEP-II design together with the beam bending in the shared QD1 magnets and in the offset QD4 magnets generate beam orbits in the PEP-II interaction region that produce SR backgrounds that are dominated by bending radiation and are relatively insensitive to beam-tail distributions. Consequently, we have adopted fairly conservative beam-tail distributions in the present PEP-II design.

In contrast, the SR backgrounds in the SuperB IR design are dominated by the particle density of the beam tails in the 7-10 σ area of the x plane. The PEP-II beam-tail distributions were used in the initial baseline background calculations for the SuperB IR. Figure 4 shows plots of various beam tail distributions and Table 2 shows the change in the detector backgrounds based on the different beam-tail distributions seen in the plot. The beam-tail background numbers include the gain in background from the offsets in the QD4 and QF2 magnets. As one can see from Table 2, a reduction in the particle density in the high σ region of the x plane rapidly lowers the detector backgrounds to levels equal to and even below the PEP-II design value. One can also see that the removal of all beam tails (the no tail entries in table 2) completely remove the SR background. It should be noted that the vertical beam tail distribution does not, at present, make any appreciable background even when we use the relatively high beam tail distribution of the PEP-II design. Hence, all background numbers include the PEP-II beam-tail distribution in the y plane except for the no tail entries.

SUMMARY

We have taken an initial look at an interaction region design for a B-factory with a luminosity of $1 \times 10^{36} \text{ cm}^{-2} \text{ sec}^{-1}$. The design has a ± 14 mrad horizontal crossing angle which separates the two beams quickly enough to

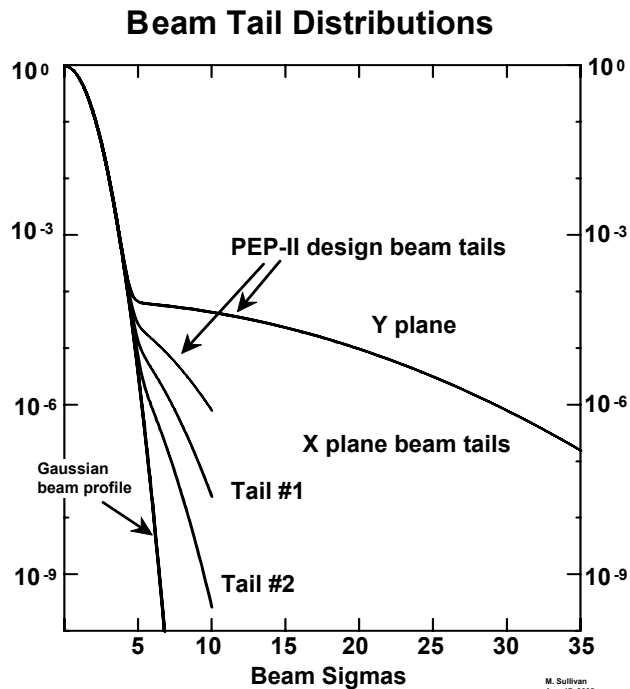


Figure 4. Plot of the various beam-tail distributions used to produce the background numbers in table 2.

permit a bunch spacing of 0.32 m or 6900 bunches in a 2200 m PEP storage ring. Because of the high-current beams there is minimal beam bending in the design. Some beam bending is unavoidable due to the shared QD1 magnet. In addition, some bending of the upstream beam orbits is introduced in order to redirect synchrotron radiation generated by the focusing of the beam away from the detector beam pipe. This reduces detector backgrounds to within an order of magnitude of the PEP-II backgrounds. Further reductions in backgrounds can be achieved by lowering the beam tail distribution in the x plane. Perhaps the present B-factories can shed some light on what the actual particle density is in the beam-tails.

The results from this initial study are encouraging. It looks like synchrotron radiation backgrounds can be controlled. More work needs to be done and further iterations of the design need to include HOM power generated by the SR masking, lost beam particle backgrounds and backgrounds from luminosity as well as magnet and vacuum chamber designs.

REFERENCES

- [1] J. Seeman, *et.al.*, "Design Studies for a 10^{36} Super-B-factory", EPAC 2004 proceedings.
- [2] J. Seeman, *et.al.*, "Parameters of a Super-B-Factory Design", these proceedings.

PARAMETERS OF A SUPER-B-FACTORY DESIGN*

J. Seeman[†], Y. Cai, S. Ecklund, J. Fox, S. Heifets, N. Li, P. McIntosh,
A. Novokhatski, M. Sullivan, D. Teytelman, U. Wienands
SLAC, Menlo Park, CA 94025, USA
M. Biagini, INFN, Frascati, Italy

Abstract

Parameters are being studied for a high luminosity e^+e^- collider operating at the Upsilon 4S that would deliver a luminosity in the range of 7 to 10 $\times 10^{35}/\text{cm}^2/\text{s}$. Particle physics studies dictate that a much higher luminosity collider than the present B-Factory accelerators will be needed to answer future new key physics questions. The success of the present B-Factories, PEP-II and KEKB, in producing unprecedented luminosity with very short commissioning times has taught us about the accelerator physics of asymmetric e^+e^- colliders in a new parameter regime. Such a collider could produce an integrated luminosity of 10,000 fb^{-1} (10 ab^{-1}) in a running year. A Super-B-Factory [1-8] with 30 to 50 times the performance of the present PEP-II accelerator would incorporate a higher frequency RF system, lower impedance vacuum chambers, higher power synchrotron radiation absorbers, and stronger bunch-by-bunch feedback systems. The present injector based on the SLAC linac needs no improvements and is ready for the Super-B-Factory.

PARAMETERS

The design of a 7 to 10 $\times 10^{35} \text{ cm}^{-2}\text{s}^{-1} e^+e^-$ collider combines an extension of the design of the present B Factories with a few new ideas and special circumstances to allow improved beam parameters to be achieved. The luminosity L in an e^+e^- collider that has a limited vertical tune shift ξ_y with flat beams is given by the standard expression

$$L = 2.17 \times 10^{34} (1+r) n \xi_y \left(\frac{EI_b}{\beta_y^*} \right) \text{ cm}^{-2}\text{sec}^{-1} \quad (1)$$

where I_b is the bunch current (amperes), n is the number of bunches, E is the beam energy (GeV), r is the vertical to horizontal emittance ratio (~ 0.01) and β_y^* is the vertical beta function (cm) at the collision point. The luminosity gain of the Super B Factory comes from the increase of the beam currents by about a factor of five, lowering β_y^* about a factor of four, and increasing the beam-beam tune shifts about 80%. The resulting gain is about a factor of 30 to 50 over that of the present B Factories. In addition, due to continuous injection with the luminosity always near the maximum as shown

successfully in the present B-Factories, the overall integrated luminosity per unit time of the Super B Factory is expected to be 10 ab^{-1} per year with a peak luminosity of $7 \times 10^{35} \text{ cm}^{-2}\text{s}^{-1}$. The parameters of a representative e^+e^- colliders at SLAC at $7 \times 10^{35} \text{ cm}^{-2}\text{s}^{-1}$ are listed in Table 1. The PEP-II tunnel at SLAC is an excellent site for this collider.

The beam energies are 8 GeV for the high-energy ring (HER) and 3.5 GeV for the low-energy ring (LER). Lowering the high-energy ring energy from the present 9 GeV reduces the overall synchrotron radiation load on the RF system and raises the instability thresholds for the low energy beam. The e^+ and e^- may be exchanged if need be as either particle can be stored in either ring using the versatile SLAC injector. The linac can provide low emittance beams with 80 Hz of e^- and 20 Hz of e^+ .

Table 1: Parameters for a Super B Factory at 952 MHz

Parameter	LER	HER
Energy (GeV)	3.5	8
RF frequency (MHz)	952	952
Vertical tune	72.64	56.57
Horizontal tune	74.51	58.51
Current (A)	15.5	6.8
Number of bunches	6900	6900
Ion gap (%)	1.2	1.2
RF klystron/cavity	24/24	18/18
RF volts (MV)	30	23
β_y^* (mm)	1.7	1.7
β_x^* (cm)	14	14
Emittance (x/y) (nm)	24/0.28	24/0.28
σ_z (mm)	1.8	1.8
Hourglass-X-angle factor	0.81	0.81
Crossing angle(mrad)	14	14
IP Horiz. size (μm)	58	58
IP Vert. size (μm)	0.7	0.7
Horizontal ξ_x	0.12	0.12
Vertical ξ_y	0.12	0.12
Lumin. ($\times 10^{34}/\text{cm}^2/\text{s}$)	70	70

*Supported by US DOE contract DE-AC03-76SF00515.

[†]seeman@slac.stanford.edu

RF FREQUENCY SELECTION

An RF frequency of 952 MHz is the leading design choice for the Super B-Factory. At the higher frequency, more bunches (about 6900) can be stored, thereby reducing single bunch effects and higher order mode losses at the high total current. SLAC in association with industry has the ability to design and manufacture CW 952 MHz klystrons producing 1 MW. RF cavities at 952 MHz can be made with a similar design to either the Cornell CESR or KEKB style superconducting RF cavities. The bore of the cavities will be enlarged to reduce the R/Q for beam stability reasons. (See Figures 1, 5 and 6.)

In the Super B Factory, the single bunch currents are only about a factor of two higher than those of PEP-II although the total current is increased by a factor of five. Furthermore, the bunch lengths are about four times shorter. These short, high-charge bunches lead to increased single bunch effects. Higher-Order-Mode (HOM) losses and resistive wall losses have to be minimized in each ring. HOM losses in the RF cavities will be reduced by opening the beam channel through the RF cavities by about 50%. [6] The resistive wall losses of the short bunches in the vacuum chambers will be reduced by a factor of two by increasing the vacuum chamber dimensions.

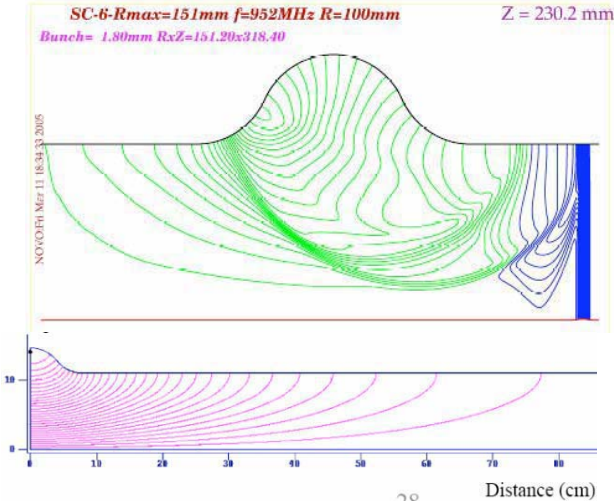


Figure 1: HOM calculation for a 952 MHz SC RF cavity with a 100 mm bore and RF fields along the beam line.

INTERACTION REGION

The interaction region is being designed to leave the same longitudinal free space as that presently used by BABAR but with superconducting quadrupole doublets as close to the interaction region as possible, as shown in Figures 3 and 4. A crossing angle is used to separate the two beams as they enter and leave the interaction point. The overall interaction region is shorter than for PEP-II, allowing a shorter detector [7].

Recent work at Brookhaven National Laboratory on precision conductor placement of superconductors in

large-bore low-field magnets has led to quadrupoles in successful use in the interaction regions for the HERA collider. New magnets of this style for the BEPC-II collider are under construction [8]. A minor redesign of these magnets will work well for a Super B Factory.

The beams must have a crossing angle about ± 14 mrad at the collision point to avoid parasitic crossing effects. The short Super B Factory bunches are made by providing extra over-voltage in the RF system and by a high phase-advance and low momentum compaction magnetic lattices as shown in Figure 2.

The increases in the beam-beam parameters from the present 0.08 range to 0.12 will be achieved by operating just above but very close to the half-integer horizontal tune where predictable, but strong, dynamic beta effects occur. Also, pushing the transverse tunes closer to specific resonances allows a higher tune shift and more luminosity but with shorter beam lifetimes. Both techniques have been successfully demonstrated at the present B Factories.

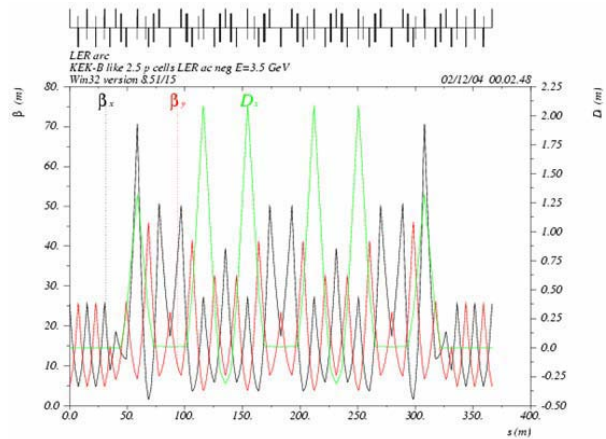


Figure 2: LER lattice with 2.5π phase advance/cell.

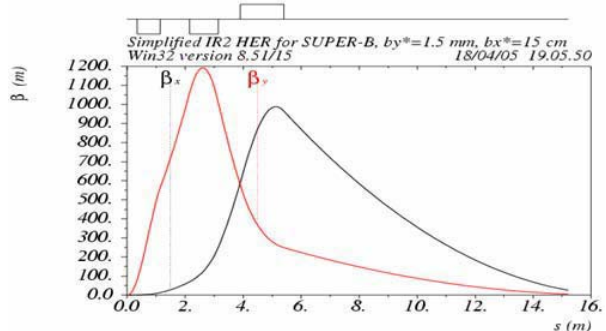


Figure 3: Beta functions in the HER interaction region.

POWER SCALING

The power required by a collider is the sum of a site base plus RF sources and magnets. A summary is shown in Table 2. With a Super B-Factory, there will be an overall base level due to the SLAC campus (~ 15 MW), the linac running for PEP-II at 30 Hz (~ 10 MW), the linac running for LCLS (~ 10 MW), and SPEAR (~ 5 MW) for a total of about 40 MW. The total Super-B-Factory RF power is

the sum of the cavity wall losses, beam synchrotron radiation, beam resistive wall losses, beam higher order mode losses (HOM), cryogenic losses and AC distribution inefficiencies. The AC transformers and high voltage power supplies are about 90% efficient. The RF klystrons are about 65% efficient. The synchrotron radiation losses are minimized by reducing the energy asymmetry of the B-Factor to 3.5 x 8 GeV and by adding dipoles to the low-energy ring to reduce the effective bending radius. The vacuum chamber bores are

enlarged to reduce the resistive wall losses that go inversely with the chamber size. The HOM losses are reduced by going to a higher RF frequency with more bunches but the same total current. The total power needed is about 128 MW. The SLAC power substation and transmission lines can easily provide up to 140 MW.

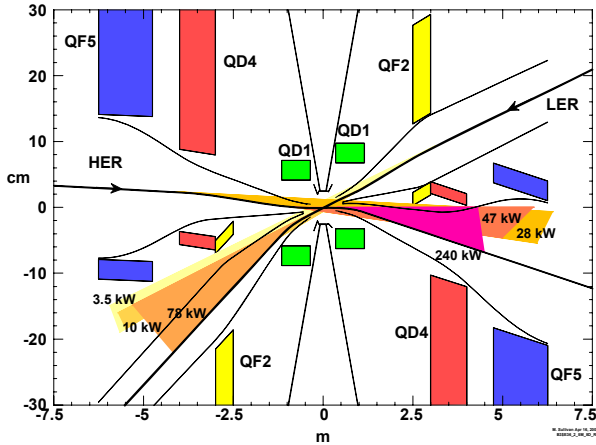


Figure 4: Interaction region for a Super B-Factor. The first quadrupole is at 35 cm from the interaction point.

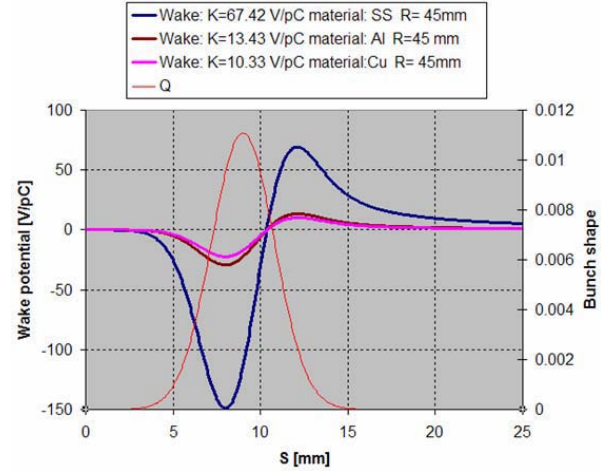


Figure 6: Resistive wall wakes for a 1.8 mm long bunch.

Table 2: AC Power needed for a SLAC Super B-Factor

Power use	LER (MW)	HER (MW)	Sum (MW)
AC HOM Losses	13	3	16
AC synch. rad. losses	30	30	60
AC magnet losses	5	5	10
AC cryogenics	1	1	2
AC other lab projects	--	--	40
Total SLAC site power	--	--	128

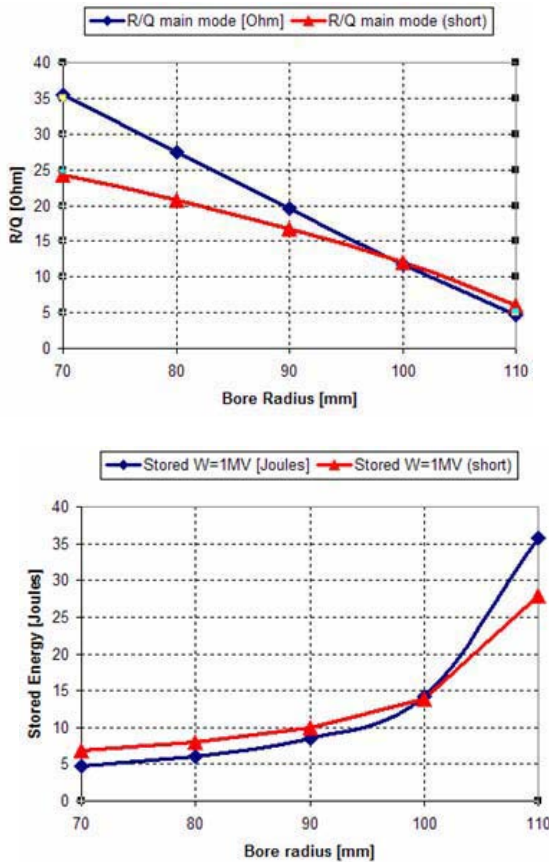


Figure 5: R/Q and stored field energy versus cavity bore.

REFERENCES

- [1] J. Seeman, "Initial Parameters for a $10^{36}/\text{cm}^2/\text{s}$ e^+e^- B-Factor," SLAC-PUB-8787, March 2001.
- [2] J. Seeman *et al.*, "Design Studies for a 10^{36} Super-B-Factories," EPAC 2004 proceedings.
- [3] "The Discovery Potential of a Super B-Factor," SLAC Report R-709 December 2004.
- [4] P. McIntosh, "PEP Super-B High Power RF," Super-B-Factor Workshop, Hawaii, April 2005.
- [5] D. Teytelman, "Longitudinal Stability for the Super-B-Factor," Super B-Factor Workshop, Hawaii, April 2005.
- [6] A. Novokhatski, "Low R/Q Cavities for Super B-Factor," Super B-Factor Workshop, Hawaii, April 2005.
- [7] M. Sullivan, "Preliminary Interaction Region Design for a Super B-Factor," PAC 2005 proceedings.
- [8] B. Parker, "Superconducting Magnets for HERA ep IR," PAC 1999, New York, p. 308.

PERFORMANCE OF THE PEP-II B-FACTORY COLLIDER AT SLAC *

J. Seeman†, M. Browne, Y. Cai, W. Colocho, F.-J. Decker, M. Donald, S. Ecklund, R. Erickson, A. Fisher, J. Fox, S. Heifets, R. Iverson, A. Kulikov, N. Li, A. Novokhatski, M. Ross, P. Schuh, T. Smith, K. Sonnad, M. Stanek, M. Sullivan, P. Tenenbaum, D. Teytelman, J. Turner, M. Weaver, D. Van Winkle, U. Wienands, M. Woodley, Y. Yan, G. Yocky, SLAC, Menlo Park, CA 94025, W. Kozanecki, CEA/Saclay, France; G. Wormser, Orsay, France; M. Biagini, INFN, Frascati, Italy; C. Steier, A. Wolski, LBNL, Berkeley, CA 94720, USA

Abstract

PEP-II is an e^+e^- asymmetric B-Factory Collider located at SLAC operating at the Upsilon 4S resonance (3.1 GeV x 9 GeV). It has reached a luminosity of $9.21 \times 10^{33}/\text{cm}^2/\text{s}$ and has delivered an integrated luminosity of 710 pb^{-1} in one day. PEP-II has delivered, over the past six years, an integrated luminosity to the BaBar detector of over 262 fb^{-1} . PEP-II operates in continuous injection mode for both beams boosting the integrated luminosity. The peak positron current has reached 2.45 A in 1588 bunches. Steady progress is being made in reaching higher luminosity. The goal over the next several years is to reach a luminosity of $2.1 \times 10^{34}/\text{cm}^2/\text{s}$. The accelerator physics issues being addressed in PEP-II to reach this goal include the electron cloud instability, beam-beam effects, parasitic beam-beam effects, high RF beam loading, shorter bunches, lower β_y^* interaction region operation, and coupling control. Figure 1 shows the PEP-II tunnel.

PARAMETERS

The present parameters of PEP-II are shown in Table 1 compared to the design. The present peak luminosity is over three times the design and the best integrated luminosity per month is 17.04 fb^{-1} , over five times the design. The highest luminosity in each month is shown in Figure 2, the integrated luminosity each month in Figure 3 and the integrated luminosity in Run 5 in Figure 4.



Figure 1. View of the PEP-II tunnel.

*Supported by US DOE contracts DE-AC02-76SF00515 and DE-AC03-76SF00098.

†seeman@slac.stanford.edu

Table 1: PEP-II May 2005 Parameters.

Parameter	PEP-II Design	PEP-II Present
HER Vertical tune	23.64	23.622
HER Horizontal tune	24.62	24.520
LER Vertical tune	36.64	36.564
LER Horizontal tune	38.57	38.512
HER current (mA)	750	1550
LER current (mA)	2140	2450
Number of bunches	1658	1588
Ion gap (%)	5	1.8
HER RF klystron/cav	5/20	9/26
HER RF volts (MV)	14.0	15.5
LER RF klystron/cav.	2/4	4/8
LER RF volts (MV)	3.4	4.04
β_y^* (mm)	15-25	11
β_x^* (cm)	50	35-49
Emittance (x/y) (nm)	49/2	31-59/1.4
σ_z (mm)	11	11-12
Lum hourglass factor	0.9	0.84
Crossing angle(mrad)	0	<0.1
IP Horiz. size Σ (μm)	222	170
IP Vert. Size Σ (μm)	6.7	7.3
HER Horizontal ξ_x	0.03	0.055
HER Vertical ξ_y	0.03	0.046
LER Horizontal ξ_x	0.03	0.053
LER Vertical ξ_y	0.03	0.064
Lumin. ($\times 10^{33}/\text{cm}^2/\text{s}$)	3.00	9.21
Int. Lum/month (fb^{-1})	3.3	17.04
Total Int. Lum. (fb^{-1})	30/year	> 262 total

The progress in integrated luminosity has come from correcting the orbits, lowering β_y^* , moving the fractional horizontal tunes in both rings to just above the half integer (<0.52), and trickle injection of both beams.

RUN 5 STATUS

PEP-II [1-7] has been providing colliding beams for the BaBar detector since May 1999. The present Run 5 started in April 2005 and will end in July 2006. There will be a one month down in October 2005 for safety checks. During the recent run, colliding beams occupied 75% of the time, 20% for repairs, and 5% for machine development and accelerator physics studies. About 87% of the data logged by BaBar was on the Upsilon 4S resonance and 13% off-resonance about 40 MeV lower. The highest luminosity in PEP-II is $9.21 \times 10^{33}/\text{cm}^2/\text{s}$ with the corresponding parameters listed in Table 1. The horizontal beam size of the LER is enlarged at this peak luminosity by about 30%. Also, the vertical beam size of the HER is enlarged by about 20% at the peak luminosity. Both increases are due to the beam-beam effect. 710 pb^{-1} has been delivered in 24 hours. The present delivered luminosity to BaBar is over 262 fb^{-1} .

The accelerator down from August 2004 to March 2005 dealt with three months of installation work followed by several months of safety training and procedure updates.

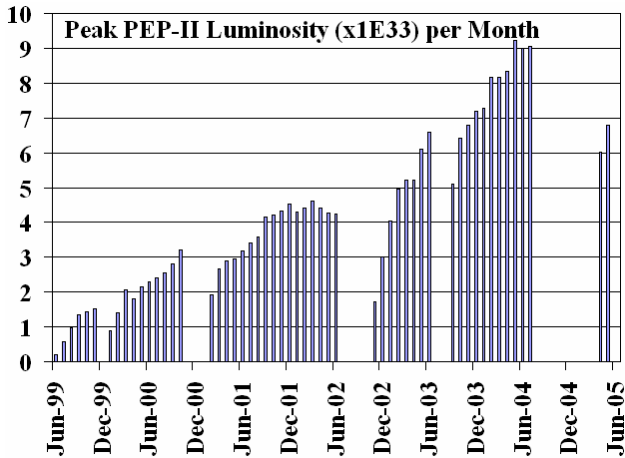


Figure 2. Peak luminosity each month since May 1999. The highest luminosity has reached $9.21 \times 10^{33}/\text{cm}^2/\text{s}$.

BEAM-BEAM INTERACTION

At low currents, the luminosity increases as the product of the electron and positron bunch charges. At higher currents the LER-x and HER-y beam sizes enlarge due to beam-beam and somewhat by interaction region parasitic collisions. The HER and LER bunch charges are appropriately balanced to produce near equal beam-beam effects. If there is a miss-balance, flip-flop effects can occur. The horizontal tunes of both rings were recently

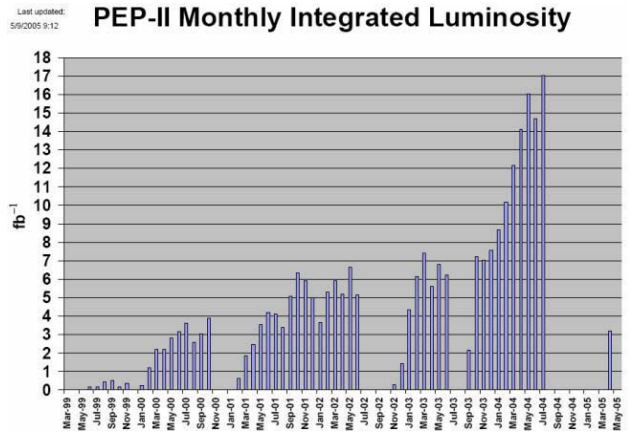


Figure 3. Integrated luminosity per month. In July 2004 PEP-II delivered over 17 fb^{-1} .

moved closer to the half integer (~ 0.51 to 0.52) and an increase of about 10% in luminosity occurred. In order to move the HER to the half integer, the horizontal beta beats in the HER had to be fixed. Moving close to the half integer tune makes any beta beats larger. Computer codes (MIA, ORM, Phase-Advance) have been used to improve the coupling and betas in the rings. The beta beats in both rings are below 50%.

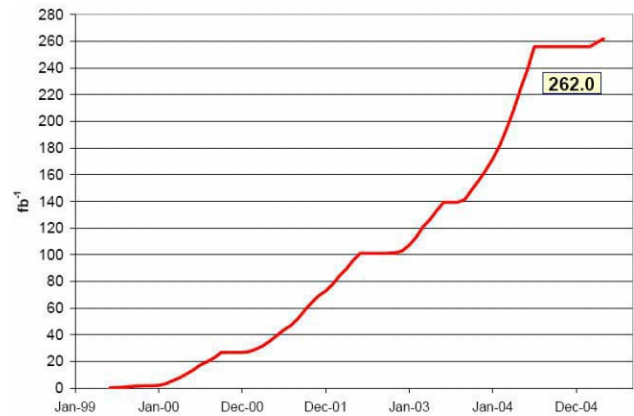


Figure 4. Delivered integrated luminosity to BaBar by PEP-II. A grand total of over 262 fb^{-1} has been delivered from May 1999 to May 2005.

Since October 2003, PEP-II has operated with bunches in every two RF buckets but with mini-gaps of a few RF buckets after about 66 bunches. A plot of the bunch luminosity over the whole train is shown in Figure 6. Over the train, there are no signs of Electron Cloud Instability ECI in the positron beam. The parasitic crossing beam-beam effects are largest in the vertical plane where the vertical betas are much larger than the horizontal betas at the parasitic collisions displaced 63 cm from the IP on both sides ($\Delta x = 3.2 \text{ mm}$). As the β_y^* is lowered the parasitic effects will become stronger but so far at most a few percent ($\sim 5\%$) luminosity loss. Beam-

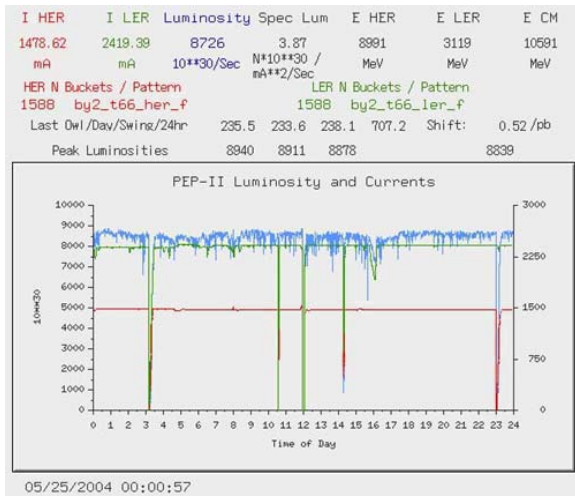


Figure 5. PEP-II’s best day showing trickle injection and a 710 pb⁻¹ integrated luminosity.

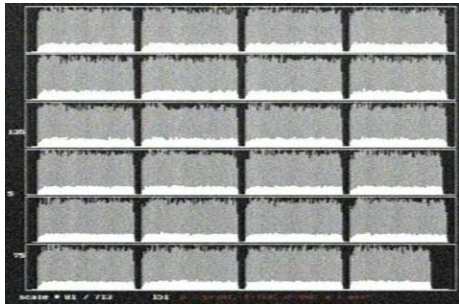


Figure 6. Bunch luminosity along the train with every 2nd RF bucket filled and a 1.8% ion gap at the end of the train. There are mini-gaps of about 3 RF buckets.

beam parameters from 0.046 to 0.065 are now routinely achieved in PEP-II that far exceed the design of 0.03.

CONTINUOUS (TRICKLE) INJECTION

Continuous injection was made to work in November 2003 when the PEP-II and BaBar teams reduced the backgrounds to an acceptable level to allow BaBar to take data continuously. The improved efficiency for data delivery was about 30% within a few days. Trickle injection for positrons uses about three injection pulses per second from the SLAC linac, resulting in the positron current being stable to about 0.1% with BaBar recording better than 98% of the data. The electron ring at PEP-II proved more difficult and studies continued until March 2004 before trickle injection was successful. About two linac pulses per second is needed to keep the electron current stable to 0.1%. Since March 2004, both PEP-II rings are trickle injected simultaneously with BaBar taking data. So PEP-II has true trickle injection with either beam injected pulse-by-pulse with very steady currents and steady luminosity, see Figure 5. The overall integrated luminosity efficiency jumped 10% with the HER ring and to just over 40% with both rings together.

FUTURE PLANS

PEP-II has an upgrade plan that is leading towards a luminosity of greater than 2.1×10^{34} in FY2007. Combining the equations for luminosity and the vertical beam-beam parameter, one derives the traditional luminosity scaling

$$L = 2.17 \times 10^{34} (1+r) \xi_y \left(\frac{EI}{\beta_y^*} \right) \text{ cm}^{-2} \text{ sec}^{-1} \quad (1)$$

equation with r the y to x aspect ratio (~ 0.04), E the beam energy, I the beam current, and β_y^* the vertical beta at the collision point. In order to get a factor of 2.3 above the present luminosity (to 2.1×10^{34}), the currents will be raised about a factor of 1.5 to 2, the tune shifts increased about 10% and β_y^* reduced from 11 mm to about 8.5 mm. The number of RF stations in the LER will be increased from four to five in order to achieve about 4.4 A. The number of RF stations in the HER will be increased from nine to ten allowing a current of 2.2 A. To shorten the bunch length to reduce the hourglass effects, a lower alpha lattice will be used in HER and a higher RF voltage.

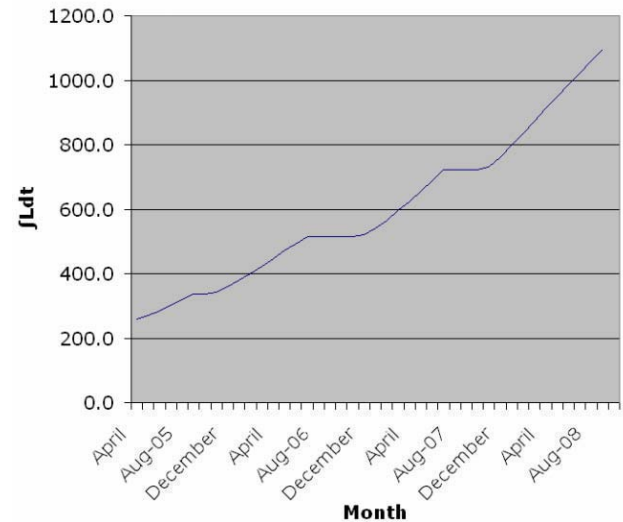


Figure 7. Projected integrated luminosity (fb⁻¹) for PEP-II into FY2008.

REFERENCES

- [1] J. Turner *et al.*, “Continuous Trickle Injection into PEP-II,” EPAC 2004 proceedings.
- [2] W. Kozanecki *et al.*, “Beam-Beam Crossing Angle Measurements at PEP-II,” PAC 2005 proceedings.
- [3] U. Wienands *et al.*, “Lepton Collider Operation with Constant Currents,” PAC 2005 proceedings.
- [4] A. Novokhatski, “HOM Calculations for Electron Storage Rings,” PAC 2005 proceedings.
- [5] Y. Cai *et al.*, “Simulations and Experiment of Beam-Beam Effects in e+e- Storage Rings,” PAC 2005 proceedings.
- [6] M. Sullivan *et al.*, “PEP-II IR Upgrades,” EPAC 2004 proceedings.
- [7] A. Fisher *et al.*, “New PEP-II LER Synchrotron Light Monitor,” PAC 2005 proceedings.

X-BAND DIPOLE MODE DEFLECTING CAVITY FOR THE UCLA NEPTUNE BEAMLINE*

R. J. England, B. O’Shea, J. B. Rosenzweig, G. Travish, UCLA, Los Angeles, CA 90095, USA
D. Alesini, INFN/LNF, Frascati, Italy

Abstract

We report progress on the design and construction of a nine-cell cavity operating in a TM_{110} -like dipole mode for use as a temporal diagnostic of the 14 MeV, 300 pC electron bunches generated at the UCLA Neptune Laboratory linear accelerator, with an anticipated temporal resolution of 50 fs at a peak input power of 50 kW. The cavity is a center-fed standing-wave pi-mode structure, operating at 9.6 GHz, and incorporating a knife-edge and gasket assembly which minimizes the need for brazing or welding. Results of initial RF testing of the prototype cavity are discussed and compared with simulation results obtained using the commercial code HFSS.

INTRODUCTION

In a traditional linear RF-based accelerator, the electromagnetic mode utilized to accelerate the beam is designed to give rise to a longitudinal electric field with zero transverse deflection for a beam traveling on the axis. Although some transverse fields may be present on-axis near the coupling irises connecting the cells, in the case of a multi-cell structure or disk-loaded waveguide, the fields generated in the central regions of the cells typically resemble the TM_{0n0} modes of a pillbox structure. Modes which resemble the TM_{1n0} dipole modes are avoided for purposes of longitudinal acceleration since they produce a strong transverse deflection of the beam. Deflecting mode structures have long been used, however, for particle separation in beams of more than one species [1, 2] and as a longitudinal bunch length diagnostic [3]. Some recent efforts have focused on longitudinal phase space reconstruction [4, 5] and creation of temporal correlations for x-ray compression [6].

Recent bunch-shaping experiments at the UCLA Neptune Laboratory [7] require the implementation of a beam diagnostic capable of resolving the temporal structure of the sub-picosecond to several picosecond duration electron bunches generated by the Neptune linear accelerator beamline and dogleg compressor with resolutions at the 50 fs level. For this purpose, we have designed a 9-cell standing-wave deflecting mode cavity operating at an X-Band frequency of 9.59616 GHz. A diagram of the proposed diagnostics section with the deflecting cavity in place is shown in Fig. 1.

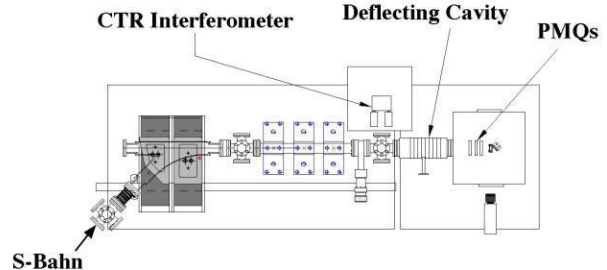


Figure 1: Layout of proposed diagnostics section with table of experimental parameter goals.

CAVITY DESIGN

The proposed diagnostic for measuring the longitudinal current profile of the compressed bunches produced by the Neptune linear accelerator and dogleg compressor is a linearly polarized TM_{110} dipole mode cavity, being developed in collaboration with the INFN Laboratori Nazionali di Frascati. By correctly designing the input power coupler, the polarity of the transverse magnetic field in this mode may be selected to correspond with either the x or y axis of the beamline. When a beam is injected into such a cavity at the zero-crossing of the RF, it experiences a transverse momentum kick along the orthogonal transverse axis whose strength is approximately linear in the arrival time of the particles. As a result, the longitudinal distribution of the beam is deflected transversely and can be imaged on a simple profile monitor located downstream [3]. This process is illustrated in Fig 2. The final transverse RMS beam size along the deflecting axis after a drift L following the cavity is given by $\sigma_x = \sqrt{\sigma_0^2 + \sigma_{def}^2}$ where σ_0 is the beam size with the deflector off and [4]

$$\sigma_{def} = 2\sigma_z L \frac{\pi f V_0}{cU/e}, \quad (1)$$

where σ_z is the RMS bunch length, f is the RF frequency, V_0 is the deflecting voltage, and U is the beam energy. The achievable temporal resolution can then be written as

$$\Delta t = \Delta x \frac{U/e}{L\pi f V_0}, \quad (2)$$

where Δx is the achievable spatial resolution of the profile monitor and the camera and optics used to view it. The transverse voltage is related to the input RF power P by $V_0 = \sqrt{nR_T P}$ where n is the number of cells and R_T is the transverse shunt impedance per cell. Based upon various spatial and hardware concerns, we have chosen a 9-cell

* Work supported by U.S. Department of Energy under Grant No. DE-FG03-92ER40693

standing-wave π -mode structure operating at a frequency of 9.59616 GHz. This gives an estimated shunt impedance of 680 k Ω per cell and a deflecting voltage of $V_0 = 550$ kV at an input power of $P = 50$ kW. At this voltage, the temporal resolution given by Eq. (2) is on the order of 50 fs. The 9-cell structure was designed using the RF modeling codes MAFIA and HFSS 9.0. An image of the cavity geometry from these simulations and a plot of the (magnetic) field profile are shown in Fig. 3, followed by a list of parameter values in Table 1.

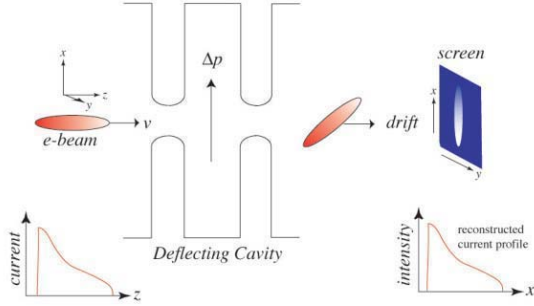


Figure 2: Illustration of the deflection of a beam by a dipole mode cavity phased at the zero-crossing of the RF.

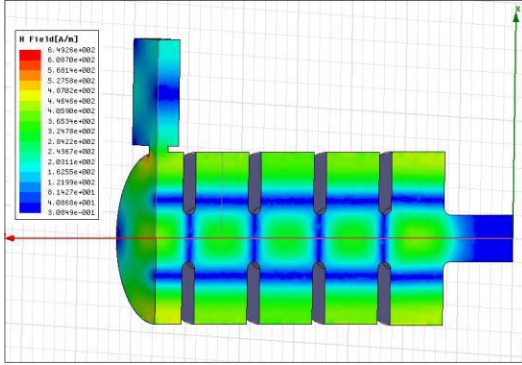


Figure 3: Plot of deflecting mode cavity geometry (quarter view) and axial transverse magnetic field profile from the center cell to the exit of the structure from HFSS simulations (quarter view).

Due to the presence of the irises which couple the cells, there is a nonzero transverse electric field in the vicinity of each iris. However, for a π -mode structure, the electric field produces a net deflection in the same direction as the magnetic field and thereby enhances the deflection of the beam.

STEEL PROTOTYPE RESULTS

The stainless steel cavity prototype design incorporates a knife-edge vacuum seal machined directly into the mating faces of the cells, which can accommodate a copper gasket or o-ring. This allows the cavity to be easily disassembled,

Table 1: Cavity Design Parameters

Parameter	Value	Units
Number of Cells	9	-
Pi-Mode Freq	9.59616	GHz
Transverse Shunt Impedance	6.1	M Ω
Deflecting Voltage	552	kV
Quality Factor	9080	-
Cell Radius	18.25	mm
Cell-to-Cell Distance	15.62	mm
Iris diameter	10	mm
Beam pipe diameter	10	mm
VSWR	1.0	-

and will also permit a vacuum test of the prototype without the need for brazing or welding, which can warp and detune the cells. A drawing of the assembled prototype cavity is shown in Fig. 4 with a quarter section removed to reveal the interior of the structure. The inner RF surfaces of the structure were electrolytically coated with a 1 micron thick layer of copper.

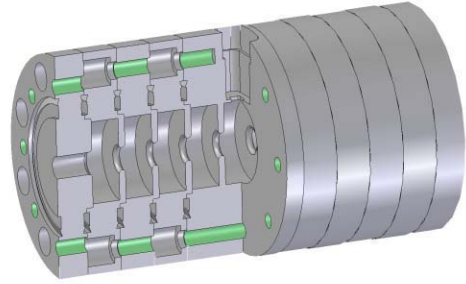


Figure 4: Cutaway drawing of the assembled 9-cell cavity design.

Note that the prototype dimensions are scaled to a slightly lower frequency than the final cavity design, due to the fact that the frequency had not yet been finalized at the time of its construction. This can be seen in the S_{11} frequency scan in Fig. 5. Only five resonances appear, indicating that the intermediate modes corresponding to odd multiples of $\pi/8$ are suppressed by the choice of a central coupler. The predicted HFSS frequency for the π -mode for this geometry (in air) is 9.4953 GHz. The π -mode frequency lies within 5 MHz of the simulation prediction. Final frequency tuning will be accomplished by heating the cavity with a PID-feedback temperature control system. The estimated frequency correction factor is $df/dT = -150$ kHz/C for steel and -142 kHz/C for copper.

It can be seen in Fig. 5 that there is good mode separation between the π -mode resonance and the nearest non-suppressed mode. In addition, the VSWR is very close to unity. The depth of the π -mode resonance is not fully apparent in Fig. 5 due to the limited resolution of the plot, but it actually extends to about -50 dB.

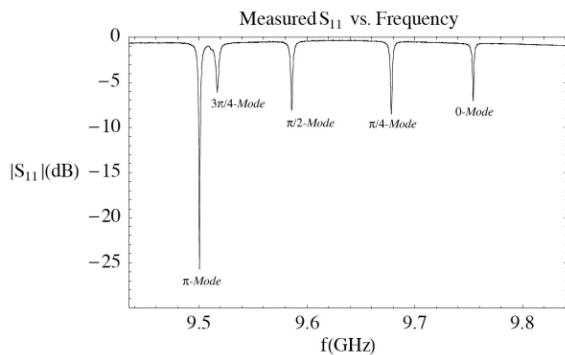


Figure 5: Plot of the RF reflectance at the input coupler of the prototype cavity showing the 5 non-suppressed resonances.

Table 2: Measured Prototype Parameters (in Air)

Quantity	Meas	Units
f_π	9.5001	GHz
$f_{3\pi/4}$	9.5169	GHz
Δf	16.9	MHz
VSWR	1.006	-
Q_0	7839	-

A bead pull was also performed on the prototype using an uncalibrated aluminum bead. The resulting shift in frequency as a function of the bead position along the cavity axis was measured using a network analyzer. By Slater’s perturbation formula, the frequency shift observed is related to the field amplitudes E_0 and H_0 along the axis by the formula [8]

$$\frac{\Delta f}{f_0} = \frac{\pi a^2}{W_0} (|E_0|^2 - \frac{1}{2}|H_0|^2) \quad (3)$$

where a is the bead diameter, and W_0 is the stored energy in the cavity.

Consequently, the positive peaks in Fig. 6 correspond with the irises where E_0 is maximum, and the negative peaks correspond with the centers of the cells where H_0 is

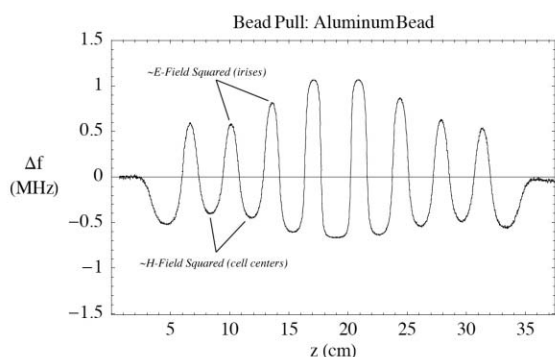


Figure 6: Bead pull field measurement of the prototype cavity using a metallic bead.

maximum. The field balance is imperfect due to difficulties involved in attempting to tune the cells of a steel cavity for a copper-based design prior to application of the 1-micron copper coating. Also note that the flattening of the peaks near the center cell is a systematic error due to the fact that the frequency deviation in this region approaches the width of the resonance. This may be corrected in the future by using a smaller bead.

CONCLUSIONS

The final cavity will be constructed of solid copper using the design parameters of Table 1. This design is expected to provide temporal resolution of the electron beam at the 50 fs level, which should be sufficient to resolve the picosecond to sub-picosecond current profiles generated by the UCLA Neptune accelerator and dogleg compressor beamline. The cell-to-cell mating will incorporate the vacuum seal design of the steel prototype, in order to simplify the process of assembling and tuning the cavity, but with viton o-rings between the mated cells. An alternative hybrid design using copper cells with stainless steel knife-edges is currently being explored for applications with more stringent vacuum requirements.

REFERENCES

- [1] P. R. Phillips. *The Separation of High-Energy Particle Beams by Microwave Techniques*. PhD thesis, Stanford University, Stanford, CA 94305, November 1960.
- [2] O. A. Altenmueller, R. R. Larsen, and G. A. Loew. Investigations of Travelling-Wave Separators for the Stanford Two-Mile Linear Accelerator. Technical Report PUB-R-017, Stanford Linear Accelerator Center, Stanford, CA, 1963.
- [3] G. A. Loew and O. H. Altenmueller. Design and Application of RF Separator Structures at SLAC. Technical Report PUB-135, Stanford Linear Accelerator Center, Stanford, CA, 1965.
- [4] P. Emma, J. Frisch, and P. Krejcik. A Transverse RF Deflecting Structure for Bunch Length and Phase Space Diagnostics. Technical Report LCLS-TN-00-12, Stanford Linear Accelerator Center, Stanford, CA, 2000.
- [5] J. Haimson. Longitudinal phase space measurements of short electron bunches using a 17 ghz circularly polarized beam deflector. In *Advanced Accelerator Concepts: Eleventh Workshop*, pages 95–108, 2004.
- [6] Derun Li and J. N. Corlett. Deflecting rf cavity design for a recirculating linac based facility for ultrafast x-ray science (lux). In *Proceedings of the 2003 Particle Accelerator Conference*, pages 1249–1251, 2003.
- [7] R. J. England, J. B. Rosenzweig, G. Andonian, P. Musumeci, G. Travish, and R. Yoder. Sextupole Correction of the Longitudinal Transport of Relativistic Beams in Dispersionless Translating Sections. *Phys. Rev. ST-AB*, 8:12801, January 2005.
- [8] J. C. Slater. *Microwave Electronics*. Van Nostrand, Princeton, NJ, 1950.

DESIGN OF A MULTI-CELL, HOM DAMPED SUPERCONDUCTING CAVITY FOR THE STRONG RF FOCUSING EXPERIMENT AT DAΦNE

David Alesini, Caterina Biscari, Roberto Boni, Alessandro Gallo, Fabio Marcellini, Mikhail Zobov, INFN/LNF, Frascati, Italy
 Carlo Pagani, INFN/LASA, Segrate (MI) and DESY, Hamburg

Abstract

A strong RF focusing experiment to be performed at the DAΦNE Φ-factory has been proposed to create and observe a bunch length modulation along the ring. The very large RF gradient required to reach the strong focusing regime can only be obtained by using a multi-cell superconducting cavity. Moreover, in order to demonstrate the feasibility of a high luminosity collider based on this principle, a total multibunch current of the order of 1A has to be stored under stable conditions in this regime. A 1.3 GHz 7-cells cavity has been designed for this purpose, based on the TESLA geometry with small modifications of the basic cell to comply with the DAΦNE revolution frequency. The number of cells has been changed from 9 to 7 to reduce the number of the cavity HOMs, while the beam tubes have been enlarged to let most of the HOMs propagate and be damped by room-temperature ferrite rings. The modes of the first longitudinal band, which include the accelerating $TM_{010-\pi}$, do not propagate in the beam tubes and have been studied with special care to prevent the overlap with the bunch revolution harmonics and to cure the effects of coupling to the synchrotron tune sidebands.

INTRODUCTION

The interest for short and intense bunches is growing in the storage ring physics community. The super-factory projects ask for short bunches to avoid the hourglass effect while reducing the vertical beta-function at the Interaction Point (IP) to increase the luminosity. On the other hand the synchrotron light users are interested in stable production of Coherent Synchrotron Radiation (CSR) that also requires short bunches, which have been so far obtained only at very low current with quasi-isochronous lattices.

Table 1: cavity parameters.

RF frequency [MHz]	1288.9
Max RF voltage [MV]	8
R/Q geometric factor [Ω]	390
Quality factor (@ 1.8 K)	10^{10}
Cavity wall power [W @ 1.8 K]	8
Loaded quality factor	$2 \div 4 \cdot 10^7$
Cavity detuning for Beam Loading (@ 8 MV, $I_b=1A$) [kHz]	- 60
RF generator power [kW]	1
Cavity length [m]	0.8

The Strong RF Focusing (SRFF) scheme [1] has been originally proposed to get short and intense bunches at the

IP in the preliminary design of a super Φ-factory aimed at reaching a luminosity of the order of $10^{34} \text{ cm}^{-2}\text{s}^{-1}$. In such a scheme a large momentum compaction factor together with a very high RF gradient across the bunch provide a modulation of the bunch length along the ring, which can be minimized at the IP.

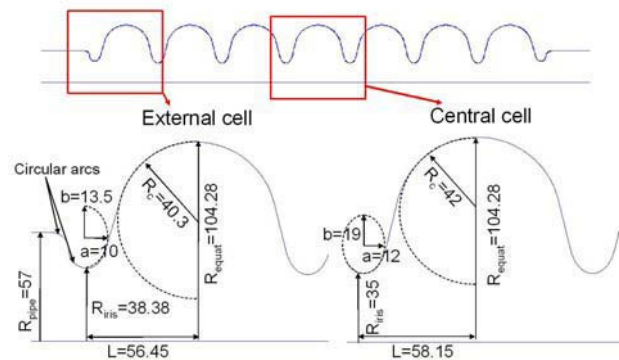


Figure 1: cavity profile and dimensions.

An accelerator physics experiment to be performed at the Frascati Φ-factory DAΦNE has been proposed to create and observe for the first time the bunch length modulation along the ring [2]. A 1.3 GHz Superconducting (SC) cavity has been designed for this purpose, based on the TESLA [3] geometry. The cavity parameters are shown in Table 1.

CAVITY DESIGN

The 1.3 GHz 7-cells cavity design is based on the TESLA geometry with small modifications of the basic cell to comply with the DAΦNE revolution frequency, as shown in Fig. 1. The number of cells has been changed from 9 to 7 to reduce the number of the cavity HOMs, while the beam tubes have been enlarged to let most of the HOMs propagate and be damped by room-temperature ferrite rings. As an example, the transmission coefficient between the two enlarged beam tubes for the 2nd and 3rd monopole bands is plotted in Fig. 2. The highest quality factors are of the order of 10^3 .

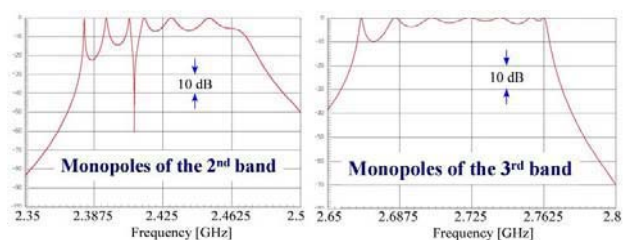


Figure 2: damped monopoles of the 2nd and 3rd band

Input coupling dimensioning

The SC cavity will be used as a harmonic cavity in addition to the standard DAΦNE NC RF system. The resistive beam loading is therefore negligible in the SC RF system. The input coupling factor of the SC cavity is defined essentially by the amount of microphonic noise that shakes the SC cavity and continuously displaces its resonant frequency.

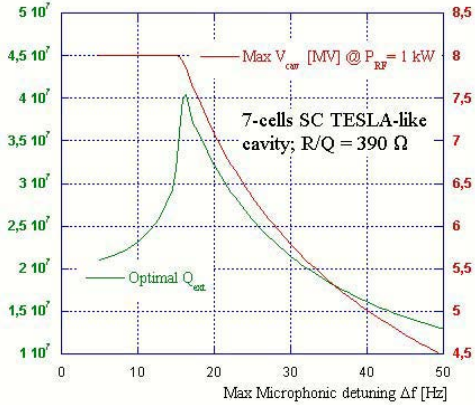


Figure 3: optimal Q_{ext} and available accelerating voltage as a function of the cavity microphonic detuning.

The optimum Q_{ext} value depends on the maximum tolerable frequency deviation of the accelerating mode, as shown in the plot of Fig. 3. If the microphonic detuning exceeds ≈ 15 Hz, the 1 kW RF power available from our solid state amplifier is no more sufficient to guarantee 8 MV accelerating voltage. In this case piezo tuners should be used to compensate the microphonic noise, or a feedback loop adapting the RF frequency of the reference oscillator to the instantaneous value of the resonant frequency of the SC cavity accelerating mode has to be implemented. Depending on the amount of the microphonic noise the optimal Q_{ext} of the input coupler ranges from $2 \cdot 10^7$ to $4 \cdot 10^7$.

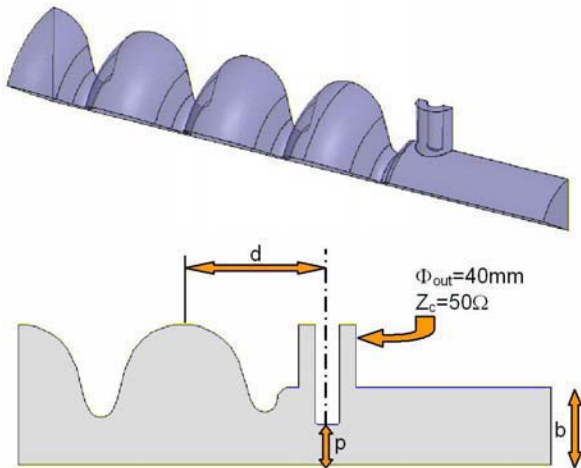


Figure 4: coupler geometry simulated by HFSS.

The input coupler of the TESLA cavity will be used. The coupler position and the inner conductor penetration

into the beam tube to get the required input coupling have been defined with 3D simulations using the HFSS code. The geometry shown in Fig. 4 corresponds to $Q_{ext} \approx 1 \cdot 10^7$ and the quality of the field flatness is excellent as shown in Fig. 5. The TESLA input coupler allows changing the coupling coefficient by varying the penetration of the inner conductor into the beam tube through a bellows system. This feature is very much useful in our case to adapt the coupling to the actual operating conditions.

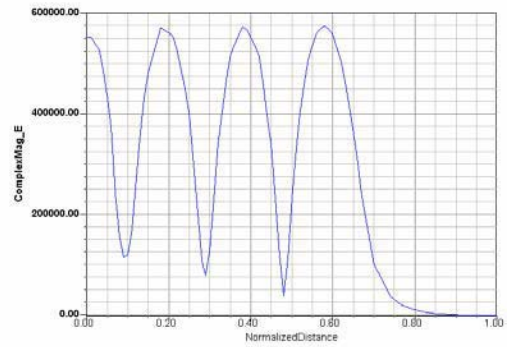


Figure 5: field flatness with coupler as obtained by HFSS.

CONTROL OF THE TM_{010} -LIKE MODES

The modes of the 1st longitudinal band (TM_{010} -like), which include the accelerating one, do not propagate in the beam tubes remaining undamped. To prevent beam disruption caused by the TM_{010} -like mode interaction with the bunch revolution harmonics and/or the synchrotron sidebands a specific strategy based on 2 concepts (mode detuning and direct RF feedback) has been defined.

The first concept is that the resonant frequencies should not overlap the bunch revolution harmonics in order to avoid anomalous power exchange between the beam and the cavity. The nominal resonant frequencies and the R/Q of these modes are reported in Table 2.

Table 2: nominal resonant frequencies an R/Q of the non propagating modes of the 1st monopole band.

Mode	f [GHz]	R/Q [Ω]
$\pi/7$	1266.73	$1 \cdot 10^{-2}$
$2\pi/7$	1269.90	$1.4 \cdot 10^{-5}$
$3\pi/7$	1274.53	$1 \cdot 10^{-1}$
$4\pi/7$	1279.72	$4 \cdot 10^{-4}$
$5\pi/7$	1284.45	1.4
$6\pi/7$	1287.75	$1.6 \cdot 10^{-3}$

Due to the cell fabrication tolerances, the real frequency values after fabrication are displaced by few hundreds kHz respect to the nominal ones and the multi-cell cavity has to be retuned by controlled plastic deformation of the cells to precisely position the frequency of the accelerating mode and restore a good field flatness.

The possibility of tuning the resonant frequency of each mode in the band safely away from the DAΦNE bunch

revolution harmonics during the accelerating mode tuning process has been investigated.

The frequency sensitivity of each mode and the field flatness of the accelerating one have been calculated as a function of the longitudinal deformation of each cell (see Figs. 6 and 7). From these results it is possible to calculate the longitudinal deformation of the cells that we have to implement in the final tuning procedure to shift the resonant frequency of one of the trapped modes by a given quantity. As an example, assuming that we need to shift by 200 kHz a selected mode in the band, we have calculated the set of the cell longitudinal deformations that gives the required shift maximizing the R/Q of the accelerating mode and minimizing the frequency shift of the other modes. The results show that, independently of the selected mode, the required cell deformations are ≤ 0.3 mm, while the frequency shift of the other modes is ≤ 200 kHz. The accelerating mode R/Q reduction is only few percent.

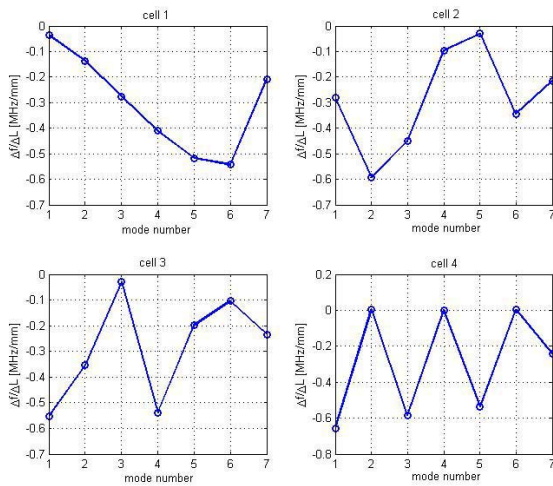


Figure 6: frequency sensitivity of the modes (cell 1 is the first cell).

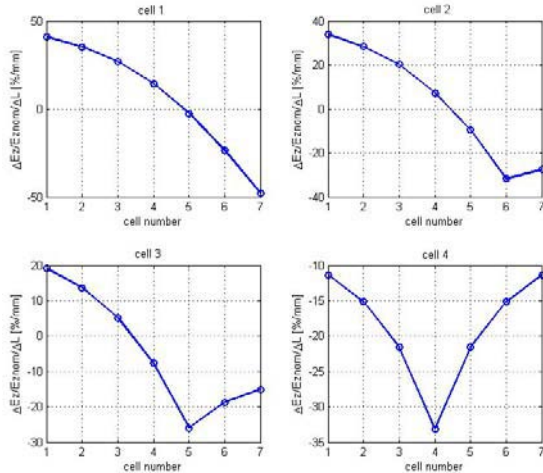


Figure 7: field flatness sensitivity of the modes (cell 1 is the first cell).

The second concept in the TM_{010} -like mode control strategy concerns the cure of the coupled bunch longitudinal instability arising from the coupling with the synchrotron sidebands. To reduce the beam coupling impedance of 1st band monopoles the cavity has to be powered through an efficient direct RF loop as sketched in Fig. 8. The use of a wideband, low group delay solid state amplifier is particularly suitable for this task. A comb filter tuned on the bunch revolution harmonics is necessary to avoid interaction with powerful spectral lines that may saturate the loop and to set optimal phase values of the open loop transfer function at the frequencies where the modes are actually located.

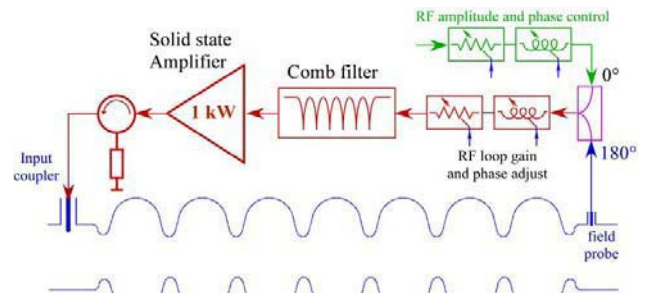


Figure 8: SC cavity powering through a direct RF loop

CONCLUSIONS

A 7-cells SC cavity based on the TESLA design has been proposed for the bunch length modulation experiment to be made at the Frascati Φ -factory DAΦNE. The basic cell has been slightly modified to resonate on the 420th harmonics of the bunch revolution frequency. The high order modes, with the exception of the TM_{010} -like ones, propagate in enlarged beam tubes and are damped in room-temperature ferrite ring loads. The control strategy of the 1st monopolar band modes (TM_{010} -like), which includes the accelerating one, relies on detuning the modes from the bunch revolution harmonics and impedance reduction through the implementation of a direct RF feedback loop.

The TESLA cavity input coupler allows adjusting the coupling coefficient, whose optimal value is defined by the amount of microphonic noise affecting the cavity accelerating mode.

The cavity design engineering will start after the official approval of the strong RF focusing experiment at DAΦNE.

REFERENCES

- [1] A. Gallo, P. Raimondi, M. Zobov, e-Print Archive: physics/0404020.
- [2] C. Biscari, “Proposal of an experiment on bunch length modulation in DAΦNE”, this conference.
- [3] B. Aune et al., “Superconducting TESLA cavities”, Phys. Rev. ST AB 3, 092001, 2001.

OPTIMIZATION OF RF COMPRESSOR IN THE SPARX INJECTOR

M. Boscolo, M. Ferrario, B. Spataro, INFN-LNF Frascati (Rome); C. Ronsivalle, ENEA-Frascati (Rome); L. Serafini, INFN-MI, Milan

Abstract

The SPARX photoinjector consists in a rf gun injecting into three SLAC accelerating sections, the first one operating in the RF compressor configuration in order to achieve higher peak current. A systematic study based on PARMELA simulations has been done in order to optimize the parameters that influence the compression also in view of the application of this system as injector of the so called SPARXINO 3-5 nm FEL test facility. The results of computations show that peak currents at the injector exit up to kA level are achievable with a good control of the transverse and longitudinal emittance by means of a short SW section operating at 11424 MHz placed before the first accelerating section. Some working points in different compression regimes suitable for FEL experiments have been selected. The stability of these points and the sensitivity to various types of random errors are discussed.

SPARX INJECTOR

The first phase of the SPARX project [1] consists in developing techniques and critical components for future X-ray facilities. One of the lines of this R&D activity foresees the use of the SPARC photoinjector [2] to test RF compression techniques aimed to the generation of electron beams with high peak brightness.

The SPARC photoinjector, now under construction in Frascati, consists of a 1.6 cell RF gun operated at S-band with a peak field on the cathode of 120 MV/m and an incorporated metallic photo-cathode followed by an emittance compensating solenoid and three accelerating sections of the SLAC type (2856 MHz travelling wave), the first one embedded in a solenoid composed by an array of 13 coils. It is aimed to provide a 155 MeV-100 A bunch with a projected emittance less than 2 μm and a slice emittance less than 1 μm for the 50% of slices driving a saturating SASE 500 nm FEL without the use of a compressor scheme.

For the SPARX RF compression tests it is planned to use the first SPARC accelerating section as RF compressor, to add a solenoid on the sections #2 and #3 and to place a 11424 MHz (the 4th harmonic of the operating frequency of the TW sections) short linac before the first accelerating structure.

RF COMPRESSOR OPTIMIZATION

RF compressor techniques, based on the simultaneous action of velocity bunching and emittance compensation have been theoretically and numerically studied [3] and partially confirmed by experimental results [4]. The SPARX injector will be devoted to perform optimized

velocity bunching studies and to provide definitive tests of the usefulness of this technique. A systematic study based on extensive numerical simulations of beam dynamics in the SPARX injector has been done by PARMELA code [5] in order to optimize all the parameters and to study the stability of the system.

No IV Harmonic Section Included

A first set of PARMELA runs was done to determine the dependence of the final current from the phase on RF compressor and to optimize the magnetic fields in the solenoids embedding the accelerating sections in order to minimize the emittance in different compression regimes without the use of the X-band section. The results, summarized in table 1, demonstrate that it is possible to reach good levels of compression with a good control of emittance, but some undesired characteristics limit the practical use of RF compression especially in view of a further compression at higher energy.

Table 1: RF compressor parameters

RF compressor phase range	B1,B2,B3 (gauss)	Current (A)	Max. Emittance (μm)
-60° / -75°	1200,0,0	117-151	0.7
-75° / -83°	1200,1400,0	151-249	0.8
-83° / -87°	1200,1400,0	249-458	1.3
-87° / -91°	Ramped from 1200 to 1800	458-1180	2.8

In fact the increase of compression gives: 1) an increasing deformation in the shape of the bunch that appears as a spike followed by a long tail 2) a highly non linear longitudinal phase space 3) a strong sensitivity to phase jitter that gives for compression factors greater than 3 a percentage variation of current of $\sim 15-25\%$ for an error phase of 1 deg on the RF compressor. These effects are due to the combination of the RF and space charge non-linearities. A partial compensation can be obtained by the use of the foreseen IV harmonic section placed between the gun and the RF compressor.

IV Harmonic Section Included

With the 11424 MHz section switched on, the optimization criterion is to bunch the beam in the centre with a linear correlation phase-energy differently from the unlinearized case where the charge piles up in the bunch head and only a portion of the electrons (typically the half) is involved by the compression process.

From simple analytical considerations the beam energy should be decreased of 1/16 of the energy gain in the RF

compressor, but due to deceleration the input energy and energy spread change give different energy gain and phase slippage in the SLAC sections, so that the amount of the needed deceleration must be determined numerically. From PARMELA simulations it results that the beam energy must be reduced from 5.64 MeV to ~3.3 MeV, that can be obtained by different combinations of phase and amplitude (E_x) in the X-band section, giving different compression factors for the same phase on the RF compressor. As it is shown in figure 3 the beam current can be raised to ~ 950 A.

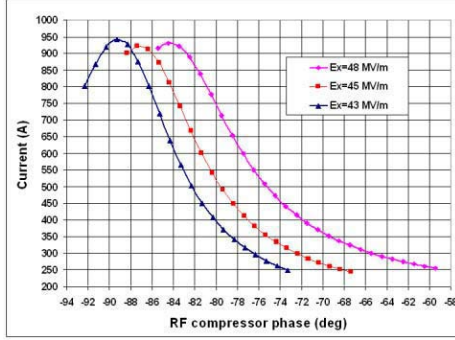


Figure 1: Final current vs RF compressor phase for different electric fields amplitude in the X. band section and the same decelerating voltage.

In the range 300-900 A these curves have been fitted by a 4th order polynomial whose derivative gives the sensitivity to the RF compressor phase jitter: in figure 4 the quantity $(dI/d\phi)/I$ is plotted vs the beam current for these three curves compared with the case of compression without IV harmonic section. The sensitivity to phase jitter is reduced of a factor ≥ 2 by the use of the IV harmonic section.

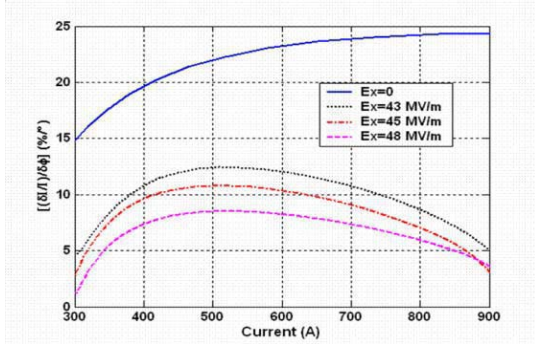


Figure 2: The percentage variation of current for an error of 1 degree in the RF compressor phase.

WORKING POINTS IN MEDIUM AND HIGH COMPRESSION REGIME

In the parameters space of figure 3 two working points have been selected also in view of the application of the system as injector of the so-called *SPARXINO* 3-5 nm FEL test facility [1] based on an upgrade of the actual Frascati 800 MeV linac including a second stage of compression of magnetic type.

The first working point (fig.3) is particularly suitable to a further magnetic compression due to its good beam characteristics in terms of current (450 A) and emittance (1.03 μm) and good linearity of ϕ -E space compared with the case in which the same average current is obtained with the IV harmonic section off (fig.4).

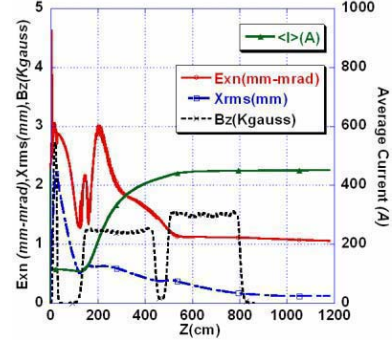


Figure 3: Average current, transverse emittance and envelope, axial magnetic field vs z for a 450 A compressed beam.

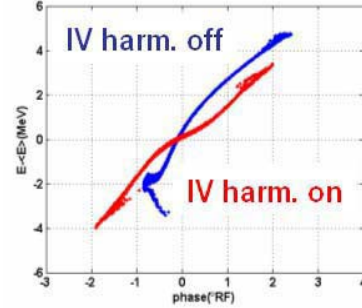


Figure 4: Longitudinal phase space for a 450 A compressed beam with and without the IV harmonic section.

The relative slice analysis for a slice length of 30 μm shown in figure 5 indicates that the compression occurs in the central part of the bunch, where the energy spread and emittance are at a minimum, that maximizes the normalized brightness, $B_n = I / (4\pi\epsilon_{nx}\epsilon_{ny})$, that reaches $6 \cdot 10^{13}$ for the central slice.

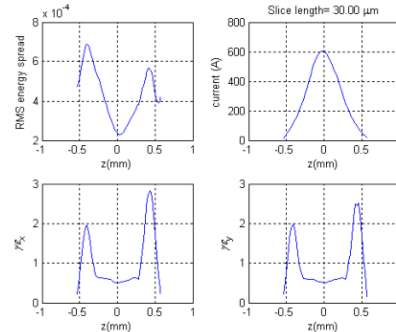


Figure 5: Slice analysis for a 450 A compressed beam.

The second working point (figs. 6,7) is interesting for its high current (860 A) and very good control of the projected (1.5 μm) and slice emittance allowing to rise the peak slice brightness to $1.13 \cdot 10^{14}$.

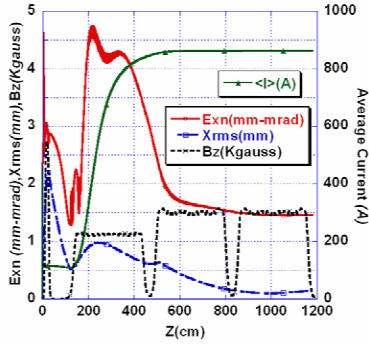


Figure 6: Average current, transverse emittance and envelope, axial magnetic field vs z for a 860 A compressed beam.

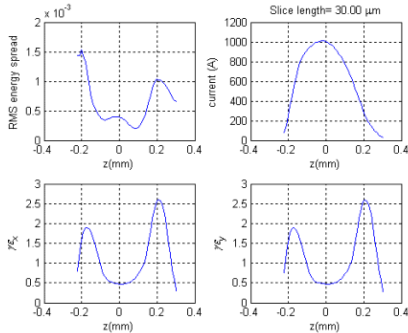


Figure 7: Slice analysis for a 860 A compressed beam.

SENSITIVITY TO ERRORS

The sensitivity of the two working points described above to various types of random errors under realistic conditions has also been studied. Following a technique already used for the SPARC working point described in [6], a statistical analysis has been done based on the results of one hundred PARMELA runs performed for each working point, each one with random errors set within the limits of table 2 using the criterion of having a maximum growth of the projected emittance of 10% and a maximum current variation of $\pm 15\%$ with respect to the nominal case.

Table 2: Variation of parameters for combined random errors study in the SPARX injector

Parameter	Error range
Phase jitter gun-linac	$\pm 1^\circ$
Phase jitter gun-X band section	$\pm 1^\circ$
Charge fluctuation	10%
Gun B field amplitude	$\pm 0.4\%$
Gun E field amplitude	$\pm 0.5\%$
Spot radius	$\pm 10\%$
Spot ellipticity	3.5%

The results of the simulations were used to construct the curves plotted in fig. 8 that give the probability to obtain an emittance greater or equal than the corresponding value on the abscissa for the two considered compressed beams compared with the non-compressed SPARC beam. For example a probability of 10% corresponds to a normalized projected emittance ≥ 1

μm at 100A and to $\sim 1.8 \mu\text{m}$ at 450 A and to $\sim 2.25 \mu\text{m}$ at 860 A.

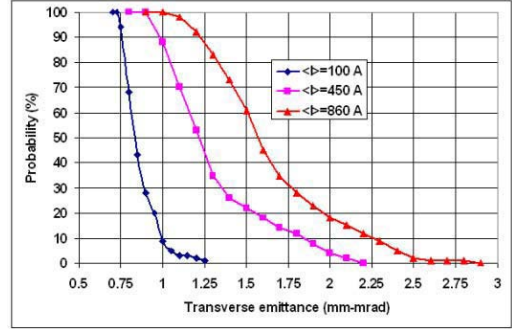


Figure 8: Probability vs emittance over 100 simulations.

The distribution of the values of the projected normalized brightness in 100 runs gives the results reported in table 3 showing that the compression gives an increase, as expected, not only of the average value but also of the standard deviation with a consequent reduction of the brightness stability.

Table 3: Projected normalized brightness in 100 runs

Current (A)	$\langle Bn \rangle$ $\text{A}/[(\text{m-rad})^2]$	σ $\text{A}/[(\text{m-rad})^2]$
100	$1.1 \cdot 10^{13}$	$0.25 \cdot 10^{13}$
450	$2.4 \cdot 10^{13}$	$0.86 \cdot 10^{13}$
860	$2.8 \cdot 10^{13}$	$1.2 \cdot 10^{13}$

Concerning the slice emittance, in all simulations it does not exceed $1 \mu\text{m}$ for the central slices at 450 A and $1.2 \mu\text{m}$ at 860 A.

CONCLUSIONS

The results of the RF compressor optimization study in the SPARX injector show that a high peak current beam (up to 1 KA in the slice) can be produced with a charge uniformly distributed through the pulse and a tolerable sensitivity on incoming phase jitter. A sensitivity study to various types of random errors in some significant operating points shows that the projected and slice emittance remain respectively below $2.5 \mu\text{m}$ and $1.2 \mu\text{m}$ in realistic operation conditions.

REFERENCES

- [1] M. Boscolo et al. "Start To End Simulations for The SPARX Project", this Conference
- [2] SPARC collaboration "Status of the SPARC Project", this Conference
- [3] M. Ferrario et al. "Beam dynamics study of an RF bunch compressor for High Brightness beam injectors", Proceedings of EPAC02, p. 1762, June 2002 Paris
- [4] S.G. Anderson et al. "Velocity bunching of high brightness electron beams", Phys. Rev. ST Accel. Beams 8, 014401 (2005)
- [5] J. Billen, "PARMELA", LA-UR-96-1835, 1996
- [6] M. Biagini et al. "SPARC photoinjector working point optimization, tolerances and sensitivity to errors", Proceedings of EPAC04, p.396, July 2004 Lucerne

SPARC WORKING POINT OPTIMIZATION FOR A BUNCH WITH GAUSSIAN TEMPORAL PROFILE

M. Boscolo, M. Ferrario, V. Fusco, M. Migliorati, INFN-LNF, Frascati, Italy
 C. Ronsivalle, ENEA-CR, Frascati, Italy
 S. Reiche, UCLA Dept. of Physics/Astronomy, USA

Abstract

We present the optimization of the working point with a Gaussian temporal profile for the SPARC photoinjector. Start to end simulations starting from a Gaussian electron beam pulse shape are discussed here, in comparison with the nominal working point performances of a 10ps flat top pulse with rise time of 1ps [1]. Machine parameters have been optimized for the Gaussian pulse shaping both for the standard operating conditions and for the radio-frequency (RF) compressor configuration. In particular, compression factors (C) 2 and 4 have been studied in details. Simulations have been performed using the codes PARMELA [2] and GENESIS [3], for the beam transport along the photoinjector and for the FEL/SASE process respectively.

The two pulse shapes we considered, Gaussian and rectangular with rise time of 1 ps, provide the same saturation length and average power of radiation emitted in the undulator, but the higher current in the beam core of the Gaussian pulse gives a higher peak radiation power at the cost of a broader radiation spectrum. These simulations were performed to investigate thoroughly one of the possible operating modes of the SPARC laser system, which naturally produces such Gaussian shaped pulses.

INTRODUCTION

A longitudinally Gaussian charge distribution has been considered as a possible pulse shaping for the SPARC photoinjector. We optimized the machine free parameters for this pulse shape with a $\sigma_{rms}=2.89$ ps and studied in details this selected working point.

Since the Gaussian time profile exhibits a better linear behavior in the longitudinal space charge field w.r.t. the flat-top profile, we decided to investigate the emittance, energy spread and longitudinal emittance of Gaussian temporal distributions. So we investigated if the emittance and energy spread values could be reduced by taking into consideration an initially Gaussian pulse.

Plots of fig. 1 show that the longitudinal phase space is more linear in the core of the Gaussian profile (right) than for the rectangular case (left), but tails are longer in the first case. However, at this longitudinal position, the correlated energy spread is slightly lower for the Gaussian profile, and the corresponding longitudinal emittance is $34.0 \mu\text{m}$, compared to $61.5 \mu\text{m}$ of the nominal rectangular case. The different characteristics of the two beam distributions are presented below. Furthermore, the chosen Gaussian pulse has been RF compressed, the dynamics of the chirped beam and the FEL/SASE predictions are discussed.

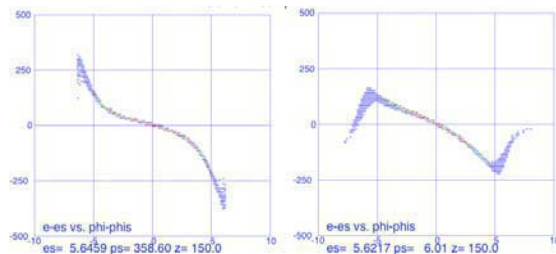


Figure 1: Longitudinal phase space at $z=150$ cm, the accelerating sections entrance. Left: 10 ps beam pulse and 1 ps rise time (defined as the time interval from 10% to 90% of the total pulse height); right: Gaussian pulse. Energy spread is 1.78% and 1.53% for the rectangular and Gaussian pulse, respectively.

In order to preserve the matching conditions with the beamline we take a Gaussian with the same σ_{rms} of the nominal rectangular pulse of bunch length $L=10$ ps. So, as the σ_{rms} of a square pulse is given by $L/\sqrt{12}$, we consider a Gaussian temporal pulse with a width of $\sigma=2.89$ ps. This assumption implies that the Gaussian beam has a 40% higher peak current. In fact, the bunch current for the rectangular and Gaussian profiles are respectively given by the following relations:

$$I_{rect} = \frac{\beta c Q}{\pi R^2 L} \quad \text{and} \quad I_{Gaussian} = \frac{\beta c Q}{\pi R^2 \sqrt{2\pi} \sigma_z} e^{-z^2/2\sigma_z^2}$$

so that for the central slice it results that

$$I_{Gaussian} = \sqrt{\frac{6}{\pi}} I_{rect} \approx 1.4 I_{rect}.$$

In principle, this consideration leads to the idea that the high current of the Gaussian beam core pulse could give promising simulation results for the FEL/SASE effects.

Table 1: Parameters that differ for the Gaussian and for the nominal case

	$\phi_{inj}(\circ)$	$B_{gun}(T)$	$B_{ITW}(T)$
Nominal	32	0.273	0.615
Gaussian	26	0.271	0.700

OPTIMIZATION OF THE GAUSSIAN WORKING POINT

The set of parameters of the SPARC photoinjector has been fixed by the optimization transport of the nominal pulse shape. We now want to match the Gaussian beam to the beam line, that is we look for a set of parameters such that the longitudinal evolution of the normalized emittance in the gun and drift leads to two relative

minima, and the minimum of the beam envelope corresponds to the relative maximum. The best profile of an electron pulse in relation to the goal of emittance minimization leads to two relative emittance minima which have the same value [4]. This is obtained by a rectangular pulse with zero rise and decay time. The longer the rise time the higher the value of the first minimum and, in turn, the higher the final emittance.

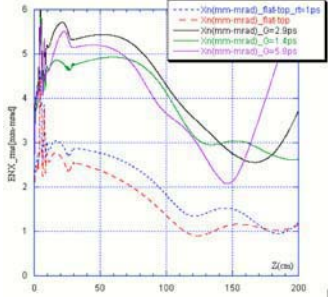


Figure 2: Beam emittance evolution along the first 200 cm of the SPARC injector without accelerating structures for three Gaussian pulses with different width: $\sigma_{rms}=2.89$ ps (black curve), $\sigma_{rms}=1.4$ ps (green curve) and $\sigma_{rms}=5.8$ ps (purple curve), compared to the nominal rectangular pulse with rise time of 1 ps (blue curve) and with no rise time (red curve).

The Gaussian beam evolution along the first 2 m of the injector without accelerating structures is shown by the black curve of fig. 2: the first emittance minimum almost disappears, very similarly to the case of a rectangular pulse shape with long rise time. In this sense we can say that a Gaussian pulse behaves like a rectangular one having long rise times. Moreover, from fig. 2 it can be also noticed that the symmetry between the two emittance minima behaviour strongly depends on the longitudinal Gaussian width. In fact, the emittance behavior is closer to the rectangular case at the decrease of the Gaussian width (see green curve compared to purple one).

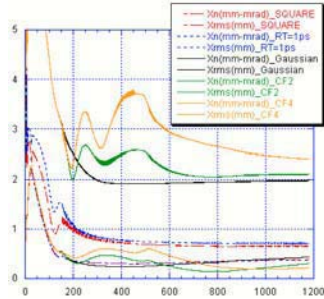


Figure 3: Beam emittance and envelope evolution along the SPARC injector. Black curve is for the Gaussian pulse ($\sigma_{rms}=2.89$ ps), compared to the nominal rectangular pulse with rise time of 1 ps (blue curve) and with no rise time (red curve). Green and orange curves represent respectively the C=2 and C=4 with the Gaussian pulse.

For the chosen Gaussian beam with $\sigma_{rms}=2.89$ ps, the matching conditions have been optimized by varying the free parameters, that are the gun solenoid field value and

the RF gun injection phase. In table 1 the slight variation values of these two parameters are reported.

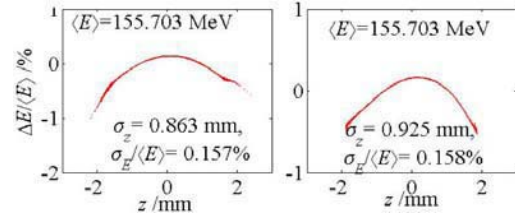


Figure 4: Longitudinal phase space for the Gaussian pulse (left plot) and for the nominal case (right plot).

Discussing now the beam characteristics at the end of the linac for the two types of initial longitudinal distributions, the longitudinal normalized emittance is $\sim 396 \mu\text{m}$ and $\sim 438 \mu\text{m}$ for the Gaussian and for the rectangular pulse, respectively. The rms energy spread is about $\Delta\gamma/\gamma \sim 0.16\%$ in both cases (see fig. 4). However, the linearity of the Gaussian case permits better energy spread corrections. The normalized emittance is $ENX=1.97 \mu\text{m}$ for the Gaussian shape, much higher than the nominal case ($ENX=0.70 \mu\text{m}$), as shown in fig. 3.

As for the slice beam properties, in the Gaussian case the slice emittance is about $ENX_{slice} \sim 1 \mu\text{m}$ with a high slice current $I_{max}(slice) \sim 130 \text{ A}$, to be compared to the nominal case where most slices have an emittance of $ENX_{slice} \sim 0.5 \mu\text{m}$ and the peak current for the central slice is $I_{max}(slice) \sim 110 \text{ A}$ (see fig. 5).

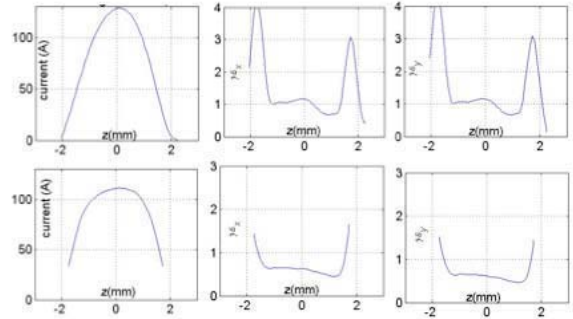


Figure 5: From left to right: slice beam current, slice radial normalized emittance and slice vertical emittance. Upper is for Gaussian case, lower for the nominal one.

FEL/SASE Simulations With the Gaussian Pulse

The slice emittance and energy spread values are good enough for the SASE/FEL process with the chosen Gaussian initial shape through the undulator, at 155 MeV. In fact, the average radiated power calculated for this case predicts saturation within 10 m (black curve of fig. 6). In any case, the photon flux is about 10-15% larger for the nominal profile than for the Gaussian one.

The radiation pulse emitted by the initially Gaussian pulse is shorter but with higher spikes (black curves of fig. 6), if compared to that of the rectangular one [5]. This behavior comes out from the electron beam pulse shape, as in the long Gaussian tails not all the slices are good enough to drive the SASE instability, moreover the beam core gives a 40% higher peak current.

The calculated normalized brightness for the nominal case is $1.1 \cdot 10^{13} \text{ A}/(\text{m rad})^2$ and almost a factor 2 lower for the Gaussian case taken into consideration here, essentially due to the higher emittance.

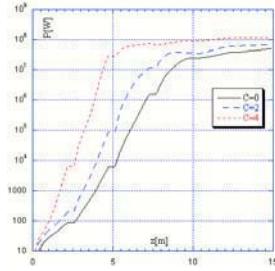


Figure 6: Average radiated power expected for a Gaussian electron beam through the SPARC undulator. The three curves represent: C=0 (black), C=2 (blue) and C=4 (red). For the three cases saturation is predicted.

CHIRPED GAUSSIAN BEAM

The same Gaussian beam pulse discussed above has been chirped with rf compression in the first accelerating section. We present here start to end simulations for the compressor factors C=2 and C=4, where $C = \sigma_z(\text{init}) / \sigma_z(\text{fin})$, that is the ratio between initial and final longitudinal σ_{rms} .

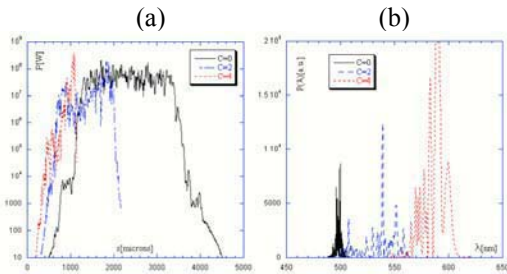


Figure 7: Frame (a) shows the radiation profile at saturation, frame (b) the radiation spectrum at saturation. The three curves represent: C=0 (black), C=2 (blue) and C=4 (red).

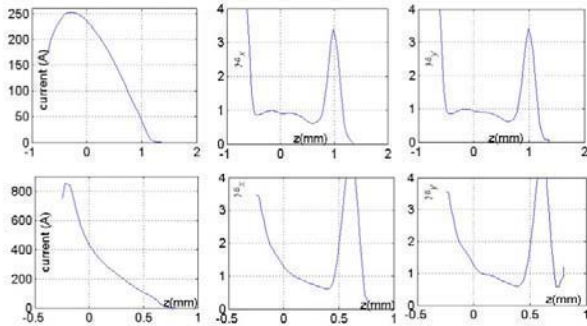


Figure 8: From left to right: slice beam current, slice radial normalized emittance and slice vertical emittance. Upper is for C=2, lower for C=4.

Simulations studies for the C=2 case predict an average beam current of $I_{\text{rms}} \sim 210 \text{ A}$. The maximum slice current is $I_{\text{max}}(\text{slice}) \sim 250 \text{ A}$ and the corresponding slice emittance is $\text{ENX}_{\text{slice}} \sim 0.9 \mu\text{m}$ (upper plots of fig. 8). This chirped beam has a rms energy spread of $\Delta\gamma/\gamma \sim 1.8\%$, as shown in

left plot of fig. 8. The current is higher than $I > 200 \text{ A}$ for about $\sim 65\%$ of the beam; the normalized brightness results $B = 0.7 \cdot 10^{13} \text{ A}/(\text{m rad})^2$.

Simulations studies for the C=4 case predict an average beam current of $I_{\text{rms}} \sim 420 \text{ A}$. The maximum slice current is $I_{\text{max}}(\text{slice}) \sim 850 \text{ A}$ and the corresponding slice emittance is $\text{ENX}_{\text{slice}} \sim 3.4 \mu\text{m}$ (lower plots of fig. 8). This chirped beam has a rms energy spread of $\Delta\gamma/\gamma \sim 1.3\%$, as shown in right plot of fig. 9. The current is higher than $I > 400 \text{ A}$ for about $\sim 65\%$ of the beam; the normalized brightness results $B = 1.1 \cdot 10^{13} \text{ A}/(\text{m rad})^2$.

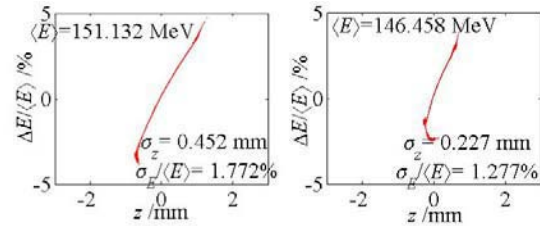


Figure 9: Longitudinal phase space for the Gaussian chirped pulse for C=2 (left plot) and C=4 (right plot).

As a stronger chirping is taken into account the beam current gets higher at the price of a higher emittance and a more distorted current profile. This behavior is, in turn, transferred to the emitted radiation profile and spectrum. In fact average radiated power increases with the compression factor as shown by the blue (C=2) and red (C=4) curves of fig. 6. However, the stronger the chirping the more distorted is the radiation profile (fig. 7 Frame (a)) and the broader is the radiation spectrum at saturation.

CONCLUSIONS

Start to end simulations for a Gaussian temporal pulse have been performed, finding a parameter set that optimizes its transportation along the linac. FEL/SASE simulations predict about same saturation length but a shorter radiation pulse with higher peak power than for the nominal pulse.

As for the chirped Gaussian beam, the stronger the chirping the higher is the average radiated power and the broader gets the radiation spectrum. Moreover, the radiation profile is more distorted, as it resembles the current profile. This effect can be corrected inserting a higher harmonic cavity, as already verified for the standard working conditions [6].

REFERENCES

- [1] D.Alesini et al, "Status of the SPARC Project", EPAC'04, Lucerne, July 2004.
- [2] J.Billen, "PARMELA", LA-UR-96-1835,1996.
- [3] S.Reiche, *Nucl. Instrum. & Meth.* A429, 243 (1999)
- [4] M. Ferrario et al., "Homodyn study for the LCLS Photoinjector", SLAC-PUB-8400, Mar 2000.
- [5] M.Boscolo, M.Ferrario, S.Reiche, "Studies of Gaussian Pulse shaping at SPARC", SPARC Techn. Note SPARC-BD-04/002.
- [6] C.Ronsivalle et al."Optimization of RF compressor in the SPARX injector", this Conference.

PRELIMINARY RESULTS ON BEAM DYNAMICS OF LASER PULSE SHAPING EFFECTS IN SPARC

M. Boscolo, M. Ferrario, M. Migliorati, INFN- Frascati, Italy
 F. Castelli, S. Cialdi, A. Flacco, INFN-Milano, Italy

Abstract

Electron beams with different initial pulse characteristics have been transported along the SPARC photoinjector. The differences we considered come from the possible profiles of the laser pulse driving the radio-frequency (rf) electron gun. Realistic deviations from the ideal flat-top pulse give for example a ramp or multi-peaks shape with a relative rise time, plateau deformation and roughness. The beam quality of the electron source is essential for the production of high brightness beams. The role played by the laser pulse is crucial, as it determines the electron beam pulse shape.

The study presented here gives some indications on the tolerances of the laser beam characteristics for the electron beam quality preservation. The different beam current profiles are transported along the injector with the PARMELA [1] code. The electron pulse as external input to PARMELA is generated directly from a laser pulse resulting from certain configurations of the SPARC laser system. The variations of normalized emittance (ENX) and envelope are discussed for the different cases. Spectral and shaping requirements on the laser pulse temporal profile for the SPARC injector are found.

INTRODUCTION

High brilliance rf electron guns are driven by laser pulses of rectangular profile [2]. However, the shape of the laser pulse is very sensitive to the setting of the pulse shaping system as well as to the alignment of the many optical elements of the laser system [3,4]. The final output waveform comes out different from the expected target pulse, as alignment and position of the components are perturbed with respect to the ideal setting. The profile deviations due to possible system perturbations have been detected with computer simulations. We assume no pulse deviation from cathode emitting surface, so that the emitted electron beam profile matches the laser profile. This assumption is fairly good for a metallic photocathode.

Because of the very small chance of having the ideal output laser pulse it is worth investigating the beam dynamics versus the different possible pulse characteristics. We take into considerations in our discussion the rise time, the amplitude and frequency modulation in the plateau and a possible ramp shape of the pulse. We stress that thanks to the shaping system the pulse characteristics can be controlled separately.

Their impact on the beam evolution along the linac has been investigated using the PARMELA code with a sample of 15000 particles. The FWHM of the generated pulses have been fixed to 10 ps, in order to compare

results with the nominal case. The SPARC accelerator has been optimized for minimizing both the total projected emittance and the slice emittance, knowing that the slice value is critical for the SASE process. However, a good matching of the beam along the accelerator is only possible if the total projected emittance is quite small.

We point out that the tool we have developed allows performing complete start-to-end simulations starting from the generation of the laser pulse up to the FEL/SASE studies through the undulator. We think this tool will result very useful during the tests of the different laser profiles and during the machine commissioning with real pulses.

EMITTANCE VERSUS ELECTRON PULSE CHARACTERISTICS

We present in the following the results of the emittance for some selected different cases.

Emittance Versus Rise Time

The best profile of an electron pulse in relation to the goal of emittance minimization leads to two relative emittance minima which have the same value [5]. This is obtained by a rectangular pulse with zero rise and decay time (defined as the time interval from 10% to 90% of the total pulse height). The longer the rise time the higher the value of the first minimum and, in turn, the higher the final emittance. This is, in fact, shown by the simulations depicted in fig.1.

The emittance increase in the end of the beam line versus the rise time, calculated for the last working conditions, reproduces substantially other investigations [6].

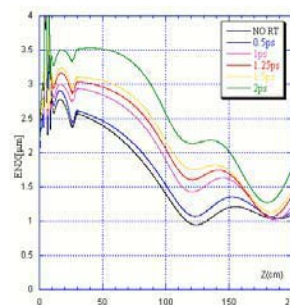


Figure 1: Beam emittance evolution along the first 200 cm of the SPARC injector without accelerating structures for different rise times.

For completeness, we have checked the behaviour with 1 ps rise time and 2 ps decay time, and vice versa. The final emittance is near equal to the one obtained with both rise and decay time selected to 2 ps. This result can be

interpreted by saying that space-charge forces tend to homogenize the phase-space occupied by the beam. The longitudinal phase spaces is very similar for the two cases, therefore there is negligible influence on the emittance.

The simulation results indicate clearly the strict requirement on the rise time. A 1 ps of rise time is a really a challenging goal for a laser system, as pointed out also in [7].

Emittance Versus Plateau Fluctuations

The profile of a pulse generated by a laser will have, in general, amplitude and frequency modulations. First effects have been investigated in [6]. Now we have separated the effects on the emittance by the two types of modulations: an amplitude modulation and a frequency modulation, an example of them are represented in fig. 2(a), and in fig. 2(b). Rise and decay times are fixed at the nominal value of 1 ps.

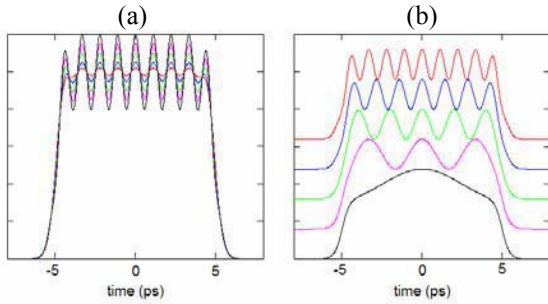


Figure 2: Frame (a): Intensity temporal profiles with different amplitude oscillations in the flat-top for a fixed frequency of 0.9 ps^{-1} . Frame (b): Intensity temporal profiles with different oscillation frequencies on the plateau for a fixed amplitude of 20%.

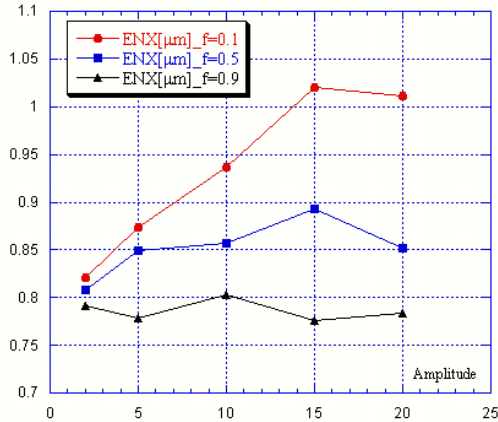


Figure 3: Projected horizontal emittance at the end of the linac versus the amplitude oscillations for frequencies of 0.1 ps^{-1} (red dots), 0.5 ps^{-1} (blue squares) and 0.9 ps^{-1} (black triangles).

The effect of the amplitude modulation is analyzed assuming frequencies of 0.9 ps^{-1} , 0.5 ps^{-1} and 0.1 ps^{-1} . The result of the investigations is shown in fig. 3. The value of

the emittance remains substantially constant increasing the amplitude of the oscillations, as long as the frequency is sufficiently high. The slope of the emittance-amplitude line decreases with the increase of the frequency.

A possible interpretation of this behavior is that a cylinder of charge with a high frequency density modulation is a dense array of charged disks. When the distance between the disks is short enough the electric field nearby the border is very similar to that of a uniform charge cylinder. This could be the reason of the equal action by the applied magnetic field on both charge distributions. In addition, we note that the longitudinal density oscillations of the electron distribution disappear after a drift of 150 cm, in the meanwhile an energy oscillation shows up, as discussed in [6] and [8].

EMITTANCE VERSUS A PULSE HAVING A RAMP PROFILE

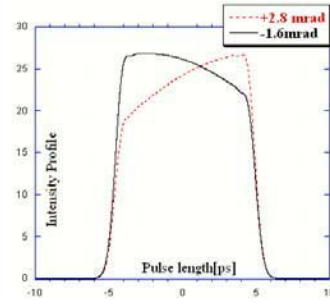


Figure 4: Intensity profiles assume a ramp shape for different values of crystal tilting angles.

The temporal profile of the laser pulse at 266 nm is required to be of rectangular fashion with fast rise time. A rectangular profile is generated inserting in a laser system a shaping device (shaper) which transforms the Gaussian-like profile generated by a laser oscillator into the target one. Moreover the propagation through the crystals generating the second and the third harmonics can produce distortions on the spatial and temporal profiles, and the shaper system must provide an active setting of the optical components to control the profile deformations, as discussed in [9].

In general light pulse manipulation is obtained by amplitude and phase modulation of its spectral components. One of the proposed pulse shaper systems can be constituted by a Dazzler located before the amplifier, and a stretcher after, or before, the crystals for the third harmonic generation. The Dazzler introduces an amplitude modulation on the spectrum and a small chirp in order to obtain a pulse of a few ps.

We now study the case in which a rectangular laser pulse, after a stretching to the requested 10ps length, crosses a harmonic generating crystal assuming a ramp fashion, due to a mismatch on the matching angle between the light propagation direction and the principal axis of the birefringent crystal. We note that a perfect alignment is a really difficult achievement. We have

considered the misalignment angles of ± 2.8 mrad and ± 1.6 mrad. Negative angles mean higher leading edge of the pulse profile (see Fig. 4).

The simulation has shown that a negative ramp leads to emittance enhancement whereas a positive ramp does not influence the emittance, as shown in Fig. 5.

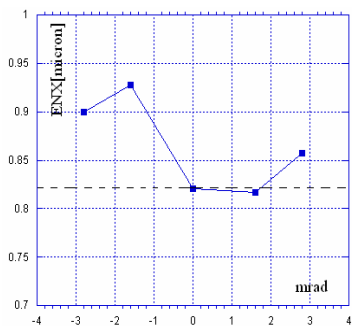


Figure 5: The projected emittance at the end of the linac versus crystal tilting angle. The dashed line is the reference emittance value for a perfectly aligned crystal.

A REALISTIC PULSE

As a final investigation we have done the simulation for the laser pulse of Fig. 6.

This laser pulse is obtained setting the laser system on the basis of the trade off between the two requirements of high conversion efficiency and good rectangular pulse profile, analyzed in [9]. Furthermore, it is assumed that one of the two up-converting crystals has a misalignment angle of 1.6 mrad.

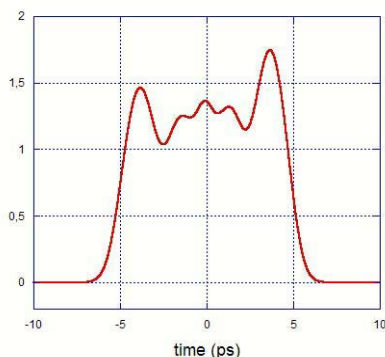


Figure 6: Profile of a realistic pulse obtained with a typical configuration of a laser system.

The objective of efficient harmonic conversion implies a high intensity of the entering pulse. Because of this, the Gaussian initial pulse was stretched only up to 2 ps before the up-conversion. The rest of the stretching is applied after the harmonic generation to the final 10 ps temporal length. This procedure of pulse forming leads to a reasonably good conversion efficiency but at the cost of an increase in the rise time to about 1.6 ps. For these choices the final electron beam results with the three peaks and with a ramp fashion.

The simulation result with this pulse gives an emittance of $ENX=0.85 \mu\text{m}$, that is nearly equal to the one obtained

with the rectangular pulse of 10 ps with 1.5 ps of rise time. Apparently, the only relevant parameter for the emittance preservation seems the rise time in this particular simulation. This result needs further investigations.

We mention that our code that generates the electron bunch does not take into consideration the effect that the quantum efficiency (QE) depends on frequency. Forthcoming studies will include this effect in the modelling.

CONCLUSIONS

The detailed study of the effects on the emittance of the different characteristics of the laser/electron pulse gives the relevance of each characteristic in relation to the emittance degradation. The emittance comes out to be sensible firstly to the rise time and secondly to small frequencies and smoothed modulations on the plateau. Fast bumps on the flat top do not provide detectable emittance variations. A weak increase of the emittance comes out when the pulse has a negative ramp shape, whereas it remains unchanged with opposite ramp.

Since the large and complex laser systems which drive an rf-gun have inherently perturbation of the setting of the many elements, and since a good rectangular pulse profile is very sensitive to perturbations, it is advisable to set the laser system in a feedback loop configuration because a proper shaping system has the adaptive capability to recover the distortions introduced by the perturbations.

ACKNOWLEDGMENTS

The work is partly supported by Ministero Istruzione Università Ricerca, *Progetti Strategici*, DD 1834, Dec.4,2002 and European Contract RII3-CT-PHI506395CARE.

REFERENCES

- [1] J.Billen, "PARMELA", LA-UR-96-1835, 1996.
- [2] M. Biagini et al., 'SPARC photoinjector working point optimization, tolerances and sensitivity to errors', Proc. of EPAC04 Lucerne, July 2004.
- [3] S. Cialdi and I.Boscolo, 'A laser pulse shaper for the low-emittance radiofrequency SPARC electron gun', Nucl. Instr. And Meth., A 526 (2004) p.239-248.
- [4] S. Cialdi and I.Boscolo, 'A shaper for providing long laser target waveforms', Nucl. Instr. and Meth., A 538 (2005) p.1-7.
- [5] M. Ferrario et al., "Homodyn study for the LCLS Photoinjector", SLAC-PUB-8400, Mar 2000.
- [6] M. Biagini et al., "Beam Dynamics Studies for the SPARC Project", Proc. of PAC03, p. 2077, 2003.
- [7] H. Loos et al., "Temporal e-beam shaping in an S-Band Accelerator", this Conference.
- [8] C. Limborg et al., "Sensitivity studies for the LCLS photoinjector beamline", Nucl. Instr. and Meth., A 528 (2004) p.350-354.
- [9] S.Cialdi, F.Castelli and I.Boscolo, "Rectangular pulse formation in a laser harmonic generation", INFN/BE-05/01; S.Cialdi, F.Castelli and I.Boscolo, submitted to J.Opt.Soc.Am. B.

MAGNESIUM FILM PHOTOCATHODES FOR HIGH BRILLIANCE ELECTRON INJECTORS

G. Gatti, F. Tazzioli, C. Vicario, INFN-LNF, Via E. Fermi 40, 00044 Frascati (Roma) Italy

I. Boscolo, S. Cialdi, University and INFN, Via Celoria 16, 20133 Milano, Italy

L. Cultrera, A. Perrone, Lecce University, Physics Dept. and INFN, Via per Arnesano, 73100 Lecce, Italy

M. Rossi, Rome University La Sapienza, Dip. di Energetica, Via A. Scarpa 16, 00101 Roma, Italy

S. Orlanducci, M. L. Terranova, Dip. Scienze Chimiche and INFN, Rome University Tor Vergata, Via della Ricerca Scientifica, 00133 Roma, Italy

Abstract

Advanced high brilliance electron injectors require photocathodes having low thermal emittance, high quantum efficiency (QE) and prompt response. They should be easy to handle and capable of working in the very high electric fields of a RF gun. Magnesium films deposited by laser ablation and sputtering techniques are discussed and QE measurements are presented.

INTRODUCTION

Advanced injectors of ultra-bright electron beams require photo-cathodes having prompt response and high QE at near UV wavelengths (266 nm) [1]. Metallic cathodes are fast (tens of femtoseconds range) but their QE, defined as the number of emitted electrons per incident photon, is rather low (order of 10^{-5} for Cu). Cesium semiconductors show a higher QE but their response is slower and the lifetime is short. In addition they are delicate to handle, requiring UHV both during transport and in operation. Among metals, Mg has a premium QE, up to 10^{-3} . The higher QE would ease the requirements on the driving laser. Therefore it has been widely tested both as bulk and in the form of films. Mg disks inserted by press fitting in the end Cu plate of a RF gun cavity have shown problems of RF breakdown at the junction [2]. Moreover, the distribution of QE varies over the emitting spot [3]. These problems could be overcome if a Mg film is deposited directly on the gun plate, provided that the film has good uniformity and adhesion to the substrate. Sputtered Mg films have been tested at low fields in a DC diode [4]. These films were 20 microns thick and deposited on Cu substrates in a 10^{-5} Pa background pressure. It was found that they are rugged and have a high QE. Exposition to air forms a protective oxide layer that can be easily removed by laser ablation (laser cleaning). However, when tested in the very high electric fields of a RF gun, the sputtered Mg films have been quickly degraded by RF discharges at the boundary.

This is attributed to bad quality of the film, especially regarding uniformity and adhesion. A key parameter determining the quality of a deposited film is the kinetic energy of the particles impinging on the substrate. Therefore we decided to study alternative deposition processes with inherent higher particle energies, as pulsed laser deposition (PLD) [5].

EXPERIMENTAL CONDITIONS

The sputtering technique is well known, so we will summarize only the PLD method that is less familiar. The PLD deposition method apparatus consists of an UHV chamber containing the Mg target to be ablated and the substrate to be coated. A powerful pulsed laser beam from a XeCl excimer laser (wavelength = 308 nm, pulse duration = 30 ns), injected through a quartz window, impinges on the target and forms a plume of Mg vapour. The substrate is placed in the plume cone at a suitable distance from the target (Fig. 1). More details are reported in [6].

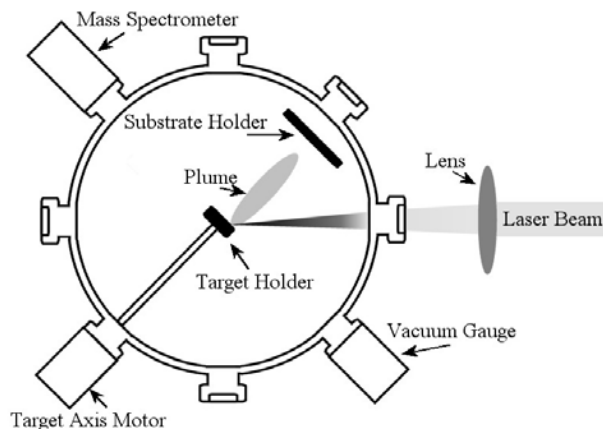


Figure 1: Sketch of the PLD apparatus

The main advantages of the PLD method, compared with the magnetron sputtering process, are the absence of gases to sustain the discharge and the high kinetic energy of the evaporated material particles reaching the substrate surface. The kinetic energy distribution depends on various parameters, principally the laser fluence. With our experimental conditions, one may estimate an average of 50 eV to be compared with 10 eV in magnetron sputtering. The high kinetic energy favours the adhesion of the coating material to the substrate. Droplets of material may form on the coated surface during deposition, unless particular masks and geometries are employed. Sputtered films can be grown to large thickness (20 microns), while PLD films are limited to less than two microns.

The QE measurement and laser cleaning apparatus consists of a test HV chamber, at 10^{-6} Pa background pressure, containing a vacuum diode of which the film to be tested constitutes the cathode. An UV 266 nm laser pulse, 30 ps duration, from a mode-locked frequency quadrupled Nd:Yag laser, is injected through a quartz window and excites the cathode. Accelerating electric fields up to 1 MV/m can be applied to the diode. The laser beam crosses the anode through a fine copper wire mesh and illuminates the cathode at normal incidence. The emitted charge is sent via a coaxial cable to the input of a high speed oscilloscope or to a high sensitivity charge amplifier. The measuring apparatus is similar to the one described in more detail in [7]. The laser cleaning is performed by focusing the beam to a 300 micron diameter and scanning it across the emitting area (2 mm diameter) by means of a movable mirror placed on a gimbal mount driven by motors.

SAMPLE PREPARATION AND MEASUREMENTS

Sputtered films.

We have acquired sputtered films from the same industry cited in the literature [3] to establish a term of comparison of our results with those reported there. The tested films were 10 microns thick and were shipped to us in pressurized envelopes under Nitrogen. We have measured them as received, without any polishing. It was easy to remove the thin layer of oxides and other compounds that had formed on the surface. However, the maximum QE we measured (10^{-4}) was an order of magnitude lower than that reported in [4]. This value, measured at low electric field, is a lower limit and can be improved. It is anyway satisfactory because the Cu cathodes commonly used can hardly reach this value with very special treatments. The structure of the films, analysed with an AF microscope, was crystalline with well-ordered columnar structure. Resistance to laser radiation was high. After bombardment with about 10^4 shots at $500 \mu\text{J}/\text{mm}^2$ laser energy density, the ablated depth was less than 1 micron.

A large film thickness consents a deeper cleaning ablation. This is important because the cleaning must be repeated periodically to re-activate the cathode, even in the RF gun UHV operating conditions

PLD films.

We have produced two sets of films. The first consisted of thin films, about 200 nm thick, covered with a 20 nm of magnesium oxide layer. The protective layer was grown by ablating the Mg target at 20 Pa oxygen atmosphere. The parameters of the deposition are listed in Table 1. The removal of the protective oxide layer is performed by scanning a focused (300 μm diameter) laser beam over the emitting spot (2 mm diameter), with an energy density of about $300 \mu\text{J}/\text{mm}^2$.

Table 1: Thin PLD films deposition parameters

Sample	1	2
Target	Mg	Mg
Substrate	Cu	Cu
Target-substrate distance	6 cm	6 cm
Laser spot size	1.2 mm ²	1.2 mm ²
Base pressure	5×10^{-6} Pa	5×10^{-6} Pa
Laser pulses		
Cleaning	2000	2000
Deposition	10000	10000
Covering	2000	2000
Laser Fluence	5 J/cm ²	9 J/cm ²
QE	2.5×10^{-6}	5×10^{-6}

After activation, the laser beam diameter is enlarged to cover the emitting spot and its energy is strongly decreased to perform the QE measurement. Before activation, the response curve of charge versus laser energy is quadratic, due to the oxide layer. After its ablation the curve becomes linear, indicating a one-photon emission process. The low thickness of the films favours punch through during laser cleaning. The maximum QE achieved with thin films was 5×10^{-6} , very low. This poor performance was attributed to oxidation of the film in depth during the covering process. To avoid this drawback it was decided to deposit thicker films, about one micron, and to cover them with a thin layer of graphite, thus avoiding oxidation. One of the advantages of the PLD technique is the possibility of depositing different materials in succession in the same deposition session, by using composite targets. In our case, the target was Mg-C, with a Mg belt surrounding a Graphite core. The laser beam was shifted in succession from one zone to the other. The deposition parameters of two of these samples are shown in Table 2.

Table 2: Thick PLD films deposition parameters

Sample	3	4
Target	Mg-C	Mg-C
Substrate	Cu	Cu
Target-substrate distance	4.5 cm	4.5 cm
Laser spot size	0.9 mm ²	0.9 mm ²
Base pressure	5 x 10 ⁻⁶ Pa	5 x 10 ⁻⁶ Pa
Laser pulses		
Cleaning Mg	5000	5000
Deposition Mg	30000	30000
Cleaning C	1000	2000
Deposition C	2000	3000
Laser Fluence	6 J/cm ²	10 J/cm ²
QE	5x10 ⁻⁵	3x10 ⁻⁴

The structure and morphology of the films analysed with AFM and SEM, turns out to be a conglomerate of amorphous lumps of material, with interstices. The uniformity and compactness of the film depend on the laser fluence. The analysis of the composition distribution on the film surface by EDX indicates that the graphite was not completely removed by the laser cleaning, probably due to its filling the interstices.

The highest QE of these thick films, measured after laser cleaning, was 3 x 10⁻⁴, quite satisfactory. It is connected with a large value of laser fluence. Therefore the direction of development is toward larger thickness and higher fluence.

THE EFFECTIVE CATHODE

The study of film deposition on the central zone of the 10 cm diameter Cu end flange of an S-band RF gun, to form the effective cathode, is in course. Deposition by sputtering requires a mask to select the zone to be coated. It is straightforward and has already been implemented elsewhere [8].

Deposition of PLD films on such a large plate poses harder problems because the ablating laser beam has to

impinge on the target nearly flush with its surface, at a very large angle with respect to the plume direction. This configuration needs development.

CONCLUSIONS AND OUTLOOK

The described tests and previous experience by others suggest that Mg films produced by sputtering or PLD are good candidates for high QE metallic photocathodes that can work in moderate vacuum.

Sputtered films can be grown to large thickness, have good uniformity and are very resistant to laser radiation. The proposed further development effort is to improve the adhesion to the substrate.

PLD films promise better adhesion but, at the actual stage of our experience, their structure is still irregular and the film surface is too easily and unevenly ablated by the cleaning laser beam. Further research is planned to find the right deposition parameters to achieve thicker, more compact and harder PLD films. We have found that a protective thin layer of graphite allows easy handling and conservation of the cathodes before installation in the RF gun.

Our final goal is to implement an effective cathode and test it in the very high fields of a RF gun.

REFERENCES

- [1] Technical Design Report for the SPARC Advanced Photoinjector.
<http://www.lnf.infn.it/acceleratori/sparc/>
- [2] X. J. Wang, M. Babzien, R. Malone, Z. Wu, LINAC 2002 Conference (2002).
- [3] D. T. Palmer, Ph.D. thesis, Stanford University, Dpt of Applied Physics, 1998.
- [4] T. Srinivasan-Rao, J. Schill, I. Ben Zvi, M. Woodle, Rev. Sci. Instrum., Vol 69, No 6, June 1998, 2292-96.
- [5] Pulsed laser deposition of thin films, Ed. D.B. Chrisey, Wiley, New York, 1994.
- [6] L.Cultrera et al., accepted by Applied Surface Science.
- [7] I. Boscolo et al., J. Appl. Phys., Vol 87, NO. 8, April 2000, 4005-4006.
- [8] X.J. Wang, IX Linac Conference, Chicago 1998, 866.

THE SPARC RF SYNCHRONIZATION SYSTEM

Alessandro Gallo, David Alesini, Marco Bellaveglia, Roberto Boni, Giampiero Di Pirro, Franco Tazzioli (INFN/LNF, Frascati (Roma))

Abstract

The SPARC project [1] consists in a 150MeV Linac aimed at driving an undulator for the production of 530nm SASE FEL radiation. A bunch transverse emittance as low as 1mm mrad and a bunch peak current of about 100A are required for this task. The RF voltages in the RF gun and in the 3 S-band accelerating sections have to be kept phase locked within 3ps to the arrival time of the laser pulse on the photocathode to guarantee the required performances. This specification will be reduced to 0.5ps in the phase II of the project when the rectilinear RF compression of the bunch will be tested. The general architecture of the SPARC RF control system together with some benchmark measurements of the basic components is presented in this paper.

RF SYSTEM BASIC ARCHITECTURE

Precise synchronization among the RF accelerating voltages (SW in the RF Gun and TW in the 3 S-band SLAC-type sections), and between these voltages and the laser pulse on the gun photocathode is very important to reach the SPARC design emittance goal in a stable, routine operation. In SPARC phase II, where the RF compression of the bunch will be tested, the laser pulse needs to be locked to the RF voltages within $\sigma_t = 0.5\text{ps}_{rms}$. The accelerating voltages need to be kept synchronized each other within an even lower figure.

The basic RF layout including the amplitude and phase control architecture is shown in Fig. 1. The RF power will be generated by two 45MW , $4.5\mu\text{s}$ pulsed klystrons. One klystron powers the RF gun, the 3^{rd} accelerating section and the RF deflector, while the other is connected through a SLED pulse compression system to the 1^{st} and 2^{nd} accelerating sections. By playing with the klystron low-level RF and with some waveguide attenuators/phase shifters placed in the various branches, it is possible to individually control the level and the phase of all the RF accelerating voltages. In order to do that, the amplitudes and phases of RF voltage samples have to be measured and recorded at each pulse, and feedback algorithms have to be implemented to correct pulse-to-pulse drifts.

About 20 pulsed RF signals, with various pulse envelope profiles, have to be demodulated to monitor their phase and amplitude. In fact, the pulses produced by the klystrons as those entering and leaving the section S_3 are almost flat in the 4.5ps duration, while those related to the SW cavities (the RF gun and the RF deflector) and those produced by the SLED system present a relevant internal structure.

The way we are proposing to handle these different kinds

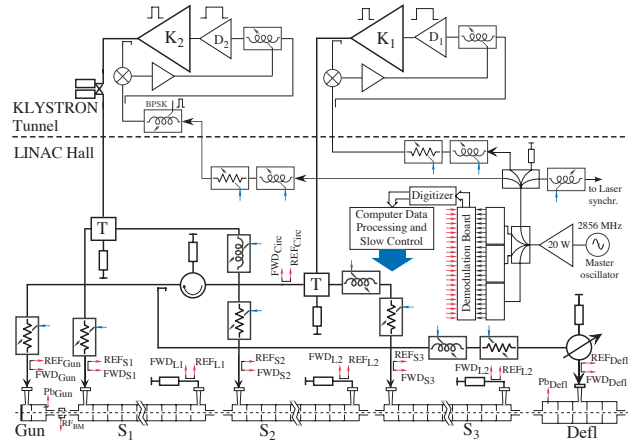


Figure 1: SPARC RF system layout

of RF pulses is to use linear I&Q demodulators followed by digitizer boards integrated in an industrial PC, as shown in Fig. 2. The LO reference signals provided to the demodulators are just amplified copies of the master oscillator. To avoid individual jitter of the various LO signals, the master oscillator is amplified just once to a medium-power level ($\approx 20\text{W CW}$) and then passively split into many copies each taken as reference for one demodulation channel. By doing that the low-level RF control is virtually completely passive, and the only expected phase jitter related to RF amplification is that coming from the klystrons and their driving stages.

The phase lock between the laser pulse and the RF reference is one of the most delicate synchronization items. The laser shot synchronization to the master RF reference will be monitored and pulse to pulse drifts will be automatically corrected.

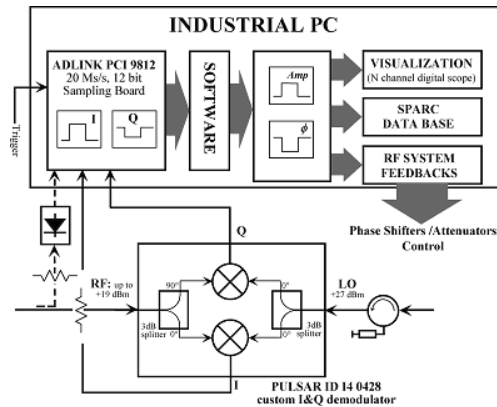


Figure 2: Demodulation channel

PULSED RF SIGNAL DEMODULATION

The amplitude and phase of each pulsed RF signal in SPARC are detected by a demodulation channel sketched in Fig. 2. The I&Q demodulator is a custom device provided by Pulsar μ -wave inc. (I4 0428TM model) under our specifications. The internal mixers are rated for a LO level as large as $+27\text{dBm CW}$, so that RF signals up to $+19\text{ dBm}$ level can be linearly demodulated. The SPARC RF signals will be directly mixed down to baseband generating I&Q signals up to the level of 1V ($\simeq +10\text{dBm}$).

The I&Q signals are then sampled at a 20Ms/s rate and 12-bit digitalized by means of a the ADLINK PCI 9812TM board. Each pulse, which is about $4.5\mu\text{s}$ long, is converted into 90 I&Q samples. These data are numerically converted in amplitude and phase of the RF in the pulse by applying some simple algebra. A typical measured phase detection characteristics from I&Q signals obtained with a Pulsar I4 0428TM powered at $LO = +27\text{dBm}$ and $RF = +16\text{dBm}$ is shown in Fig. 3.

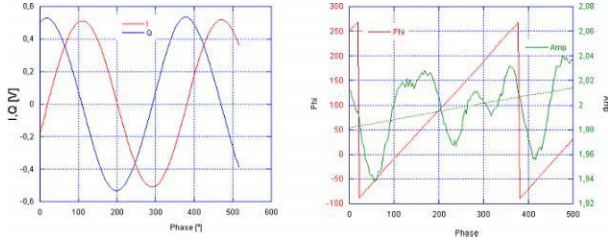


Figure 3: I&Q voltages and phase detection curve

The phase resolution of the demodulation channel has been measured on the bench. The phase of an RF pulse having the SPARC time structure ($4.5\mu\text{s}$ duration, 10Hz rep. rate) has been acquired and recorded for a large number (10^4) pulses. The phase value associated to each pulse has been obtained by averaging over the 90 I&Q samples contained in the pulse. A typical statistical distribution of the record is reported in the histogram of Fig. 4.

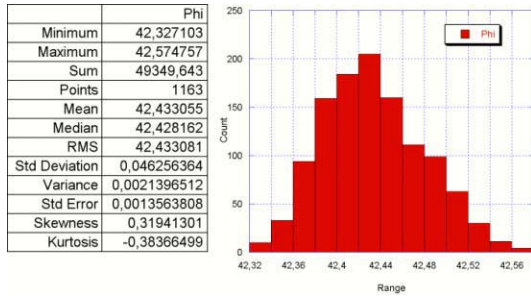


Figure 4: Pulse-to-pulse phase measurement distribution

The standard deviation of the displayed record is $\sigma_{\text{phase}} = 0.046^\circ @ f = 2856\text{MHz}$, which corresponds to a measured temporal resolution of $\simeq 45\text{fs}$. This value already meets the SPARC synchronization system requirements, and it may be further improved since it has been

obtained with a 10-bits digitizer board (instead of the 12-bits one foreseen for this task) and at a $+10\text{dBm}$ RF pulse level, a value that does not fully benefit the I&Q mixer dynamic range.

LASER-RF SYSTEM SYNCHRONIZATION

The stability of the synchronization between the laser pulse and the RF reference is crucial task. The laser system will be synchro-locked to a RF/36 signal (79.33MHz) generated in the SPARC timing system. The time jitter of the Tnal UV laser shot respect to the RF synchro-lock has been specified by the laser system manufacturer to be $\sigma_{t_{\text{laser}}} \leq 500\text{fs}_{\text{rms}}$.

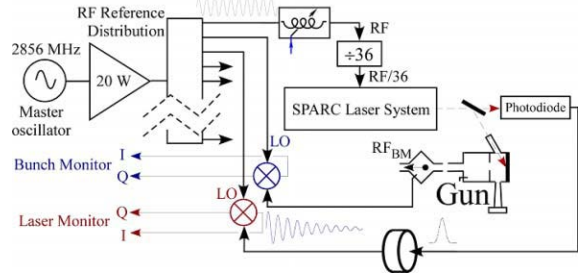


Figure 5: Laser pulse synchronization monitoring

Pulse-to-pulse phase drifts of the laser-to-RF lock have to be measured and corrected by a dedicated feedback algorithm. In order to measure the stability of the synchronism between the laser shot and the RF reference line, we are proposing the scheme reported in Fig. 5. The laser shot is converted in a long lasting RF exponential pulse generated by a RF cavity tuned at 2856MHz excited with a short pulse from a fast photodiode illuminated with a sample of the laser pulse. The RF phase of the exponentially decaying pulse with respect to the RF reference signal is measured again by means of an I&Q mixer. The same phase measurement will be performed on the bunch released by the RF gun. In this case the exponential pulse will be produced by a 2856MHz "bunch monitor" cavity placed between the RF gun and the accelerating section S_1 excited directly by the bunch.

This approach to the phase measurement of pulses whose duration is much shorter than the RF period has been tested on the bench. The measurement layout is sketched in Fig. 6. Short pulses are obtained by exciting a step recovery diode at the 28^{th} sub-harmonics (102MHz) of the linac RF frequency. The repetition rate of the pulses is reduced from 102MHz to 100kHz by gating the pulse train through a fast RF switch. The pulse train emerging from the RF switch is filtered by a 2856MHz cavity that convert it in a series of a RF pulses with exponential profiles and decay time of about 500ns each. The exponential pulses are amplified and demodulated with an I&Q mixer driven with a LO reference signal obtained extracting the 28^{th} harmonics from the original 102MHz pulse train by means of a PLL circuit.

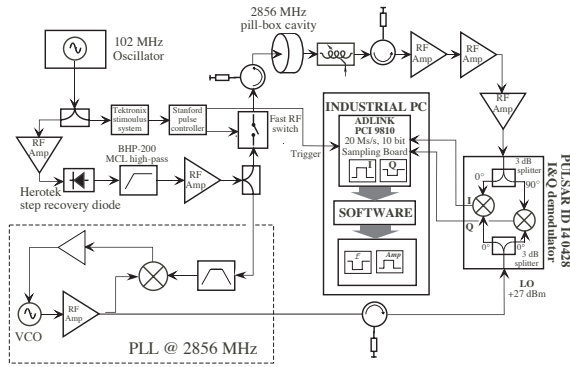


Figure 6: Short pulse synchronization bench measurement

The spectral content at 2856MHz of the 100kHz short pulses train is quite low, so it is necessary to put many RF amplification stages along the path to the demodulator input to restore a suitable level of the signal. This should not be necessary in the final layout of Fig. 5 since higher levels of the signals to be monitored are expected. Typical I&Q signals acquired for a single short pulse with this set-up and the extrapolated amplitude and phase are reported in Fig. 7. A statistical distribution of the pulse phase values over a record of 10^5 pulses is reported in Fig. 8. The measured standard deviation of the distribution is 0.63° . The resolution obtained with this set-up is reasonably good and we believe that it may be improved in the final set-up where less RF amplification will be needed and 14-bit, 65Ms/s sampling boards (ADLINK PCI 9820TM) will be used. Other methods for measuring the synchronization stability of short pulses based on triggered oscillators phase measurement are presently under study by the Sincrotrone Trieste group [2].

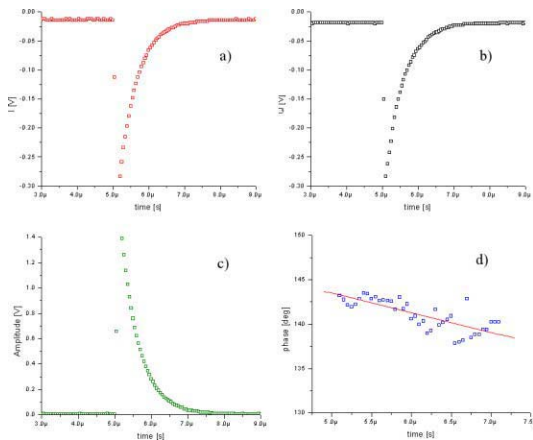


Figure 7: Typical I&Q signals acquired for a single short pulse (a, b) and extrapolated amplitude (c) and phase (d)

FEEDBACK SYSTEMS

The information on the RF phase of each monitored signal will be used to correct the measured deviations by

means of dedicated feedback loops. However, as a consequence of the Nyquist theorem and being the pulse repetition rate of the linac 10Hz , the phase noise in the system can only be corrected in a frequency band below 5Hz . Only thermal drifts are within this band, while noise generated by mechanical vibrations (microphonic noise), power supply ripple and electronic interferences can not be corrected in this way and have to be limited as much as possible at the system design stage.

Concerning the phase noise introduced by the RF power stations we are studying the possibility of implementing an intra-pulse phase lock feedback around them. Being the station group delay of the order of 150ns (mainly due to the klystron frequency response) a feedback loop with 1MHz bandwidth, capable to get to regime in $1\mu\text{s}$, is in principle doable. In this way the noise introduced by the RF power stations could be corrected inside each pulse and in a wide bandwidth. A model of this system has been tested on the bench, easily reaching the expected performances. The system will be tested on the SPARC RF power stations after their installation before the end of this year.

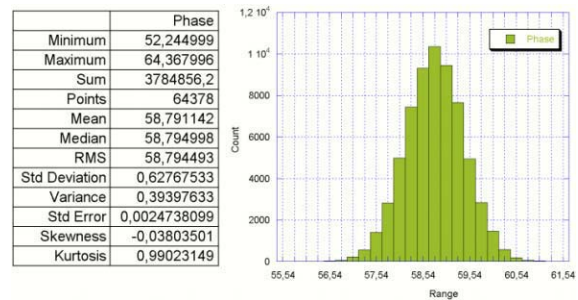


Figure 8: Distribution of short-pulse phase measurements

CONCLUSIONS

The quality of the SPARC RF control is crucial to reach the goal of the project in terms of low emittance and high brilliance of the bunch.

The system has been completely designed and is going to be assembled since all the needed components have been acquired. The resolution of the demodulation channel has been measured on the bench and it is $\approx 50\text{fs}$. A possible layout for measuring the stability of the synchronization of short pulses respect to the reference RF has been bench tested with a measured resolution of $\approx 600\text{fs}$. The system hardware will be improved to reach a finer resolution.

The whole SPARC RF low level control system will be completed and installed by the end of this year.

REFERENCES

- [1] M. Ferrario et al., “Status of the SPARC project”, EPAC 2004 Proceedings, Lucern (Switzerland), pag. 399, ISBN: 92-9083-231-2
- [2] M. Ferianis, private communication

KLYSTRON LINEARIZER FOR USE WITH 1.2 MW 476 MHZ KLYSTRONS IN PEP-II RF SYSTEMS*

J. Fox**, T. Mastorides, D. Teytelman, D. Van Winkle, Y. Zhou
Stanford Linear Accelerator Center, Menlo Park, CA 94025, U.S.A

A. Gallo, LNF-INFN, Frascati, Italy

Abstract

The direct and comb loop feedback around the RF cavities in PEP-II is critical in reducing longitudinal instabilities driven by the cavity impedance. The non-linear 1.2 MW klystron is in the signal path for these feedback loops. As a result, the effective small-signal gain of the klystron at 85% saturation reduces the impedance control by factors of 5 to 20 as compared to a linear power amplifier. A klystron linearizer circuit has been developed which operates in series with the power amplifier and acts to equalize the small and large signal gains through the combination. The technique must implement a 1 MHz linear control bandwidth over roughly 15 dB of RF signal level variation. The dynamics of this system is operating point dependent, and the channel must have dynamic gain compensation to keep the linearity compensation loop stable over changes in operating point. The design of this non-linear signal processing channel (incorporating RF and DSP techniques) and measured results from full-power klystron testing are presented.

INTRODUCTION

The low level RF systems in PEP-II use direct and comb loop feedback techniques to reduce the driving impedance from the cavity fundamental impedance [1]. These techniques use the 1.2 MW high power klystron as a signal element in a feedback path. The high power klystron has a saturating input/output characteristic as the drive power is increased towards maximum output power at a given high voltage power supply voltage. As a result, the large signal gain of the klystron (P_{out}/P_{in}) is significantly different from the small signal gain (dP_{out}/dP_{in}) - for a typical operating point the small signal gain is reduced by factors of 5 to 20. The direct/comb loop impedance control effectiveness is reduced due to this saturation effect (the cavity impedance is reduced by $1/\text{small signal gain}$), so that instability growth rates due to the cavity impedance can be much greater than can be readily controlled via the longitudinal and low group delay woofer instability control systems [2,3].

We have developed a klystron linearizer function which acts in series with the klystron, so that the series product of the two has a constant (linear) small signal gain over variations in klystron output level. The heart of this

technique is an amplitude sensing feedback network, sampling the klystron input and klystron output, and adjusting an RF drive level modulator to keep the ratio of the two signals through the klystron path a constant. Such an amplitude linearizing loop is not a new idea [4], and in recent years related linearizer techniques have become important for communications amplifiers[5]. The application of this technique to the LLRF systems and instability control was initially suggested by Alessandro Gallo. Our implementation (Figure 1) only corrects the klystron amplitude or magnitude non-linearity - any phase nonlinearity vs. operating level is not corrected with this technique. However in our application is it amplitude modulation which must be transferred through the klystron by the direct/comb loops to suppress phase modulation of the beam[6,1], and so this simpler amplitude only control loop was developed.

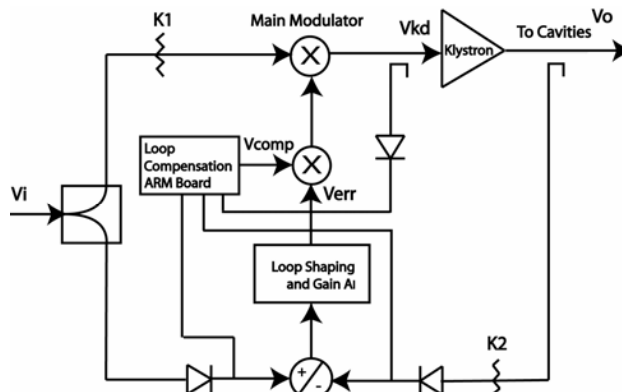


Figure 1: Loop implementation.

IMPLEMENTATION

Table 1 lists the important specifications for the circuit.

Table 1: Linearizer specifications

Center frequency	476 MHz
Amplitude linearity correction range	15 dB
Closed loop bandwidth	1 MHz
Compensation loop bandwidth	10 Hz
Noise Floor—additive below carrier	<-40 dB

The circuits are implemented in a mix of RF and baseband electronics. Figure 1 shows the drive path to the high power klystron, with a wideband RF modulator (Analog Devices 834) as the gain controlling element. A fraction of the LLRF V_i signal is coupled to a diode detector to measure forward power, similar diodes are

* Work supported by U.S. Department of Energy contract DE-AC02-76SF00515

** jdfx@slac.stanford.edu

used with a directional coupler and attenuators in the high power klystron drive and output. The Vi and klystron output signals are processed via baseband amplifiers, and a high gain summing node and error amplifier are used to generate the error signal controlling the RF modulator.

The basic topology is straightforward; however there are several important design considerations. As the action of the linearizer is to boost the level of modulation signals, the linearizer operating point must be carefully matched against the klystron saturation curve - if the modulation levels drive the klystron to saturation (the inflection point in the power out curve) the sign of the linearizer loop gain inverts, and the positive feedback pushes the loop “over the top”, causing the power output of the klystron to decrease. Starting the RF station, with LLRF signals but no klystron HV, causes this condition and the linearizer must have special circuits and software to recognize this situation. Another issue is the loop gain of the feedback path is a function of the system input level. Figure 2 shows the variation in closed loop bandwidth vs. +/- 1dB variation in input level. For the required 13 dB operating range the linearizer loop gain must be compensated to avoid peaking or loop instability. Referring to figure 1, the loop gain is:

$$T_L = \frac{V_i^2}{V_{kd}} V_{comp} K_1 A_i \quad (1)$$

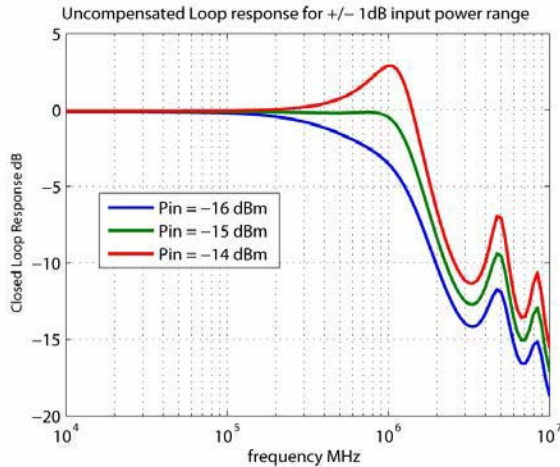


Figure 2: loop bandwidth vs. input level.

The closed loop response of the linearizer loop must be well-damped, and it is important to have nearly 1 MHz bandwidth in the loop to achieve good impedance control over the full direct loop bandwidth. To compensate the loop gain variation, a second wideband modulator in the feedback control loop adjusts the loop gain at different system input levels, as shown in figure 1. The compensation voltage is set to be (where k_c is a scaling constant, and V_{kd} is the klystron drive level):

$$V_{comp} = \frac{k_c V_{kd}}{V_i^2} \quad (2)$$

Our initial implementations used an analog technique to implement the $1/x^2$ function - the linearizer prototype uses a digital microcontroller (ADUC7020), which measures the input drive level and klystron drive levels via the diode detectors, and digitally computes a correction voltage to be applied to the modulator controlling the feedback loop gain. This digital process samples at 1 KHz rate and allows the loop gain to track the slow variations in klystron operating point. The digital controller coefficients and operating software allow flexibility in choosing compensation loop bandwidth. The digital controller software also allows the development of monitoring and fault recording functions to study the linearizer in operation.

The linearizer is designed to correct the compression of the klystron small signal gain, and it must do so over the operating range of the high power klystron. While the power required from the klystron varies with beam current over a 100kW to 1.2 MW range, the actual operating point variation of the klystron drive signal is relatively small, as the design of the LLRF regulating loops adjust the klystron high voltage supply to keep the klystron input drive level at a regulated operating point. With this input level regulated, the linearizer then only must correct for the small signal gain variation due to saturation effects, which determines the 13 - 15 dB dynamic range of the linearizer.

These initial linearizers are being developed to demonstrate the feasibility of the technique and to understand via beam measurements the necessary linearizer performance. As it is not possible to easily quantify the contribution of the linearizer if only 1 of four accelerator klystrons is linearized, we constructed 5 complete prototype linearizers, with the intent to operate 4 in the PEP-II LER (with 1 for high power klystron test stand operation). These prototype units have complete RF functionality, though the external remote control interface is minimal, and configuration of the linearizer largely determined via front panel hardware settings. The front panel allows adjustment of the operating points (reference and feedback path gains) and a signal loop tool feature allows the in-situ measurement of the linearizer loop gain necessary to adjust the $1/x^2$ compensation. An external monitor module is used to bring out internal signals as well as send logic signals indicating incorrect operating points of the internal loops and limiter functions.

LINEARIZER TESTING

Testing such a non-linear circuit function requires some special care. Initial testing and development of the linearizer technique used a klystron model circuit (a low power non-linear circuit which mimicked the RF saturation and amplitude non-linearity of the high power system). High power tests were also performed on a klystron test stand, where the full power behavior of the linearizer and klystron combination could be exercised.

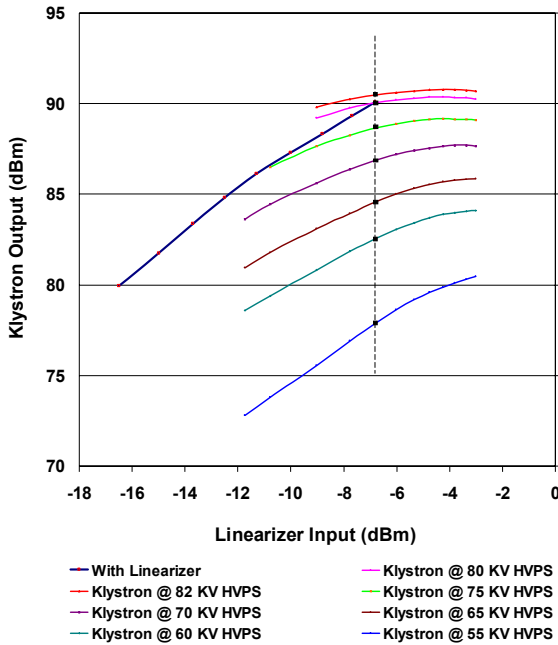


Figure 3: Klystron power output vs. linearizer input (DC power sweep) showing linearized small signal gain as well as saturated klystron transfer functions. 90 dBm is 1 MW.

Figure 3 shows a full-power amplitude sweep of the linearizer-klystron combination on the test stand with the family of unmodified klystron input-output characteristics for the HV supply range of 55 – 82 KV. The klystron drive level is held constant at 44 dBm over the power sweep via the HV supply regulation. The linearizer action is clearly seen in the linearized klystron output, as is the compression of the klystron, especially at the high output powers.

It is also important to study the dynamic behavior of the linearizer. One useful test is to study the response to an amplitude modulated carrier. The carrier to sideband ratio should remain constant in a linear amplifier. Observing the linearizer output (the compensated klystron signal from the linearizer) shows the increased levels of the sidebands, (as well as harmonics of the modulation) which are then compressed in the klystron.

Table 2: Carrier/Sideband Ratios at different modulation depths for 476 MHz carrier, 10 KHz modulation.

Carrier/Sideband Ratios	2.6% AM	10% AM
Input Signal	-37.7 dB	-25.9 dB
Linearizer Output (to Klystron)	-31.6 dB	-20.1 dB
Klystron Output	-39.0 dB	-27.1 dB
Raw Klystron (no linearizer)	-44.6 dB	-32.2 dB

Table 2 shows the carrier/sideband ratio at various points in the processing chain for 2.6% and 10% modulation. The un-linearized output shows compression of the 2.6% small-signal modulation by -7 dB, while the

linearized klystron output spectrum shows the original carrier/sideband ratio is restored to within -1.3 dB. This residual error is due to the finite gain of the control loop.

SUMMARY AND FUTURE DIRECTIONS

At the time of the PAC conference 4 linearizer units are installed in the LER and we are anticipating initial beam testing in late spring 2005. A preliminary test with a single linearizer in summer 2004 showed a measurable growth rate reduction[7], but more careful configuration of the linearizer operating point, and linearization of all klystrons in the LER, is required for quantitative measurements of the growth rates. This information is important in predicting the operation of the LLRF and broadband longitudinal feedback for upgraded operating currents and additional RF cavities[8]. We are particularly interested in understanding the depth of small-signal modulation present in the operating machine over variations in current, injection, transient disturbances, etc. which will determine the practical limits of this technique.

ACKNOWLEDGEMENTS

The authors thank the ARDA and Accelerator departments for funding this initial prototype technology effort.

REFERENCES

- [1] F. Pedersen, “RF Cavity Feedback”, B Factories, The State of the Art in Accelerators, Detectors and Physics, SLAC-400, pp. 192 - 207
- [2] D. Teytelman, L. Beckman, D. Van Winkle, J. Fox, A. Young (SLAC), “Development and Testing of a Low Group-delay Woofer Channel For PEP-II”, EPAC-2004- THPLT155, SLAC-PUB-10559, Jul 2004.
- [3] J. Fox, et al, “Programmable DSP based Multi-Bunch Feedback: Operational Experience from Six Installations” Proc. Beam Inst. Workshop, Cambridge MA 2000
- [4] F. E. Terman, R. R. Russ, “Some Notes on Linear and Grid-Modulated Radio Frequency Amplifiers”, Proc. IRE, 1941, Vol . 29, pp 104-107.
- [5] Ultra RF Application Notes , “An Overview of Linear Amplifier Systems”, <http://www.cree.com/ftp/pub/appnote1.pdf>
- [6] D. Teytelman, “PEP-II Low-level RF tutorial”, presented SLAC 6-7 August 2003
- [7] D. Teytelman, “Klystron linearizer test results”, PEP-II group meeting, 24 June 2004
- [8] J. Seeman, et al, “Design for a 10^{16} Super-B-Factory at PEP-II”, EPAC2004-MOPLT143, SLAC PUB 10548, Jul 2004.

PHASE-SPACE DYNAMIC TRACKING BY A TWO PICKUPS DATA ACQUISITION SYSTEM

Alessandro Drago, Maria Enrica Biagini, Susanna Guiducci, Catia Milardi, Miro Preger, Cristina Vaccarezza, Mikhail Zobov (INFN / LNF, Frascati, Italy)

Abstract

A two pickups dynamic tracking data acquisition system has been developed at LNF for the DAΦNE Phi-factory. Two oscilloscopes sample horizontal and vertical sum and difference signals from two pickups simultaneously; the sampling clock is locked to the DAΦNE timing system. A horizontal kick excites the beam motion and initiates the acquisition. Turn-by-turn signals are converted to beam position and stored on a server in a database using timestamp labels. Oscillation amplitude versus time, phase space distribution and frequency domain analysis have been evaluated for several lattices and different settings of sextupoles and octupoles. Results are used to check the DAΦNE non-linear model.

INTRODUCTION

DAΦNE, the Frascati Φ-Factory [1], is in operation since 1999. It produces e^+/e^- collisions at 1.02 GeV c.m. energy, for three experiments: KLOE (kaon physics), FINUDA (nuclear physics) and DEAR (atomic physics), running one at a time. Non-linearities in the magnetic structures have been identified in sextupoles and wigglers.

A non-linear model [2] has been developed and a single BPM dynamic tracking acquisition system has been developed [3] to check it by recording turn-to-turn beam position. Recently this system has been upgraded to collect simultaneous signals from two beam position monitors in order to deliver the phase-space shape of the beam centroid motion.

The hardware and software schemes are described in the following section and examples of collected measurements are presented.

SYSTEM DESCRIPTION

The hardware scheme is plotted in Fig. 1. To study the phase-space behavior of the beam, a low current single bunch is stored in the main ring.

An oscillation of the bunch is excited by pulsing the injection (horizontal) kicker, and, at the same time, data acquisition is initiated. The system has 8 input channels collecting transverse difference and sum signals from two beam position monitors. Two oscilloscopes acquire these signals by sampling clocks delivered by the DAΦNE Timing system [4] and synchronized before the measurements by means of a phase shifter module with two independent manual knobs.

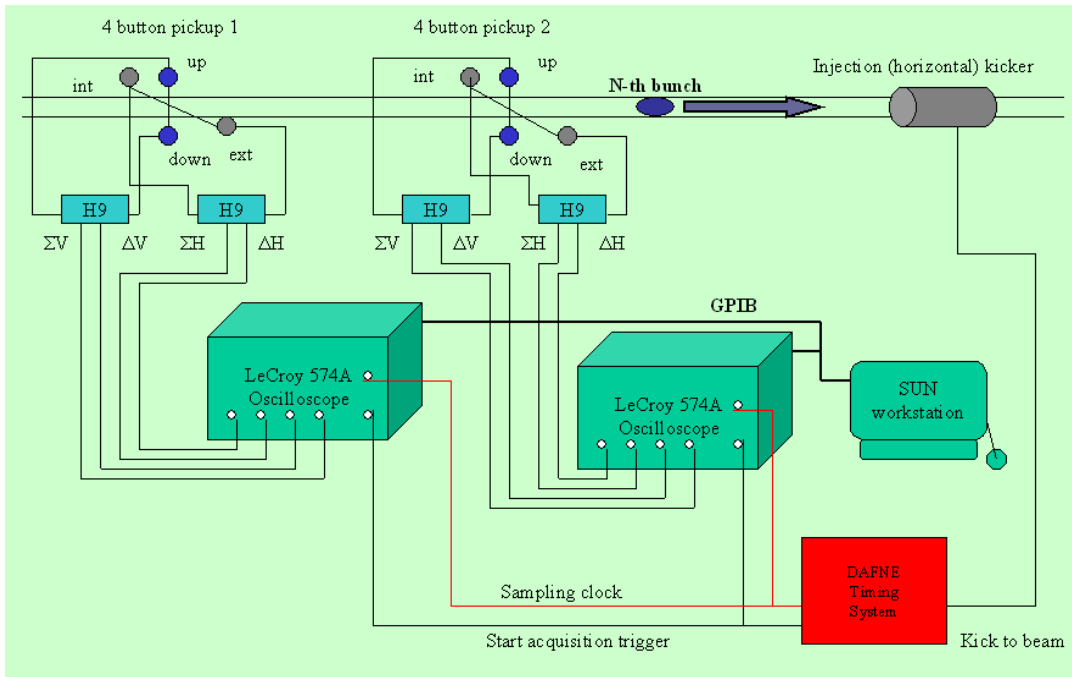


Fig. 1: Scheme of the setup used to record data from two beam position monitor: the beam is kicked by the injection kicker in the horizontal plane.

The use of oscilloscopes instead of a multichannel sampler makes it easier to check if the timing is correct and if the transients are well acquired. However, there is an uncertainty of one turn on the alignment between data from the first oscilloscope and the second one, which have to be fixed offline by the user by the means of the software tools.

A SUN workstation downloads through an IEEE-488 bus the data from the oscilloscopes and several LABVIEW programs allow data storage and off-line analysis. Fig. 2 shows a directory tree ordering the files by particle type (e^+ or e^-) date and time. Data in the files are in ASCII to be easily read by user programs or spreadsheets.

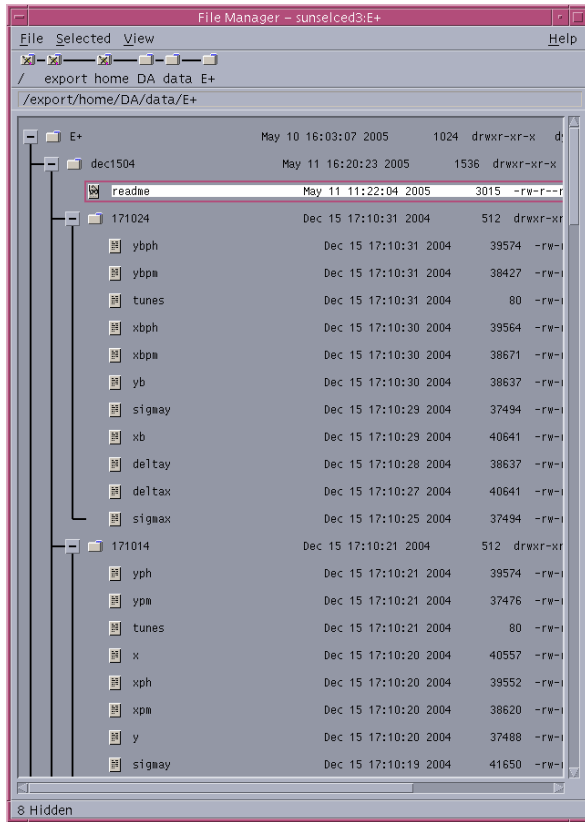


Figure 2: Directory tree and files stored by the data acquisition system.

The date folder contains a readme file, where the operator writes the relevant machine conditions, as well as beam current and kick amplitude. The date folder contains also the time folders with the measurement files describing the oscillation of the beam centroid. The files called sigmax, deltax, sigmay, deltay are rough data taken from the scopes in Volts. The files called x and y contain the calibrated horizontal and vertical displacements (in mm) from the first BPM. Those called xb and yb are the same from the second one; xph, yph, xbpn and ybpn contain the corresponding Hilbert transforms of x, y, xb and yb.

The two BPMs are rather close to each other in the ring. The betatron phase advance between them is ≈ 26 degrees in both planes and the magnetic structure between the first BPM (BPBES108) and the second one (BPBES202) consists in two quadrupoles and three drift space without any non linear component. Therefore the betatron transfer matrix between the two BPMs is straightforward, and one can obtain the phase space trajectories at both monitors from the recorded beam positions at each turn.

Denoting by M the transfer matrix between the two BPMs, X_1 the transverse position of the beam at the first monitor, X'_1 its angle with respect to the ideal trajectory (a straight line between the two monitors), X_2 and X'_2 the corresponding quantities at the second monitor, we can write:

$$\begin{aligned} X_2 &= M_{11}X_1 + M_{12}X'_1 \\ X'_2 &= M_{21}X_1 + M_{22}X'_1 \end{aligned}$$

from which we find the two angles corresponding to the two beam positions at each turn and therefore reconstruct the phase space trajectories at each monitor.

$$\begin{aligned} X'_1 &= \frac{X_2 - M_{11}X_1}{M_{12}} \\ X'_2 &= \frac{(M_{12}M_{21} - M_{11}M_{22})X_1 + M_{22}X_2}{M_{12}} \end{aligned}$$

Fig.3 and Fig.4 show the phase trajectories of the beam at the two monitors. The dots are beam position and angle at each one of the first 50 revolutions after the kick, the line is the best ellipse fitting the measured data. Values of the optical functions at the monitor azimuth in the ring are derived from the fitting ellipse parameters.

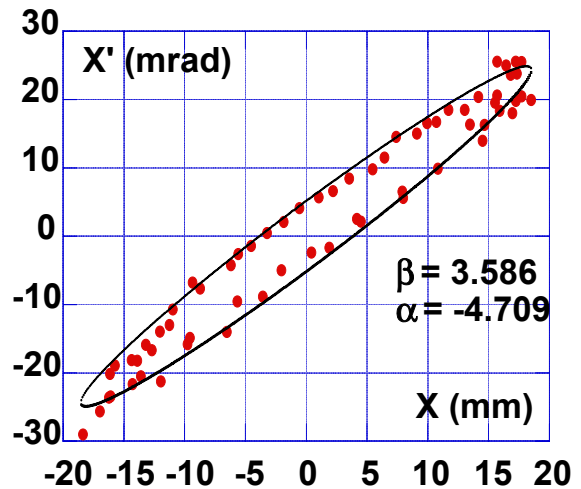


Figure 3: First 50 turns phase-space tracking after a kick at BPBES108.

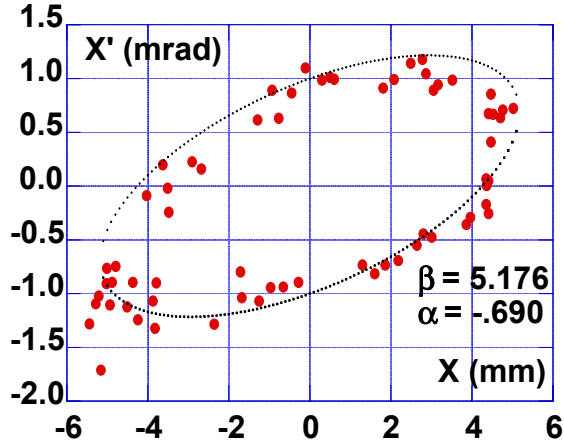


Figure 4: First 50 turns phase-space tracking after a kick at BPBES202

MEASUREMENTS ON THE BEAM

Measurements on the e+ ring have been performed at the end of 2004. In particular, on the last day of data acquisition, the positron ring has been characterized by a complete set of measurements for two different lattices: the regular “collision” lattice at and a second one with a slightly larger value of the momentum compaction.

For each lattice, the beam centroid position has been recorded for different kicker amplitudes, (from 10 to 20 kV). with sextupoles on and octupoles on as in the normal operation lattice, with sextupoles on and octupoles off and with sextupole at low intensity and octupoles off. The case with sextupoles completely off was not recorded because even small amplitude kicks led to beam loss.

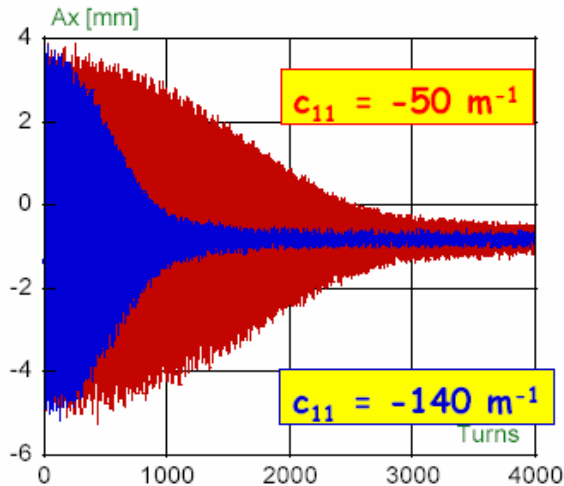


Figure 5: Beam decoherence: octupoles on (red) and off (blue).

An example of data analysis is plotted in Fig. 5, showing the horizontal displacements amplitude (A_x) during successive revolutions. Beam decoherence is shown for a lattice with octupoles on (red) and off (blue). The c_{11} parameter correlating tune shift to oscillation amplitude can be estimated from the data.

By performing a Fourier transform of the recorded data it is possible to evaluate directly the tune shift versus oscillation amplitude for different lattices.

Fig.6 shows a comparison between the two cases of the previous figure. The oscillation amplitude is given in units of the beam transverse size. The vertical scale is the fractional part of the betatron tune.

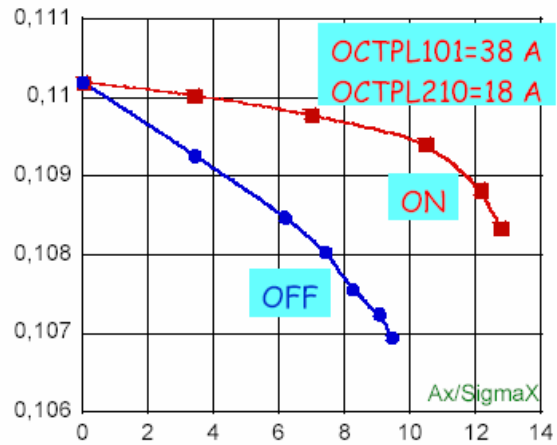


Figure 6: Tune shift versus amplitude: octupoles on (red) and off (blue).

ACKNOWLEDGEMENTS

We are grateful to to D.Pellegrini for the careful design of the two channels phase shifter module used to time the sampling clocks in input to the oscilloscopes.

REFERENCES

- [1] M.Zobov et al., "DAΦNE Operation and Plans for DAFNE2", ROAA001, this conference.
- [2] C.Milardi et al., "Developments in Linear and Non-Linear DAFNE Lattice", PAC2003, Portland, Oregon, May 12-16, 2003; LNF-03/012(P), 11/07/03.
- [3] A.Drago, A.Stella, "The Dynamic Tracking Acquisition System for DAΦNE e+/e- Collider", DIPAC2001, May 13-15, 2001, Grenoble, France.
- [4] A.Drago et al., "Implementation and Performance of the DAΦNE Timing System", 6th European Particle Accelerator Conference (EPAC 98), Stockholm, Sweden, 22-26 June 1998, p.1661, LNF-98/023 (P).

THE CARE ACCELERATOR R&D PROGRAMME IN EUROPE*

O. Napoly, R. Aleksan, A. Devred, CEA/DSM/DAPNIA, Saclay, France, R. Garoby, R. Losito, L. Rinolfi, F. Ruggiero, W. Scandale, D. Schulte, M. Vretenar, CERN, Geneva, Switzerland, H. Mais, D. Proch, DESY, Hamburg, Germany, A. Ghigo, INFN/LNF, Frascati, Italy, V. Palladino, INFN, Napoli, Italy, T. Garvey, F. Richard, LAL, Orsay, France, E. Gschwendtner, University of Geneva, Switzerland, A. Den Ouden, Twente University, Enschede, The Netherlands

Abstract

CARE, an ambitious and coordinated programme of accelerator research and developments oriented towards high energy physics projects, has been launched in January 2004 by the main European laboratories and the European Commission. This project aims at improving existing infrastructures dedicated to future projects such as linear colliders, upgrades of hadron colliders and high intensity proton drivers. We describe the CARE R&D plans, mostly devoted to advancing the performance of the superconducting technology, both in the fields of RF cavities for electron or proton acceleration and of high field magnets, as well as to developing high intensity electron and proton injectors. We highlight some results and progress obtained so far.

THE CARE PROJECT

The CARE project is an Integrated Infrastructure Initiative supported by the European Commission (EC) within the 6th Framework Programme (FP6). Over the years 2004-2008, it aims at improving existing accelerator infra-structures such as those listed in Table 1. Twenty two contracting laboratories and a large number of associated institutes and industrial partners participate in this integrating effort. The CARE general organisation and participation are available on the CARE web site [1] together with the detailed description of work [2].

THE CARE OBJECTIVES

The main objective of the CARE project is to generate a structured and integrated European area in the field of accelerator research and related R&D. The programme includes the most advanced scientific and technological developments relevant to accelerator research for Particle Physics. It is articulated around 3 Networking Activities that provide the long-term scientific vision, and 4 Joint Research Activities which integrate scientific and technical developments over several laboratories.

Networking Activities

The aim of the Networking Activities is to foster and strengthen European knowledge to evaluate and develop efficient methods to produce intense and high-energy electron, proton, muon and neutrino beams as recommended by the European Committee for Future

Accelerators (ECFA). They will establish collaborative and prioritised R&D programs aimed at establishing roadmaps toward the longer-term construction of new facilities of worldwide interest.

Table 1: The main existing infrastructures

Laboratory	Accelerator	Description
CCLRC-RAL	ISIS	Accelerator complex for the neutron and muon facility
CEA	IPHI CryHoLab	High intensity proton injector Hor. ^{tal} cryogenic test stand
CERN	PS, SPS, LHC CNGS CTF3	Proton accelerator complex Neutrino beam Electron two-beam linac test facility
CNRS-Orsay	NEPAL	Test stand with photo injector Coupler test laboratory
DESY	PETRA, HERA TTF	Electron and proton accelerator complex Electron superconducting linac test facility and FEL
FZR	ELBE	Electron linear accelerator
GSI	SIS, ESR	Heavy-ion accelerator complex
INFN-LNF	DAPHNE	Electron-positron collider
PSI	SINQ	Accelerator complex for the neutron and muon facility

Three Networking Activities span the full duration of the project

- ELAN (Electron Linear Accelerator Network) for electron accelerators and linear colliders;
- BENE (Beams in Europe for Neutrino Experiments) for neutrino and muon beams;
- HHH (High energy High intensity Hadron beams) for hadrons rings and colliders.

Joint Research Activities

Four Joint Research Activities aim at developing critical and/or beyond the actual state-of-the-art components and systems to upgrade the infrastructures:

- SRF (Superconducting RF): the development of the superconducting cavity technology for the acceleration of electrons with gradient exceeding 35MV/m and the development of the necessary RF technology;
- PHIN (Charge production with Photo-injectors): the improvement of the technology of photo-injectors, in

*Work supported by the European Community-Research Infrastructure Activity under the FP6 "Structuring the European Research Area" programme (CARE, contract number RII3-CT-2003-506395).

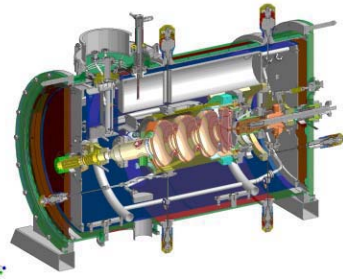


Figure 5: Cryomodule design for the SC-RF gun

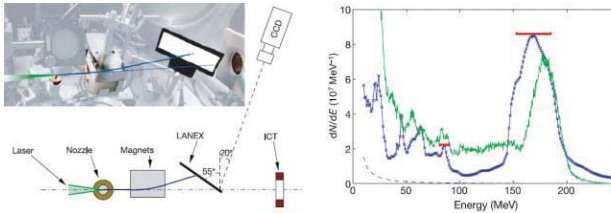


Figure 6: Laser-plasma acceleration: left, experimental setup and, right, data (blue) vs. simulation (green) results

The Joint research Activity: HIPPI

- RF studies have been completed and prototypes are in fabrication for a Cross-H DTL at GSI and a Cell Coupled DTL at CERN (see Fig.7).
- A $\beta=0.47$ elliptical cavity fabricated at INFN-Milano reached 16 MV/m accelerating gradient with $Q_0 = 5 \cdot 10^9$ at a vertical RF test in CEA-Saclay (see Fig. 8).
- Superconducting spoke resonators and CH prototype cavities, ranging $\beta=0.1$ to $\beta=0.35$, have been designed at FZJ-Jülich, CNRS-Orsay and IAP-Frankfort (see. Fig.9), and fabricated in industry. RF tests have started.
- A multi-laboratory comparison of 3D high intensity linac codes with space charge solvers has been initiated and a benchmarking experiment in the UNILAC DTL at GSI is being prepared.



Figure 7: Drift Tube Linac designs

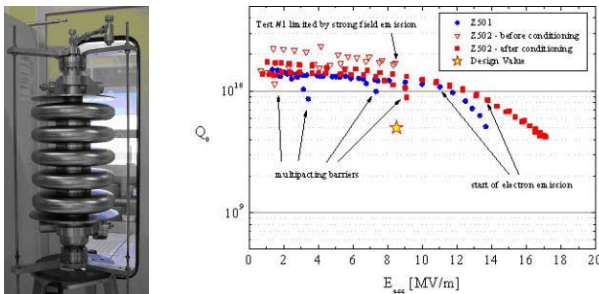


Figure 8: Vertical test of $\beta=0.47$ elliptical cavity



Figure 9: Superconducting spoke resonators (left, FZJ; middle CNRS-Orsay) and CH cavities (right, IAP-FU)

The Joint research Activity: NED

- NED and HHH co-organized in March at Archamps the workshop “Accelerator Magnet Superconductors” [7] to review present R&D and define directions of developments in connection with European industries.
- Magnetic designs for large bore and high field dipole magnets have been studied at CERN in order to define the characteristics of Nb₃Sn strands suitable to reach a 15 T field for two different apertures (see Table 2).
- Two contracts for Nb₃Sn conductor development have been awarded to Alstom/MSA (France) and SMI (The Netherlands).

Table 2: Nb₃Sn dipole parameters

Bore [mm]	Design Type	B ₀ [T]	Energy [kJ/M]	Max Pres. [MPa]	Outer Diam. [mm]
88	Layer	14.42	1810	148	1004
160	Slot	13.87	3959	129	1734

CONCLUSION

The CARE project started successfully a multi-laboratory collaborative effort following the multi-year plan of integrated R&D programmes. Many parts of the programme are synergetic like the tuner and coupler developments between SRF and HIPPI. Driven by particle physics, the CARE project has also strong synergies with other programmes supported by the European Union like EURISOL for nuclear physics, XFEL and EUROFEL for free electron lasers and ITER for fusion research. Dissemination of the acquired knowledge proceeds via the CARE publication repository [8] and the organisation of activity workshops and of the CARE annual meeting.

REFERENCES

- [1] <http://esgard.lal.in2p3.fr/Project/Activities/Current/>
- [2] http://esgard.lal.in2p3.fr/Project/Activities/Current/Overall/CARE_Annex1_16Jan04.pdf
- [3] <http://care04.desy.de/>
- [4] <http://dphs10.saclay.cea.fr/Doc/Care/care-rapport-index-2005.php>
- [5] <http://physicsatmwatt.web.cern.ch/physicsatmwatt>
- [6] <http://care-hhh.web.cern.ch/CARE-HHH/HHH-2004>
- [7] http://amt.web.cern.ch/amt/events/workshops/WAMS2004/wams2004_index.htm
- [8] http://dphs10.saclay.cea.fr/Doc/Care/care_index.php

COMMISSIONING AND FIRST MEASUREMENTS ON THE CTF3 CHICANE

A. Ghigo, D. Alesini, G. Benedetti, C. Biscari, M. Castellano, A. Drago, D. Filippetto, F. Marcellini, C. Milardi, B. Preger, M. Serio, F. Sgemma, A. Stella, M. Zobov
INFN/LNF, Frascati (Roma)

R. Corsini, T. Lefevre, F. Tecker, CERN, Geneva, Switzerland

Abstract

The transfer line between the linac and the first recombination ring (Delay Loop) of the CTF3 project has been installed at CERN in spring-summer 2004. In the transfer line a magnetic chicane is used to tune the length of the bunches coming from the linac in order to minimize the Coherent Synchrotron Radiation contribution to the beam energy spread in the recombination system. The first measurements of the beam parameters at several linac and stretcher settings are described. We report the compression curve as a function of the optical parameter R_{56} representing the dependence of the longitudinal position of a particle on its energy, obtained by measuring the bunch length with a 3 GHz RF deflector.

INTRODUCTION

The Compact Linear Collider (CLIC) project is a multi-TeV electron-positron collider for particle physics based on the two-beam acceleration concept; a high-intensity drive beam powers the main beam of a high-frequency (30 GHz) linear accelerator with a gradient of 150 MV/m, by means of transfer structure sections.

The aim of the CLIC Test Facility (CTF3) is to make exhaustive tests of the main CLIC parameters [1]. An international collaboration participates to the construction of the machine and the LNF contributes to the realization of a large part of the recombination system, consisting of two rings which will multiply the bunch frequency and peak current by a factor of ten. In particular the INFN Frascati laboratories responsibility is to design and realize the first of the two rings of the bunch train compression system, the Delay Loop (DL), and the transfer line that connects the Linac to the DL including a magnetic chicane used to vary the bunch length (see Fig. 1).

CTF3 is under construction in the LEP preinjector complex building at CERN. It uses where possible the existing magnets, power supplies, equipments and ancillary system. In summer 2004 the chicane and the transfer line have been installed and aligned in the tunnel; the vacuum chamber connected and tested together with the diagnostics devices [2]. In autumn 2004 the commissioning of this part of the machine started and a full set of measurements on the electron beam characteristics has been performed. The beam transverse emittances have been measured with the quadrupole scan method monitoring the beam sizes on a carbon OTR screen. The bunch length with different optical function configurations in the magnetic chicane has been measured using a 3GHz radio-frequency deflector.

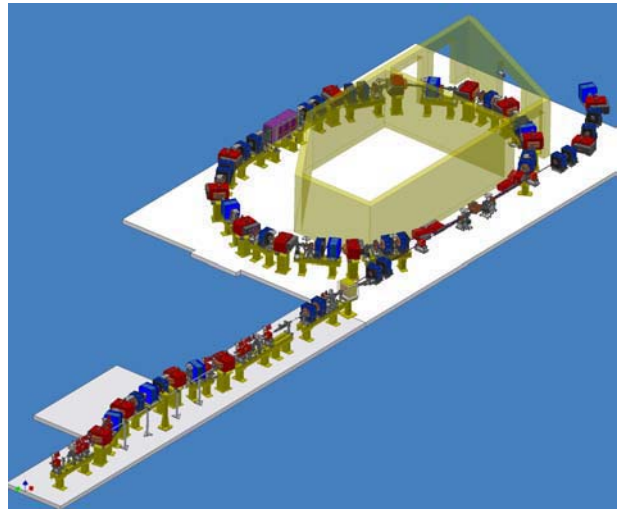


Figure 1: Layout of the Transfer line and Delay Loop.

TRANSFER LINE COMMISSIONING

The transfer line elements have been tested before the commissioning. In particular the vacuum chambers were baked-out in the Frascati Laboratories and shipped in light nitrogen overpressure. After installation the achieved vacuum was better than $8 \cdot 10^{-9}$ Torr in all the chambers without any heating. The tests of the magnets power supplies, the beam position monitor (BPM) electronics and the magnets polarity control have been completed before starting the operation shifts.

The commissioning of the transfer line, including the magnetic stretcher-compressor chicane, has been performed in eight weeks of operation starting from October 2004, sharing the time with the power extraction system (PETS) experiment [3] that use a dedicated line connected, through a dog-leg, at the low energy linac section.

The first beam has been transported up to the spectrometer through the chicane by-pass after matching the optical function at the linac exit with two triplets placed at the chicane end. The chicane has been used the first time with the quadrupoles off, obtaining a good measurement of the beam energy, of the dispersion function and of the BPM calibration. The trajectory has been reconstructed with the beam position monitor system resulting well centered with no corrector magnets on. After the first check the beam has been transported with different configurations of the optics that permit, by varying the quadrupoles currents, to change the bunch length in a very wide range at the chicane exit. The full transport efficiencies for the different optical configura-

tions have been monitored summing the calibrated signals of the beam position monitors.

MEASUREMENTS

Measurements on beam characteristics have been done with different sets of conditions. We summarize here the most representative, which corresponds to the beam parameters listed in Table I.

Table I: Beam parameters used in the measurements

Charge per bunch	1.3 nC
Bunch length at linac exit	6 ps
Beam energy	100 MeV
Energy spread	1.2 %
Number of bunches in the train	600
Bunch train duration	200 ns
Average current	3.8 A

Energy and energy spread measurements

Energy and energy spread along the bunch train, as well as individual bunches, have been measured with the spectrometer at the line end and with the beam position monitors in the dispersive regions. During the measurements the energy of the bunches along the train must be constant; an efficient control system of the klystron phase permits to square the RF pulses that power the accelerator sections.

Emittance measurements

The horizontal and vertical emittances have been measured with the quadrupole scan method, observing the the beam transverse dimensions on a carbon OTR screen as the current in an upstream quadrupole was varied. The produced OTR radiation has been collected by a large aperture optics in a CCD camera.

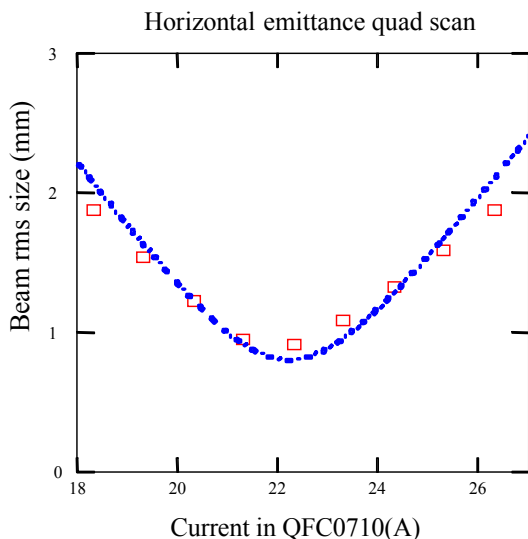


Figure 2: Horizontal beam size vs. quadrupole current.

The image has been stored and processed by a frame grabber and integrated in the control system.

The values of the horizontal and vertical emittances measured are 112 and 103 mm*mrad respectively, in good agreement with the expected 100 mm*mrad value. An example of the measurement performed at the linac end is shown in Fig. 2.

Bunch length measurements

The power extraction efficiency from the drive beam calls for precise control of the bunch spacing and of the beam emittance along the whole frequency multiplication system. The emittances, both transverse and longitudinal, are affected by the collective effects depending on bunch length and energy spread. The chicane between the Linac and the DL has been designed with a wide range of R_{56} tunability, where, being D the dispersion function and ρ the constant bending radius in the dipoles

$$R_{56} = \frac{1}{\rho} \int_{\text{dipoles}} D(s) ds$$

is the first order transfer matrix element relating the particle position along the bunch with its energy deviation $\Delta p/p$:

$$ct = (ct)_o + R_{56} \frac{\Delta p}{p} + T_{566} \left(\frac{\Delta p}{p} \right)^2 + \dots$$

and T_{566} is the corresponding second order transfer matrix term depending on the chromaticity of the line. The tunability range is large essentially for diagnostic purposes. The chicane with quadrupoles off has $R_{56} = 0.46$ m and very small T_{566} . By increasing the horizontal focusing, R_{56} goes to negative values and $|T_{566}|$ together with the other 2nd order terms increases and the beam distribution becomes non-gaussian.

A 3GHz RF deflector [4], placed after the chicane, has been used for the bunch length measurements. The head and the tail of each bunch, passing through the deflector cavities at field zero crossing point, are deflected vertically and in opposite direction; the longitudinal distribution is converted into vertical distribution on an OTR screen intercepting the beam and measured via an optical system and CCD camera.

An accurate image analysis permits to reduce the errors due to the background coming from the CCD and the OTR screen.

We obtained a calibration for the measurement by relating the displacement of the beam distribution centroid in pixels with the phase of the RF wave. The calibration result is a ratio of pixels per degrees valid for a certain value of the RF power and a certain distance of the screen from the deflector.

We have chosen to calculate the RMS value of the beam to characterize its width rather than the standard deviation obtained by a gaussian fit of the profile, because in most cases the beam profile was not gaussian at all and the fit was not congruent with the profile. In case of gaussian beam the RMS and the fit give the same results. However the disadvantage of taking the RMS value is the weight of the tails in the calculation, so that a very

accurate filter is needed to make a precise selection of the beam. We used IACO, a Labview and Matlab based software, that applies a filter on a digital image. The filter subtracts the background found by a statistical treatment of the image and then via an iterative algorithm removes the isolated x-ray produced spikes. At the end of every interaction the program compares the value of parameters such as sigma and centroid, stopping when their changes are negligible (less than $\frac{1}{2}$ pixel).

For each measurement we took many images; the program averages over all the values of the parameters coming from different images inside the same directory (measurement), giving out the average centroid and sigma (x and y) for each directory, and respective errors.

The transverse distribution of the bunch at the OTR screen position is the convolution between the deflected longitudinal profile and the vertical dimension of the bunch at the same position (σ_y). To achieve good resolution the vertical dispersion induced by the RF deflector has been chosen bigger than σ_y . For each measurement at different R_{56} the spot size without deflection has been stored in order to normalize the measure.

The bunch length is determined by measuring the vertical distribution size.

The beam has been accelerated on crest along the linac, except on the last section where 30% off crest on the negative side gives a correlation in longitudinal phase space.

The value of the chicane R_{56} has been varied from 0.45 to -0.2 m. According to the ELEGANT code simulations, the maximum expected compression corresponds to $R_{56} = 0.2$ m (see Fig. 3), and this has been confirmed by the measurements with a very good agreement.

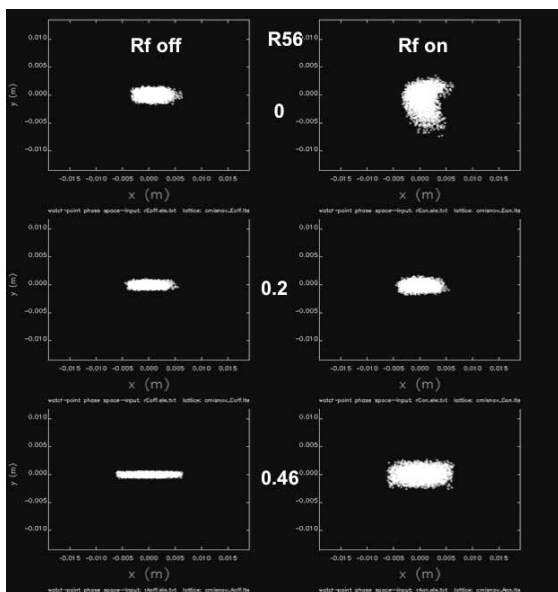


Figure 3: Simulated beam transverse distributions for three different values of R_{56} .

The minimum bunch length is less than 0.5 mm. The comparison between the simulated transverse distribu-

tions on the screen and the measured ones (Fig. 4) shows also a very good agreement, sign of good modelling of the whole system (Fig. 5).

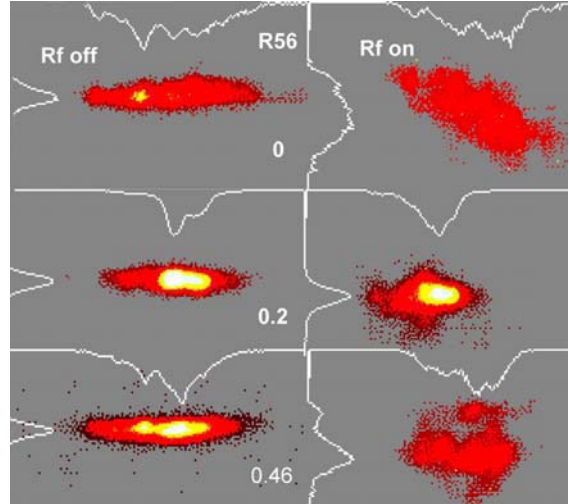


Figure 4: Beam transverse distributions on the OTR for the same conditions of Figure 3.

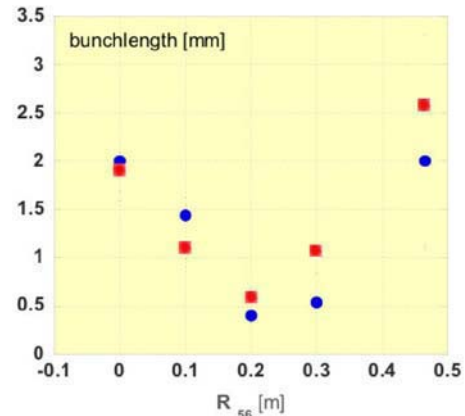


Figure 5: Bunch length vs R_{56} factor: dot measured, squares simulated.

CONCLUSIONS

Installation and commissioning of CTF3 transfer line between linac and Delay Loop has been completed. The first set of measurements of the beam characteristics such as emittance, bunch length tunability with R_{56} and transfer efficiency are in good agreement with the expected values.

REFERENCES

- [1] G. Geschonke, A. Ghigo (ed.) et al.: "CTF3 Design Report", CERN/PS 2002-008(RF), LNF-02/008(IR).
- [2] A. Ghigo et al., "Status of CTF3 Stretcher-Compressor and Transfer Line", Proceedings of EPAC2004, 5-7 July, 2004 Lucerne, Switzerland; LNF-04/18(P), 30/07/04.
- [3] C. Achard et al.: "30 GHz power production at CTF3", this Conference.
- [4] D. Alesini et al.: "Longitudinal Phase Space Characterization of the CTF3 beam with the RF Deflector", Proceedings of EPAC2004, 5-7 July, 2004 Lucerne, Switzerland; LNF-04/18(P).

STATUS OF THE SPARC PROJECT

D.Alesini, S.Bertolucci, M. Bellaveglia, M.E.Biagini, R.Boni, M.Boscolo, M.Castellano, A.Clozza, G.Di Pirro, A.Drago, A.Esposito, M.Ferrario, L. Ficcadenti, D. Filippetto, V.Fusco, A.Gallo, G. Gatti, A.Ghigo, S.Guiducci, M.Incurvati, C.Ligi, F.Marcellini, M.Migliorati, A.Mostacci, L.Palumbo, L.Pellegrino, M.Preger, R.Ricci, C.Sanelli, M.Serio, F.Sgamma, B.Spataro, A.Stecchi, A.Stella, F.Tazzioli, C.Vaccarezza, M.Vescovi, C.Vicario, *INFN-LNF, Frascati, Italy*

F.Alessandria, A.Bacci, I.Boscolo, F.Broggi, S.Cialdi, C.DeMartinis, D.Giove, C.Maroli, M. Mauri, V.Petrillo, M.Romè, L.Serafini*, *INFN-MI and Univ. of Milano, Milano, Italy*

D.Levi, M.Mattioli, G.Medici, P. Musumeci, D. Pelliccia, M. Petrarca, *INFN-Roma1, Rome, Italy*

A. Cianchi, L.Catani, E.Chiadroni, E. Gabrielli, S.Tazzari, *INFN-Roma2, Rome, Italy*

F.Ciocci, G.Dattoli, A. Dipace, A.Doria, F.Flora, G.P.Gallerano, L.Giannessi, E.Giovenale, G.Messina, P.L.Ottaviani, S.Pagnutti, G.Parisi, L.Picardi, M.Quattromini, A.Renieri, G.Ronci, C.Ronsivalle, M.Rosetti, E.Sabia, M.Sassi, A.Torre, A.Zucchini, *ENEA-Frascati, Italy*

S. De Silvestri, M. Nisoli, S. Stagira, *Politecnico/Milano, Milano, Italy*

J.B. Rosenzweig, *UCLA - Dept. of Physics and Astronomy, Los Angeles (CA), USA*

D.H. Dowell, P.Emma, C.Limborg, D.Palmer, *SLAC, Palo Alto (CA), USA*

Abstract

The SPARC project has entered its installation phase at the Frascati National Laboratories of INFN: its main goal, the promotion of an R&D activity oriented to the development of a high brightness photoinjector to drive SASE-FEL experiments, is being vigorously pursued by a collaboration among ENEA-INFN-CNR-Universita` di Roma Tor Vergata-INFN-ST. In this paper we will report on the installation and test of some major components, like Ti:Sa laser system, RF gun and RF power system. Advancements in the control and beam diagnostics systems will also be reported, in particular on the emittance-meter device for beam emittance measurements in the drift space downstream the RF gun. Recent results on laser pulse shaping show the feasibility of producing 10 ps flat-top laser pulses in the UV with rise time below 1 ps. First FEL experiments have been proposed, using SASE, seeding and non-linear resonant harmonics.

INSTALLATION OF MAIN COMPONENTS

The SPARC project is by now in its advanced installation phase at LNF; tests of related equipments and instrumentation are also under way. The 150 MeV S-band photo-injector and the 12 m undulator for the FEL experiments are located inside an underground bunker, which hosts as well the clean room containing the Ti:Sa laser system driving the photo-cathode. As discussed elsewhere [1], the project aims at conducting a bouquet of

advanced experiments in the production, characterization and control of high brightness electron beams, as those required by X-ray FEL's and advanced high gradient acceleration techniques (plasma, IFEL, etc.).

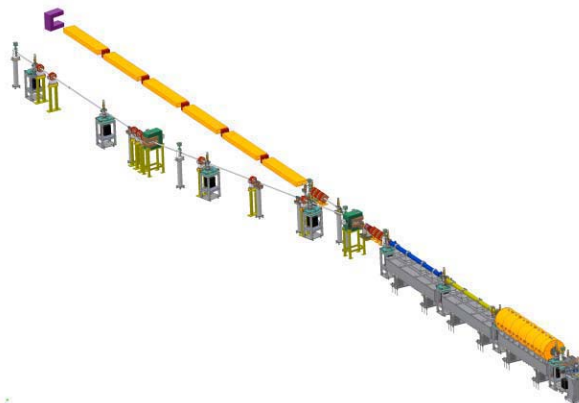


Figure 1: Layout of SPARC photo-injector, with RF-gun, 3 S-band accelerating sections and FEL undulator (6 modules). Beam line for undulator by-pass is also shown.

The layout of the machine, shown in Fig.1, displays a RF-gun, 3 S-band SLAC-type accelerating sections, and a 6-module 12-m long undulator for SASE and seeded FEL experiments in the 88-500 nm wavelength range.

The installation of the RF source and distribution system started last month. The klystron pulsed power modulators, supplied by PPT, have been positioned in the SPARC klystron hall, as well as the klystrons (45 MW,

2856 MHz, TH2128C model manufactured by Thales), as shown in Fig.2. The modulator connections with various controls and ancillary systems are being made. Modulators can switch the klystrons at a maximum rep. rate of 10 Hz, with HV pulses of 310 kV – 340 A.

The modulator power test, scheduled at the end of this month, will be performed initially with the klystron operating in diode-mode. The installation of waveguide distribution network and RF devices (circulators, shifters, etc.) will begin next month.



Figure 2: SPARC klystrons with oil tanks installed in the SPARC building (upper facility room or klystron hall).

The 1.6-cell RF gun and the emittance-compensation solenoid have been delivered at LNF in February from UCLA [2]. The gun supports are being modified to gain full control of the gun axis alignment. The water flow into the gun has been measured up to 5 l/m, a value that should allow control of the gun temperature at the level required for operation up to 10 Hz. The magnetic solenoid yoke has been assembled and it is also going through some minor mechanical modifications. The solenoid uses 4 different coils that can be independently excited. The magnetic field will be measured to check for axis misalignments and to record longitudinal magnetic field profiles in the different current configurations. The full system should be fully tested, mounted and aligned by mid summer and ready for RF power tests in September.

Two accelerating sections will be delivered next July by Mitsubishi, while one of the two sections given by SLAC to SPARC, as part of a collaboration agreement, is under test. As shown in Fig.1, the first accelerating section will be embedded (see yellow zone) in an array of solenoids, required to produce a magnetic field for additional focusing in order to comply with the Ferrario working point[3] matching conditions for emittance compensation. Thanks to a newly funded European project, EUROFEL, an additional array of solenoids will be built and installed around the second section, in order to further improve the performances of emittance compensation in particular when RF compression is applied [4].

The Ti:Sa laser system, built by Coherent, is now under final acceptance tests. The oscillator is already installed inside the clean room in the SPARC bunker, while the amplifier is being shipped by Coherent to LNF for final acceptance tests of the whole laser system: these will be

conducted next month at LNF. The HIDRA-50 amplifier system, made of one regenerative and two multi-pass amplifiers, has already reached the specs in the infra-red, delivering 50 mJ of output pulse energy with 104 fs pulses and good beam quality ($M_x^2=1.9$ and $M_y^2=1.6$). Preliminary tests in the UV (266 nm), performed after the third harmonic crystal and the UV stretcher, showed the capability to reach 1.8 mJ of pulse energy with quite good pulse-to-pulse stability, *i.e.* less than 4.5%, and a fairly good beam quality, *i.e.* $M_x^2=2.7$ and $M_y^2=1.9$. These tests will be further completed at LNF soon.



Figure 3: HIDRA-50 amplifier for the SPARC laser.

A preliminary measurement of the time jitter between the laser oscillator and an external reference 79 MHz RF wave was performed at LNF. The signal from a photodiode looking at the optical pulse train, properly filtered and amplified, was mixed with a portion of the 79 MHz wave driving the oscillator phase-locking loop.

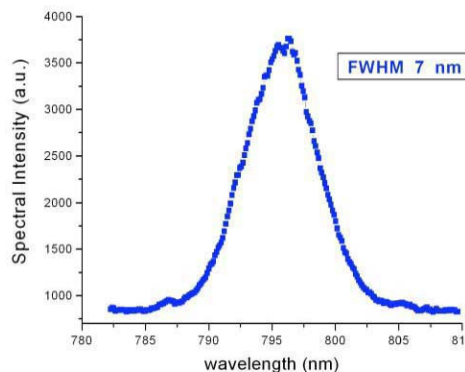


Figure 4: Output spectrum of laser oscillator.

The relative phase between the two signals was measured by monitoring the mixer output: an upper limit of 1.4 ps was found. A characterization of the oscillator output spectrum was also performed, showing a quite good behavior (see Fig.4).

The emittance-meter device has been completed, as shown in Fig.5, and is ready to be installed in the drift line after the RF gun and focusing solenoid system, in

order to conduct measurements of the rms normalized transverse emittance as a function of the drift length. This measurements will be performed at the beginning of next year running the beam at the RF-gun exit energy of 5.7 MeV, before installation of the 3 accelerating sections.



Figure 5: Emittance-meter device with long bellows.

BEAM DYNAMICS STUDIES

Beam dynamics studies have moved further than previously reported[1]. The study of beam quality achievable using Gaussian laser pulses has been performed[5], while the ultimate beam brightness achievable applying RF compression in the SPARC photo-injector, reported in [4], is shown to reach a record value of $1.1 \cdot 10^{14} \text{ A}/(\text{m}\cdot\text{rad})^2$, implying a peak current up to 1 kA with a normalized slice transverse emittance (in the central part of the bunch) of $0.5 \mu\text{m}$.

R&D ACTIVITY

Laser Pulse Shaping

Previous measurements of laser pulse shaping using the Dazzler were reported in [1], showing promising results. A more complete experiment involving electron bunch production with shaped laser pulses was conducted at BNL-DUV by a SPARC-SLAC-BNL/DUV collaboration, and is reported in [8]. An R&D activity on laser pulse shaping with LCM masks is also in progress and will eventually be integrated in the SPARC laser system.

X-band cavities

The design and realization of an X-band accelerating section for linearizing the longitudinal phase space of the SPARC beam is under way. The structure, operating on the π standing wave mode, is a 9 cell structure fed by a central coupler and is designed to achieve 42 MV/m accelerating gradient. Beam-pull measurements performed on a copper prototype at room temperature were in very good agreement with numerical predictions. Mechanical details of the realized prototype and RF properties of the structure as a function of the assembly characteristics are discussed in more details in [6].

FEL EXPERIMENTS

SPARC participates to the EUROFEL programme also in the seeding experiments work package. We foresee the installation of a chamber for generating short pulses (few tens of fs) of high order harmonics of the Ti:Sa generated in gas (266nm, 160 nm, 114nm, 88nm), and to feed the FEL amplifier with this seed pulse. The chamber and the related hardware will be provided by the CEA-SPAM (Service de Photons, Atomes et Molécules) which also participate to the experiment through the EUROFEL framework. Diagnostics of the output radiation in terms of spectrum and pulse duration will provide relevant information about the FEL amplification process. The SPARC radiation will be monitored by diagnostic stations located in between the six undulator sections to follow the dynamics of the pulse propagation in different FEL regimes, from the shot noise to the exponential growth, to the saturation and beyond.

CONCLUSIONS

Main components of the SPARC project are under installation and test: we expect to conduct the first beam emittance-meter experiments during the first months of next year. The first beam at full energy out of the Linac is due within June 2006. The SPARC system will be upgraded during the next 5 years to become an advanced accelerator facility as described in [7].

REFERENCES

- [1] D. Alesini et al., *NIM A528* (2004) 586
M. Ferrario et al., Proc. EPAC-2004, pag. 399, ISBN: 92-9083-231-2A
Renieri et al., *Status report on the SPARC Project*, Proc. of FEL-2004.
- [2] J.B. Rosenzweig et al., *RF and Magnetic Measurements on the SPARC Photoinjector and Solenoid at UCLA*, these proceedings.
- [3] M. Ferrario et al., *Homodyn Studies for the LCLS RF Photoinjector*, in *The Physics of High Brightness Beams*, J.Rosenzweig and L.Serafini ed., World Sci. ISBN 981-02-4422-3, June 2000
- [4] C. Ronsivalle et al., *Optimization of RF Compressor in the SPARX Injector*, these proceedings.
- [5] M. Boscolo et al., *Working Point Optimization for a Bunch with Gaussian Profile*, these proceedings.
- [6] D. Alesini et al., *Design and RF Measurements of a X-Band Structure at SPARC*, these proceedings
- [7] D. Alesini et al., *The Project PLASMONX for Plasma Acceleration Experiments and a Thomson X-ray Source at SPARC*, these proceedings
- [8] S. Yuzhen et al., *Temporal E-beam Shaping in an S-Band Accelerator*, these proceedings

*Luca.Serafini@mi.infn.it

DESIGN AND MEASUREMENTS OF AN X-BAND ACCELERATING CAVITY FOR SPARC

D. Alesini, M. Ferrario, B. Spataro, INFN/LNF, Frascati (Rome), Italy

A. Bacci, INFN/LASA, Segrate (Milan), Italy

A. Falone, M. Migliorati, A. Mostacci, L. Palumbo, University “La Sapienza”, Rome, Italy.

Abstract

The paper presents the design of an X-band accelerating section for linearizing the longitudinal phase space in the Frascati Linac Coherent Light Source (SPARC). The structure, operating on the π standing wave mode, is a 9 cells structure fed by a central coupler and it has been designed to obtain a 42 MV/m accelerating gradient. The 2D profile has been determined using the electromagnetic codes Superfish and Oscar-2D while the coupler has been designed using HFSS. Bead-pull measurements made on a copper prototype have been done and the results are illustrated and compared with the numerical ones. Mechanical details of the realized prototype and RF properties of the structure as a function of the assembly characteristics are also discussed.

INTRODUCTION

The use of an X-Band structure operating at 11.424 GHz is required to compensate the non-linearity distortions due to the RF curvature during acceleration and compression[1] of the SPARC Phase II[2]. The schematic layout is reported in Fig. 1. The X-Band structure, designed to obtain 42 MV/m accelerating gradient, is a 9 cells π -mode structure fed by a central coupler. The fourth harmonic of 2.856 GHz has been chosen for space availability reasons and also because the technologies in the X-Band power sources and modulators have been already developed for future linear collider projects.

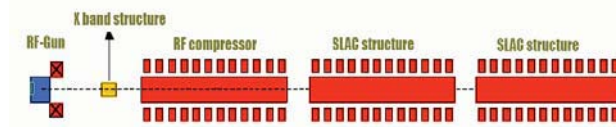


Figure 1: schematic layout of SPARC phase II.

THE X BAND STRUCTURE DESIGN

2D Profile

The detailed analysis of the structure design without coupler is reported in [3]. The 2D structure dimensions are reported in Fig. 2 and have been determined with the 2D electromagnetic (e.m.) codes Superfish [4] and Oscar-2D[5]. The choice of 9 cells has been done to achieve a total accelerating voltage $V=5$ MV with 3 MW of peak input power. No dedicated dampers of the parasitic higher order modes have been adopted since the X-Band structure operates on single bunch. Other cavity parameters are reported in Table 1.

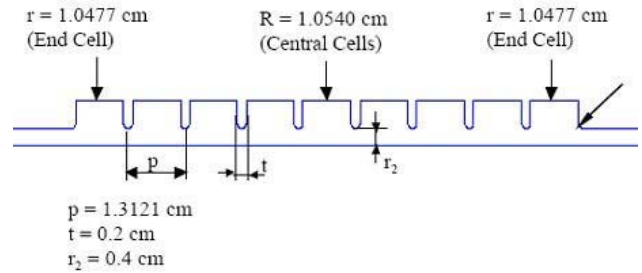


Figure 2: 2D profile of the X-band structure.

Table 1: X-band cavity parameters

Quality factor Q	8400
R/Q [Ω / m]	9165
Average dissipated Power [W]	270
Peak axial E-field [MV/m]	57.5
Kilpatrick factor	1.197
Peak surface electric field [MV/m]	105

Coupler Design

Concerning the coupler design, it has been decided to feed the cavity in the central cell in order not to excite the mode $8/9\pi$ that has the frequency nearest to the π mode and zero field in the central cell. Therefore with a central coupler we have a much greater separation of the modes and, consequently, the working mode is less perturbed by the closest one. To reduce the coupler window dimensions we have decided to taper the smaller dimension of the standard X-band waveguide (10.16 mm) to the dimension of 4 mm. The coupling cell is sketched in Fig. 3.

The dimension of the coupler window (w) and of the central cell radius (R_c) have been tuned in order to obtain simultaneously a coupling coefficient $\beta = 1$, a resonant frequency of the whole system (cells+coupler) equal to 11.424 GHz and to preserve a good field flatness. This has been done using the e.m. code HFSS [6] by following two steps:

a) we have simulated a single cell with coupler and the dimensions of the coupler window and cell radius have been tuned in order to obtain a coupling coefficient $\beta = 9$ (exactly 9 times the coupling coefficient that we would reach with the complete structure) and a cell resonant frequency equal to 11.424 GHz;

b) we have simulated the complete structure with the dimensions found in the previous case and we have slightly adjusted the dimensions of the coupler cell and

window to obtain a perfect field flatness at the resonant frequency of 11.424 with $\beta = 1$.

After this procedure we have obtained the external quality factor $Q_{EXT}=7900$ and the coupling coefficient $\beta = 1.09$ with a good field flatness (within few percent).

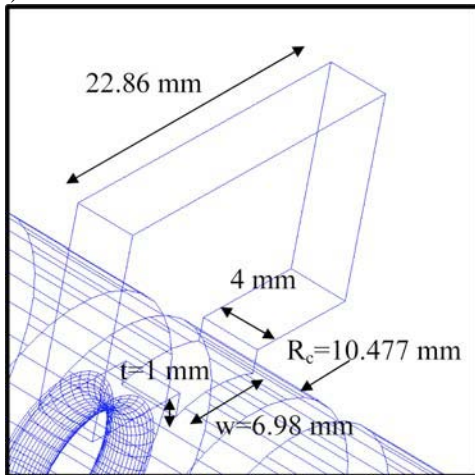


Figure 3: sketch of the coupling cell.

COPPER PROTOTYPE AND MEASUREMENT SETUP

A full scale copper prototype has been constructed and it is shown in Fig 4. The 9 cell structure has been designed for brazing, but the RF tests refer to a mechanically joined structure. The structure has been realised by mechanical machining with a numerically controlled lathe and the obtained precision is below 0.01 mm, while the surface roughness is not worse than $0.4 \mu R_a$. The surface finishing was obtained directly by mechanical machining with custom cutting tools, avoiding any polishing technique and only silicon and sulphur free cutting fluid was used. Each cell dimension has been checked with a quality control test. The final machining was done at constant temperature in order to guarantee as much as possible the uniformity of the mechanical dimensions of the cells.

The assembling procedure foresees the joining of the nine cells using two stainless steel disks used to press the structure by means of three 8 mm diameter copper rods. A torque of 5 Nm corresponds to a pressure of roughly 80 N/mm^2 .

Two type of different measurements have been done:

a) transmission (or reflection) scattering coefficients measurement between the two lateral antennas or between the antennas and the central coupler;

b) bead pull measurements.

With the first type of measurements we have found the resonant frequency, the β coefficients of the input ports and the unloaded or external quality factors of π (or other) mode(s). With the second type of measurements we have found the longitudinal electric field on axis and we have calculated the shunt impedance of the structure.



Figure 4: copper prototype of the X band structure.

MEASUREMENTS RESULTS

The transmission coefficient between the two small antennas and between the antenna and the central coupler are reported in Figs. 5a and 5b respectively. As previously observed, we can excite only 5 over 9 possible modes by the central coupler because we impose a non-zero field in the central cell. On the contrary with the two antennas we can excite all the possible modes. The quality factor of the resonance has been measured as a function of pressure realized by the rods. The measured quality factors, unloaded and external, agree with the theoretical one within few percent even if the structure is not brazed. As an example the quality factor of the resonance has a function of pressure realized by the rods is reported in Fig 6.

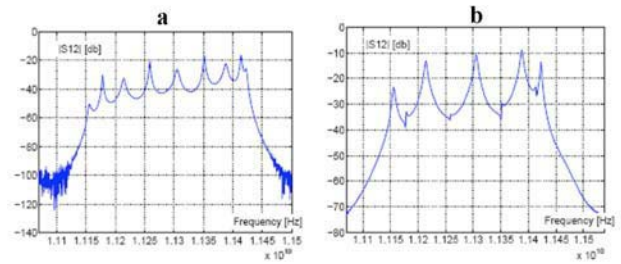


Figure 5: transmission coefficients between the two small antennas and coupler input port.

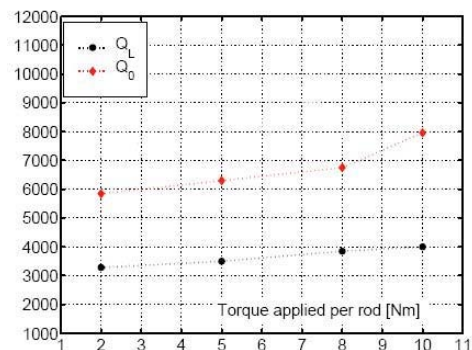


Figure 6: measured quality factor of the π mode resonance as a function of pressure realized by the rods.

The measured dispersion curve, compared with the one obtained from HFSS and SUPERFISH, is reported in Fig. 7.

With the bead pull technique we have measured the electric field on axis. A careful optimization of the measurement setup has been done in order to minimize the systematic errors and to better understand the uncertainty of the measurements. The most important reasons of induced errors in the measurements were:

a) the effect of nylon wire that induced an unwanted perturbation in the frequency measurement. To cancel this systematic error different measurements have been done with different nylon wire diameters. A typical phase resonance measurement with different wire diameters is reported in Fig. 8. The best results have been obtained with the smallest wire and the final small systematic error has been completely cancelled considering the frequency shift with and without the perturbing object;

b) the effect of the drops of glue used to fix the perturbing object. It gave a perturbation in the frequency measurement of the order of 10% of the total frequency variation. To take into account this effect different measurements have been done in order to subtract the systematic perturbation to the measure;

c) the effect of jitter in the longitudinal coordinate between different measurements and within a single measure. This problem, given by the stepping motor, has been reduced using a weight no more than 75 g, and correcting off-line the measurement results.

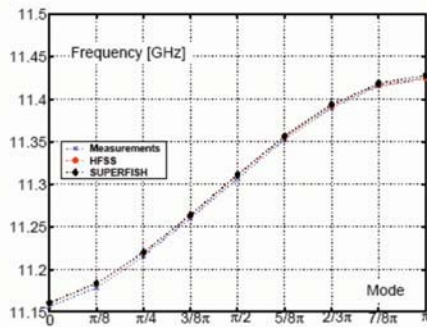


Figure 7: measured dispersion curve.

To calculate the R/Q of the structure it has been necessary to determine the form-factor of the different perturbing objects. Using Slater's theorem we have calibrated the form factor comparing the perturbation induced by the perturbing object in a cavity with known field with the analytical result. For this purpose, It has been used a pill-box cavity working at 1.91 GHz on the TM_{010} mode. Using different resonant mode of the pillbox cavity we have also checked that the form-factor does not depend on the frequency. The measured longitudinal electric field on axis, after the tuning procedure, is plotted in Fig. 8. The reached field-flatness is of the order of 1% at the nominal resonant frequency of 11.424GHz.

The calculated R_{sh}/Q_s normalized to the cavity length is ≈ 9500 and it is in very good agreement with the simulation results.

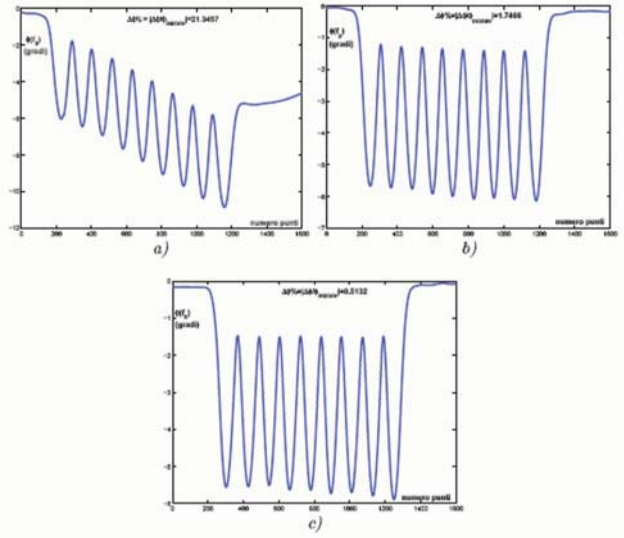


Figure 8: phase of resonance measurement with different wire diameters: a) 0.18 mm; b) 0.148 mm; c) 0.083 mm.

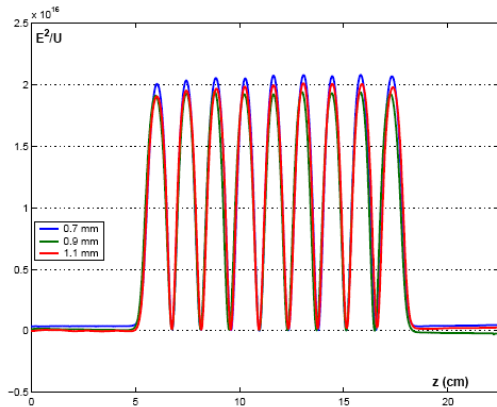


Figure 8: measured longitudinal electric field on axis.

CONCLUSIONS

In the paper we have presented the design of the X-band accelerating section for linearizing the longitudinal phase space in the Frascati Linac Coherent Light Source (SPARC). Quality factors, resonant frequency and electric field measurements have been done on a copper prototype. Even if the prototype is not brazed the reached quality factors are very close to the theoretical ones. Concerning the electric field measurement with the bead pull technique we have discussed the most important reasons of induced errors and how to cancel these effects. Brazing tests are now in progress in the LNF for the construction of the final device.

REFERENCES

- [1] P.Emma, LCLS-TN-01-1, SLAC 2001.
- [2] SPARC Injector TDR, www.lnf.infn.it.
- [3] A. Bacci et al., LNF 03/008(R), Frascati, (2003).
- [4] J. H. Billen and L. M. Young, Part. Acc. 7 (4), 1976.
- [5] P. Fernandes and R. Parodi, PAC 1982.
- [6] www.ansoft.com.

START TO END SIMULATION FOR THE SPARX PROJECT

R. Boni, M. Boscolo, M. Ferrario, V. Fusco, M. Migliorati, L. Palumbo, B. Spataro, C. Vaccarezza,
M. Vescovi, INFN-LNF, Frascati, Italy
L. Giannessi, M. Quattromini, C. Ronsivalle, ENEA Frascati, Italy
L. Serafini, INFN-MI, Milano, Italy

Abstract

The first phase of the SPARX project now funded by MIUR (Research Department of Italian Government) is an R&D activity focused on developing techniques and critical components for future X-ray FEL facilities. The aim is the generation of electron beams with the ultra-high peak brightness required to drive FEL experiments. A FEL source realization is foreseen within this program, which comprises two lines of activity: a) the use of the SPARC high brightness photoinjector to test RF compression techniques and the emittance degradation in magnetic compressors due to CSR, b) the production of radiation in the range of 3-5 nm, both in SASE and SEEDDED FEL configurations, in the so called SPARXINO test facility, based on the upgrade of existing Frascati 800 MeV LINAC. In this paper we present and discuss the preliminary start to end simulations results for SPARXINO.

INTRODUCTION

SPARX is the project for a SASE-FEL X-ray source proposed by ENEA, INFN, CNR and Università Tor Vergata. The first phase has been funded by MIUR and by INFN: it is mainly focused on two lines. The use of the SPARC high brightness photoinjector [1] to develop experimental test on RF compression techniques and other beam physics issues, like emittance degradation in magnetic compressors due to CSR. Production of soft and hard X-rays in a SASE-FEL with harmonic generation, in the so called SPARXINO test facility, upgrading in energy and brightness the existing Frascati 800 MeV Linac presently working as injector system for the DAΦNE Φ-factory [2]. In the next sections we describe a preliminary layout of the SPARXINO test facility, the required R&D efforts and the start to end simulation results.

THE SPARXINO TEST FACILITY

A spectral range from 10 nm to 1 nm has been considered for the radiation. SASE-FEL's in this wavelength range require high brightness beam at the undulator entrance. In Table 1 a preliminary parameter list is reported for such a source, while in Fig. 1 the schematic layout is shown. It

Table 1: Electron beam parameters.

Beam Energy	1.2	GeV
Peak current	1-2.5	kA
Emittance (average)	2	mm-mrad
Emittance (slice)	1	mm-mrad
Energy spread (correlated)	0.1	%

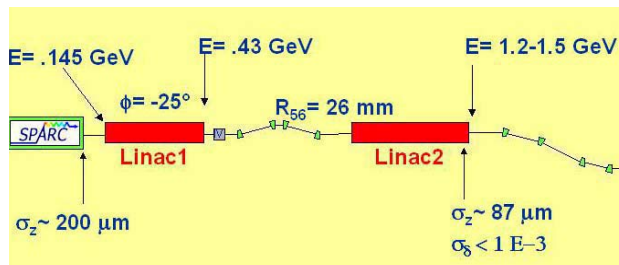


Figure 1: Schematic layout of the SPARXINO test facility.

consists of an advanced high brightness photoinjector followed by a first linac, Linac1, that drives the beam up to 430 MeV with the correlated energy spread required to compress the beam in a subsequent magnetic chicane. The second linac, Linac2, drives the beam up to 1.2 GeV while damping the correlated energy spread taking profit of the effective contribution of the longitudinal wake fields provided by the S-band accelerating structures.

The photoinjector

This linac design integrates a rectilinear RF compressor in a high brightness photoinjector, as proposed in [3], thus producing a 300-500 A beam in the early stage of the acceleration. The SPARXINO linac will be the first SASE FEL experiment operating with RF and magnetic compressors in the same linac. According to the simulation results the beam compression at low energy (<150 MeV), still in the space charge dominated regime, turns out to be feasible provided that a proper emittance compensation technique is adopted [4], a possibility that is not viable in a magnetic chicane. Moreover the propagation of a short bunch in the Linac1 reduces the potential emittance degradation caused by transverse wake fields, while a proper phasing of the linac can control the longitudinal wake fields.

The injector design for the SPARXINO test facility is based on the SPARC high brightness photoinjector [5]. It considers a 1.1 nC bunch 10 ps long (flat top) with 1.1 mm radius, generated inside a 1.6-cell S-band RF gun of the same type of the BNL-SLAC-UCLA one [6] operating at 120 MV/m peak field equipped with an emittance compensating solenoid. Three standard SLAC type 3-m TW structures each one embedded in a solenoid boost the beam up to 150 MeV. With a proper setting of the accelerating phase and solenoid field amplitude it is possible to increase the peak current preserving the beam transverse emittance. For the case presented here a setting has been chosen that provides a bunch average current of 450 A with a normalized rms emittance below

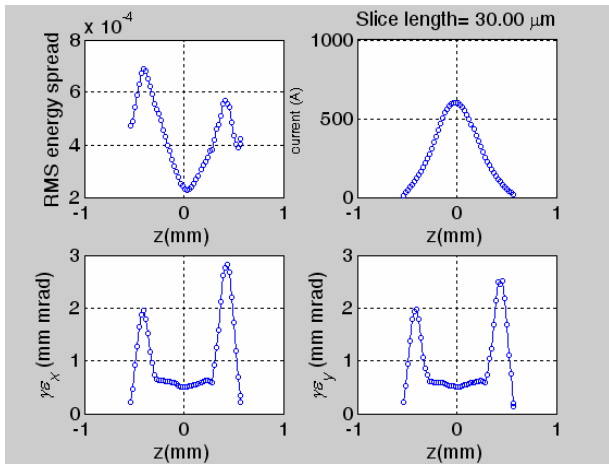


Figure 2: Energy spread, peak current and transverse emittance along the bunch, at the photoinjector exit.

1 mm-mrad [7]. The energy spread, peak current and transverse emittance along the bunch, at the photoinjector exit, are shown in Fig. 2, as obtained from Parmela simulation [8].

The Linac

The SPARXINO linac is based on the upgrade of the existing DAΦNE injection facility. The DAΦNE injection system is a 60 m long LINAC [9] equipped with 15 S-band (2.865 GHz) SLAC-type 3 m long accelerating structures driven by four 45 MW klystrons each followed by a SLED peak power doubling system. At present it delivers 0.8 μs RF pulses at a repetition rate of 50 Hz as required for the DAΦNE operation. A quadrupole FODO focusing system is distributed along the entire linac. It accelerates the positron bunches emerging by the Positron Converter, up to the maximum energy of 550 MeV and the electron bunches up to 800 MeV. A drift space about 15 m long is available at the linac output for the installation of the undulator. The Linac energy upgrade to 1.2 GeV can be achieved, as shown in Fig. 3, by upgrading the accelerating field of the existing units up to 25 MV/m. The Linac waveguide network must also be modified in order to supply two accelerating units per RF station. This system configuration requires four new 45 MW klystrons. More over the availability for inserting four more SLAC-type sections will provide the possibility to reach a final energy of 1.5 GeV. High beam brightness can be achieved by installing a

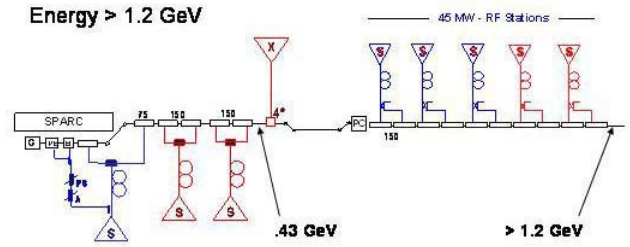


Figure 3: Scheme of the Frascati linac upgrading for SPARXINO and DAΦNE operation.

copy of the 12 m long SPARC photoinjector upstream the DAΦNE linac, with a minor modification of the existing building, and a magnetic compressor at $E \approx 430$ MeV just at the entrance of the existing Positron Converter thus keeping the possibility to operate the linac as DAΦNE injector. Nevertheless the full compatibility of the SPARXINO test facility with the DAΦNE actual operation or future upgrade is one of the basic issues of our study.

The lattice

Moving from the necessity of using existing facilities the main task was the integration of both the photoinjector and the magnetic compressor sections in the DAΦNE linac lattice, together with the design of a high energy dogleg able to drive the final electron beam to the undulator area while matching the existing building constraints. The proposed layout is schematically shown in Fig. 4; it provides the insertion of the photoinjector and the magnetic chicane before the existing Positron Converter (PC), while keeping untouched the positron source itself and the downstream 10 accelerating sections, (Linac2), and the existing quadrupole arrangement. The five accelerating sections that presently drive the DAΦNE electron beam on the PC target, will be moved to the interspace between the photoinjector exit and the magnetic chicane in order to provide the designed energy and chirp for the magnetic compression stage (Linac1). Finally the DAΦNE thermoionic gun together with the prebuncher and buncher sections will be placed on a 15 degrees beam driving the electron beam to the entrance of the Linac1. At the end of Linac2 the SPARXINO beam first travels in the existing DAΦNE transfer lines for about 34 m, then is extracted and driven up to the undulator entrance via a

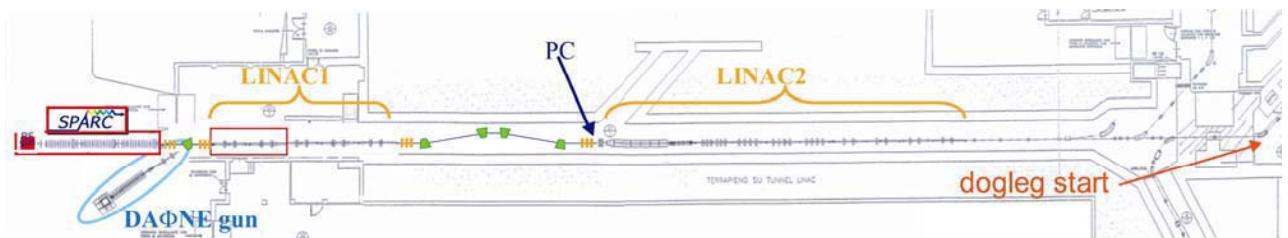


Figure 4: SPARXINO proposed layout.

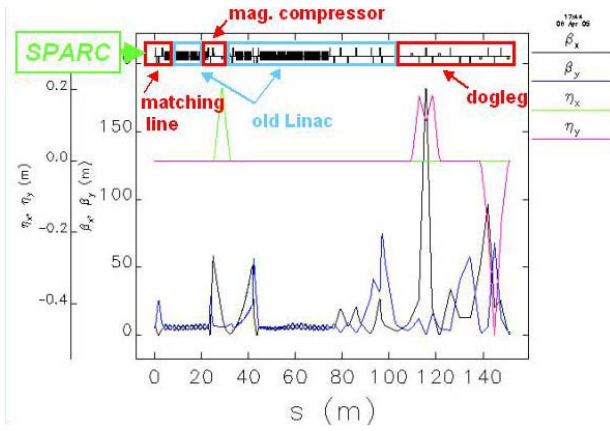


Fig. 5: Dispersion and betatron function for SPARXINO starting from the exit of the photoinjector up to the high-energy dogleg end.

four bend vertical dogleg that provides a total vertical offset of ≈ 3.4 m without affecting the final beam quality. This is meant to leave a total access to the DAΦNE experimental area at the road level, while driving the electron beam at the foreseen underground undulator and experimental area. In Fig. 5 the optic functions are reported starting from the photoinjector exit up to the end of the high-energy dogleg.

SIMULATION RESULTS

On the basis of the described layout the photoinjector out coming beam, ($\langle I_{\text{peak}} \rangle \approx 450$ A, slice analysis in Fig. 2), has been tracked using Elegant code [10] with 50k particles. The results are reported in Fig. 6 – 7. The final beam has a peak current $I_{\text{peak}} \approx 1.2$ kA, a rms length of $\approx 87 \mu\text{m}$, and a transverse normalized emittance $\epsilon_{x,y} < 1 \mu\text{m}$ on both planes along most of the bunch length. Applying Ming-Xie’s formulas [11] for the case of $\lambda=5$ nm a saturation efficiency is reached of ≈ 85 % for a 22 m saturation length, undulator $k = 1.54$ and undulator period of 2.80 cm, with a saturation power of $P_{\text{max}} \approx 3$ GW.

CONCLUSIONS

The SPARX R&D project has been approved by the Italian Government and funded in June 2004 with a three years schedule. The critical components for an X-ray FEL source, such as the RF-compression scheme, magnetic chicane, etc. will be tested during the phase II of the SPARC project and assembled in a high energy and high brightness linac, the SPARXINO test facility, by upgrading the existing Frascati linac. A first general layout for SPARXINO has been proposed taking into account the compatibility with the actual DAΦNE operation and its future upgrade, together with the existing building constraints. Start to end simulations have been presented using an innovative scheme of bunch compression which comprises a mixed RF and magnetic compression technique.

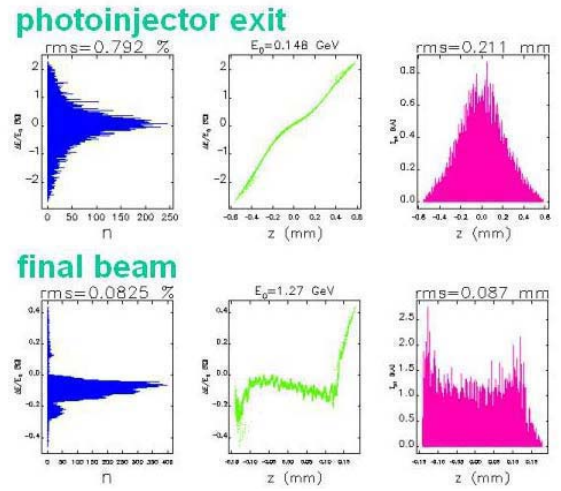


Figure 6: Energy (left) and axial (right) e^- distributions and longitudinal phase space (center) at the photoinjector exit (up) and at the high-energy dogleg end (bottom).

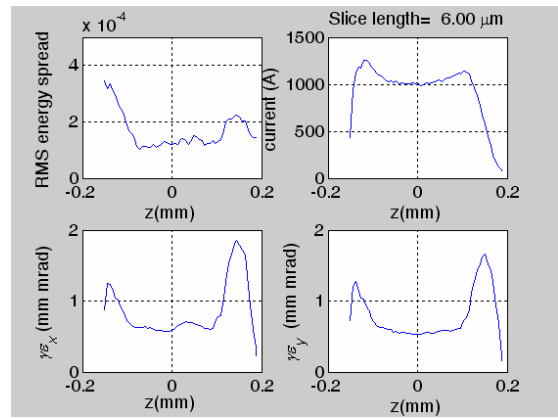


Figure 7: Energy spread, peak current and transverse emittance along the bunch, for the final beam.

REFERENCES

- [1] SPARC Project Team, Sparc Injector TDR www.lnf.infn.it/acceleratori/sparc/.
- [2] G. Vignola *et al.*, “DAΦNE, The Frascati Phi-factory”, Proc. of PAC 1993, Washington
- [3] L. Serafini and M. Ferrario, Velocity Bunching in PhotoInjectors, AIP CP 581, 2001, pag.87
- [4] M. Boscolo *et al.*, Beam Dynamics Study of RF Bunch Compressors for High Brightness Beam Injectors, Proc. of EPAC 2002, Paris.
- [5] L. Serafini, RPPT013, this conference
- [6] D.T. Palmer, The next generation photoinjector, PhD. Thesis, Stanford University
- [7] C. Ronsivalle *et al.*, WPAP009, this conference.
- [8] J. Billen, “PARMELA”, LA-UR-96-1835, 1996
- [9] S. Kulinski *et al.*, DAΦNE Tech. Note LC-4
- [10] M. Borland, "elegant: A Flexible SDDS-Compliant Code for Accelerator Simulation," Advanced Photon Source LS-287, September 2000.
- [11] M. Xie, “Design optimization for an X-ray Free Laser driven by SLAC linac”, Proc. of PAC 1995, Dallas

RECENT RESULTS FROM AND FUTURE PLANS FOR THE VISA II SASE FEL

G. Andonian, R. Agustsson, P. Frigola, A. Murokh, C. Pellegrini,
S.Reiche, J. Rosenzweig, G. Travish, UCLA, Los Angeles, CA 90095, USA
M. Babzien, I. Ben-Zvi, V. Litvinenko, V. Yakimenko, BNL, Upton, NY 11973, USA
I. Boscolo, S. Cialdi, A. Flacco, INFN-Milano, Milano, Italy
M. Ferrario, L. Palumbo, C. Vicario, INFN/LNF, Frascati, Roma, Italy
J. Huang, PAL, Pohang, S. Korea

Abstract

The VISA II (Visible to Infrared SASE Amplifier) project, a consequent experiment to the successful VISA enterprise, entails the use of a chirped electron beam to drive a high gain SASE FEL. The resulting ultra-short pulses will be characterized using an advanced FROG (Frequency Resolved Optical Gating) technique, as well as a double differential spectrum (angle/wavelength) diagnostic. Implementation of sextupole corrections to the longitudinal aberrations affecting the high energy-spread chirped beam during transport to the VISA undulator is studied. Start-end simulations, including radiation diagnostics, are discussed. Initial experimental results involving a highly chirped beam transported without sextupole corrections, the resulting high gain lasing, and computational analysis are briefly reported.

INTRODUCTION

As the promise of X-ray free electron lasers (FEL) comes close to realization [1, 2], the creation and diagnosis of ultra-short pulses is of great relevance to the SASE (Self-Amplified Spontaneous Emission) FEL (Self-Amplified Spontaneous Emission) community. Femtosecond long, Ångstrom wavelength radiation will provide the spatial resolution desired for scientific investigations at the time scales of atomic process, such as biological sampling (single molecule diffraction) [3]. Such sources are designed to operate at hundred femtosecond pulse lengths with a clear demand to push to shorter time scales.

A proposal to obtain such ultra-short pulses [4], by manipulating frequency chirped FEL output, serves as the catalyst for the VISA II experiment. The aim of the VISA II project is to operate the SASE FEL with the highest electron beam chirp allowable at the upgraded systems of the Brookhaven National Laboratory Accelerator Test Facility (BNL ATF). The production, and subsequent measurement, of strongly chirped SASE FEL radiation based on electron beam chirping is the objective of this multi-institutional collaborative effort.

EXPERIMENT DESCRIPTION

Summary of Prior Results

The VISA experiment layout is described in detail in Ref. [5]. The VISA project successfully demonstrated saturation of a SASE FEL within a 4 meter undulator at 840 nm. An electron bunch compression mechanism, exploiting the nonlinear properties of transport along the dispersive line of the ATF, was discovered to increase the peak current from 55 A to 240 A. Electron beam dynamics in the gun, transport, and undulator were modeled with the simulation codes PARMELA [6], ELEGANT [7], and GENESIS 1.3 [8] respectively. SASE FEL properties, such as pulse energy, profile, and angular distribution were modeled with GENESIS. The harvest of the start-end suite of codes was accurately benchmarked against experimental findings. The complete characterization of the SASE FEL properties included gain lengths, spectra, energies and observation of nonlinear harmonics [9].

Present Results and Analysis

Follow-up measurements at VISA took place with the employ of a highly chirped electron pulse, with longitudinal compression, and subsequent FEL amplification. An anomalously large bandwidth, up to 15% full width, was observed at high gain accompanied by atypical far-field angular radiation patterns (Fig. 1).

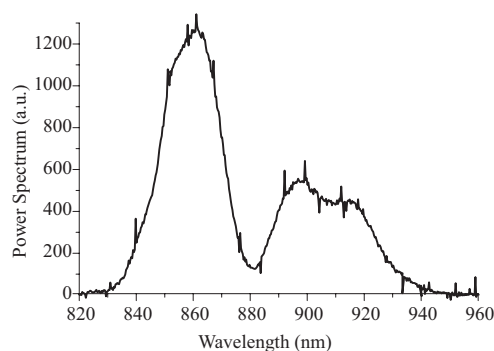


Figure 1: Sample shot of observed SASE FEL spectrum with anomalously large bandwidth. Start-end simulations were able to reproduce key facets of the spectrum.

An electron bunch, of approximately 330 pC, with 1.7% energy spread, was propagated through the undulator. Due to nonlinear compression, the peak current of the pulse reached 300 A. The compression, as well as the SASE FEL output, was extremely stable and insensitive to RF and laser timing jitter. After transport, the electron beam displayed a highly nonlinear longitudinal phase space. The average measured SASE radiated energy was approximately 2 μ J and displayed an extraordinary wavelength distribution. The spectrum is notable for a characteristic double peak structure, accompanied by a mean bandwidth value of 12% full width (in excess of 100 nm), as seen in Fig. 1.

Start-end simulations were able to reproduce the unique features of the radiation and held the key for the physical understanding behind this previously unobserved FEL amplification. Indeed, GENESIS simulations reproduced the large bandwidth and the associated double spiked structure. The secondary spike was due to amplification of an off-axis mode. The mode was excited by the non-ideal centroid and envelope motion of the beam through the undulator's quadrupole focusing lattice. Mismatches of the beam's lasing core to the focusing lattice caused excursions in beam size near 30 μ m in both transverse planes. Additional transverse motion causes a red-shift in the radiated wavelength and an ensuing inclination to amplify the off-axis modes.

Double Differential Spectrometer

An additional diagnostic has been developed to unfold the relationship between frequency and angle of the FEL radiation. This diagnostic employs the use of an adjustable slit, two cylindrical lenses for focusing, a set of gratings, and a CCD. A slice of the FEL output is passed through the slits, then focused onto the gratings (1200 in^{-1}). The resulting image displays the photon beam with frequency along one axis, and transverse angle along the other axis. The double-differential spectrometer is calibrated with the spectral lines of an Argon lamp. The resultant outcome is a direct study of the intensity of the beam presented in a most familiar form, $\frac{d^2 I}{d\omega d\theta}$, the double differential spectrum.

Some recent data of this diagnostic is shown in Fig. 2. The overall parabolic structure of the beam in (θ, ω) space is evident, with even richer multi-mode patterns also present.

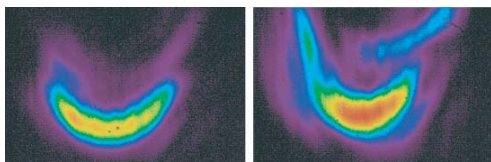


Figure 2: The overall parabolic structure (left) is clear in the images from the double differential spectrometer, where the angle is represented along the horizontal axis and the frequency along the vertical. More exotic and richer structures have also been observed (right).

Start-end simulations have been carried out to examine

these results further. The GENESIS post-processing unit has been upgraded to compute the double differential spectrum for the experimental parameters at VISA. Preliminary runs display the aforementioned parabolic structure and even some higher order modes are apparent, confirming the dual lasing modes observed in previous runs (Fig. 3).

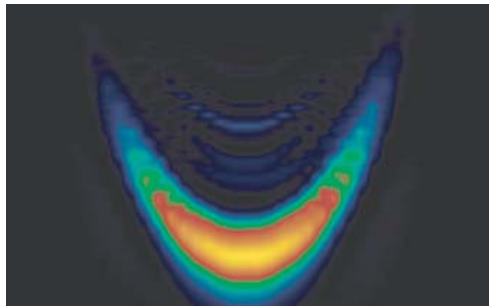


Figure 3: Output from a GENESIS simulation confirms the parabolic nature observed in VISA. Angles lie along the horizontal axis, frequencies along the vertical.

Far-field Angular Distribution

A unique ancillary component of the experiment is the observed angular distribution profile in the far-field. This measurement was made by allowing the output radiation, to propagate, without focusing lenses, to a screen approximately 3 m ($10 Z_R$) away. The patterns observed were hollow in nature, like previous VISA results, but more pronounced in angle. Spiral shaped patterns accompanied the hollow modes. The helicity of this patterns will be studied via a mode converter, described later in this note.

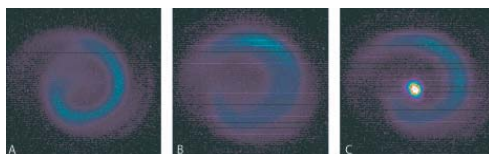


Figure 4: Far-field angular distribution profiles from VISA demonstrating the atypical spirality and helicity (A,B) and superimposed with a red diode alignment laser for reference (C).

UPCOMING MEASUREMENTS

Chirped Beam Operation

The main goal of the VISA II experiment is to inject a linearly chirped electron beam into the undulator to produce frequency chirped SASE FEL radiation. Although the bunch compression mechanism facilitates high-gain lasing, it restricts the management of beam properties through transport. Preservation of the electron beam chirp applied at the linac will be accomplished by the manipulation of nonlinear longitudinal compression by the use of

sextupole magnets placed at points of high horizontal dispersion. The sextupoles will mitigate second order effects, particularly by diminishing the T_{566} element, of the transport matrix, to a negligible value [10].

Measuring the T_{566} term directly presents a challenge as compression is required for high gain lasing in VISA II. The actual value that can be quantified is the T_{166} element. This value is measured by comparing the effect of incremental changes in the magnetic fields of all magneto-optic elements along the beamline to the change in position of the electron beam centroid at a point of non-zero dispersion. The correlation between the T_{166} and T_{566} terms is used to quantify the effects of the sextupoles.

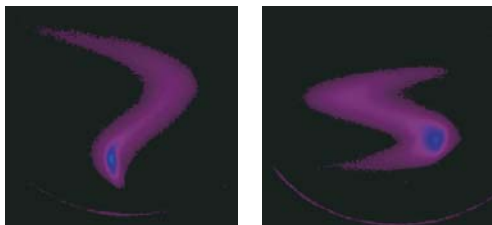


Figure 5: Two transverse profiles of the electron beam in the dispersive section of the transport with sextupole magnets energized. To create such extreme profiles the settings of the sextupoles were exaggerated from the ideal values computed using simulations.

Optical Diagnostics

Once electron beam chirp is preserved, subsequent SASE FEL lasing at high gain is achieved. The resulting radiation will be frequency chirped. A standard method of measuring the structure of short pulse, frequency chirped light is frequency resolved optical gating (FROG) [11]. For the expected parameters of the VISA II SASE FEL, FROG seems to be the most viable candidate.

One aspect of FROG, or GRENOUILLE (a close relative of FROG designed to simplify alignment issues by employing fewer, multi-purpose optical elements), that is a concern for the proposed measurement is the resolution of the spectrogram. For the radiated profile presented in previous results and properties noted in GENESIS simulations, namely the anomalously large spectral width and the hollow mode angular distribution pattern, the FROG technique needs modification to efficiently serve its purpose. The proposed modifications revolve around the GRENOUILLE diagnostic, which employs the use of a thick crystal with the dual purpose of recombination and dispersion of the split signal. The system is too constrained by the doubling crystal to properly resolve the radiation expected from the VISA II FEL. The thick lens must be replaced by a thin lens and a dedicated spectrometer. In addition, a larger (several megapixel) CCD must replace the camera that is used in the commercial version of this diagnostic.

Simulations concerning the feasibility of this measurement have been conducted. GENESIS outputs for the

chirped beam case show a clear effect for idealized beam shapes. These results have been analyzed for varying degrees of chirp. Indeed, the inversion algorithm is robust enough to handle other exotic shapes and patterns which have been simulated and reconstructed via the commercial FROG software (Femtosoft) for the VISA II experiment.

Mode Converter and Polarizer

The investigation of hollow mode and spiral shaped far-field angular radiation patterns at VISA continues via a diagnostic mode converter. The mode converter is design to transform light with Hermite-Gaussian modes to Laguerre-Gaussian modes; the transfer of orbital angular momentum is the observable [12]. The $\pi/2$ mode converter is constructed of two cylindrical lenses, separated by a distance of $d = \sqrt{2}f$, and the resultant light will have distinct observable properties.

The VISA project will also examine the study of Transition Undulator Radiation (TUR) [13], the radiation emitted by the electron bunch as it passes through the entrance and exit of the undulator, due to its change in longitudinal velocity. In fact, this radiation is thought to be radially polarized, describing yet another possible explanation for the helicity of the observed far-field patterns from the planar undulator at VISA. The quantization of this effect requires minimal alteration of already existing diagnostics with the addition of grid polarizers to determine the polarization of the radiation.

This work supported by Dept. of Energy Contract no. DE-FG-98ER45693, and Office of Naval Research no. N000140210911

REFERENCES

- [1] M. Cornacchia *et al.*, Linac Coherent Light Source Design Study Report no. SLAC-521 (1998)
- [2] TESLA-FEL, Deutsches Elektronen Synchrotron 2001-05 (2001)
- [3] R. Neutze *et al.*, Nature **406**, 752 (2000)
- [4] C. Schroeder *et al.*, J. Opt. Soc. Am. B **19**, 1782 (2002)
- [5] A. Murokh *et al.*, Phys. Rev. E **67**, 066501 (2003)
- [6] L.M. Young, J.H. Billen, Los Alamos National Laboratory Report No. LA-UR-96-1835 (rev. 2000)
- [7] M. Borland, Advanced Photon Source LS-287 (2000)
- [8] S. Reiche, Nucl. Instrum. Methods A **429**, 243 (1999)
- [9] A. Tremaine *et al.*, Phys. Rev. Lett. **88**, 204801 (2002)
- [10] J. England *et al.*, Phys. Rev. ST Accel. Beams **8**, 012801 (2005)
- [11] R. Trebino, *Frequency Resolved Optical Gating*, Kluwer Academic Publishers (2000)
- [12] M.W. Beijersbergen *et al.*, Optics Comm. **96**, 123-132 (1993)
- [13] S. Reiche *et al.*, Proceedings of the 2004 FEL Conference, 193-196, Trieste, Italy.

ELECTRON CLOUD BUILD-UP STUDY FOR DAΦNE*

R. Cimino, A. Drago, C. Vaccarezza, M. Zobov, INFN-LNF, Frascati, Italy
 G. Bellodi, CCLRC/RAL/ASTeC, Didcot, Oxford
 D. Schulte, F. Zimmermann, CERN, Geneva
 G. Rumolo (GSI, Darmstadt), K. Ohmi, KEK, Ibaraki
 M. Pivi, SLAC, CA, USA

Abstract

After the first experimental observations compatible with the presence of the e-cloud effect in the DAΦNE positron ring, a more systematic study has been performed regarding the e-cloud build-up. The measured field map of the magnetic field has been taken into account in the simulation for elements present in the four 10 m long bending sections, representing 40% of the whole positron ring. The obtained simulation results are presented together with the recent experimental observations performed on the vacuum behaviour of the positron ring.

INTRODUCTION

DAΦNE is an electron-positron collider with 1.02 GeV centre of mass energy (Φ-factory) [1]. The collider consists of two symmetric main rings, 97 m long, lying in the same horizontal plane and sharing two Interaction Regions (IR). Two experiments can be installed in the IRs and run separately: three detectors have been realized so far, KLOE, DEAR and FINUDA. KLOE (IR1) and DEAR (IR2) have taken data until December 2002, while FINUDA has been installed in September 2003 in the IR previously occupied by DEAR (IR2) and took data until April 2004. Starting from May 2004 the KLOE experiment is running again. For each circulating beam the maximum design current value is 5 A over 120 bunches, at an average dynamic pressure of 1 nTorr; up to now the maximum achieved current value is 2.4 A for the electron beam (not physical but administrative limit) and 1.3 A for the positron one.

After the 2003 shutdown for the FINUDA detector installation, and some optics and hardware modifications, the appearance of a strong horizontal instability for the positron beam at a current $I \sim 500$ mA, triggered the study of the e-cloud effect in the DAΦNE collider. Until 2003 the presence of the e-cloud induced instability was not clearly evident, due to the fact that even in the case it existed, other limitations to the luminosity were much stronger such as for example the beam-beam effect, parasitic crossings and so on. Nevertheless some different behaviour between the positron and electron ring were observed: a larger positive tune shift induced by the positron beam current [2], a fast horizontal instability whose rise time cannot be explained only by the beam interaction with parasitic HOM or resistive walls [3]; finally the comparison of the observed behaviour of the vacuum pressure vs. the total current between the electron and positron ring seems to provide a clearer evidence for

the presence of the e-cloud instability as reported in the following sections. A more systematic study of the electron cloud build-up was started including the DAΦNE wiggler field map in the simulation code. Furthermore the first results of a measurement programme of the relevant surface parameters for the DAΦNE vacuum chamber were adopted in the simulation. The obtained results are presented in this paper providing the input for a detailed instability study.

THE DAΦNE POSITRON RING

The Main Ring vacuum chamber is designed in such a way that most of the Synchrotron Radiation that is emitted in the four arcs is stopped in the antechambers by water-cooled copper absorbers. Each arc is a single-piece only vacuum chamber, about 10 m long, hosting two dipoles and a wiggler magnet, together with three quadrupoles and two sextupoles. The vacuum vessel inside the arc actually consists of two chambers connected through a narrow slot [4]. The beam circulates in the first chamber, while the synchrotron radiation photons hit a system of copper absorbers located in the second one (antechamber) in such a way that more than 95% of the photon flux is intercepted in the antechamber. The arc vessel is made by two halves of Al alloy 5083-H321 plates, which, after machining, are welded along the middle plane. The inner surface is mirror finished (roughness = 0.2 Ra). The straight sections were made by extrusion of the same aluminum alloy, with a round cross section of $\varnothing=88$ mm. Four splitter dipoles bend the

Table 1: DAΦNE parameter list for FINUDA and KLOE experiment configurations.

	KLOE 2002	FINUDA 2003	KLOE 2004
E (GeV)	.51		
h	120		
N_b	49	100	108
ε_x (μrad)	.74	.34	.34
κ	0.003	0.003	0.003
σ_z (mm rms)	15÷25	10÷25	10÷25
I_{tot} (A)	1.8/1.1	2.4/0.8	2.4/1.3
L_{peak} ($\text{cm}^{-2}\text{s}^{-1}$)	0.8×10^{32}	0.6×10^{32}	1.4×10^{32}

electron and positron beams nearby the entry/exit of the two interaction regions; the splitter chambers, 1.5 m long, were machined from the same Al alloy, with normal finishing. For the KLOE and FINUDA detectors two beryllium alloy (ALBeMet) vacuum thin chambers are provided, 70 cm and 50 cm long respectively. The parameter list for the KLOE and FINUDA experiment configurations are reported in Table 1.

PRESSURE RISE WITH CURRENT

After the first indications of the e-cloud build-up in the positron ring a signature was looked for in the vacuum behaviour for the two beams. A closer monitoring of the residual pressure was performed and the gauge readings were recorded every 15 s by the DAΦNE control system and logged in the daily data sheet together with the main operating parameters such as beam current, luminosity, beam lifetime and so on. In both the electron and positron rings 14 Bayard Alpert vacuum gauges are located, one in each of the two interaction regions, one per arc, and one upstream and down stream of each arc respectively. Looking at the gauge readings and comparing the observed behaviour between the electron and positron ring some relevant differences are found as it is shown in Fig 1. In this figure the pressure readings are plotted as recorded from the gauges located in the straight sections in both the electron and positron ring. Looking at the plots over a whole day acquisition the positron beam exhibits a non-linear behaviour of the pressure together with a blow-up for definitely lower current values than those circulating in the electron ring. It has to be mentioned that a typical worsening of the effect was observed at each machine operation resuming even after a short stand-by period (typically one maintenance week). Nevertheless the vacuum recovery takes less than two days while a steady overall improvement due to beam conditioning is

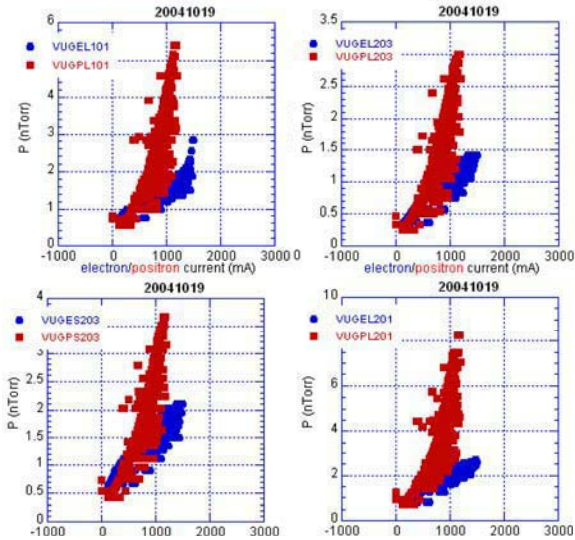


Figure 1: Vacuum pressure read-out vs. total current as recorded in four straight section locations for the electron (blue dots) and positron (red dots) rings.

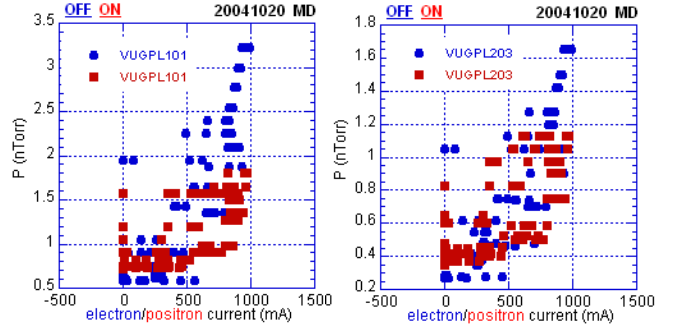


Figure 2: Vacuum pressure read-out vs. total current as recorded in 2 straight section of the positron ring where a 50 G solenoid field was turned on (red dots) and off (blue dots).

present. The pressure readings for the arcs are not reported due to the fact that in this case each vacuum gauge is located in the antechamber close to the pumping station, (Titanium Sublimation Pumps plus Sputter Ion Pumps), definitely far from the beam region. Later in the 2004 run, a small fraction of drift sections (about 2 m) were wrapped with a coil to provide a solenoid field of about $B_z \approx 50$ G. The vacuum pressure read-out is reported in Fig. 2 for the solenoid ON-OFF cases: quite a 50 % pressure burst reduction was locally obtained, but no remarkable effect showed up on the collider luminosity.

SIMULATION RESULTS

A more systematic study of the e-cloud build-up was started considering the stray and fringing magnetic field effect on the straight sections, including the magnetic field map in the wiggler simulation, and taking into account the recently measured surface parameters.

The wiggler magnetic field characterization was performed measuring the vertical magnetic field component B_y , over a 16×330 rectangular point matrix on the x - z plane [5]. Starting from the measured values a bi-cubic spline fit was performed with the help of the NAG FORTRAN subroutines, and the obtained coefficients were used for the field reconstruction. At the first order approximation the three components can be obtained from:

In Fig. 3 the field reconstruction result are reported

$$B_x = \frac{\partial B_{y0}(x,z)}{\partial x} y, \quad B_z = \frac{\partial B_{y0}(x,z)}{\partial z} y,$$

$$B_y = B_{y0} - \frac{1}{2} \left(\frac{\partial^2 B_{y0}(x,z)}{\partial x^2} + \frac{\partial^2 B_{y0}(x,z)}{\partial z^2} \right) y^2.$$

showing the fit quality. The subroutine was included in the E-CLOUD code [6] and the obtained e-cloud linear density is shown in Fig. 4 while in Table 2 the simulation parameters are reported. It has to be pointed out that in the case of wiggler the presence of the slot has been taken into account considering only the photons that hit the slot

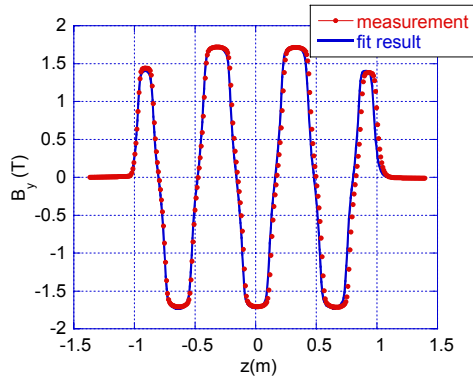


Figure 3: Wiggler magnetic field along the longitudinal axis as obtained from measurement (red dots) and fit reconstruction (blue line).

edges. The vacuum chamber photoelectron yield $Y \approx .19 \div$

Table 2: Ecloud simulation parameter list

Bunch population	N_b	2.1×10^{10}
Number of bunches	n_b	100
Missing bunches	N_{gap}	20
Bunch spacing	L_{secp}	.8 m
rms bunch length	σ_z	18 mm
rms horizontal size	σ_x	$1.1 \div 1.4$ mm
rms vertical size	σ_y	$0.05 \div 0.1$ mm
Max sec. emission yield SEY	δ_{max}	1.9
Energy at max at SEY	ε_{max}	250 eV
Al eff. photoelectron yield	y_{eff}	0.2
Vac. chamber hor. aperture	$2 h_x$	$88 \div 120$ mm
Vac. chamber ver. aperture	$2 h_y$	$20 \div 88$ mm
Bending field	B	$0 \div 1.7$ T
Primary electron rate	$d\lambda_e/ds$	$0.0088 \div 0.26$
Photon reflectivity	R	50-60 %
elastic electron reflection	Cimino-Collins	

.2 and the reflectivity values have been obtained from the measurements performed by Mahne *et al.* [7] on an Al 5083-H321 sample with the same surface finishing as the actual vacuum chamber. The simulations for the drift sections, where most of the photons not intercepted by the arc slot hits the vacuum chamber wall, have also been performed adopting the measured parameters. The results are shown in Fig. 5 for three cases: simple drift, drift plus a moderate magnetic field of $B_y \approx .1$ T, to take into account some residual fringing and stray field, finally drift with a solenoid of $B_z \approx 50$ G.

CONCLUSIONS

After the first indications of the electron-cloud effect in the DAΦNE positron ring, more systematic measurement and simulation activity have started. A signature of the e-cloud build-up was found in the different vacuum behaviour of the electron and positron rings, as shown. The measured field-map for the wiggler magnetic field has been included in the simulation code, together with

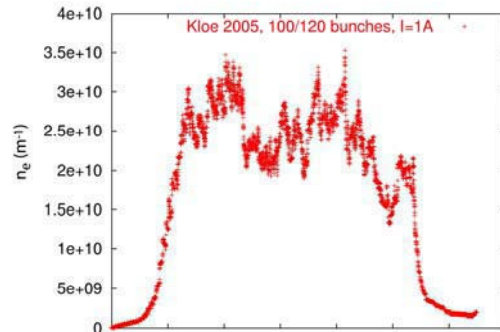


Figure 4: Electron cloud build-up along one bunch train for the wiggler. (Primary electron rate $d\lambda_e/ds = 0.0088$)

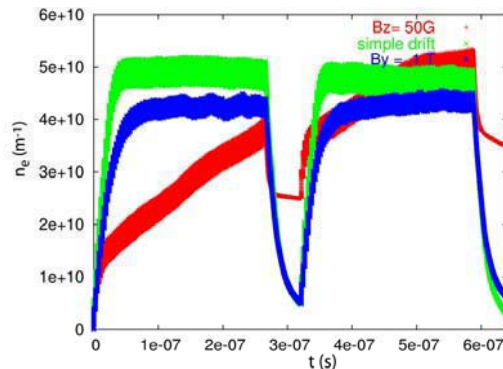


Figure 5: Electron cloud build-up along two bunch trains for the drift downstream of the arc: a) simple drift, b) drift with residual magnetic field of $B_y \approx .1$ T, c) drift with a 50 G solenoid. (Primary electron rate $d\lambda_e/ds = 0.26$)

some DAΦNE surface parameters as come out from the measurements [7]. The simulation results, here shortly reported, show a significant value of the electron linear density for a beam current of $I_b \approx 1$ A. The study is underway in order to understand whether the obtained electron-cloud density can be related to the observed fast horizontal instability [3] and the large positive tune shift.

REFERENCES

- [1] G. Vignola, *et al.*, PAC'91, San Francisco.
- [2] C. Vaccarezza, *et al.*, ECLLOUD04, Napa Valley proc.
- [3] A. Drago *et al.*, MPPP024, these proceedings
- [4] V. Chimenti *et al.*, PAC93, Washington
- [5] M. Preger, DAΦNE Tech. Notes, L-34
- [6] G. Rumolo, F. Zimmermann, CERN-SL-Note-200-016
- [7] N. Mahne *et al.*, FPAP002, these proceedings

* This work is partly supported by the Commission of the European Communities under the 6th Framework Programme "Structuring the European Research Area", contract number RIDS-011899

EXPERIMENTAL DETERMINATION OF E-CLOUD SIMULATION INPUT PARAMETERS FOR DAΦNE*

N. Mahne, TASC-INFM Trieste (Italy)

A. Giglia, S. Nannarone, TASC-INFM Trieste (Italy) and Univ. Modena e RE, Modena (Italy)

R. Cimino, C. Vaccarezza, LNF-INFN Frascati (Italy)

Abstract

DAΦNE is an electron-positron collider with 1.02 GeV center of mass energy. For each circulating beam the maximum design current is 5 A. Preliminary simulations predicted e-cloud induced beam instabilities in the positron ring. Such calculations were based on literature results on aluminum reflectivity, photon yield, etc., not directly measured from the actual DAΦNE chamber wall material. Here we show how calculations strongly depend on the assumed reflectivity and photon yield values. These two quantities have been measured using synchrotron radiation on samples prepared and made of the same aluminum alloy (Al 5083) used for the storage ring of DAΦNE. The obtained experimental results are implemented in the calculations.

INTRODUCTION

Low-energy background electrons in particle accelerators can interfere with the correct operation of the machine itself; there are operating conditions that can lead to large amplification of the electronic cloud. The electrons can be produced directly by ionization of the residual gas molecules or by irradiation of the vacuum chamber surfaces by synchrotron radiation, ions, beam particles, or electrons themselves. If the cloud density becomes sufficiently large, the beam-cloud interaction can degrade the particle beam. In positive charged particle rings, the electron cloud can oscillate synchronously with the particle bunches, giving rise to an exponentially growth of the electron density. This phenomenon, called *multipacting*, is manifested by an anomalous vacuum pressure rise and can produce beam instabilities. In order to predict, and possibly prevent these problems, some simulations must be performed on the formation and development of the electron cloud in accelerator rings.

These arguments apply also to the case of the DAΦNE Φ-Factory[1,2,3,4]: it is a twin ring 510 MeV electron-positron collider facility at INFN-LNF Frascati National Laboratories (Italy). The collider consists of two symmetric and concentric main rings, about 100m long, laying in the same horizontal plane, sharing two interaction regions (IR), in which the electron/positron beams cross at a small tunable angle of ± 12.5 mrad. The luminosity peak value is given by:

$$L_{peak} \propto \frac{I^+ I^-}{4\pi\sigma_x\sigma_y}$$

where I^+ and I^- are the colliding beam total currents and σ_x and σ_y are the beam sizes in the collision point. Any effect that prevents the above quantities to reach their

design values has to be studied and counteracted, as it is the case of the e-cloud buildup that limits the maximum positron current in the storage ring, as explained above.

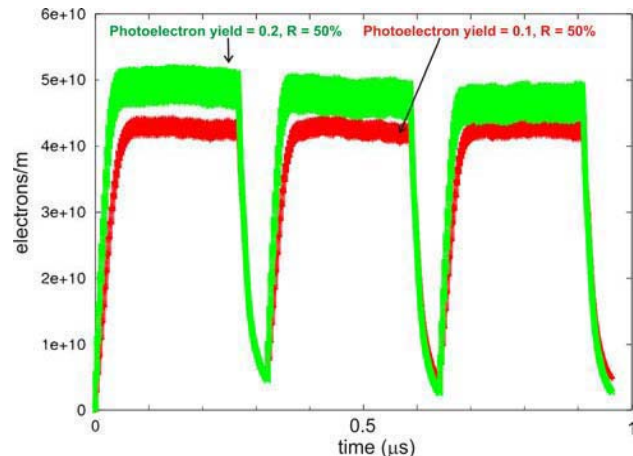


Figure 1: mean e-cloud linear density in the storage ring calculated for two different photoelectron yield values (0.2 and 0.1) with a reflectivity of 50%.

CALCULATIONS

Several codes are available to evaluate e-cloud density around the circulating beam, but most of the parameters are strictly dependent upon the vacuum chamber geometry, the material choice, and its surface finishing.

Here we concentrate on the relevance of photon reflectivity and photon yield on the simulated e-cloud build up. The E-CLOUD code [5] has been used to simulate the average e-cloud linear density as a function of reflectivity and photoelectron yield. This is shown Fig 1-2 where it is clear the importance of using the appropriate parameters. In Fig. 1 the e-cloud linear density is reported for two different photoelectron yield values, while in Fig 2 the electron density is plotted changing the reflectivity. The effect on the electron density is relevant for both the two cases and shows how much is important the exact knowledge of these parameters in order to obtain a reliable estimation of the e-cloud effect impact on the collider performance and its remedy efficiency.

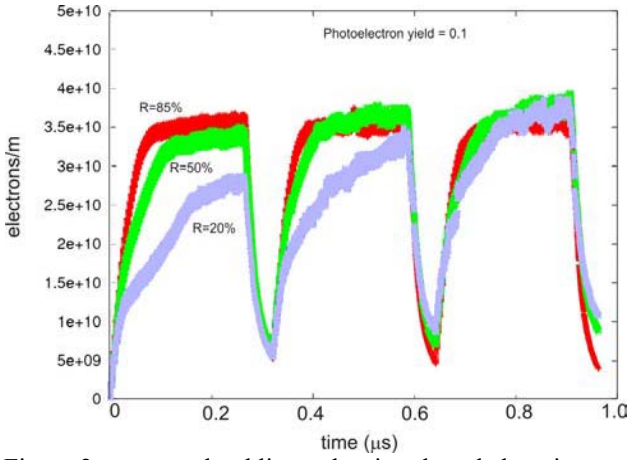


Figure 2: mean e-cloud linear density plotted changing the value of the reflectivity (85%, 50%, and 20%) with a photoelectron yield of 0.1.

EXPERIMENTAL RESULTS

The reflectivity $R(\omega)$ and the photoelectron yield $Y(\omega)$ have been measured at the BEAR beamline at Elettra (Trieste, Italy) [6] in the photon energy range from 10 to 1000 eV, using a calibrated photodiode (AXUV100 by the IRD Inc.) [7] and a picoammeter for the measure of the drain current. The sample is made of the material used for the vacuum vessel (an aluminum alloy Al 5083-H321). The six degrees of freedom of the spectroscopy chamber of the beamline [8] allowed us to measure the specularly reflected light impinging onto the sample at three different incidence angles (85° , 45° , and 5°), and the diffused light setting the photodiode far from the specular direction. A tungsten mesh, absorbing about 10% of the incoming flux, calibrated with the directly illuminated photon detector, was used to constantly monitor the incoming flux. The results are presented in Fig 3 and 4 for the specular reflectivity. The diffused light was also measured and was negligible in all cases. We can calculate the total light intensity reflected by the DAΦNE walls. It is given by:

$$I_r = \int_0^\infty d\omega I(\omega) R(\omega)$$

where $I(\omega)$ is the synchrotron radiation photon flux produced in the bending sections of DAΦNE with a ring current of 1 A. The integrated reflectivity I_r/I ($I = \int_0^\infty d\omega I(\omega)$) calculated for the incidence angles 85° , 45° , and 5° is reported in the following table.

θ_i	I_r / I
85°	27%
45°	0.2%
5°	0.1%

Fig 5 shows the number of photons reflected by the DAΦNE walls as function of the incident photon energy.

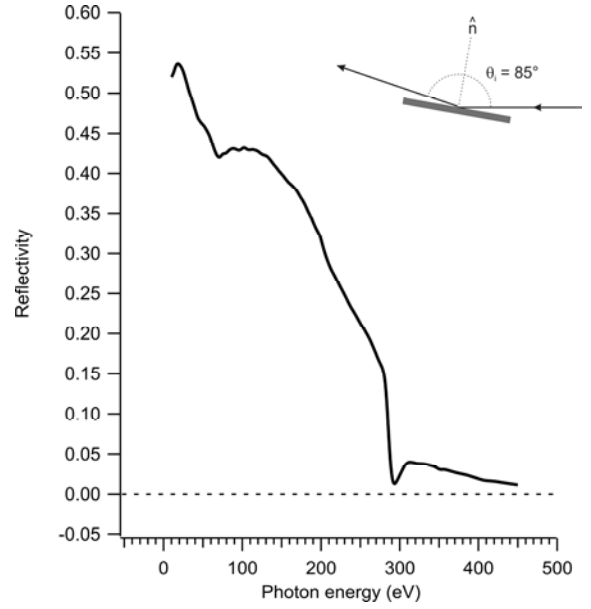


Figure 3: Reflectivity measurement with an incidence angle of 85° .

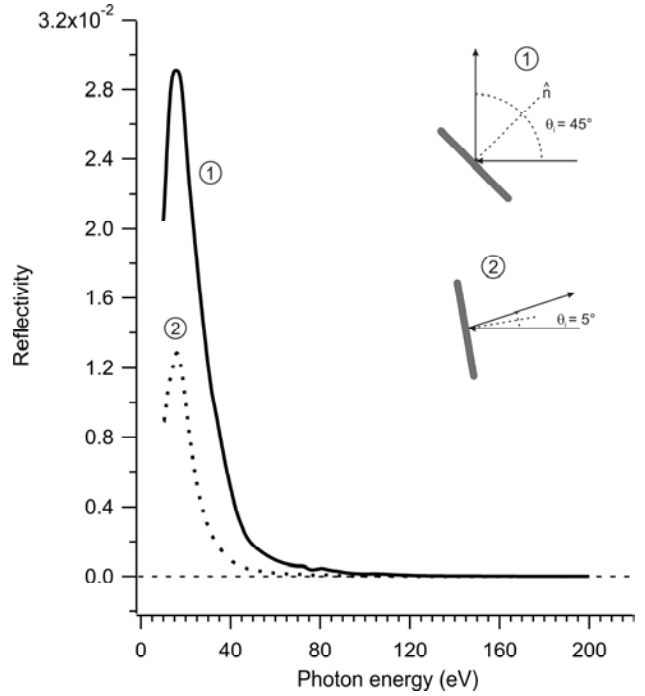


Figure 4: Reflectivity measurement with an incidence angle of 45° (1) and 5° (2).

The used experimental apparatus permits us to determine the photoelectron yield (PY), i.e. the number of electrons produced by an incident photon. The number of electrons emitted by the material is determined measuring the current I_{sample} drained by the sample when it is illuminated by the photon flux. The calculated photoelectron yield values are plotted in Fig 6.

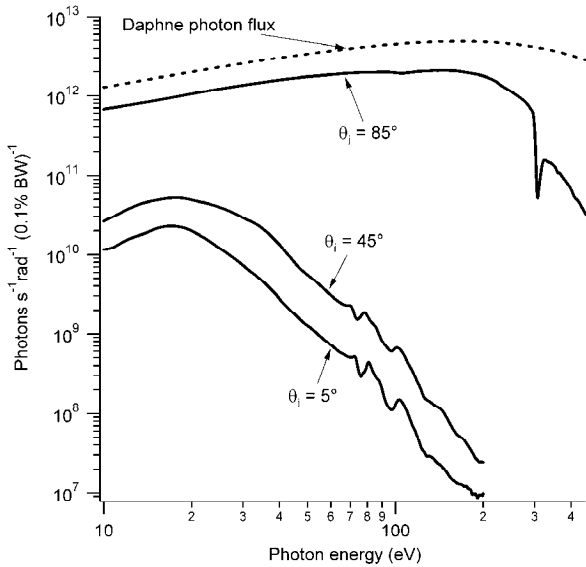


Figure 5: Number of reflected photons obtained by the reflectivity curves at incidence angle $\theta_i = 85^\circ, 45^\circ, 5^\circ$.

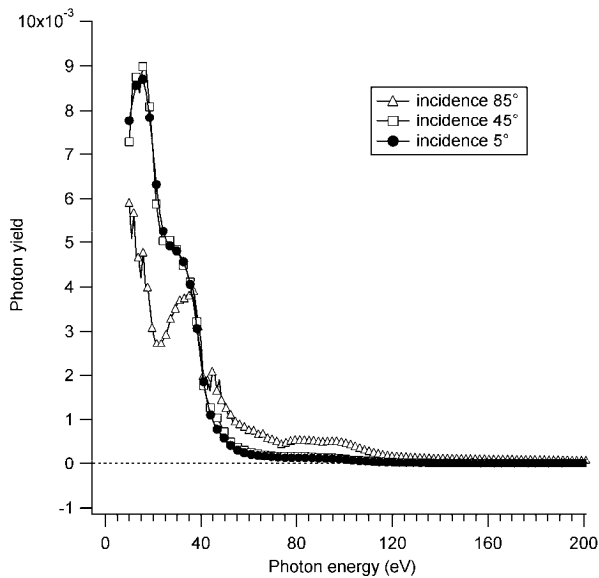


Figure 6: Photoelectron yield of the Al sample measured at incidence angles $85^\circ, 45^\circ, \text{ and } 5^\circ$.

The total PY is calculated by integration of the plot and it gives the total number of electrons produced by the material when it is illuminated by photons in the range 10-1000 eV. The total PY is about 0.2 in all three cases even though the shape of the three curves are slightly different. For grazing incidence (85°) the PY is higher than that measured at 45° and 5° for photon energies greater than about 40 eV, while at smaller incidence angles the PY is much more significant at lower energies. The PY curves for incidence 45° and 5° are almost the same at low energies (between 10 eV and 100 eV).

CONCLUSIONS

Electron cloud simulations have been performed to study the dependence of the obtained results from the

values of reflectivity and photoelectron yield used to perform the simulations. The results suggest the need of using experimentally determined values to be able to extract reliable predictions of e-cloud build up. Synchrotron radiation studies showed that the parameters used so far in the simulations are different from the experimental data obtained from the Al samples representative of the DAΦNE vacuum chamber. The code has been implemented with the measured values. This suggests the need to extract experimental values for reflectivity and photoelectron yield of the material used in other accelerator machines where electron cloud simulations are required.

REFERENCES

- [1] V. Chimenti, A. Clozza, H. Hsieh, G. Baffone, C. Vaccarezza, The DAΦNE main ring vacuum system. In *1993 Particle Accelerator Conference*, May 1993.
- [2] A. Clozza, V. Cimenti, C. Vaccarezza, An UHV vacuum system for DAΦNE. In *5th European Particle Accelerator Conference*, Jun 1996
- [3] The DAΦNE project team. DAΦNE: The Frascati Φ-factory. In *1991 Particle Accelerator Conference*, May 1991.
- [4] C. Vaccarezza, M. Biagini, A. Clozza, A. Drago, S. Guiducci, M. Zobov, G. Bellodi, G. Rumolo, F. Zimmermann. Experimental observations and e-cloud simulations at DAΦNE. In *EPAC2004*, 2004.
- [5] G. Rumolo, F. Zimmermann, CERN-SL-Note-200-016.
- [6] S. Nannarone, F. Borgatti, A. DeLuisa, B.P. Doyle, G.C. Gazzadi, A. Giglia, P. Finetti, N. Mahne, L. Pasquali, M. Pedio, G. Selvaggi, G. Naletto, M.G. Pelizzo, G. Tondello. The BEAR beamline at Elettra. In *AIP Conference Proceeding*, volume 405, 2004. See also <http://new.tasc.infm.it/research/bear/scheda.php>
- [7] Absolute XUV silicon photodiode (AXUV series). International Radiation Detectors Inc. also available at <http://www.ird-inc.com>.
- [8] L. Pasquali, A. DeLuisa, S. Nannarone. The UHV experimental chamber for optical measurements (reflectivity and absorption) and angle resolved photoemission at BEAR beamline at Elettra. In *AIP Conference Proceeding*, volume 705, page 1142, 2004.

* This work is partly supported by the Commission of the European Communities under the 6th Framework Programme “Structuring the European Research Area”, contract number RIDS-011899.